MODELING AND DESIGN OF COMPACT MICROWAVE COMPONENTS AND SYSTEMS FOR WIRELESS COMMUNICATIONS AND POWER TRANSMISSION

A Dissertation

by

PAOLA ZEPEDA

Submitted to the Office of Graduate Studies of
Texas A&M University
in partial fulfillment of the requirements for the degree of

DOCTOR OF PHILOSOPHY

May 2003

Major Subject: Electrical Engineering

MODELING AND DESIGN OF COMPACT MICROWAVE COMPONENTS AND SYSTEMS FOR WIRELESS COMMUNICATIONS AND POWER TRANSMISSION

A Dissertation

by

PAOLA ZEPEDA

Submitted to Texas A&M University
in partial fulfillment of the requirements
for the degree of

DOCTOR OF PHILOSOPHY

Approved as to style and content by:

Kai Chang
(Chair of Committee)

Robert Nevels
(Member)

Karan Watson
(Member)

Donald Naugle
(Member)

Chanan Singh
(Head of Department)

May 2003

Major Subject: Electrical Engineering

ABSTRACT

Modeling and Design of Compact Microwave Components
and Systems for Wireless Communications
and Power Transmission. (May 2003)
Paola Zepeda, B.S., École Polytechnique de Montréal;
M.S., École Polytechnique de Montréal
Chair of Advisory Committee: Dr. Kai Chang

The contribution of the work here presented involves three main topics: Wireless Power Transmission (WPT) technology, phased array systems, and microwave components design and modeling. The first topic presents the conceptual design of a WPT system at 2.45GHz with 90% efficiency and 1MW of DC output power. Second, a comparative study between 2.45 and 35GHz WPT operation is provided. Finally, the optimization of a taper distribution with reduced thermal constraints on a sandwich transmitter is realized. For a 250- and 375-m antenna radius, 89.7% of collection efficiency with 29% reduction in maximum power density (compared to the Gaussian), and 93% collection efficiency with 39% reduction of maximum power density, are obtained respectively with two split tapers. The reduction in maximum power density and the use of split taper are important to alleviate the thermal problems in high power transmission.

For the phased array project, the conceptual design of a small-scale system and in-depth analysis using two main approaches (statistical and field analysis) is realized. Practical aspects are addressed to determine the phased array main design features. The statistical method provides less accurate results than the field analysis since it is intended for large arrays. Careful theoretical analysis led to good correlation between statistical, field analysis and experimental results.

In the components chapter, efficient loop transitions used in a patch antenna array are designed at K- and W-band. Measured insertion loss (IL) K-band loop is under 0.4dB. The K- and W-band antenna array measured broadside gains are 23.6dB at 24.125GHz and 25dB at 76.5GHz with return loss under 9.54dB from 24 to 24.4GHz and 12 dB from 75.1 to 77.3GHz, respectively. Also, a multilayer folded line filter is designed at 5.8GHz and compared to planar ring filters. Improved measured bandwidth from 2GHz to 7.5GHz and IL of 1.2dB are obtained with approximately half the size of a planar ring resonator. Thirdly, a simplified switch model is implemented for use in broadband phased-shifters. The model presents very good fit to the measured results with an overall total error under 3%, magnitude error less than 8%, and phase errors less than ±0.4º.

DEDICATION

I would like to thank my husband Benoit for all his love, encouragement and generous help.
This project would not have been possible without the support from my family,
especially my parents Alejandro and Teresa, and sister Joanna.

ACKNOWLEDGMENTS

I would like to express my deepest gratitude to my advisor Dr. Kai Chang for guiding me through my research. I would like to thank Dr. Robert Nevels, Dr. Karan Watson and Dr. Donald Naugle for serving on my committee and for their helpful comments on the material presented. I am grateful for the fruitful discussions with Dr. Chunlei Wang and Mr. Ming-Yi Li.

I am grateful to the Modeling Group at Triquint Semiconductors, for supporting me with an internship. This industrial experience brought valuable “real-world” data and considerations to my work. In particular, I would like to thank Mr. Martin Jones, Mr. Jim Carolls, Mr. Ken Wills and Mr. Matt Coutant for their suggestions, comments and support. I am also very grateful to Dr. Julio Nararro from Omni-Patch Designs for mentoring me on many aspects of antenna design. Moreover, I appreciate the help and support from Dr. Frank Little of the NASA Center for Space Power at Texas A&M, from Dr. Goeff White of Boeing and from the US Air Force.

I especially thank my friends Hooman Tehrani, Jeffrey Miller, Bernd Strassner, Christopher Rodenbeck, James McSpadden and Jarett Guill for many wonderful memories.

Most of all, I am grateful for the love, support and companionship of my husband Benoit. His constant encouragement and understanding enabled me to confront the many challenges of the past five years. The love and encouragement of our parents and families were also sources of great inspiration.

TABLE OF CONTENTS

LIST OF TABLES

LIST OF FIGURES

FIGURE Page

FIGURE Page

FIGURE Page

FIGURE Page

FIGURE Page

CHAPTER I

INTRODUCTION

In the past 50 years, microwave components have progressed towards higher performance and frequency, thanks to new solid-state devices, increased precision in fabrication and compact layout techniques (such as microwave integrated circuits, micro-machined, and multi-layer circuits), as well as faster design iterations with more accurate models. Moreover, communication technologies using phased-array systems have evolved towards higher scanning resolution and speed, as well as optimal synthesized patterns through the use of adaptive beam-forming networks. Also sharing the same microwave spectrum are the ISM (Industrial, Scientific and Medical) applications in which a growing interest has been demonstrated for WPT (Wireless Power Transmission) systems. These applications involve the transmission of very high microwave power levels over large distances and are suitable for space applications as well as earth-based remote terrain for electricity distribution. WPT can be considered as a three-dimensional means of transferring electrical power from one location to another without the support of wires or cables. WPT systems fulfill the necessity of integration to the environment at relatively low cost of implementation. For example, in [1], it has been estimated that power carried through a microwave beam can be four times less expensive than electricity produced by photovoltaic panels. One of the most important requirements of a WPT system is to have a high electric power transfer efficiency (overall DC to DC efficiency). William C. Brown initially developed WPT prototype systems in the sixties using microwave energy to power a small helicopter [2]. A large amount of research followed for space applications involving very large distances of propagation of high microwave power levels for the future potential of feeding satellites or space shuttles as illustrated in Fig. 1.1. The applications of feeding power to Earth from solar power satellite stations have also been extensively studied [3]. A simplified block-diagram of a WPT system is shown in Fig. 1.2.

This dissertation follows the style and format of the *IEEE Transactions on Microwave Theory and Techniques*.

Fig. 1.1: Example of WPT system for space applications.

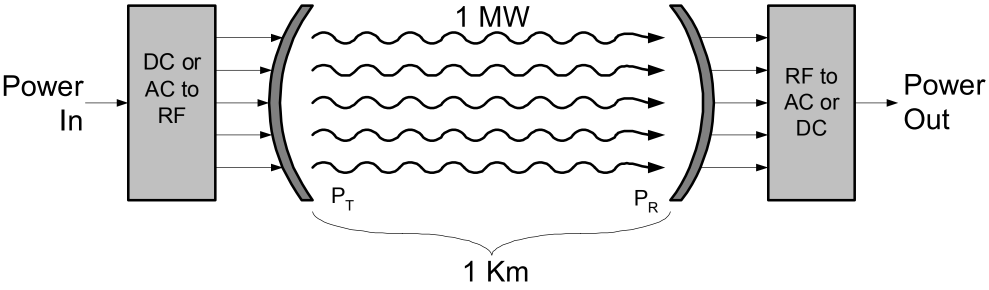

Fig. 1.2: Global WPT system.

The DC or AC power is first converted into RF power and applied to the antenna according to the aperture taper. The power P_T is transmitted in free space and received as P_R on the receiver aperture or rectenna (rectifying antenna). It is then converted back to DC power according to the rectenna efficiency. For the choice of antennas used for the transmitter and the rectenna, one must consider the high power handling of the components and the collecting efficiency. For example, waveguides are a common choice for radiating high levels of microwave power [4],

[5]. For the rectenna, some electronics is required to be mounted on the receiving antenna in order to rectify the RF signal and filter it into a DC level [6].

Phased arrays are complex systems that necessitate careful choice of configuration, components and analysis approach. A phased array system consists mainly of an antenna array, which can focus its main beam towards a direction different from broadside (perpendicular to the array plane). The beam angle is controlled by the phase distribution on the element array. The phase is adjusted electronically (using electronic phase shifters with analog or digital control). Phase arrays are sometimes used as substitute for fixed antennas, allowing more flexibility on the shaping of the beam due to the large number of elements. However, in most cases, phased array systems are used primarily to allow steering of the beam or to generate multiple beams. Study of the general phased array system focusing on the choice of configuration can be found in [7], [8], and [9]. Many additional publications are available on more specific phased array topics. Multi-beam systems (which date back to the beam formers introduced by Jesse Butler in the sixties [10]) radiate simultaneous beams at different angles. This allows for broad coverage and more flexibility in pattern shaping without the use of electrical or mechanical scanning of the main beam. Multi-beam systems have been used in electronic countermeasure, satellite communications, multiple-target radar, and adaptive nulling. The feed networks used for multi-beam systems include mainly the power divider beam former network (BFN), Butler matrix, Blass and Nolen matrices. The use of discrete phase shifters in these beam formers limits the system bandwidth, as these components are usually narrowband. They also contribute directly to the system cost as the number of radiating elements is increased. Moreover, Butler or Nolen matrices generally require complex and cumbersome power divider networks. We also have multi-beam systems using optical control. These are generally used for designs with large bandwidth requirements with true-time delay fiber-optics instead of phase shifters. They allow 2-dimensional (2D) scanning with linear array and offer very fast control for switch networks while keeping a low loss. Unfortunately, optically controlled multi-beams are also particularly expensive.

The choice of components is a necessary step in the conceptual design of a phased array. Such components include the type of feed, phase shifter (analog vs. digital) [11], as well as radiating elements [12]. One also needs to predict the performance and level of errors for the preliminary system. The two main analysis methods are the statistical and the field analysis approaches [13], [14]. The former is used when the number of elements is over 10, and the later is more accurate for the smaller arrays with stronger edge effects and mutual coupling.

As mentioned, large antenna systems as in power transmission applications or as phased arrays require careful design at the components level to ensure high efficiency and low cost. Many specifications are met after optimization of individual units or components in the system and are rather independent on the interaction with other blocks. Among the numerous and most important microwave components that have been used for diverse wireless applications are the transitions that integrate two blocks using different media without sacrificing the impedance matching. Characteristics such as low loss and high-power handling have promoted the widespread use of waveguides. As alternatives, Microwave Integrated Circuits (MICs) and Monolithic Microwave Integrated Circuits (MMICs) were developed to improve reproducibility and reliability while reducing the size and cost of components and systems [15]. Many mass-produced and low-cost commercial applications such as intruder detectors, doppler radars (both at K-band) and collision avoidance radar (at W-band) involve the use of transitions between waveguide media and MICs. The integration of waveguide and planar technologies requires the use of efficient transitions such as the loop transition. Two-dimensional arrays of loop transitions have been used for many past applications as antenna feeders for rectangular or circular waveguide radiators [16] and measurements have been limited to the S-band [17] and X-band [18].

Other essential microwave components in complex array systems are the filters units. For bandpass operations, a certain number of resonators are required to provide a selective response. This results in large planar circuit area to accommodate the necessary resonators. The use of a multilayer configuration provides improved compactness by stacking the same number of resonators. At the same time, broadside coupling is added between resonators bringing in more design flexibility. Many types of multilayer filters have been studied in the past. For example, aperture coupled resonators that were traditionally implemented in cavities or using dielectric resonators have recently been realized using multilayer microstrip or stripline circuits [19]. When using dual-mode patch or ring resonators, the aperture allows the tuning of the coupling between the two modes by varying the length of the orthogonal slots, as seen in Fig. 1.3 (a). This design presents a large loss that is probably due to the weaker coupling between the separated resonators by the added aperture layer, as opposed to a direct broadside coupling. There is also the multilayer version of the end-coupled bandpass filter which overlaps the half-wave resonators edges with coupling resonators on other layers [20] as illustrated in Fig. 1.3 (b). This could help in adding more poles in the stopband and zeros in the passband. The design is more compact when compared to its planar counterpart but still extends considerably in the propagation direction compared to the stacked patch or ring resonators. A folded coupled line filter has been reported in the literature that uses folded half wavelength resonators for compactness [21], as shown in Fig. 1.3 (c). Vertical metallizations are needed to connect the two coupled lines which complicates the fabrication process.

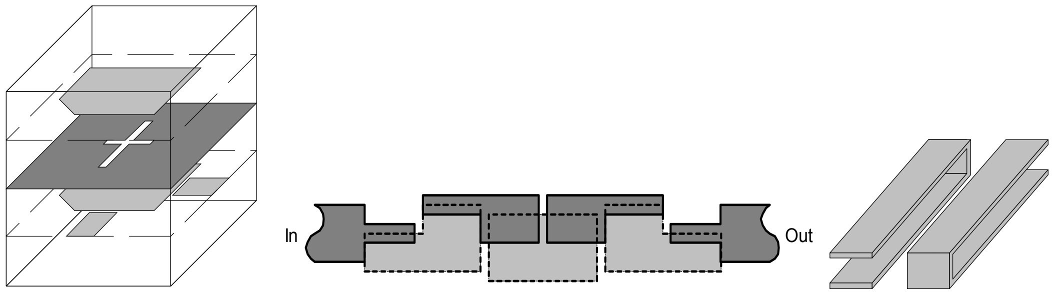

(a) (b) (c)

Fig. 1.3: Different multilayer filter structures. (a) Aperture coupled stripline dual-mode resonators; (b) overlap end-coupled bandpass filter; (c) broadside and edge coupled folded half-wavelength resonators.

The analysis of multilayer filters have been realized in the frequency domain using quasi-static Spectral Domain Approach (SDA) which is a full wave (and therefore very accurate) method. One drawback is that the formulation is very dependent on the geometry of the problem, which makes it less versatile [22]. The analysis has also been reported to be less accurate for gaps and open-ends in open structures such as multilayer microstrip (non-shielded). Finite Element Method (FEM) has also been used to analyze multilayer structures. A hybrid analysis based on

FEM improved the conventional method to a full-wave precision and allows the calculation of the total characteristic impedance of the multilayer structure [22].

Also as important, the design of digital phase shifters for high frequency phased array systems requires accurate switch models over a broadband range. The Field Effect Transistor (FET) switch follows conventional layout rules for GaAs integrated circuits [23]. A model can be created from carefully studying the layout topology. In order to obtain initial values for the model parameters, one needs to use theoretical analysis in conjunction with empirical data [24].

In this dissertation, chapter II will present research on three areas of WPT. The first section describes the conceptual design of a complete WPT system under specific requirements. The second section studies many considerations in choosing the operating frequency for a WPT system. Finally, the third section proposes a methodology for optimizing the energy distribution on the transmitting antenna. The study of a WPT system served as the preliminary design for a future demonstration of a functional WPT system. Through calculations of key parameters, the feasibility of a point-to-point WPT link will be studied. The main purpose is to calculate the system parameters that optimize the overall efficiency $\eta_{\mathrm{DC(AC)\text{-}DC}}$ of the power transmission. The size of the transmitter and receiver antennas as well as the total number of elements contained in each aperture will be determined. Each component of WPT system is described and corresponding efficiencies are defined. The influence of some important system parameters on the efficiencies will be demonstrated. A possible configuration for the transmitter and the receiver fulfilling the efficient transfer of electric power requirement will be presented. The selection of the operating frequency has a significant impact on the planning of a wireless power transmission (WPT) system. The electromagnetic spectrum can be divided in three types of radiation, here given in order of increasing frequency: radio waves, optical rays and high energy waves. The high energy waves consist of X-Rays and Gamma Rays. Microwaves are located between the radio and optical frequency bands and can be considered as part of radio waves. As the frequency is increased, the energy of the radiation grows progressively from heat production to ionizing effect (modification of the molecular structure). Waves produced in the microwave band are of low energy and have no ionizing effect on materials.

A sandwich transmitter is used in Wireless Power Transmission (WPT) systems for compactness by bringing the electronics platform closer to the transmitter aperture. The high level of radiated power (order of gigawatts) by the antenna prohibits the use of aperture tapers with concentrated energy regions that could locally overheat the electronics. The purpose of the third topic of chapter II is to determine an optimal taper for a sandwich array used in space solar power satellite to transmit power to earth. The sandwich array incorporates the necessary control circuitry close to the aperture and therefore, helps reduce the length of connection cables between them.

Chapter III deals with the analysis methodology for the design of a small-scaled phased array. The research objectives are to perform a preliminary analysis on a phased array system in order to determine its optimal configuration. The system was designed by other parties in the context of a group project and will be presented briefly with descriptions of the main components for clarity. The conceptual design was performed at high level and does not include the specific components design and their integration, which were realized by other team members. This high level design involves decisions at system level that are based, among others, on available test equipment and fabrication resources. Some of the options include the choice between a multibeam or scanned array, active or passive array, dual frequency transceiver or two separate arrays for receive and transmit functions, type of architecture to be used for the two-dimensional implementation, etc. Cost and reliability should also be included in this preliminary definition of the system. It should be noted that some decisions were also made as a group once the preliminary analysis has been realized and presented. Further design decisions were taken for the various components involved in the system such as choosing between commercially available digital phase shifters or designing a custom analog phase shifter. The analysis predicts the scan resolution, the phase quantization lobes, the beam pointing error, etc. It is also necessary to evaluate, for example, the scan loss (gain roll-off), the bandwidth, the half power beam width, as well as determine the number of elements and the optimal spacing with grating lobes and scan blindness considerations. This involves making tradeoffs between some performance parameters. The analysis was realized using the two most important methods: the field analysis and the statistical method. A comparative study between the efficiency of these two methods is newly introduced by using the statistical method to evaluate a small-scale array as a first order approximation. The prediction agrees fairly well with the measurements.

At last, chapter IV presents the design of an efficient transition, the study of a multilayer filter and the modeling of a high-speed switch will be covered. The use of a rectangular waveguide feeding a microstrip patch array through two types of loop transition at K-band is demonstrated. The distribution of energy from the single feed input is realized in a planar series feeding configuration. Simulation results for the loop are obtained from a three-dimensional full-wave simulator. The antenna array is designed and optimized at 24.125 GHz. The theoretical results and the overall efficiency are verified with measurements on a K-band 8×8 planar microstrip patch antenna array. The use of a rectangular waveguide feeding through a loop transition to a microstrip patch array with series feeding configuration at W-band is also demonstrated. The loop performance optimization is based on available models [17]. The planar microstrip patch antenna array measured performance at W-band validates the theoretical results.

For the multilayer filter design, the first attempt was to observe the differences between a two-dimensional two-stage square ring resonator and a multilayer stacked ring resonator implementation with same ring size and resonant frequency. Since there were no available gap-coupled square ring resonators design in the literature at the time, a custom configuration was optimized to serve as a reference for the two-layer stacked ring resonators. Then a modified multilayer folded line structure was studied and presents potential in ultra-wideband performance.

For the switch model project, the main objective is to optimize the fitting and simplify the preliminary model for a three-terminal intrinsic FET switch. Feed models should be created for each terminal in the switch. The original three port switch model with physical line lengths defining the FET intrinsic length was documented for 18 different FET sizes. A symmetrical equivalent circuit was used to model odd number of fingers FET. This allows a reduction in the number of variables since the drain and source parameters become equal. The physical line length consists of half of the FET length on the drain and source port for symmetry. Since the purpose of the switch is to be used in a phase shifter application, the phase of S_{21} is the most important parameter to fit. The desired characteristics of the model are a large scalability and broadband fitting. The goal is to obtain a phase fitting error of less than ±2° over the entire range of frequencies and scaling. Moreover, the magnitude fitting error for S_{21} should be kept under 5%.

CHAPTER II

WIRELESS POWER TRANSMISSION SYSTEMS

WPT can be considered as a three-dimensional means of transferring electrical power from one location to another without the support of wires or cables. Many considerations must be taken into account in order to maximize the energy transfer efficiency.

This chapter will present research on three areas of WPT. The first section describes the conceptual design of a complete WPT system under specific requirements. The second section studies the many considerations in choosing the operating frequency for a WPT system. Finally, the third section proposes a methodology for optimizing the energy distribution on the transmitting antenna.

2.1 Conceptual design of earth-based wireless power transmission system

This section will demonstrate the feasibility of a wireless power transmission system based on a number of specifications and constraints. The purpose is to determine the main design parameters that lead to an optimal overall DC (or AC) to DC efficiency using minimal antenna and rectenna size. It is required that one megawatt of DC power be collected at the receiver end. The RF power is transferred through an aperture-to-aperture range of one kilometer. The system operates at the ISM frequency of 2.45 GHz.

2.1.1 Specifications and requirements

In order to define the various parameters used throughout this section, Table 2.1 includes a list of symbols. The systems specifications and assumptions for optimum performance are given in Table 2.2.

Table 2.1: List of symbols for WPT system.

Symbol	Definition
A_r	Receiver aperture area
A_t	Transmitter aperture area
A_{tem}	Maximum effective transmitter aperture area
D	Distance between the transmitter and receiver
D_0	Optimal antenna directivity from a uniform illumination
D_r	Receiver aperture diameter
D_t	Transmitter aperture diameter
f	Frequency
g	Slot normalized conductance
HPBW	Half power beam width
l_i	Length of resonant inclined slot
l_l	Length of resonant longitudinal slot
λ_0	Free-space wavelength
λ_g	Guided wavelength
G_t	Transmitter gain
η_a	Antenna efficiency
η_c	Collection efficiency
η_{mag}	Magnetron efficiency
$\eta_{\mathrm{DC(AC)\text{-}DC}}$	Overall end-to-end efficiency
$\eta_{overall,\ \mathrm{RF\text{-}DC}}$	Transmitting RF to DC output efficiency
η_{rect}	Rectenna conversion efficiency
η_t	Overall DC (or AC) to RF transmitter efficiency

Table 2.1 (Continued).

Symbol	**Definition**
$2L_t$	Side length of a square transmitter aperture
$2L_r$	Side length of a square receiver aperture
N	Number of radiating slots on waveguide
N_{mag}	Number of magnetrons
N_r	Number of elements in the rectenna
N_t	Number of elements in the transmitter
N_w	Number of fed waveguides
o_i	Offset of resonant inclined slot
o_l	Offset of resonant longitudinal slot
P_{mag}	Magnetron power
P_d	Power density
$P_{d,peak}$	Maximum power density at the center of the antenna aperture
$P_{\mathrm{DC(AC)}\,i}$	Total DC (or AC) input power
$P_{\mathrm{DC}o}$	Total output DC power
P_r	Total received RF power
P_t	Total transmitted RF power
r_{HP}	Half power beam radius at the receiver
R_r	Receiver aperture radius
R_t	Transmitter aperture radius
s_i	Spacing between resonant inclined slots
s_l	Spacing between resonant longitudinal slots

Table 2.1 (Continued).

Symbol	**Definition**
τ	Goubau's parameter
θ	Angle of inclination for series slot
w_i	Width of resonant inclined slot
w_l	Width of resonant longitudinal slot
Z_r	Waveguide impedance seen by the feedguide

Table 2.2: Systems specifications and assumptions.

Specifications				**Assumptions**					
D (km)	f (GHz)	λ_0 (m)	$P_{DC(AC)o}$ (MW)	**Beam shaping**	η_a (%)	η_c (%)	η_{mag} (%)	η_{rect} (%)	P_{mag} (W)
1	2.45	0.1224	1	10 dB Gaussian	100	90	80	85	5000

Using these known parameters, the size of the apertures A_t and A_r, the power density P_d, the remaining system efficiencies as well as the transmitter and receiver configurations can be determined. The requirements are to calculate relatively small aperture sizes for minimum cost and fabrication complexity and optimum efficiencies in order to reduce losses and maximize the power transfer. The determination of the unknown parameters will require some tradeoffs as will be seen in later sections to fulfill the system requirements.

2.1.2 System configuration

A WPT system consists basically of three main functional blocks. A first block is needed to convert the electricity (DC or AC) into microwaves. After being radiated through an array of microwave radiators, the RF power is carried within a focused microwave beam that travels across free space towards a collector. This receiving block will convert the RF energy back to

DC electricity. A simplified schematic in Fig. 2.1 shows the basic components of a WPT system with associated efficiencies.

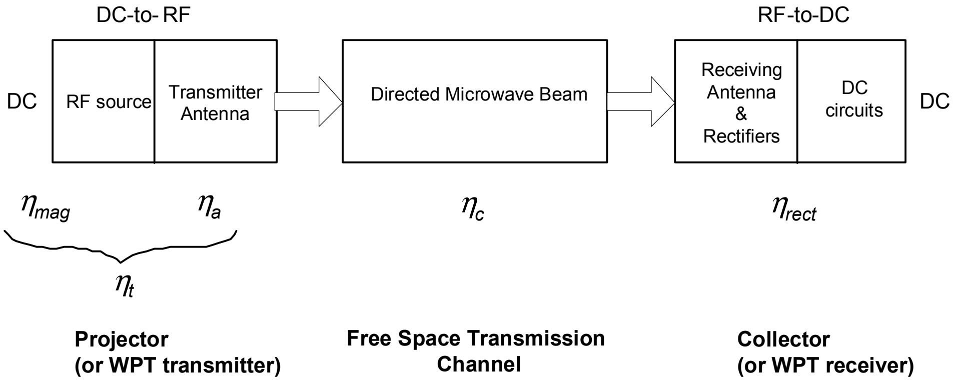

$$\eta_{\mathrm{DC(AC)\text{-}DC}} = \eta_t\, \eta_c\, \eta_{rect}$$

Fig. 2.1: Wireless power transmission system schematic.

In the following sections, a more detailed description of the transmitter and receiver subsystem efficiencies and components is provided.

2.1.3 Efficiencies

The efficiency of a module is basically equivalent to its transfer function. The general definition of any efficiency used hereafter is the ratio of output power P_{out} over input power P_{in}

$$\text{Efficiency} = \frac{P_{out}}{P_{in}} \times 100\ \%. \qquad 2.1$$

The overall efficiency of a WPT system, $\eta_{\mathrm{DC(AC)\text{-}DC}}$, is the ratio of the DC output power at the receiver end over the DC (or AC) input power at the transmitter end. As illustrated in Fig. 2.1, this end-to-end efficiency includes all the sub-efficiencies starting from the DC (or AC) supply feeding the RF source in the transmitter part to the DC/DC power interface at the receiver output. It is comprised of three distinct sub-efficiencies: the electric to microwave conversion efficiency (or transmitter efficiency), the collection of beam efficiency and the microwave to electric conversion efficiency (or receiver efficiency). In order for the global efficiency to be sufficiently high, it has been shown that the transmitter illumination needs to be an optimal taper as will be seen later. One must also ensure excellent DC(AC)-to-RF conversion capabilities as well as efforts on the efficient output of the microwave generator up to the DC output of the rectenna.

The antenna efficiency at the transmitter end, η_a, as illustrated in Fig. 2.1, represents the ability of the antenna to efficiently radiate the distributed RF power fed from the RF source and launched into free-space. The matching between the antenna and the air characteristic impedance as well as the level of ohmic losses will mainly determine the antenna efficiency.

Another efficiency, which is very important since related to many other design parameters, is the collection efficiency, η_c. Once selected, the value of η_c along with some other assumptions will define the WPT system configuration. The collection efficiency is expressed as the received RF power over the transmitted RF power characterizing the receiver capability to efficiently collect the incident impinging energy. η_c is proportional to a design parameter, τ, which is expressed as Goubau's relation [2], [25]

$$\tau = \frac{\sqrt{A_r A_t}}{\lambda_0 D} \qquad 2.2$$

The involved parameters are illustrated in Fig. 2.2 and defined in Table 2.1.

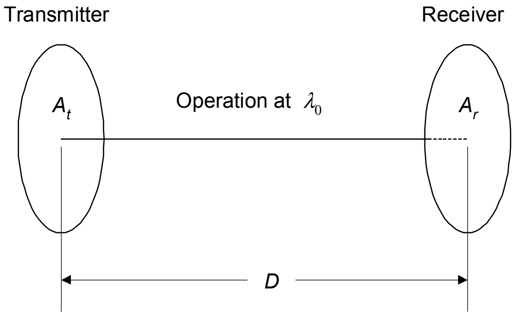

Fig. 2.2: WPT system illustrating Goubau's relation.

Goubau's relation as a function of radii is given as (for circular apertures)

$$\tau = \frac{\pi R_t R_r}{\lambda_0 D} \qquad 2.3$$

where R_t and R_r are the aperture radii of the transmitter and the receiver antenna, respectively. As seen from Fig. 2.2, equations 2.2 and 2.3 apply to circular apertures. If using rectangular apertures for the two antennas, the τ parameter expression slightly differs from equation 2.2 and results in a lower collection efficiency (maximum difference of 3 %). The advantage in using rectangular apertures is the simpler fabrication and system mounting. In order to optimize both the collection efficiency and the simplicity of fabrication, square apertures using absorber at the corners can be used in lieu of circular apertures as shown in Fig. 2.3.

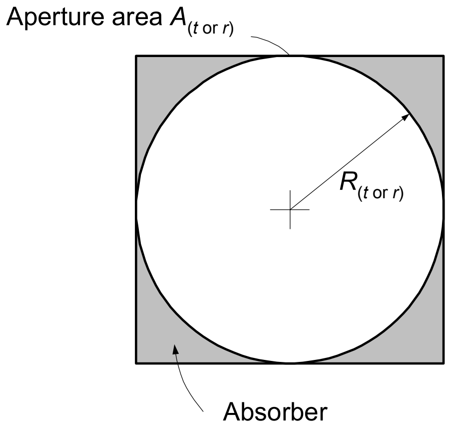

Fig. 2.3: Rectangular aperture configuration using absorber.

The collection efficiency is also a function of the atmospheric attenuation, which depends on operating wavelength, weather and power density. For ground-based systems this attenuation is generally assumed negligible on a clear day for 2.45 GHz operating frequency.

As can be seen from equations 2.2 and 2.3, Goubau's relation can be used to determine the size of the apertures involved. These calculations along with the optimization of the individual component efficiencies using the available specifications will be demonstrated in the following sections. Also, a more detailed study of the collection efficiency will be provided later when describing the receiver subsystem.

The overall RF to DC efficiency is a combination of the collection efficiency, η_c, and the conversion efficiency, η_{rect}. The choice of the rectifier and the level of incident power at the receiver end mainly determine the later. In the following sections, the optimization process for this receiver efficiency is presented.

As an example, a satisfactory overall efficiency $\eta_{\mathrm{DC(AC)\text{-}DC}}$ could involve an average subsystem efficiency of 85 % for each of the three intermediate WPT functional blocks. This results in a global system efficiency of about 60 %. A more economical design would require lower subsystem efficiencies, which can be satisfactory depending on the application needs and resources [1]. A relatively high DC(AC)-to-DC efficiency of 52.8 % was predicted to be attainable for short distances (<10 km) only [26]. With better matching of the components, Brown and Eves [27] predicted an increase of the overall DC to DC efficiency to a maximum value of 76 %.

2.1.4 Beam characteristics

The radiation pattern obtained from the transmitting antenna is a function of the size as well as the illumination taper across the antenna aperture. The transmitter illumination taper also affects the collection efficiency. As can be seen from the curves found in [2], a taper close to uniform illumination can result in a very inefficient aperture to aperture transmission of power. This low collection efficiency is due to a narrow main beam with high sidelobe levels produced by the uniform illumination. A uniform taper is used when thermal dissipation is critical on the transmitter aperture and a maximum power density at boresight is desired in a system.

To reach a collection efficiency near 100%, the distribution should be a truncated Gaussian taper [2], [25]. This optimal taper distribution will produce a more spread main beam with very low sidelobe levels over 20 dB below the main beam. For example, with a 10 dB Gaussian taper, the first sidelobe level is 23 dB below the main beam. The degree of truncation or taper level is defined as the ratio of the center over the edge power intensity. A larger taper will increase the collection efficiency and lower the sidelobes. From [3], an economically optimal taper was found to be of 10 dB.

However, by using a taper distribution instead of a uniform illumination, a higher power density will result at the transmitter aperture. Also, the flattening and widening of the main beam with a taper distribution will require a larger receiver aperture. As can be seen, there exists a tradeoff between low sidelobes levels and narrow beamwidth. Therefore, the choice of the taper will depend on the system constraints of collection efficiency, sidelobe levels, peak power density, and size of the apertures.

A truncated 10 dB Gaussian taper distribution can be created with a number of RF sources such as magnetrons for example, with varied power outputs set by the specified power density taper. The quantized power distribution can be illustrated in Fig. 2.4 as a given step function following the reference system case found in [3]. Here p and p_0 are the aperture power intensity and peak power intensity, and r and R_t are a radius variable and the transmitter aperture radius, respectively. As an example, ten steps are used for an appropriate approximation the Gaussian function.

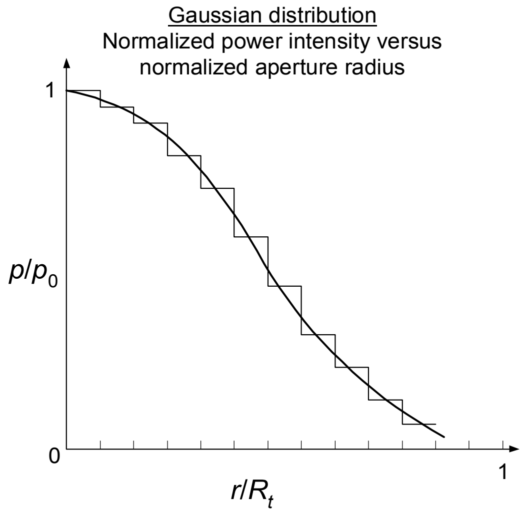

Fig. 2.4: Magnetron quantized power distribution across A_t.

2.1.5 Power density using the WEFF Tool

An important feature of the receiver is the capacity to efficiently convert the incident RF power density into DC power. This conversion efficiency is strongly dependent on the power density distribution across the receiver aperture.

The incident maximum power density can be derived as follows. Assuming a uniform taper at the transmitter and no conduction, matching or polarization match losses, an optimal directivity of

$$D_0 = \frac{4\pi A_{tem}}{\lambda_0^2} \qquad 2.4$$

is obtained which means that the power of the main beam is magnified by D_0 in a certain direction. A_{tem} is the maximum effective transmitter antenna area. For an aperture type antenna with the assumptions given above, $A_{tem} = A_t$. This magnification is reduced by the decay of the field strength with distance as expressed by the factor $1/(4\pi D^2)$. The distance D needs to be relatively large for the system to operate in the far field as will be seen later. Combining these two opposing effects into one expression, the peak power density at the center of an aperture is obtained

$$P_{d,peak} = \frac{P_t A_{tem}}{\lambda_0^2 D^2}. \qquad 2.5$$

The power density function across the face of the receiver follows the Gaussian taper curve decaying from the center peak value towards the edges. The DC output power will feature the same radial decrease. To specify the Gaussian power density distribution on the receiver, the peak power density from equations 2.5 and the Half Power Beam Width, HPBW, are needed [6]. The HPBW in degrees is calculated with

$$\text{HPBW}^\circ = \sqrt{\frac{32400\lambda_0^{\,2}}{4\pi A_{tem}}}\,. \qquad 2.6$$

With the HPBW, the half power beam radius at the receiver, r_{HP}, is obtained from

$$r_{\text{HP}} = \frac{\text{HPBW}^\circ \pi}{360} D\,. \qquad 2.7$$

The Gaussian power density distribution on the receiver aperture is then given by

$$P_d(r) = P_{d,peak}\,\mathrm{e}^{-\left(\frac{r}{r_{\text{HP}}}\right)^2 \ln(2)}\,. \qquad 2.8$$

To get the average power density, the power density function $P_d(r)$ can be integrated over the aperture area, which gives the total power at the receiver, and is divided by the receiver area

$$P_{d,average} = \frac{\int P_d(r)dA_r}{A_r} \qquad 2.9$$

From this equation, a higher power density admits a smaller A_r to achieve the same output power. The power handling capacity of the receiver depends on the area A_r and the power density ratings of the rectifying elements.

Therefore, with the total incident power hitting the receiver and the maximum power density capacity of the receiving device, the minimum area for one element can be determined. The maximum power rating depends on the type of diodes and breakdown voltages used. For example, if using GaAs diodes as rectifiers, the range of power density that can be handled efficiently is 600 W/m^2 or higher [28].

An example of power density levels measured at Texas A&M University on a rectenna (rectifying antenna) element operating at 2.45 GHz along with their corresponding collection efficiency is given:

$$\frac{70\,\text{mW}}{\text{cm}^2} \text{ at } 90\ \%$$

$$\frac{5\,\text{mW}}{\text{cm}^2} \text{ at } 85\ \%$$

As a reference, a proper range of average DC power density at the output of the receiver end for many WPT applications is in the order of 108mW/cm^2 from [29].

With design equation 2.5, a peak power density of 188 mW/cm^2 is found. Using equation 2.9 and specifying the total received power at 1 MW, an average power density of 60.3 mW/cm^2 is obtained. Using equation 2.8, the power density distribution for a 10 dB Gaussian taper is calculated as shown in Fig. 2.5.

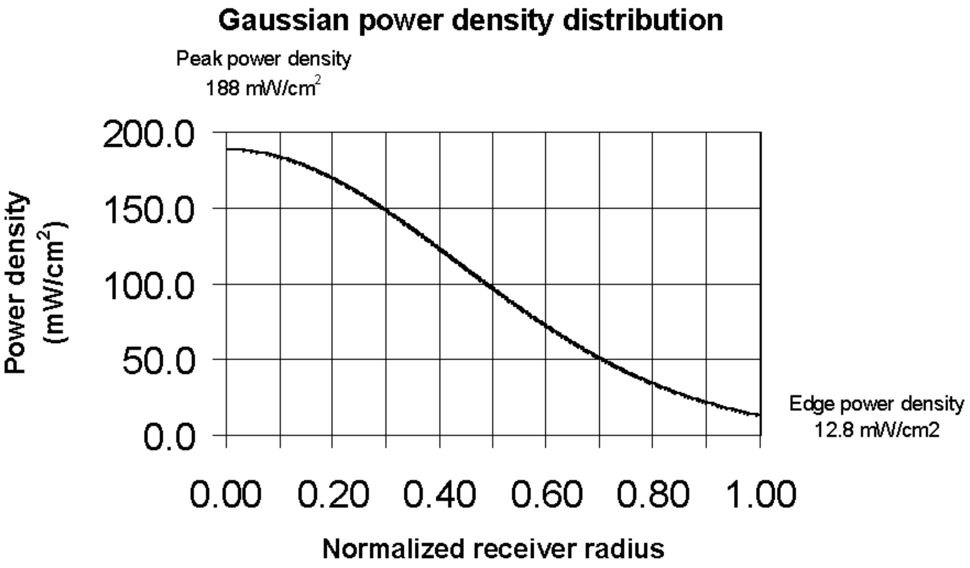

Fig. 2.5: Gaussian power density distribution on receiver aperture.

WEFF, a software developed in Texas A&M University [30] was used to optimize the results. WEFF is a FORTRAN program that can assist in the analysis and design of WPT systems with circular transmitter and rectenna apertures. WEFF was developed to model the effect that a variation in the power density (W) incident to the rectenna has on the rectenna efficiency (EFF) [31].

WEFF considers the RF power in the taper or the squared electric field distribution at the transmitter aperture as being the power source. WEFF uses several system specifications (such as frequency of operation, distance between antenna & rectenna, dimensions of antenna and rectenna, aimed collection efficiency, etc.) entered by the user along with the taper description and rectenna design characteristics to evaluate the WPT system performance. Fig. 2.6 illustrates a typical result screen from WEFF. As seen, the required RF transmitted power (no. 5), antenna and rectenna radius (no. 3 and 4), and resulting maximum power densities at center (no. 10 and 11) are displayed after the user has entered the input parameters corresponding to the specifications (entry no. 1, 2, 7, and 12). The 10 dB Gaussian taper is specified in the menu "T" for taper setup. More details on the use of WEFF can be found in the instruction manual [30].

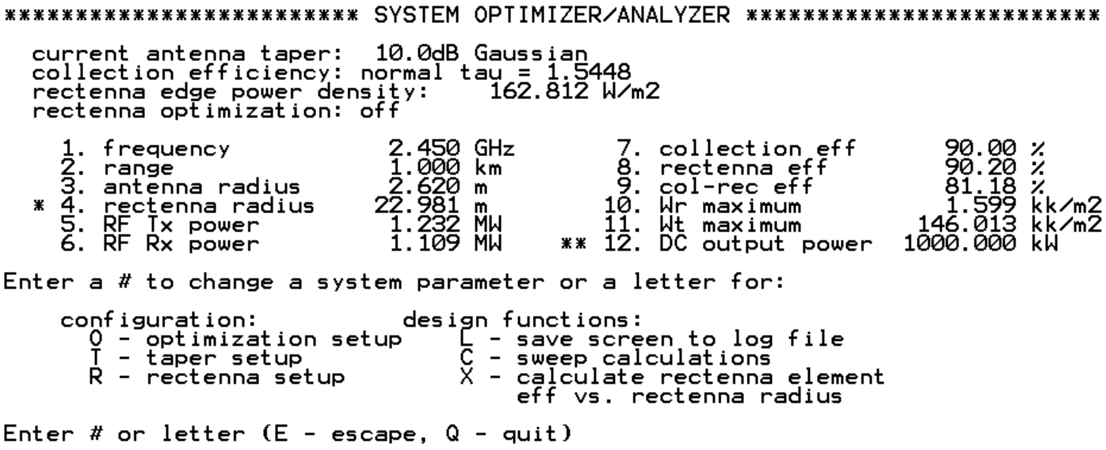

```
************************* SYSTEM OPTIMIZER/ANALYZER *************************
  current antenna taper:  10.0dB Gaussian
  collection efficiency: normal tau = 1.5448
  rectenna edge power density:    162.812 W/m2
  rectenna optimization: off

    1. frequency           2.450 GHz       7. collection eff      90.00 %
    2. range               1.000 km        8. rectenna eff        90.20 %
    3. antenna radius      2.620 m         9. col-rec eff         81.18 %
  * 4. rectenna radius    22.981 m        10. Wr maximum           1.599 kk/m2
    5. RF Tx power         1.232 MW       11. Wt maximum         146.013 kk/m2
    6. RF Rx power         1.109 MW    ** 12. DC output power  1000.000 kW

Enter a # to change a system parameter or a letter for:

    configuration:          design functions:
      O - optimization setup    L - save screen to log file
      T - taper setup           C - sweep calculations
      R - rectenna setup        X - calculate rectenna element
                                    eff vs. rectenna radius

Enter # or letter (E - escape, Q - quit)
```

Fig. 2.6: Typical result screen from WEFF.

In order to obtain η_c, WEFF uses scalar diffraction solutions, which are approximate solutions of Maxwell's equations, to express the field E_R on the rectenna as a function of E_T, the transmitter field. The near field or Fresnel diffraction field integral used is

$$E_R(\rho,z)=\frac{jk}{2\pi}\frac{e^{-jkz}}{z}e^{-\frac{jk}{2z}\rho^2}\iint_{A'}E_T(\rho')e^{-\frac{jk}{2z}\rho^2}e^{\frac{jk}{z}\rho\rho'\cos(\phi-\phi')}dA' \qquad 2.10$$

where *k* is the wave number, and the aperture taper and *A'* is the area of integration in the cylindrical coordinates space [31].

As seen from Fig. 2.6, this program calculated a maximum power density of 160 mW/cm^2 at the center of the receiver with the system specifications. The edge power density given by WEFF is 16.3 mW/cm^2. Since WEFF optimizes the results taking into account the power handling capacity of the rectifying diode used in the receiver, those values will be considered for this system. The power density taper calculated by WEFF is similar to that shown in Fig. 2.5 with slightly different peak and edge values.

2.1.6 Frequency

The selection of the operating frequency has a significant impact on the configuration of the planned WPT system. The electromagnetic spectrum can be divided into three types of radiation, here given in order of increasing frequency: the radio waves, the optical rays and the high-energy waves. Microwaves are located between the radio and optics frequency bands. As the frequency is increased, the effect of the radiation grows progressively from heat production to ionizing effect (modification of the molecular structure). Waves produced in the microwave band are of low energy and have no ionizing effect on materials.

Spreading the microwave beam over a large cross section area can further lower the hazard level. The power density can be reasonably reduced to about 10 mW/cm^2, the US safety standard for microwave exposure, which is a considerably smaller amount compared to the sunlight energy radiating 100 mW/cm^2 [1]. The beam can also be spread out by increasing the wavelength (or reducing the operation frequency) or the distance between the transmitter and the receiver.

In this study, the system operates at the ISM frequency of 2.45 GHz. This choice presents various advantages. Working at lower frequencies allows the transmitted microwave beam to travel through the atmosphere without suffering from excessive attenuation. Moreover, WPT technology at 2.45 GHz has been proven efficient. Hence, it is a common practice to use the low cost commercially available microwave oven magnetron tubes as sources for the transmitter at 2.45 GHz. Furthermore, lower frequency technologies are more mature and the designs generally present higher efficiencies.

However, for the same transmission distance, low frequency systems require relatively large antenna and receiver size. Operating at a higher frequency allows for reduction in component size. For the same antenna size and collection efficiency, a higher frequency permits a larger distance of transmission to operate in the far field but the hardware complexity becomes greater. It will also cause some degradation in the collection efficiency in adverse weather conditions since the atmospheric loss is larger for higher frequency systems.

2.1.7 Size of apertures

Using the system specifications, the general procedure to determine the size of the transmitter and receiver aperture follows. After selecting a satisfactory collection efficiency, a corresponding τ is obtained from charts found in [2]. Then, with specified values for D and λ_0, the aperture product $A_r \cdot A_t$ is calculated from equation 2.2. To obtain the individual aperture sizes, the far field condition, as defined later in equation 2.11, should be used to specify A_t. The far field condition limits the transmitting antenna diameter to a maximum value D_t. A minimum receiver diameter D_r can be derived using the previously calculated aperture product.

In the following subsections, the aperture sizes will be calculated and the effect of the aperture dimensions on the system performance will be studied.

2.1.7.1 Transmitter size

The aperture size of an antenna A_t is a function of many operating WPT parameters such as the operating frequency, f, (or wavelength, λ_0), the distance between the transmitter and the receiver, D, and the desired collection efficiency, η_c, as expressed in Goubau's relation 2.2. By selecting τ from Brown's chart [2] to achieve an acceptable aperture-to-aperture efficiency, η_c, the aperture product $A_t \cdot A_r$ can be determined. A satisfactory η_c of 90 % is aimed at with a corresponding $\tau = 1.5448$. Substituting the specified values for λ_0 and D, $A_t \cdot A_r = 3.57\times10^4$ m^4.

The determination of the size of the WPT system based solely on the collection efficiency and the antenna taper is a first order analysis, but gives satisfactory dimensions for a preliminary design. Some other system drivers for calculating the aperture size include the level of the receiver power density. When the transmitter aperture size is enlarged, a higher gain and peak power density are produced and a smaller receiver size is needed. Inversely, a smaller transmitter size requires a larger receiver since the beam is spread with a lower resulting gain and peak power density. This causes an overall increase in the system costs.

To maintain a constant η_c given a fixed A_r, A_t and D should vary proportionally. Therefore, when operating with a very large D, A_t has to increase in order for the beam to become more concentrated and enhance the collection effect at the receiver end. However, A_t can become extremely large which is often impractical and expensive for short range applications. The antenna and receiver size along with the required power density must be determined in ways to minimize the transmitted energy cost. Another important constraint is a maximum thermal limit for the antenna with a simultaneous maximum efficiency.

WEFF software allows calculating the aperture size by taking into account many of the factors enumerated above and more. From WEFF calculations, the optimum $\tau = 1.5448$ for $\eta_c = 90$ %. This leads to a product $A_t{\cdot}A_r$ of 3.57×10^4 m^4 which is very similar to that calculated with the previous equations.

Independently of the collection efficiency, the antenna size is also dictated by the far field condition, which is expressed as

$$D \geq \frac{2D_t^{\ 2}}{\lambda_0} \qquad 2.11$$

where D_t is the diameter of the antenna aperture.

At far field distances, a narrow coherent beam is formed with a radial symmetry of the field illumination for a circular aperture. If operating in the near field, the beam formation requirement is not fulfilled and beam degradation results from sidelobes and scattering loss, and asymmetrical distribution across the receiver aperture occurs. In order to operate in the far field range, A_t is limited by

$$A_t < \frac{\pi D \lambda_0}{8} \qquad 2.12$$

A_t is constrained to be smaller than 47.8 m^2 or the antenna diameter is required to be less than 7.8 m. WEFF calculates a transmitting antenna diameter (D_t) equal to 5.2 m (A_t = 21.2 m^2). This value fulfills the far field condition since it is smaller than the maximum allowed antenna diameter of 7.8 m. Because of this antenna diameter reduction, the receiver diameter given by WEFF will consequently be larger than when calculated by aperture product using the maximum limit on A_t to maintain the collection efficiency at 90 %.

This receiver diameter enlargement is necessary to handle the incoming power without exceeding the rectifying diodes power ratings. Using D_t of 5.2 m, the calculated peak power density at the center of the receiver is 160 mW/cm^2. This is about the maximum allowable power density as can be seen from Fig. 2.7 for 2.45 GHz operation. If D_t is increased, the area of the transmitting antenna is increased and the peak power is also increased as given by equation 2.5. The power density level will exceed the power handling capacity of the current state-of-the-art rectenna.

To overcome this problem, high efficiency and high breakdown voltage rectenna diodes need to be developed. With high breakdown voltage rectenna diodes, the transmitter antenna diameter can be increased to its maximum limit of 7.8 m for far field operation and the receiver diameter can be reduced from 46 m (calculated with WEFF) to 30 m with the same collection efficiency of 90 %.

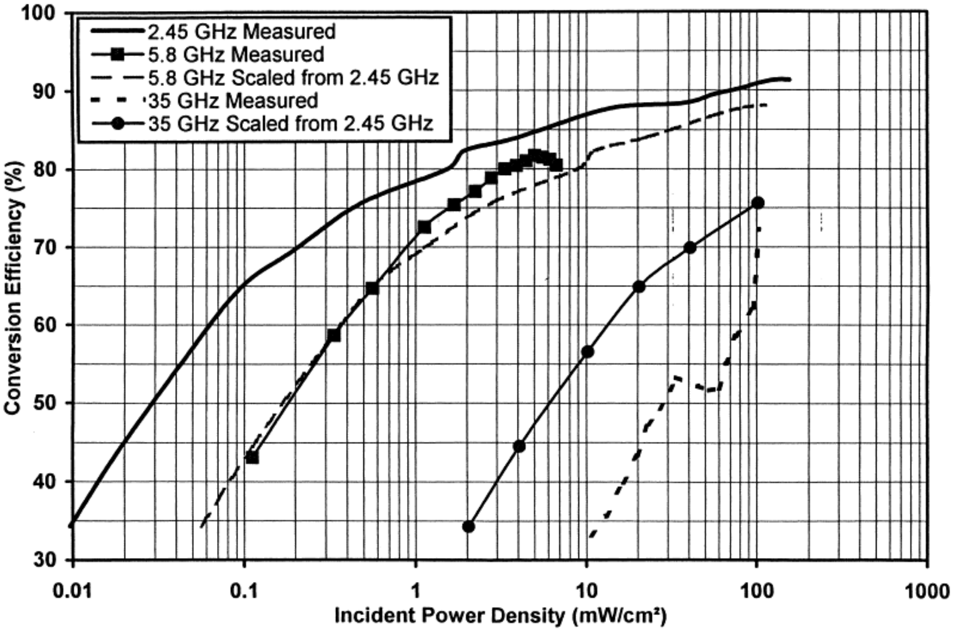

Fig. 2.7: State-of-the-art rectenna performances.

2.1.7.2 Receiver size

The receiver aperture size, A_r, is proportional to the transmission distance and will be selected to properly collect the incoming transmitted power, P_t. Also, the interaction of the diameter of focused power beam (or spot) relative to the receiver geometry determines to a large extent the receiver aperture. Of course, as A_r increases, the collection effect is greater resulting in a larger collection efficiency, η_c. According to Goubau's relation 2.2, to keep the collection efficiency constant, A_t and A_r may be changed for a given D and λ_0, as long as the product $A_t \cdot A_r$ remains constant. This relation is shown in Fig. 2.8 from WEFF data points using the system specifications.

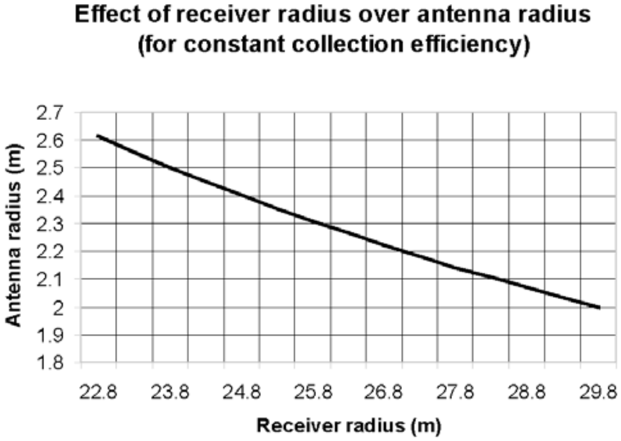

Fig. 2.8: Relation between A_t and A_r for a constant η_c.

For a Gaussian taper illumination at the transmitter, the power density at the receiver will be maximal at the center and decrease logarithmically towards the edges. The most useful power is considered to be between the center maximum power and the circle of half-power, which features a power density half of that found at the center of the receiver. The receiver aperture size should be close to the useful power area. It is advisable to use a circular shape for the receiver since it more closely matches the power circle geometry and therefore intercepts power more efficiently. Also, the maximum power density tolerated by the rectifier element limits the receiver's minimum element area.

Using the aperture product and A_t calculated in section 2.1.8.1, a minimum A_r of 745.1 m^2 ($D_r \geq$ 30.8 m) is calculated from equation 2.2. Again, using WEFF simulator, $A_r = 1.662\times10^3$ m^2 (diameter of 46 m). As explained at the end of section 2.1.8.1, WEFF has evaluated a larger receiver diameter than the minimum value predicted by the far field condition and Goubau's relation in order to maintain the power density level under the diode maximum power rating.

2.1.8 Transmitter preliminary design

The transmitter, as depicted in Fig. 2.1, is the WPT block that converts the DC (or AC) energy into RF power and radiates this microwave energy through the form of a focused beam into free-space. The DC(AC)-to-RF energy converter is the microwave source. An antenna or array of radiators follows the source to radiate the distributed RF energy into a taper illumination of the electromagnetic field.

One common configuration for the WPT transmitter is an array of slot antennas fed by magnetron sources. The following subsections describe this transmitter configuration.

2.1.8.1 Source

Vacuum tubes such as the well-known magnetron (found in the domestic microwave oven), the traveling wave tube, and the klystron are all high power microwave sources that convert the DC (or AC) power into RF power. Magnetrons are very inexpensive and efficient devices. Typical DC(AC)-to-RF conversion efficiencies, η_{mag}, are in the range of 70 % to 90 %. An amplitron (magnetron converted into a broadband amplifier) can provide a maximum efficiency of 80 % [2]. Klystrons are not as efficient as magnetrons and more expensive. The use of active antennas is another more recent method to produce a high power microwave beam with flexible steering capabilities. Although solid-state FET sources are very simple, they still provide inferior efficiencies compared to high power tubes.

Magnetrons have been selected to serve as the transmitter sources for this project. The output power range of an oven magnetron, P_{mag}, varies from 300 to about 1,500 W. A modified microwave oven magnetron as been reported in [28] to supply up to 1 kW of RF power on average. Higher power magnetrons used for industrial heating can provide up to 5 kW of output power. We assume an RF output power of about 5 kW from an optimal magnetron used for microwave power transmission applications.

2.1.8.2 Radiator

The selection of the radiator depends somewhat on the choice of the microwave source. With magnetron sources, a flat slotted waveguide array panel can appropriately serve as the radiating antenna. The slotted waveguide antenna is very well suited for power transmission because it features an excellent aperture or antenna efficiency, η_a, (> 95 %) and high power handling capability. Also, due to its low cost, this radiator is also an appropriate choice for the large transmitter aperture needed to maximize the collection efficiency. Beside the advantages enumerated above, this structure is fairly lightweight and low cost. Therefore, the slotted waveguide is recommended as the transmitter antenna for this project.

The slotted waveguide presents a narrow bandwidth from 0.5 % to 2 % due to the cutoff frequency inherent to the dominant mode propagation in the waveguide. This is not a harmful feature since the system is operating at a stable frequency of 2.45 GHz. However, a narrow bandwidth can present some constraints on the thermal expansion and mechanical tolerances of the antenna. Further details on the antenna configuration will follow.

2.1.8.3 Antenna configuration

As explained above, for this relatively low frequency of operation, a reliable configuration using magnetrons and slotted waveguide arrays is preferable due to its simplicity and low cost.

The configuration for the transmitter subsystem consists of a number of slotted waveguide subarrays each driven by one magnetron feeding through the feedguide and where longitudinal resonant slots are used as the radiating elements as shown in Fig. 2.9.

These typical configurations follow those suggested in [3]. The coupling between the magnetron and the aligned slotted waveguides is provided through a feedguide at the back of the radiating waveguide (Front view), perpendicular to the radiating waveguide axis, as shown in Fig. 2.9. The coupling between the feedguide and the radiation waveguides is realized through inclined slots. Two possible feeding configurations are illustrated in the Front view. However, it has been shown that the end feeding losses are lower than those from the center feeding. Using an aluminum feedguide, the ohmic losses are reported to be lower that 1 % [3].

Since both the radiating waveguide and the feedguide should support a dominant mode standing wave at 2.45 GHz, the standard waveguide WR-340 is used with inner wall dimensions of 8.64 cm × 4.32 cm (3.4″ × 1.7″). On the radiating waveguide, resonant longitudinal slots modeled by a shunt conductance are used. The slot parameters need to be calculated in order to provide good matching and high coupling to free-space for maximum radiation. As shown in Fig. 2.10, these parameters are the slot length, l_l, the slot width, w_l, the slot offset from the waveguide axis, o_l, and the spacing between adjacent slots, s_l.

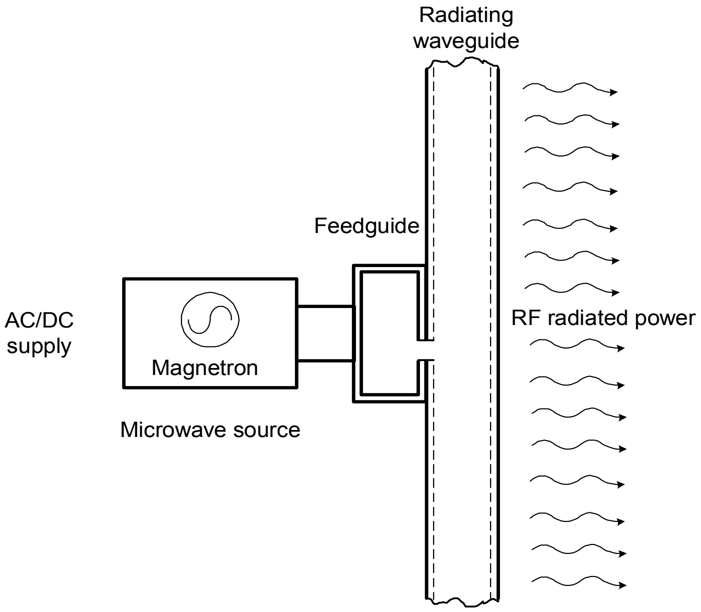

Side view

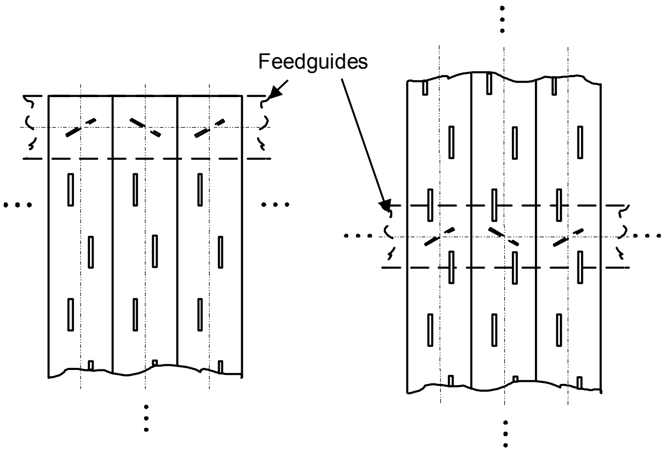

End feeding

Center feeding

Front view

Fig. 2.9: Subarray configuration with magnetron feeding slotted waveguides.

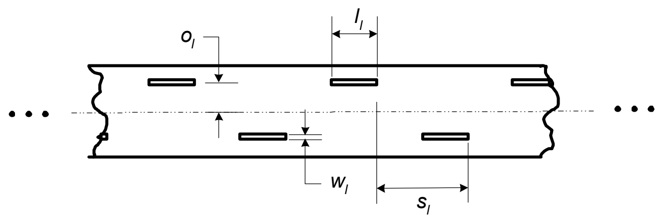

Fig. 2.10: Radiating slot parameters.

The slot length is chosen to ensure a resonant slot at the design frequency. A good approximation for l_l is $\lambda_0/2$. At 2.45 GHz, the slot length becomes $l_l = 6.12$ cm (2.41″). The slot width is a fraction of the slot length (≤ 1/10 of l_l) and may be taken as $l_l/16$ for a narrow slots design giving $w_l = 0.38$ cm (0.15″).

The offset is chosen to give the desired slot conductance needed for impedance matching. The relation of the offset to the conductance is found through well-known equations or design charts published by Stern and Elliott [4] among others. A good approximation of the needed normalized conductance g is $1/N$ where N is the number of longitudinal slots on the radiating waveguide.

Finally, the radiating slots are usually spaced by $\lambda_g/2$ to avoid grating lobes, where λ_g is the guided wavelength. This parameter depends on the waveguide dimensions and operating frequency. This resonant spacing will help determine the total number of elements. At 2.45 GHz and for a WR-340 waveguide, $s_l = 8.7$ cm (3.42″).

These parameters have been calculated without considering the mutual coupling between the neighboring radiating waveguides or even the interaction of the adjacent slots on the same waveguide (the later coupling becomes negligible with the third or fourth slot). Therefore, these values should be considered as preliminary. They need to be adjusted iteratively when integrating the other waveguides in an experimental environment or simulation setup with mutual coupling calculations.

The feedguide interfacing the magnetron output and the radiating slot waveguides is illustrated in Fig. 2.11. It consists of series inclined slots on the broadwall of a WR-340 waveguide with spacing defined by the radiating waveguide spacing (coinciding with the resonant spacing). The inclined slots are defined by a resonant length of $\lambda_0/2$ and an inclination angle θ that controls the level of coupling to the radiating waveguide. As shown, the slots have alternating inclination directions with respect to the axis to maintain an adequate power phasing from the radiating waveguide.

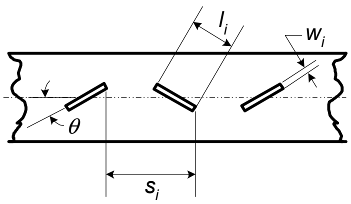

Fig. 2.11: Feedguide and feeding slot parameter.

The waveguide impedance seen by the feedguide, Z_r, is proportional to $\sin^2(2\theta)$. For maximum coupling to the radiating waveguides, Z_r has to be $1/N_w$ times the feedguide characteristic impedance, N_w being the total number of fed waveguides. If there is a large number of radiating waveguides in the subarray, a small coupling will be needed from the feedguide slot resulting in a small inclination angle.

2.1.8.4 Efficiencies

The magnetron efficiency, η_{mag}, is a conversion efficiency that can be defined as the ratio of the RF output power over the DC (or AC) input power. η_{mag} can vary from 60 to 70 % for microwave oven magnetrons. Off-the-shelf magnetrons used for industrial microwave heating as well as for laboratory models feature 85 % efficiency and can go up to 90 % at 3 GHz [2], [3]. We assume a relatively efficient magnetron adapted for this project with $\eta_{mag} = 80$ %.

The antenna efficiency, η_a, is usually assumed to be close to 100 %. It is defined as the ratio of the antenna gain G_t over the directivity D_0. This efficiency gives an indication of the mismatch and ohmic losses in the waveguide feed system which are estimated to be less than 0.1dB when using aluminum for a well designed slotted waveguide, as stated in [3]. In [26], the transmitter efficiency was of 96 % using high quality slotted waveguides. For simplicity, $\eta_a = 100$ % is assumed in this preliminary study.

2.1.8.5 Power levels

The RF output power of the transmitter has been specified as 1 MW / $\eta_{overall,\ \mathrm{RF\text{-}DC}}$ where $\eta_{overall,\ \mathrm{RF\text{-}DC}}$ is the transmitter RF to DC output efficiency. This later efficiency can be obtained from WEFF or determined from the product of the previously calculated η_c and assumed η_{rect}. WEFF generates $\eta_{overall,\ \mathrm{RF\text{-}DC}}$ = 76.5 % corresponding to the calculated value from η_c = 90 % and η_{rect} assumed as 85 %. The total transmitted RF power is then equal to 1.307 MW. Of course as the collection efficiency is increased, the required transmitted power is smaller for the same DC power output.

The DC (or AC) input power required to provide such RF transmitted power depends on the magnetron efficiency. It is assumed that each magnetron will provide 5 kW of RF power. The magnetron efficiency is set at 80 %. With these parameters, the system requires a DC (or AC) input power of 1.63 MW. The transmitter will therefore need a total of 262 magnetrons.

2.1.8.6 Number of elements

The total number of elements or slots can be determined from the spacing between neighboring elements and the total antenna aperture area. Assuming a half-wave ($\lambda_g/2$) spacing between elements of 0.087 m (3.42″) at 2.45 GHz, the total number of antenna slot elements is $A_t/(\lambda_g/2)^2$ = 2806 if operating in the far field.

As stated earlier, one magnetron will be used to feed a slotted waveguide subarray. In our case, the number of magnetrons corresponding to the number of subarrays is calculated based on the required RF output power. Using magnetrons that provide about 5 kW of RF power and setting η_a to 100 %, a total of 262 magnetrons are needed to generate 1.307 MW of RF transmitted power. From the total number of elements, each magnetron would feed a subarray of 3×3 elements for a uniform illumination. Since the radiated power is preferably tapered to approximate a Gaussian distribution, the magnetron near the center should feed a subarray with a smaller number of slot elements to radiate more power from each slot element. Inversely, the outer magnetrons on the periphery on the antenna should feed a larger subarray of slot elements.

2.1.8.7 Noise/harmonic reduction and retrodirective techniques

To avoid electromagnetic interference (EMF) and satisfying FCC requirements, it is important to have a low noise output at exactly 2.45 GHz with a low harmonic radiation. Magnetrons generate spurious noise. Brown [5] used an internal feedback scheme to reduce the spurious noise produced by magnetrons. This feedback mechanism would reduce or turn-off the external source of filament power after turn-on. Also, a very accurate, low phase noise, low power source can be used to phase-lock a high power magnetron with reduced harmonic radiation. This high power magnetron is then used to injection lock all other magnetron sources through mutual coupling in the antenna array. This technique has been demonstrated with solid-state sources [32]. Using this method, a very clean output signal with low phase noise and low harmonics can be achieved.

Retrodirective technique can be used to realign the transmitter with the receiver in mobile applications. Although the beam alignment is not necessary for the proposed demonstration, a retrodirective technique can be used to shut down the system if the beam is drifted away from the receiver due to malfunction. A simple retrodirective method is to have a low power pilot beam from the transmitter to the center of the rectenna array. This pilot beam can operate at different frequency. Four sensitive receivers near the rectenna center can be used to determine the direction of the incoming beam. Other methods such as an interferometer phasing system using multiple tones or computer controlled beam steering from sum/difference channel data have been suggested [26] to realign the main beam.

2.1.8.8 Transmitter specifications

Table 2.3 summarizes the various parameters optimized in the previous sections for the transmitter subsystem design.

2.1.9 Collector preliminary design

The receiver function is to collect the incoming RF power and convert it back to DC electricity. An appropriate choice of device to accomplish these tasks is the diode type rectenna, which as the name indicates is a receiving antenna that rectifies. In these rectennas, the electromagnetic waves are collected by antennas and rectified by diodes. A rectenna can basically be divided into four main components: the antenna, the RF filter, the diode rectifier, and DC filter as illustrated in Fig. 2.12.

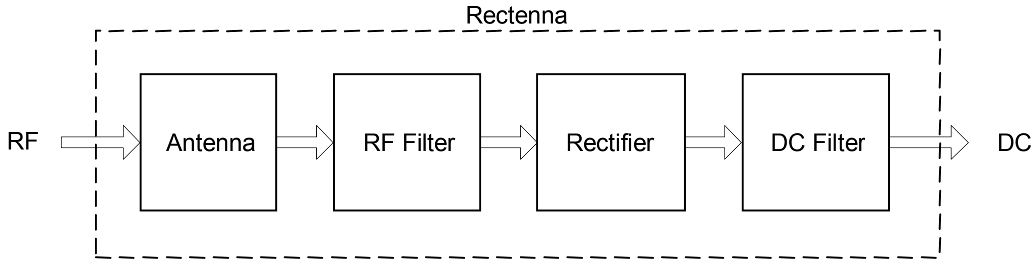

Fig. 2.12: Schematic of rectenna components.

Table 2.3: Transmitter parameters.

Diameter	5.2 m
Center frequency	2.45 GHz
Array type	Transmit
Source type	Magnetron (5 kW)
Radiator array	Slotted waveguide
Radiating slot type	Longitudinal
Length of radiating slot	6.12 cm (2.41″)
Width of radiating slot	0.38 cm (0.15″)
Radiating slot spacing	$0.5\ \lambda_g = 8.7$ cm (3.42″)
Number of magnetrons (or subarrays)	262
Number of radiating slots	2806
Number of slots/subarray	Varied (2×2 near center, 4×4 or 5×5 near edge)
Antenna taper	10 dB Gaussian
Transmitter overall efficiency	80 %
DC (or AC) input power	1.63 MW
Total RF radiated power	1.307 MW
Polarization	Linear

2.1.9.1 Receiving elements

In rectennas, the waves are collected by antennas. These antennas are usually half-wave dipoles. An optimum distance of $0.63\lambda_0 = 7.7$ cm separates them at 2.45 GHz. This type of antenna is chosen for its omnidirectional features. This allows the collection efficiency to be less dependent on the angle of incidence of the transmitted beam. If other types of antennas are used, the directional sensitivity may increase which in some cases may be critical. The half-wave dipole design for the rectenna has been extensively studied, tested and reported by Brown and Texas A&M in numerous journals and conference papers [2], [33], and [34].

2.1.9.2 Rectifiers

The waves are rectified by solid-state diodes generating a relatively low-voltage DC. The diode parameters can be optimized for maximum conversion efficiency, η_{rect}. Si and GaAs diodes are possible candidates that can be selected based on a tradeoff between the cost, the power handling limit and the efficiency. For our study, it is advisable to use GaAs diodes, which feature high η_{rect}. Brown has used mainly GaAs IMPATT diodes for his research on rectennas and McSpadden et. al. [33] has added reports on the robustness of these diodes. This type of diode has also been modeled in WEFF for power density calculations.

2.1.9.3 Filters

Filtering is a necessary function in a rectenna element to purify the incident signal. Two types of filters are used: an RF filter to block the reflected signal from the diodes which can be re-radiated through the dipoles and a DC filter to clean the output voltage. The harmonics produced by the diodes during the rectification process need also to be blocked to prevent radiation.

2.1.9.4 Rectenna configuration

The rectenna integration incorporates the diode into the rectenna element. This rectenna element includes a filtering circuit and the radiator. Then, the complete rectenna elements are integrated into the entire rectenna array as illustrated in Fig. 2.13 for a planar configuration.

2.1.9.5 Number of elements

It is good practice to have some redundancy in the number of elements in case of failure for reliability. Since the illumination decreases towards the edges of the rectenna collecting the taper beam, a larger number of perimeter dipoles would share the same diode in order to increase the receiver antenna gain.

For half-wave dipoles, the area of a rectenna element is $(0.63\lambda_0)^2 = 5.94\times10^{-3}$ m^2. The total number of elements is obtained after dividing from the total area. A total number of 279782 half-wave dipoles are needed for a circular aperture and one diode/element is used as a first preliminary design. To reduce the number of elements a triangular lattice can be used instead of the rectangular lattice shown in Fig. 2.13.

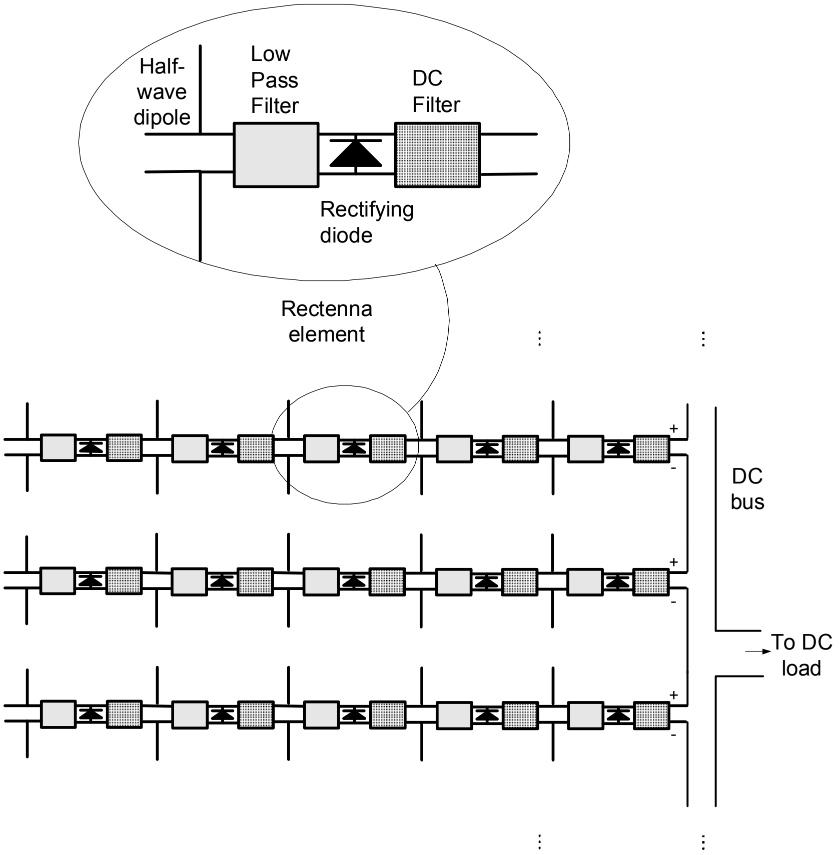

Fig. 2.13: Planar rectenna configuration.

2.1.9.6 Power level

As mentioned earlier, the power handling capacity of a rectenna depends largely on its element area and the power density ratings of the individual components. The amount of intercepted energy from the rectenna is a direct function of the antenna aperture, since a smaller antenna would produce a wide spread beam hence leaving less power to be collected by the rectenna. This is according to Goubau's relation. Using the specified collection efficiency of 90 % and the previously calculated transmitted power, the total received RF is 1.176 MW.

2.1.9.7 Efficiencies involved in receiver design

The receiver efficiency can be expressed as the transfer function of this subsystem. In terms of power ratio, the rectenna overall efficiency is equal to the DC output power divided by the incident RF power. This transmitting RF to DC output efficiency, $\eta_{overall,\ \mathrm{RF\text{-}DC}}$, is the product of 2 sub-efficiencies: the collection or capture efficiency, η_c, and the conversion or rectification efficiency, η_{rect}. $\eta_{overall,\ \mathrm{RF\text{-}DC}}$ is strongly dependent on the amount and the distribution of the incident power density. η_{rect} represents the capacity to convert the microwave energy entering the antennas into DC output from the rectenna. A description of both efficiencies follows.

a) Effect of collection efficiency

As defined earlier, the collection efficiency, also called the aperture-to-aperture efficiency, capture efficiency, or absorption efficiency, is the ratio of the received power at the rectenna aperture over the microwave transmit power. It is one of the most important efficiencies for a rectenna.

The received field pattern is defined as the Fourier-Bessel transform of the transmitter aperture radial taper. For maximum collection efficiency, an optimum power density distribution must be selected for the antenna aperture. A non-uniformly illuminated aperture increases the collection efficiency and it has been observed that the optimal taper is of Gaussian type.

The collection efficiency should be very high if the impedance looking into the receiver is matched to the free space impedance. Generally, this matching requires some tuning after the rectenna components have been built.

The collection efficiency can be approximated by an exponential function of Goubau's parameter τ as

$$\eta_c = (1 - \mathrm{e}^{-\tau^2}) \times 100\% \qquad 2.13$$

As A_t becomes greater, the directivity and the incident power density also increase leading to higher collection efficiency as seen through τ. This translates into a tradeoff between the size and the efficiency.

The collection efficiency is proportional to the power density and the incremental area of the rectenna. The challenge in the beam collection optimization is to have low sidelobe levels while defining A_r to match the main beam of the transmitter. Also, if the frequency is increased with a constant A_t, A_r can be reduced but the collection efficiency will degrade due to increased atmospheric loss, as mentioned previously.

WEFF can facilitate the analyses of WPT systems versus η_c. From WEFF simulations a collection efficiency of 90 % is found satisfactory.

b) Effect on conversion efficiency

The conversion efficiency, η_{rect}, can be considered at the component level since it mainly represents the rectifying capabilities of the solid-state diode. This is why it is also commonly called the rectenna or rectifier efficiency. The conversion efficiency is also a function of losses in the half-wave dipoles and the entire rectifying circuit. The later should efficiently lower harmonics to maximize the conversion of microwave power into DC power. η_{rect} can be defined as the product of the efficiency of the individual dipole elements by the conversion efficiency of the rectifying diode. At a more general level, the rectifier efficiency can be quantified as the ratio of the DC output power over the RF received power.

Since it is proportional to the received power, the conversion efficiency will depend on the power density at the rectenna. It actually depends on the incident power hitting the rectifying diodes (connected to the $\lambda_0/2$ dipoles). This is why it is very important to put efforts in developing higher efficiency diodes even for lower incident power level. Also, when the transmitter aperture is reduced, the conversion efficiency will decrease. This is due to less power interception by the rectenna since the beam is spread out.

The rectenna elements will have to be designed to have an optimal power density, P_d, otherwise the conversion efficiency will decrease as P_d is shifted from the optimum. If all the rectennas elements are identical, then the conversion efficiency varies with the power density across the aperture. There is a tradeoff to be made between designing a rectenna with elements procuring the optimum power density (depending on the position on the rectenna area) giving an overall higher conversion efficiency with making all the elements the same providing costs savings.

An average conversion efficiency of 69 % was obtained in [2]. η_{rect} has been found to range from 70 % (with 0.04 mW/cm^2 of incident power density) to 90 % (10 mW/cm^2) for a 2.45 GHz system in 1981 [3]. Three percent of improvement over the achievable conversion efficiency was predicted for the next decade. More recent publications [27], [33] feature a typical value of 85 % for the conversion efficiency and a possible maximum value of 92 %. After simulation tuning in WEFF, an optimal conversion efficiency of 90 % using GaAs diodes is obtained. Since this is an ideal value, we assume a more conservative conversion efficiency of 85 % closer to the real value which includes the various diode parasitics and losses in the rectifying circuit.

2.1.9.8 Receiver specifications

The receiver design parameters are presented in Table 2.4 featuring previously calculated values.

2.1.10 System description

Since the power flux in the system is intimately related to the components efficiencies, a link table (Table 2.5) is presented to illustrate the relation at various stages in the system as were calculated previously. Table 2.6 and Table 2.7 are a recapitulation of the transmitter and receiver main parameters.

Table 2.4: Rectenna parameters.

Diameter	46 m
Center frequency	2.45 GHz
Array type	Receive
Element spacing	$0.63\ \lambda_0 = 7.7$ cm
Receiving elements	Printed half-wave dipole antenna
Rectifying device	GaAs diode
Element effective area	$59.4\ \text{cm}^2\ (\ (0.63\lambda_0)^2\ )$
Number of rect. elements	279782
Polarization	Linear
Total received power	1.176 MW
Collection efficiency	90 %
Conversion efficiency	85 %
Peak power density	$160\ \text{mW/cm}^2$
Edge power density	$16.3\ \text{mW/cm}^2$
DC output power	1 MW

Table 2.5: System link.

System process	Power levels	Efficiency
DC (or AC) input to RF conversion through magnetron	$P_{\text{DC(AC)}i} = 1.63$ MW $P_{mag} = 5$ kW	$\eta_{mag} = 80\%$
RF radiated power through the antenna	$P_t = 1.307$ MW	$\eta_a\ =\ 100\ \%$
Beam collection at the receiver	$P_r = 1.176$ MW	$\eta_c\ = 90\ \%$
RF input power converted to DC output power	$P_{\text{DC(AC)}o} =\ 1$ MW	$\eta_{rect} =\ 85\ \%$
DC(AC)-to-DC overall power transfer	N/A	$\eta_{\text{DC(AC)-DC}} = 61\ \%$

Table 2.6: System link for transmitter.

Transmitter Specifications	
Diameter	5.2 m
Center frequency	2.45 GHz
Array type	Transmit
Source type	Magnetron (5 kW)
Radiator array	Slotted waveguide
Element spacing	0.5 λ_g = 8.7 cm (3.42″)
Number of magnetrons	262 (number of subarray)
Number of slot elements	2806
Number of elem./subarray	Varied (2×2 near center, 4×4 or 5×5 near edge)
Antenna taper	10 dB Gaussian
Transmitter efficiency	80 %
Total radiated power	1.307 MW
Polarization	Linear

Table 2.7: System link for rectenna.

Rectenna Specifications	
Diameter	46 m
Center frequency	2.45 GHz
Array type	Receive
Array geometry	Triangular lattice
Element spacing	$0.63\ \lambda_0 = 7.7$ cm
Receiving elements	Printed half-wave dipole antenna
Rectifying device	GaAs diode
Element effective area	59.4 cm^2
Number of rect. elements	279782
Polarization	Linear
Total received power	1.176 MW
Collection efficiency	90 %
Conversion efficiency	85 %
Peak power density	160 mW/cm^2
Edge power density	16.3 mW/cm^2
DC output power	1 MW

2.2 Comparison of 2.45 and 35 GHz WPT systems

In this section we present a comparison between 2.45 GHz and 35 GHz for a WPT system. The following considerations are reviewed: atmospheric attenuation, choice of components, size of apertures, efficiencies, and costs.

2.2.1 Interference

At 2.45 GHz, the system operates at the center of the 100 MHz wide Industrial, Medical and Scientific (ISM) band. The advantage in working within this band is that any service in the band can tolerate interference from other users. This relaxes some filtering constraints on the transmitter of the WPT system although there still is the need to provide electromagnetic compatibility outside the band through harmonic suppression using low-pass and band-stop filters at both antennas.

35 GHz is in a window of low atmospheric loss. Interference at 35 GHz is lower since high frequency regions are still not encumbered by too many users. Another advantage is that the separation between harmonics is larger. Even if designs are realized at 35 GHz, it should be noted that no allocation has yet been given for WPT applications [28]. This frequency in the millimeter wave band is actually more widely used for radar. Fig. 2.14 presents the electromagnetic spectrum with various allocated bands and corresponding applications.

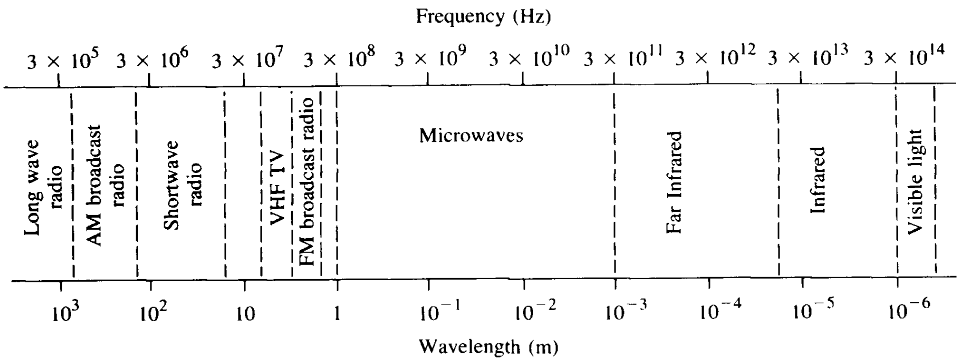

Typical Frequencies	
AM broadcast band	535–1605 kHz
Shortwave radio	3–30 MHz
FM broadcast band	88–108 MHz
VHF TV (2–4)	54–72 MHz
VHF TV (5–6)	76–88 MHz
UHF TV (7–13)	174–216 MHz
UHF TV (14–83)	470–890 MHz
Microwave ovens	2.45 GHz

Approximate Band Designations	
L-band	1–2 GHz
S-band	2–4 GHz
C-band	4–8 GHz
X-band	8–12 GHz
Ku-band	12–18 GHz
K-band	18–26 GHz
Ka-band	26–40 GHz
U-band	40–60 GHz

Fig. 2.14: The electromagnetic spectrum. [35]

2.2.2.Radiation hazards

As was mentioned in the introduction, the microwave and millimeter wave bands do not generate ionizing energy. The hazard level of heating can be further lowered by spreading the microwave beam over a large cross section area. This can be done by either increasing the wavelength (or reducing the operation frequency) or the distance between the transmitter and the receiver. If a small scale system with a limited range of transmission is designed, the lower frequency of 2.45 GHz is favored for a biologically harmless beam power density level. With such large apertures and transmission distances in the S-band, the maximum RF power density is about one-thirtieth the intensity of sunlight [36].

Millimeter wave power systems produce more intense beams and should be located in non public sites as dry as possible and at high altitudes [36]. The low-humidity requirement will be explained in the following section on atmospheric losses.

2.2.3 Atmospheric losses

Operating at 2.45 GHz allows the transmitted microwave beam to travel through the atmosphere without suffering from excessive attenuation. This attenuation is caused by absorption and scattering from atmospheric particles such as rain drops, dust or clouds. This attenuation is accentuated when the wavelength is comparable to the particles size. For ground-based systems this attenuation is generally assumed negligible at 2.45 GHz because of the large operation wavelength. Although higher frequencies present higher atmospheric losses, 35 GHz is also a good candidate because of the minimum dip it presents in the atmospheric attenuation spectrum [37]. Rain attenuation levels at 35 GHz will not be prohibitive most of the time except in tropical regions [37]. For a nearly weather independent system lower frequencies should be favored (< 3 GHz) as shown in Fig. 2.15 which plots the absorption by the atmosphere as a function of frequency above 10 GHz [38]. Fig. 2.16 shows the attenuation down to 3 GHz.

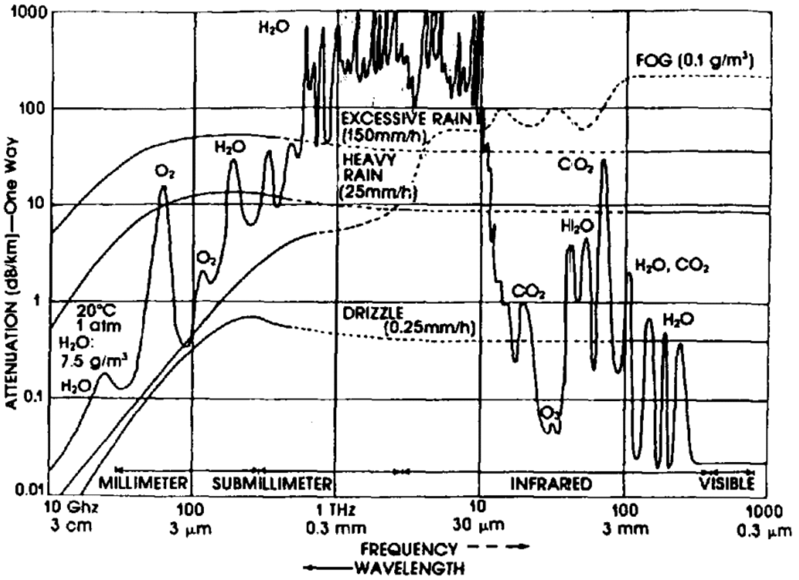

Fig. 2.15: Atmospheric attenuation spectrum. [38]

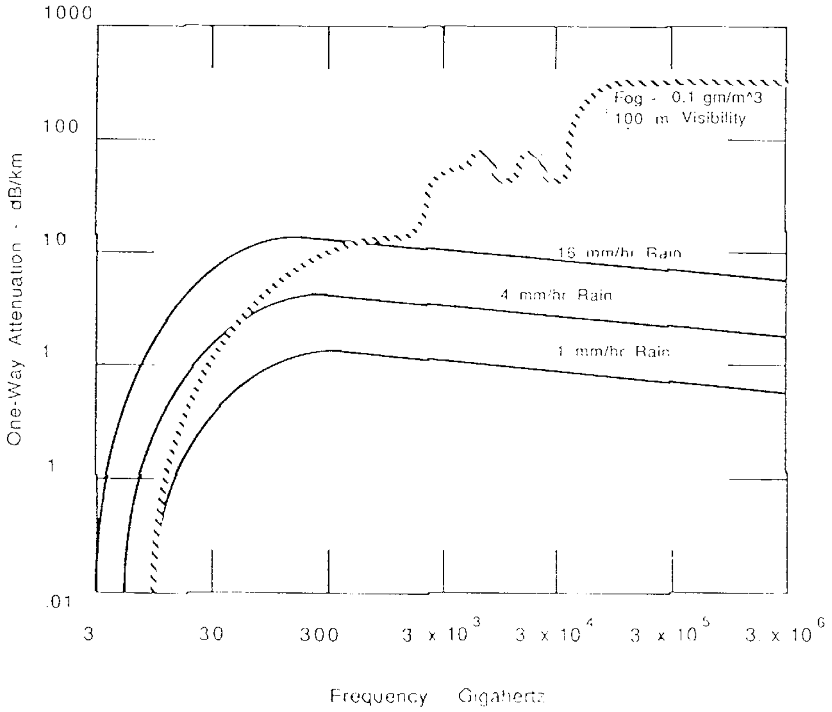

Fig. 2.16: Atmospheric attenuation from 3 GHz. [28]

As can be seen, there is a lower attenuation around 35 GHz compared to other high frequencies in the millimeter wave band. From [28], an atmospheric attenuation of about 30 % was evaluated for a given WPT system operating at 35 GHz compared to almost no attenuation for its 2.45 GHz counterpart.

2.2.4 Collection efficiency

The collection efficiency, which characterizes the aperture-to-aperture microwave beam transmission, is a function of the atmospheric attenuation which depends on the operating wavelength and the power density. Therefore, higher frequency systems will suffer from a degradation in the collection efficiency in adverse weather conditions since the atmospheric loss is higher.

2.2.5 Transmitter

The impact of the operating frequency on the transmitter design is discussed in the following subsections.

2.2.5.1 Source selection

WPT technology at 2.45 GHz has been thoroughly researched. The magnetron is a much less complex device compared to other high power tubes. It is common practice to use the low cost commercially available microwave oven magnetron tubes as sources for the transmitter at 2.45 GHz. Furthermore, lower frequency sources generally present higher DC(AC)-RF conversion efficiencies. Off-the-shelf magnetrons used for industrial microwave heating as well as for laboratory models feature 85 % to 90 % efficiency at 3 GHz [2], [3]. For higher frequencies in the range of 10-20 GHz the maximum efficiency can drop down to 70 %.

Gyrotrons are capable of providing very large power levels at higher frequencies (hundreds of kW) but their use seems somewhat impractical mostly due to high cost and complexity [37]. Their efficiency is rather low reaching a maximum of about 50 % [28]. Klystrons are high power (50-70 kW) and low-noise devices suited for higher frequency operation although their state-of-the-art efficiency is still lower than that of the magnetrons. Efficiencies of 75 % at S-band have been recorded and lower efficiencies should result at higher frequency operation [3].

2.2.5.2 Antenna size

Longer wavelengths require larger apertures in order to produce a focused beam. This beam width is approximated by the product of the range and wavelength divided by the aperture diameter [36]. The aperture size of an antenna A_t can be quantified as a function of many operating WPT parameters including the operating frequency, f, (or wavelength, λ_0) as seen in Goubau's relation 2.2.

As mentioned previously in section 2.1.10.7, the collection efficiency is proportional to the parameter τ (see equation 2.13). For the same transmission distance, low frequency systems require relatively large antenna and receiver size. This can translate into high fabrication costs.

Operating at a higher frequency allows for reduction in component size. This reduction will require tighter tolerances and result in larger costs to achieve them. As seen in 2.2, to reduce the antenna and rectenna size and keep the collection efficiency constant (i.e. parameter τ constant) with a fixed distance, the frequency can be increased.

To evaluate the percentage of size reduction, equation 2.2 is used along with the far-field condition to obtain the following size scaling expression:

$$\frac{D_{f_1}}{D_{f_2}} = \sqrt{\frac{f_2}{f_1}} \qquad 2.14$$

where D_{f1} and D_{f2} are the aperture diameter (transmitter or receiver) at the operating frequency f_1 and f_2 respectively. At 35 GHz, the apertures will undergo a size reduction of 74.6 % from 2.45 GHz.

2.2.6 Rectenna

The following will present the effect of the frequency on some rectenna parameters.

2.2.6.1 Rectenna size

As discussed earlier, at 35 GHz the rectenna diameter D_r can be reduced by 74.6 % from 2.45 GHz for the same distance and collection efficiency.

2.2.6.2 Rectenna conversion efficiency

The rectenna conversion efficiency η_{rect} has been found to range from 70% (with 0.04 mW/cm^2 of incident power density) to 90% (10 mW/cm^2) for a 2.45 GHz system in 1981 [3]. The efficiency is slightly above 90 % with a power density up to 100 mW/cm^2. Values higher than 85 % have actually been measured in a field demonstration [3].

A rectenna conversion efficiency was found to be 70 % with a power density of 100 mW/cm^2 for a 35 GHz rectenna [28], [37].

2.2.6.3 Rectenna diode cost

The relative cost for the rectenna is usually measured in cost divided by a certain quantity for example, the area. At 2.45 GHz, the area can be around 4 times larger than at 35 GHz. The cost obviously depends on many factors. As a general rule, the price is always inversely proportional to the produced quantity of components or the availability of the technology. The market force is the main cause for the component price reduction at 2.45 GHz. The limited production of devices at 35 GHz can be explained by the significant design complexity at higher frequencies due to dimension tolerances and increasing parasitics.

2.2.6.4 Rectenna diode packaging

For both 2.45 GHz and 35 GHz different kinds of packages are possible depending on the environment. If the power transfer is realized in space, temperature and cosmic radiation considerations have to be addressed for the diode packaging design.

Of course as frequency is increased, packaging parasitics have to be taken into account. The high frequency diodes are normally in open packages to reduce the packaging parasitics and will require protection in harsh environment. Passivation layers can be used to cover the devices for protection.

2.2.7 Summary of comparison

For a quick reference, Table 2.8 summarizes this study based on current technologies.

Table 2.8: Comparison table for WPT system performance at different operating frequencies.

Consideration	**2.45 GHz**	**35 GHz**
Atmospheric loss	Low	High
Interference with other users	Moderate	Low
Antenna and rectenna size	Large	Small (almost 4 times)
Collection efficiency	High	Low (in adverse weather)
Rectenna efficiency	High 90 %	Low 70 %
Transmitter source Cost Efficiency	Magnetron $10-$20/magnetron in large quantity 70 % - 90 %	Gyrotron/Klystron Expensive max 70 % (klystron) 30 % - 50 % (gyrotron)
Rectenna diode cost	Low	High
Rectenna diode packaging	Sealed	Open (Protection required)
Research status	Mature	In development

2.3 Optimal antenna taper design for a sandwich transmitting array

In this section, tapers with reduced thermal constraints such as split beam tapers are used in lieu of the conventional single beam 10 dB Gaussian taper. For each studied taper, the performance results are calculated and optimized using WEFF and GUIWEFF. GUIWEFF, a program developed as part of this dissertation, is a graphical interface to WEFF for automatic power transmission analysis and optimization. Given a set of system specifications, thermally efficient tapers are obtained with high collection efficiency and low Sidelobe Level (SLL). More details on GUIWEFF will be provided in section 2.3.2.3.

A 10 dB Gaussian taper aperture, typically considered as the optimal taper [31], is used to obtain high collection efficiency (90% for a 250-m antenna). Since the resulting RF radiated power is very high at the center of the transmitter, the electronics located near the center may be overheated beyond its thermal ratings as represented in Fig. 2.17. Split tapers can be used to reduce thermal constraints by presenting lower power intensity at the center of the aperture. On the other hand, this power attenuation will reduce the collection efficiency. A comparison needs to be done between the collection efficiency of the 10 dB Gaussian aperture taper and split tapers with less thermal constraints. Mathematical functions can be found [39] to produce such tapers. The sandwich array system is required to have the specifications summarized in Table 2.9. The specified frequency of 5.8 GHz is used for rectenna applications. Morever, this choice results in higher compactness for antennas than the other ISM frequency of 2.45 GHz.

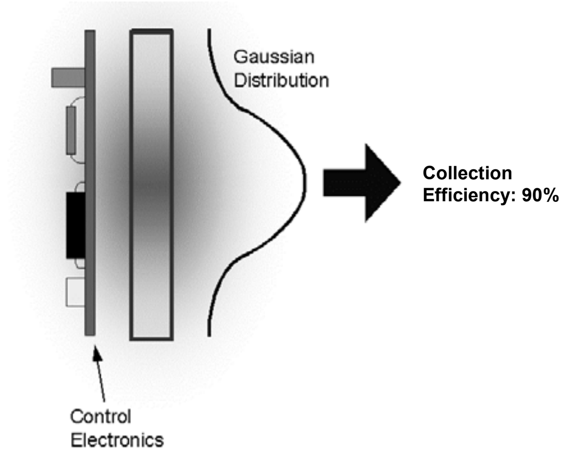

Fig. 2.17: Gaussian over aperture of sandwich array. Color gradation represents heat.

Table 2.9: System specifications.

Parameter	Value
Frequency of operation	5.8 GHz
Antenna position	Geosynchronous orbit
Rectenna position	Earth based
Antenna-rectenna distance	36,800 km
DC output power	1.2 GW
Transmitter radius (R_T)	250 m and 375 m

Using WEFF, we could find that a reference beam providing optimal efficiency was reported to be the 10 dB Gaussian beam, reaching approximately 90% of collection efficiency [31]. In order to reduce the thermal constraints at the center of the antenna, the taper needs to be attenuated with split beams.

The following sections present a study of WPT performance for a family of thermally efficient tapers and their optimization. Section 2.3.1 will define the basic performance entities along with commonly used tapers. Section 2.3.2 will present the optimization approach for the tapers considered. Results and discussion are provided in sections 2.3.3 and.2.3.4 respectively.

2.3.1 Theoretical background

2.3.1.1 Collection efficiency and SLL

In order for the global efficiency to be sufficiently high, it has been shown that the transmitter illumination needs to be an optimal taper as will be seen later. A non-uniformly illuminated aperture, such as the Gaussian, increases η_c. Also, as the antenna surface increases, the directivity (or antenna gain) and the incident power density also increase leading to a higher η_c as will be observed in section 2.2.4. This translates into a tradeoff between compactness and efficiency.

The received field pattern is defined as the Fourier-Bessel transform of the transmitter aperture. The chosen taper of illumination at the elements of the antenna array will therefore generate a radiated field pattern that consists of a main beam, where the major part of the power is concentrated, and of some undesired parasitic lobes adjacent to the main beam. The level of these lobes is referred to as the SLL and needs to be reduced in order to increase the efficiency as well as for interference and safety concerns in WPT systems.

2.3.1.2 Gaussian and Uniform taper

The Gaussian taper has a smooth decrease towards the edges which reduces the SLL. Reported optimal results are obtained when the level of the edges is 10dB below the main central beam, therefore the name 10 dB Gaussian. Fig. 2.18 shows the 10 dB Gaussian taper shape in magnitude and dB scaling over the normalized antenna diameter.

The 10 dB Gaussian taper equation is given by:

$$z = e^{-1.1513 \cdot \rho^2} \tag{2.15}$$

where ρ is the position along the radius of the antenna. Table 2.10 presents simulation results obtained from WEFF, characterizing the 10 dB Gaussian taper for the cases of an R_T of 250 m and 375 m (W_{MAX} is the maximum power density on the antenna aperture). The system specifications are as given in Table 2.9 with a rectenna radius of 3.744 km to ensure a collection efficiency of 90 % with a 10 dB Gaussian taper and a DC power output of 1.2 GW with a 250-m antenna. This rectenna radius is kept constant for the following studied tapers to compare between systems of same dimensions. It can be seen that the efficiency increases with the antenna area since the directivity is higher.

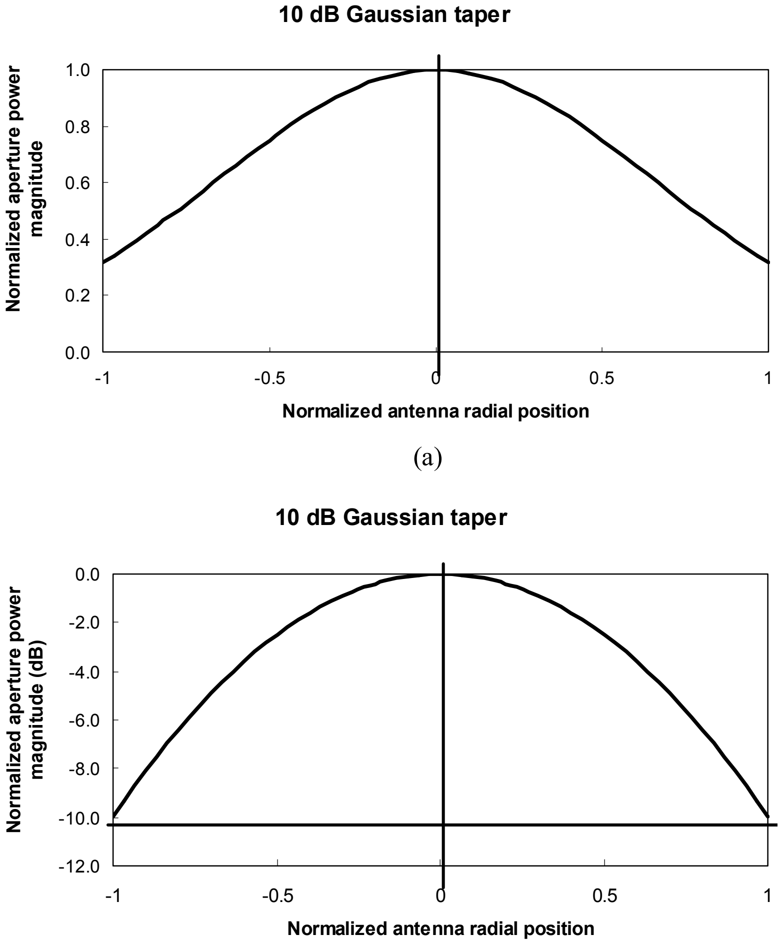

(a)

(b)

Fig. 2.18: 10 dB Gaussian taper. (a) In magnitude and (b) dB.

Table 2.10: Performance of the 10 dB Gaussian taper applied on a 250-m and 375-m antenna.

ρ	η_c	P_T	P_R	W_{MAX}	*SLL*
m	%	GW	GW	kW	dB
250	90	1.60	1.44	20.8	-24.4
375	96.5	1.46	1.41	8.5	-24.4

In order to decrease the maximum power density over the antenna area, the most obvious solution is the Uniform taper, shown in Fig. 2.19. After simulating this taper with WEFF for R_T of 250 m and 375 m, the performance characteristics as shown in Table 2.11 were obtained using the same specifications as for the 10 dB Gaussian. As expected, the results obtained from WEFF show that the power density at center of the antenna is much lower than for the 10 dB Gaussian taper (a 56% decrease). However, the overall efficiency of the taper also dropped. This translates into a total transmitted power increase to ensure a constant converted DC power at the rectenna (which means higher power consumption and more powerful RF amplifiers). Also, the SLL's have increased considerably. This also contributes to a decrease in efficiency. Clearly, a more optimal taper between this extreme and the 10 dB Gaussian with high efficiency and low maximum power density is needed.

Table 2.11: Performance of the Uniform taper applied on a 250-m and 375-m antenna.

ρ	η_c	P_T	P_R	W_{MAX}	*SLL*
m	%	GW	GW	kW	dB
250	82.4	1.74	1.44	8.88	-17.6
375	84.6	1.65	1.40	3.74	-17.6

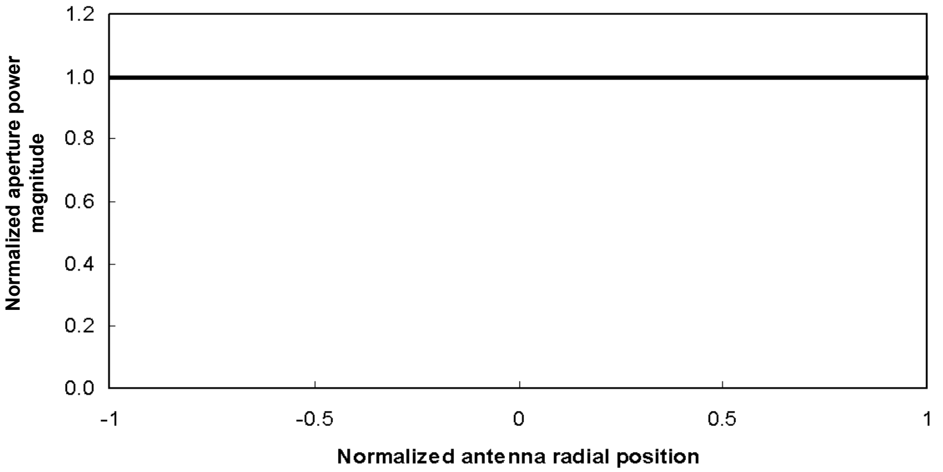

Fig. 2.19: Uniform taper.

2.3.2 Proposed taper optimization

The study of various split or distributed energy tapers is conducted through the automated use of WEFF with the GUIWEFF interface, as will be described in section 2.3.2.3. The coefficients in the taper distribution formulas will be automatically varied in order to optimize the level of the collection efficiency, and to reduce of the power density and the SLL.

2.3.2.1 Studied tapers

A set of 7 taper equations was chosen arbitrarily to approach the optimum 10 dB Gaussian taper efficiency [39]. These tapers all have from one to three levels of design flexibility (a, b and c) which allows the altering of the taper shape. For each equation, ranges for the three variables must be determined in order to obtain suitable shapes as will be explained later in this section.

It is known that an array with smoother amplitude distribution (larger tapering) produces smaller SLL but creates a larger Half Power Beam Width (HPBW) thus a smaller gain. Indeed, referring to published tables [40], the comparison shown in Table 2.12 can be established. D_T is the transmitter antenna diameter and λ is the wavelength. As seen from the table, the edges tapering reduces the aperture efficiency since a smaller area is illuminated with high excitation levels therefore forcing the broadside gain to drop. On the other hand, the SLL's are higher for the Uniform taper because of the edge discontinuity. As a rule of thumb, there is a tradeoff between the SLL and the HPBW when choosing an aperture taper. Table 2.13 provides the list of equations, with their maximum values used for normalization. The table also provides the maximum values of the functions, as well as the range of validity for the variables. The calculations for the maximums and ranges are given after the table. The following list provides the definition for each taper acronym:

- SSFL: Squared Sinus with Finite Level
- SG: Split Gaussian
- SGHC: Split Gaussian with High Center
- OC: Oval of Cassini
- SC: Split Circular
- SR: Split Radial
- SRS: Split Radial Squared

Table 2.12: Overview of effect of edges and taper shape on directivity and SLL.

Taper	**Uniform**	**Triangular**	**Cosine**	**Cosine ^{2}**
	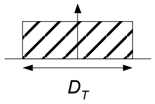 	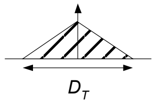 	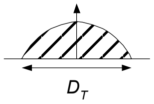 	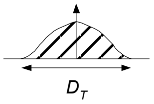
Directivity	$2(D_T/\lambda)$	$0.75[2(D_T/\lambda)]$	$0.81[2(D_T/\lambda)]$	$0.661[2(D_T/\lambda)]$
SLL	-13.2	-26.4	-23.2	-31.5

Table 2.13: Equation for each taper and the associated maximum value used for normalization.

Taper	Equation	Maximum value	Limits
SSFL	$z = \sin(\pi\rho)^2 + a$	$1 + a$	N/A
SG	$z = e^{-c\cdot[a(\rho \pm b)]^2}$	1	N/A
SGHC	$z = e^{-c\cdot\rho^2} - ae^{-c\cdot(b\rho)^2}$	$\left(ab^2\right)^{-1/b^2-1}$ $-a\left(ab^2\right)^{-b^2/b^2-1}$ for $b \neq 1$ $1-a$ for $b = 1$	$a < e^{-c\cdot\left(1-b^2\right)\rho^2}$
OC	$z = \sqrt{(1-2a^2+a^4+4a^2\rho^2)^{1/2} - (\rho^2+a^2)}$	$\dfrac{1-a^2}{2a}$	a<0.707 $a^2 >$ $-2\rho^2+1\pm 2\rho\sqrt{\rho^2-1}$
SC	$z = \sqrt{1-[a(\rho \pm b)]^2}$	1	$a < \dfrac{1}{\rho \pm b}$
SR	$z = 1-[a(\rho \pm b)]^2$	1	$a < \dfrac{1}{\rho \pm b}$
SRS	$z = \{1-[a(\rho \pm b)]^2\}^2$	1	$a < \dfrac{1}{\rho \pm b}$

The following presents the calculations for the non-obvious cases of taper maximums.

SGHC

$$\frac{dz}{d\rho} = 2a\rho cb^2 e^{-c(b\rho)^2} - 2c\rho e^{-c\rho^2} = 0 \qquad 2.16$$

$$\rho = \pm\sqrt{\frac{\ln\left(ab^2\right)}{c\left(b^2-1\right)}} \text{ and } \rho = 0 \qquad 2.17$$

$$z_{\max} = e^{\frac{-\ln\left(ab^2\right)}{b^2-1}} - ae^{\frac{-b^2\ln\left(ab^2\right)}{b^2-1}} \qquad 2.18$$

$$z_{\max} = \left(ab^2\right)^{\frac{-1}{b^2-1}} - a\left(ab^2\right)^{\frac{-b^2}{b^2-1}} \qquad 2.19$$

OC

$$\frac{dz}{d\rho} = \frac{1}{2}\left[\sqrt{1-2a^2+a^4+4a^2\rho^2} - \rho^2 - a^2\right]^{-1/2} \cdot \left[\frac{1}{2}\left(1-2a^2+a^4+4a^2\rho^2\right)^{-1/2} \cdot 8a^2\rho - 2\rho\right] \qquad 2.20$$
$$= 0$$

case 1:

$$\sqrt{1-2a^2+a^4+4a^2\rho^2} - \rho^2 - a^2 = 0 \qquad 2.21$$

By setting $u=\rho^2$, we obtain:

$$u = a^2 \pm \left(a^2-1\right) \qquad 2.22$$

$$\rho = \pm\sqrt{2a^2-1} \qquad 2.23$$

Since ρ cannot be negative, we are left with only the positive value. Once in the original equation for OC, we obtain 0. Therefore this is a minimum (since z cannot be negative either).

case 2:

$$\left(1-2a^2+a^4+4a^2\rho^2\right)^{-\frac{1}{2}}\cdot 8a^2\rho-2\rho=0 \tag{2.24}$$

$$\rho=\pm\frac{\sqrt{3a^4+2a^2-1}}{2a} \tag{2.25}$$

Once in the equation for z, we obtain:

$$z_{\max}=\frac{1-a^2}{2a} \tag{2.26}$$

SC, SR and SRS

By inspecting the equations, it is clear that the maximum value is 1. Depending on the values on a and b, the value of z may not reach this maximum, and therefore the maximum may be lower than 1. However, it can be proven that these conditions would also lead to a complex or negative value for some values of ρ. For this reason, in the case of SRS, the maximum value of z is always given as follows:

$$\frac{dz}{d\rho}=-2a\left[a\left(\rho\pm b\right)\right]=0 \tag{2.27}$$

$$\rho=\mp b \tag{2.28}$$

$$z_{\max}=1-\left[a\left(\mp b\pm b\right)\right]^2=1 \tag{2.29}$$

The same procedure can be used for SC and SR.

To each of these taper equations we can also associate a limit on the range of ρ. Here we will provide the non-obvious calculations for the limit of the taper equations. It should be noted that all the limits are found assuming that the coefficients are always positive.

SGHC

$$z = e^{-c\cdot\rho^2} - ae^{-c\cdot(b\rho)^2} > 0 \qquad 2.30$$

$$a < e^{-c\cdot\left(1-b^2\right)\rho^2} \qquad 2.31$$

This requires a careful study of the value of *b* in the specified range with respect to 1 for a given *c*. For example, if *b* <1 then the limit becomes a decreasing exponential over the range of the taper aperture as seen on Fig. 2.20.

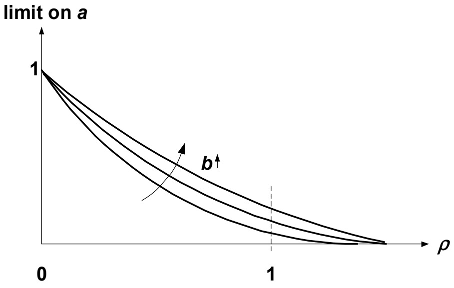

Fig. 2.20: Curves of minimum limit over the taper normalized radius for an increasing *b*.

This requires that *a* be under the limit at $\rho = 1$ for *b*_min, as given by

$$a < e^{-c(1-b\_\min^2)} \qquad 2.32$$

Depending on the range of *a* chosen by the user, some or all values may be eliminated because of the minimum limit. The same reasoning can be applied for *b*>1. In this case the increasing exponential will present a minimum limit of 1 for *a*.

There is also the special case when $b = 1$ and the SGHC taper equation becomes that of a 10 dB Gaussian. Since the 10 dB Gaussian taper has been defined as our reference and is single beam, we do not consider this case of SGHC taper.

OC

For this equation, we have two cases: the two square roots must be positive to obtain a real taper value. The first case is:

$$(1-2a^2+a^4+4a^2\rho^2)^{1/2}-(\rho^2+a^2)>0 \tag{2.33}$$

$$\rho^4-2a^2\rho^2-1+2a^2<0 \tag{2.34}$$

$$a^2<\frac{1-\rho^4}{2\left(1-\rho^2\right)} \tag{2.35}$$

Worst case is $\rho = 0$, therefore:

$$|a|<\frac{1}{\sqrt{2}} \tag{2.36}$$

The second case is:

$$1-2a^2+a^4+4a^2\rho^2>0 \tag{2.37}$$

$$a^4+a^2(4\rho^2-2)+1>0 \tag{2.38}$$

$$a^2>-2\rho^2+1\pm 2\rho\sqrt{\rho^2-1} \tag{2.39}$$

SC, SR and SRS

$$1-[a(\rho \pm b)]^2 > 0 \tag{2.40}$$

This leads to four cases:

$$+1 > +a(\rho + b),\ -1 > -a(\rho + b),\ +1 > +a(\rho - b) \text{ and } -1 > -a(\rho - b) \tag{2.41}$$

These lead to:

$$a < +\frac{1}{\rho \pm b} \tag{2.42}$$

Fig. 2.21 illustrates a typical shape for each of the tapers.

2.3.2.2 Calculation of maximum power density

The purpose of GUIWEFF is to minimize W_{MAX} over the antenna area, in order to protect the underlying electronics. The following describes the procedure to compute W_{MAX} for any given taper shape with the help of WEFF. The taper $T(\rho)$ given to WEFF is normalized to $0 < T(\rho) < 1$ and $-1 < \rho < 1$. An example is shown in Fig. 2.22.

Based on the set of given specifications (R_T, required output DC power, antenna-rectenna range, etc.), WEFF computes a $\alpha(\rho)$, which is a scaled version of $T(\rho)$ to satisfy an internal normalization condition. Another internal scaled version of $T(\rho)$ is $T_S(\rho)$, used to stretch the ρ axis to the desired R_T. The actual near-field signal $|E_T(\rho)|^2$ transmitted from the antenna is a third scaled version from $\alpha(\rho)$. Fig. 2.23 illustrates the family of scaled tapers used by WEFF.

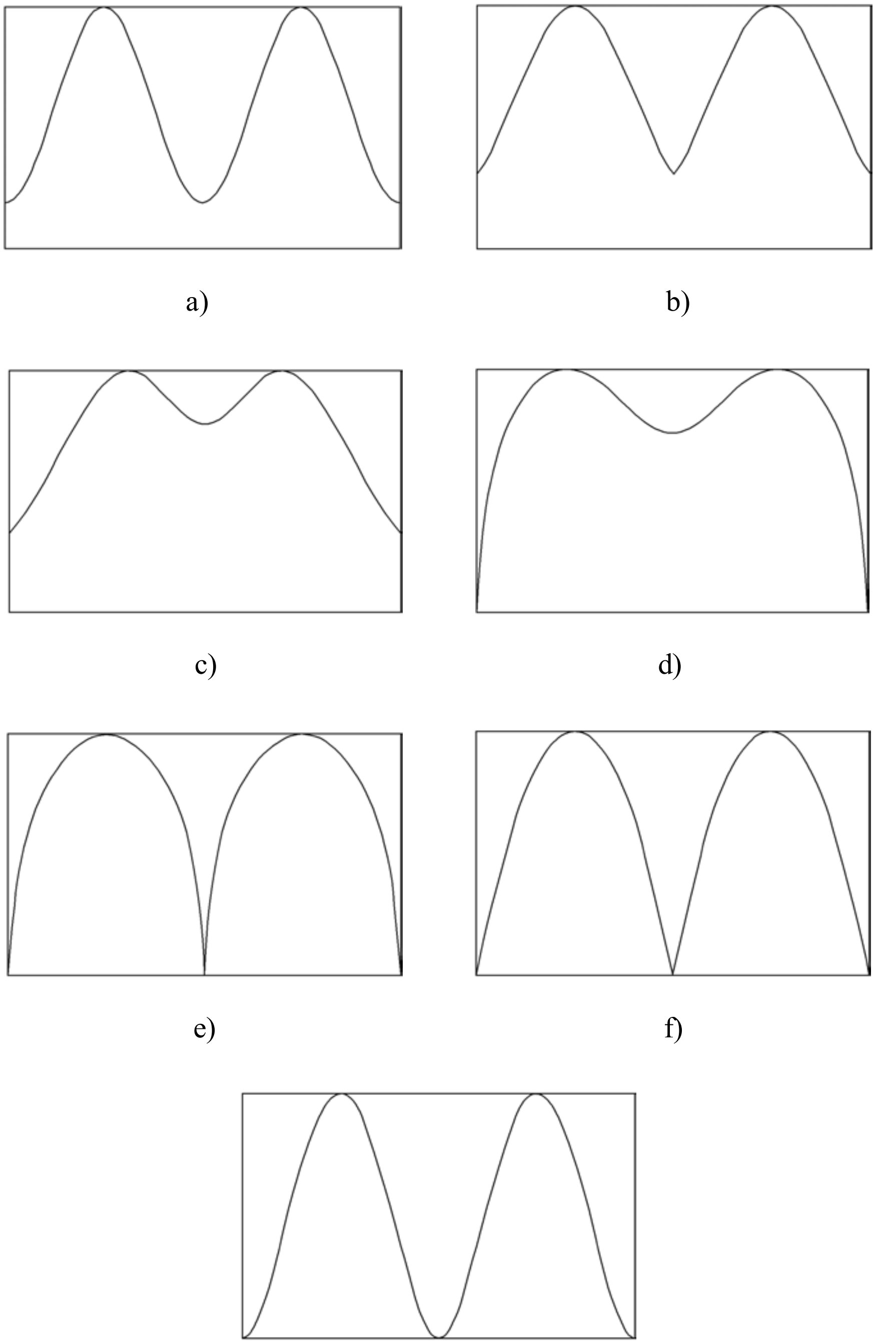

a) b) c) d) e) f) g)

Fig. 2.21: Split tapers used for the optimization process.
a) SSFL, b) SG, c) SGHC, d) OC, e) SC, f) SR, g) SRS.

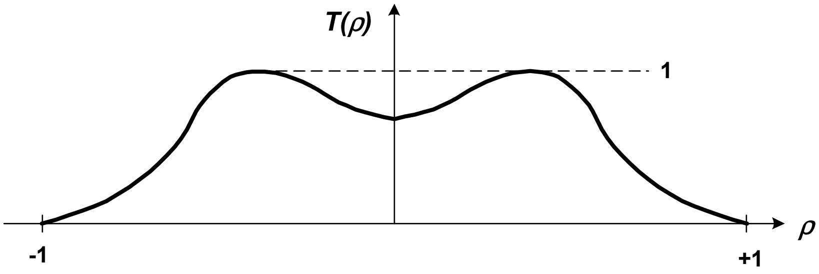

Fig. 2.22: Example of a normalized taper supplied to WEFF.

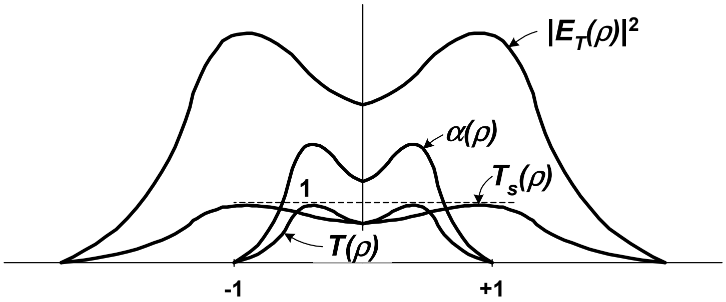

Fig. 2.23: Scaled versions of the submitted taper used in WEFF.

WEFF processes the taper and generates the value of total transmitted power (P_T) at the antenna, which is given by:

$$P_T = \frac{1}{2\eta}\iint_A |E_T|^2 dA \qquad 2.43$$

where η is the intrinsic impedance in free space (equal to 377), and A is the antenna area. Setting $E_T = BT_S(\rho)$, where B is the overall normalization factor, the power density relation becomes:

$$W_T(\rho) = \frac{{E_T}^2}{2\eta} = \frac{B^2 T_s^2(\rho)}{2\eta} \qquad 2.44$$

The maximum value of $W_T(\rho)$ is W_{MAX}, the maximum power density. $W_T(\rho)$ is internal to WEFF and is not accessible by the user. Since $T_S(\rho)$ is normalized to a maximum of 1, it can be established that:

$$W_{\mathrm{MAX}} = \frac{B^2}{2\eta} \tag{2.45}$$

equation 2.43 can be computed as the integral over the antenna surface in cylindrical coordinates

$$P_T = \int_0^{2\pi}\int_0^{R} W_T(\rho)\cdot \rho d\rho d\phi \tag{2.46}$$

which brings:

$$B^2 = \frac{\eta P_T}{\pi}\cdot\frac{1}{\int_0^R T_s^2(\rho)\cdot \rho d\rho} \tag{2.47}$$

Combining with equation 2.45:

$$W_{\mathrm{MAX}} = \frac{P_T}{2\pi\int_0^R T_s^2(\rho)\cdot \rho d\rho} \tag{2.48}$$

The task then reduces to computing the integral of the input taper stretched over the antenna radius. The solution to this integral is different for each taper case. The following gives the solution for the case of SGHC. From Table 2.13, we have:

$$T_s(\rho) = e^{-c\cdot\left(\frac{\rho}{R}\right)^2} - ae^{-c\cdot(b\frac{\rho}{R})^2} \tag{2.49}$$

where R is the total radius of the antenna, used for normalization. The integral to evaluate is given by:

$$\int_0^R T^2{}_s(\rho)rdr = \int_0^R e^{-2c\cdot\left(\frac{\rho}{R}\right)^2} rdr - 2a\int_0^R e^{-c\cdot(\frac{\rho}{R})^2\left(1+b^2\right)} rdr + a^2\int_0^R e^{-2c\cdot(b\frac{\rho}{R})^2} rdr \tag{2.50}$$

which gives:

$$\int_0^R T^2{}_s(\rho)rdr = \frac{R^2}{c}\left[\frac{-e^{-2c}}{4} + \frac{a}{1+b^2}e^{-c(1+b^2)} - \frac{a^2}{4b^2}e^{-2cb^2} + \frac{1}{4} - \frac{a}{1+b^2} + \frac{a^2}{4b^2}\right] \tag{2.51}$$

The solution for the integral in the case of SGHC is fairly simple. However, for other cases, it is not possible to obtain a closed-form solution. For this reason, we will compute this integral numerically in GUIWEFF.

The numerical integral has been calculated by summing area segments under the taper step function as shown in Fig. 2.24. Implemented in a cylindrical coordinates system, the integral enforces a weight to each area segment given by the radial position. This increases the contribution from peripheral segments with respect to the central segments. Therefore, tapers with largely separated beams will generally produce a higher maximum power density.

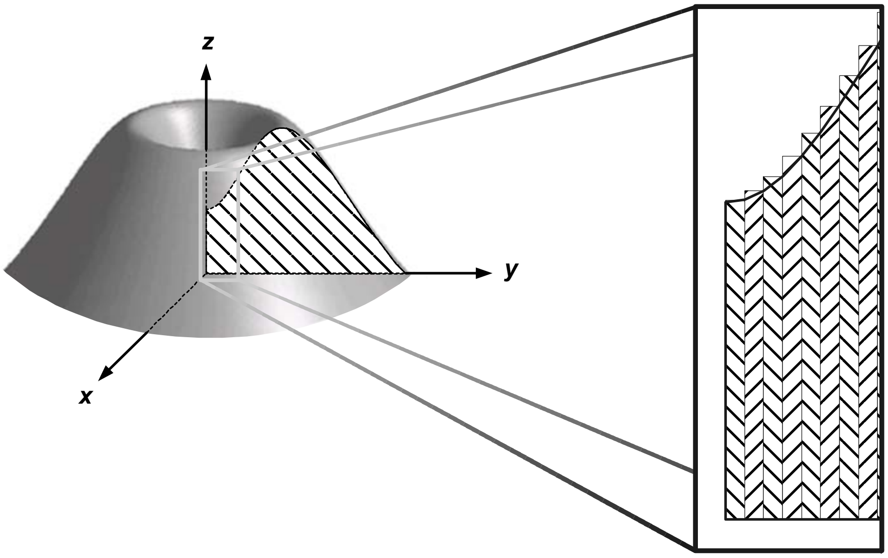

Fig. 2.24: Area segments used in numerical integral calculation.

Here we will provide a simple example of the maximum power obtained by both the closed-form (for the SGHC case) and the numerical method in GUIWEFF. In this typical case, we use *a* = 0.3, *b* = 15 and *c* = 1.1513. The antenna radius is 250 m, and WEFF reports a RF transmitted power of 1603.2 MW. From equation 2.51, we have:

$$\int_0^{250} T^2{}_s(\rho) r dr_{theo} = \frac{12148}{(0.977099)^2} = 12728 \qquad 2.52$$

Then, from 2.48, we obtain:

$$W_{\mathrm{MAX,theo}} = \frac{1603.2 \cdot 10^6}{2\pi \cdot 12728} = 20.047\ \mathrm{KW} \qquad 2.53$$

Using the numerical integration method in GUIWEFF with 200 points, we obtain a maximum power of 20.022 kW. This results in an error of only 0.1%. This error comes from the finite number of points used in the integration, and this number is limited to 200 in WEFF. However, a

0.1% error is very acceptable. Taking 50 points would result in a 0.7% error, while taking 2000 points (impossible because of WEFF) would yield a 0.3% error.

2.3.2.3 GUIWEFF overview

Due to the large number of possible combinations of taper variables (a, b, and c, for 7 tapers, for a total of approximately 3000 cases), a considerable amount of simulation time and, more importantly, of user interaction with WEFF is required. A total of 26 commands and parameters must be entered for each taper simulation. Also, manual processing of raw data must be performed after each simulation in order to display and choose the best performing taper. Clearly, automating the operations required by WEFF was necessary.

The new user interface, called GUIWEFF, has been written in TCL (Tool Command Language), which is a scripting language and an interpreter. The graphical portion of the interface has been written with TK, which is TCL's graphic package. GUIWEFF presents the following features and advantages:

- Improved and simplified graphical user interface customized for the present application
- Automation of the simulation procedures
- Processing and displaying of performance results
- Automated selection of optimal taper based on pre-defined criterion
- Can be used to optimize a taper for any given performance goal in terms of SLL, efficiency, W_{MAX}, total transmitted power, total received power, etc.

These improvements result into a considerable increase in simulation efficiency (3000 simulations with post-processing, all in 5 hours). Fig. 2.25 shows an example of GUIWEFF's user interface.

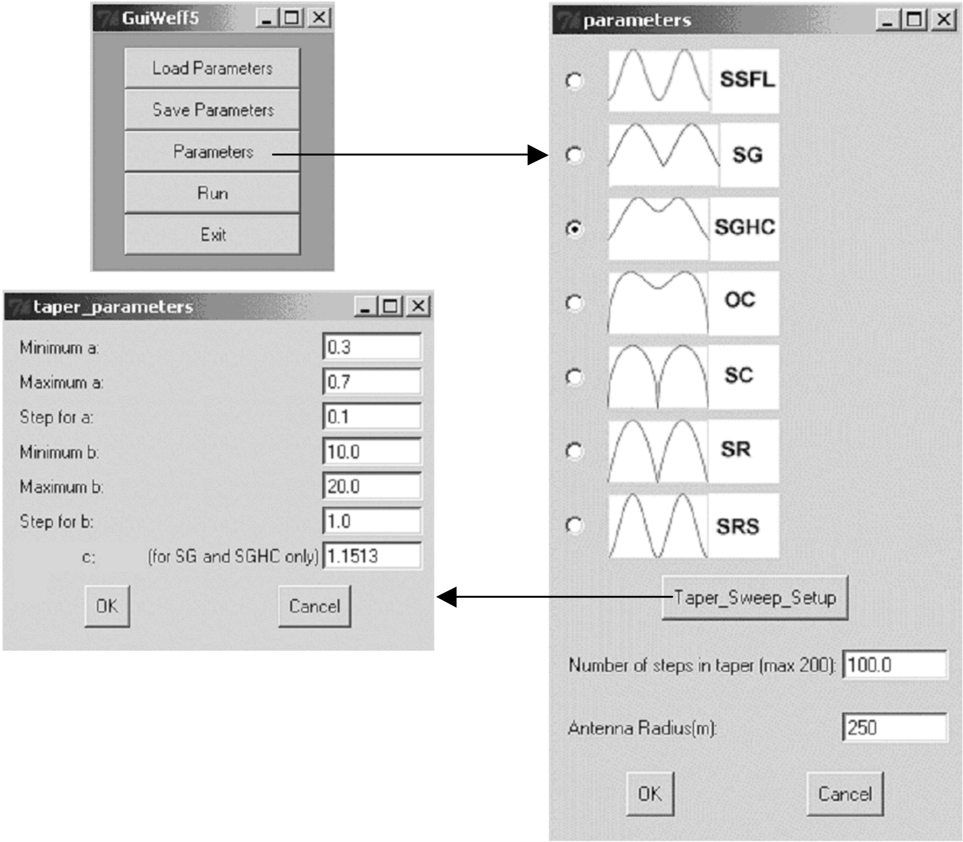

Minimum a: 0.3
Maximum a: 0.7
Step for a: 0.1
Minimum b: 10.0
Maximum b: 20.0
Step for b: 1.0
c: (for SG and SGHC only) 1.1513

○ SSFL
○ SG
● SGHC
○ OC
○ SC
○ SR
○ SRS

Number of steps in taper (max 200): 100.0
Antenna Radius(m): 250

Fig. 2.25: User interface for GUIWEFF.

Fig. 2.26 shows the general algorithm used in GUIWEFF. The taper data and power integral computations are done for each combination of *a* and *b* over the specified range. The resulting taper along with other user-specified entries are sent to WEFF through the execution of a pre-defined script. The RF transmitted power, η_c, and SLL are read from the result file generated by WEFF after each simulation. This data is used in the calculation of the W_{MAX} over the taper aperture and for the score evaluation, as detailed below. Finally, GUIWEFF will automatically select the optimal taper and display the corresponding performance results. A more detailed algorithm is given in the Appendix A.

2.3.2.4 Criteria of selection and score

It is important to consider the effect that each variable has on the shape of the taper. This helps directing the optimization process. Fig. 2.27 illustrates the effect of *a*, *b*, and *c* on the shape of each taper equation. Each graph shows the variation of one parameter while the other(s) are kept fixed at a value in their mid-range. The chosen ranges of variation are given below each graph. Table 2.14 provides more detailed information on the effect of each parameter on the taper shapes.

Table 2.14: Summary of effect of equation parameters over shape of tapers.

Effect	**SGHC**			**SG**			**SC**		**SR**		**SRS**		**SSFL**	**OC**
	***a*↑**	***b*↑**	***c*↑**	***a*↑**	***b*↑**	***c*↑**	***a*↑**	***b*↑**	***a*↑**	***b*↑**	***a*↑**	***b*↑**	***a*↑**	***a*↑**
Center power ↓	x					x	x		x				x(2)	x
Slit narrowing		x	x											
Peaks narrowing			x(1)	x							x			
Peaks separation					x			x		x		x		x
Edge reduction						x	x		x				x(2)	
Edge smoothing						x								

(1): mostly from outside   (2): same level

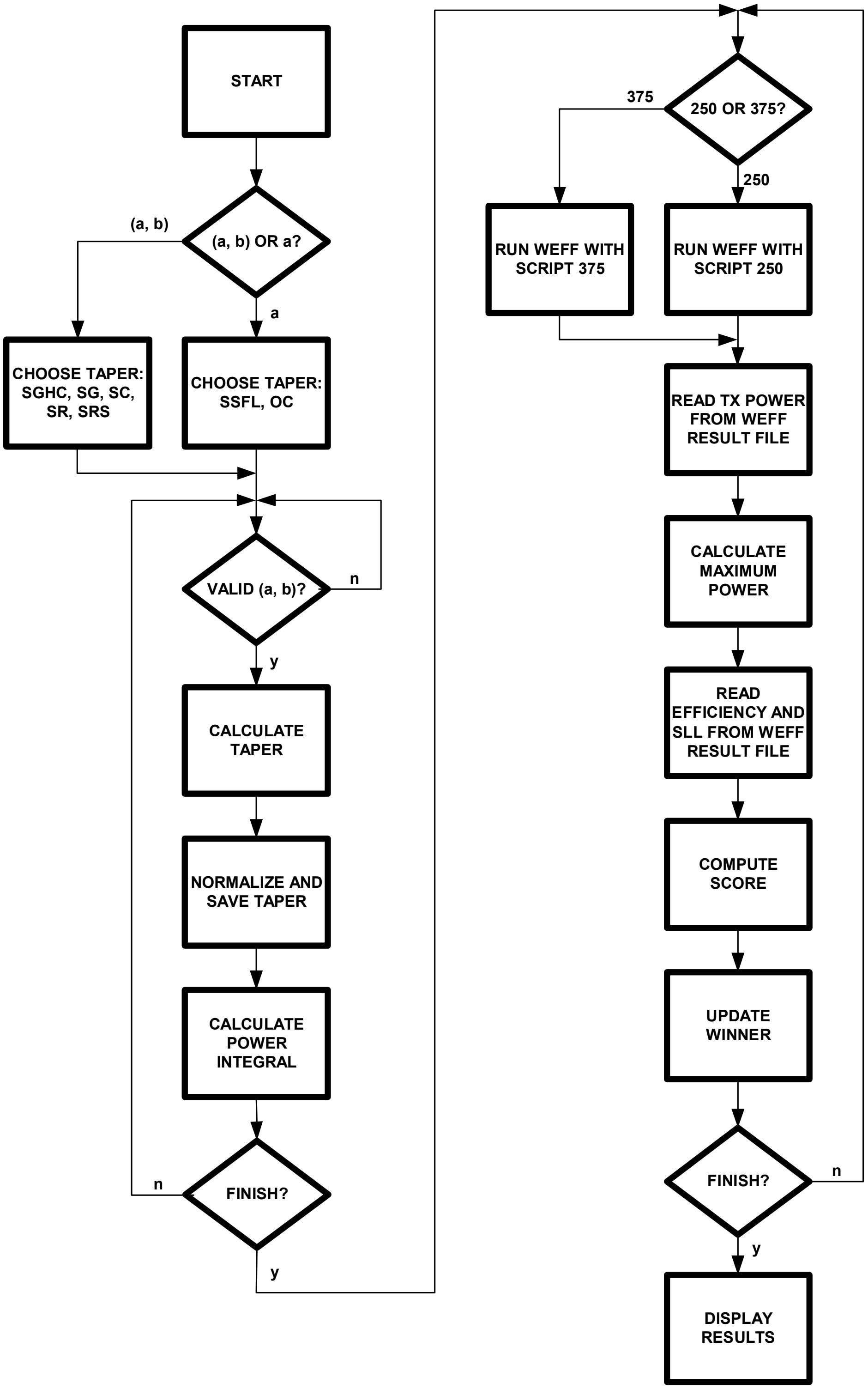

Fig. 2.26: Algorithm of GUIWEFF.

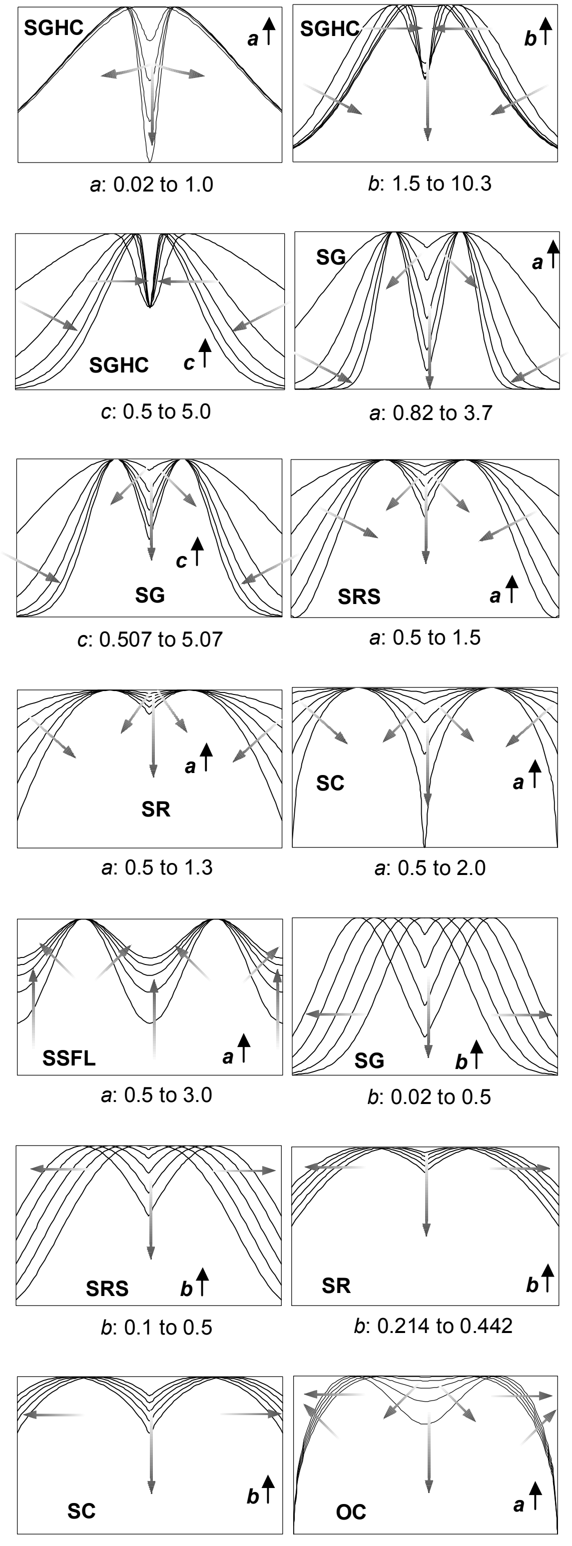

a: 0.02 to 1.0 *b*: 1.5 to 10.3

c: 0.5 to 5.0 *a*: 0.82 to 3.7

c: 0.507 to 5.07 *a*: 0.5 to 1.5

a: 0.5 to 1.3 *a*: 0.5 to 2.0

a: 0.5 to 3.0 *b*: 0.02 to 0.5

b: 0.1 to 0.5 *b*: 0.214 to 0.442

b: 0.386 to 0.614 *a*: 0.6 to 0.68

Fig. 2.27: Effect of variation of parameters *a*, *b*, and *c* on shape of taper.

To obtain an initial range of variation on parameters *a*, *b* and *c* for each taper, one must observe the acceptability region of the resulting taper shape. For example, the slope of the taper at $\rho = 1$ (for a taper normalized between $\rho = -1$ and 1) should always be negative. This criterion ensures acceptable SLL values as seen previously. Some general rules that need to be observed in order to obtain suitable taper shapes are as follows:

- $T(\rho) > 0$ for $-1 < \rho < 1$
- $\partial T(\rho)/\partial\rho < 0$ at $\rho = 1$
- *a*, *b*, and *c* should be chosen such that result values are real

For some tapers, certain combinations of *a*, *b*, and *c* may not be valid within a given range due to mathematical singularities. GUIWEFF will sort the valid pairs and eliminate the singularities as a first selection. To have more details on the mathematical validity of some taper equations given a combination of *a*, *b*, and *c* please refer to section 2.3.2.1.

The final selection of the optimal taper is determined mainly by η_c but also by the SLL and the thermal constraints which both vary oppositely to the efficiency. GUIWEFF will provide these results for each taper. In order to evaluate the overall performance of the taper, one needs to assign a comparative score. First, normalization factors were used to bring each characteristic in the order of units. Then a weight was applied to each, which gives more importance to required characteristics. Finally, the score for each taper is computed using the following formula:

$$score = w\_Eff \cdot norm\_Eff \cdot Eff + \frac{w\_SLL}{norm\_SLL \cdot SLL} + \frac{w\_W_{\mathrm{MAX}}}{norm\_W_{\mathrm{MAX}} \cdot W_{\mathrm{MAX}}} \qquad 2.54$$

where *norm_Eff*, *norm_SLL*, and $norm\_W_{\mathrm{MAX}}$ are the normalization factors, *w_Eff*, *w_SLL*, and w_W_{MAX} are the weights for each characteristic.

2.3.3 Results and optimal tapers

Fig. 2.28 and Fig. 2.29 present the simulation results obtained from GUIWEFF for the 7 tapers over a valid range of parameters, for 250-m and 375-m antennas, respectively. The single beam

10 dB Gaussian taper is also included to serve as a reference and help appreciate the level of performance improvement of the optimal tapers.

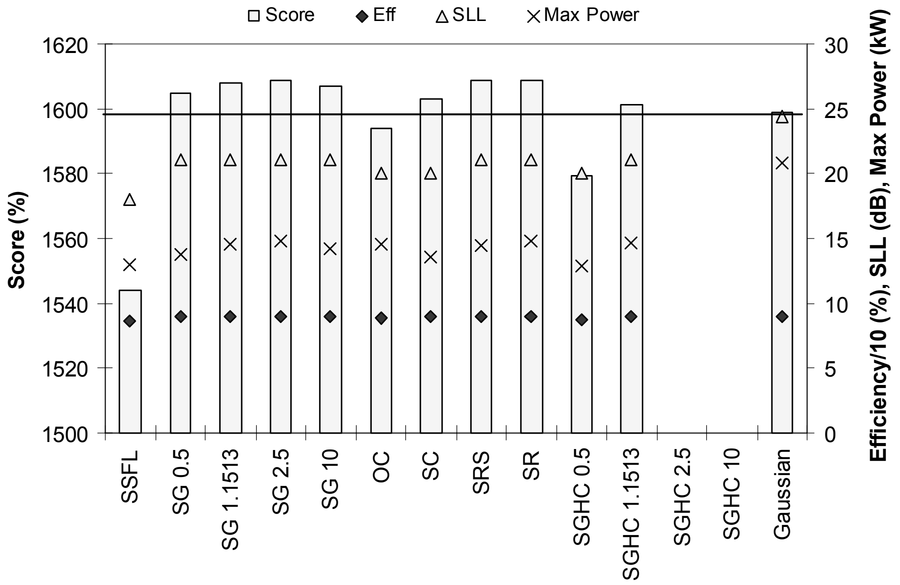

Fig. 2.28: Optimal results for all tapers vs. 10 dB Gaussian taper for $R_T = 250$ m.

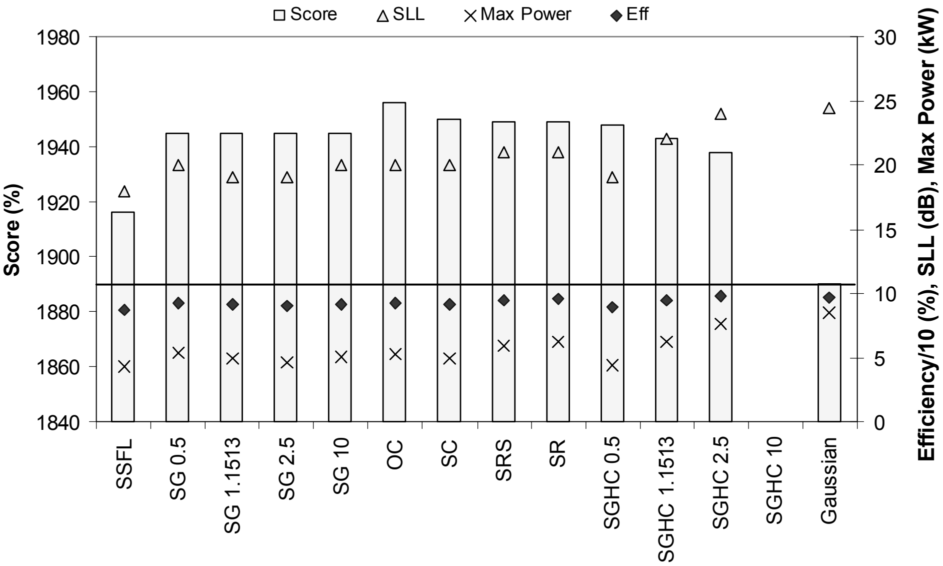

Fig. 2.29: Optimal results for all tapers vs. 10 dB Gaussian taper for $R_T = 375$ m.

The number next to SG and SGHC labels on the x-axis represents the fixed value of parameter c. The missing data for some tapers such as SGHC for a c of 2.5 indicates that the taper cannot meet the system specifications with the required level of collection efficiency and reduction of maximum power density. The SLL's are presented as positive values to share the same axis with the other positive entities. As can be seen the larger score of optimal tapers with respect to the 10 dB Gaussian can be mainly attributed to the noticeable decrease in W_{MAX}.

The percentage (%) of improvement (positive sign) or degradation (negative sign) in performance with respect to the 10 dB Gaussian taper can be observed in Table 2.15. For example, for the 250-m antenna case, the SSFL taper presents a η_c that is 4.67 % below the value obtained with the 10 dB Gaussian (η_c = 90 %). Therefore, η_c = 85.8 % for SSFL. The first sidelobe level in dB is increased by 26 % from that of the 10 dB Gaussian (SLL = -24.4 dB) giving SLL = -18 dB for SSFL. The maximum power density over the antenna aperture is decreased by 37.5 % from that of the 10 dB Gaussian (20.8 kW) giving W_{MAX} = 13 kW. This comparison of maximum power densities is realized using the same antennas area and resulting DC ouput power for all studied tapers as specified in Table 2.9.

Those tapers featuring N/A did not meet the required level of performance as defined in GUIWEFF for neither η_c nor W_{MAX} nor both.

The power density distribution of all optimized tapers with respect to the 10 dB Gaussian taper is illustrated in Fig. 2.30 for an antenna radius of 250 m and in Fig. 2.31 for an antenna radius of 375 m.

Table 2.15: Percentage of improvement (+) or degradation (-) versus 10 dB Gaussian taper.

Tapers	**Results for 250-m antenna**			**Results for 375-m antenna**		
	η_c**(%)**	**SLL(%)**	W_{MAX}**(%)**	η_c**(%)**	**SLL(%)**	W_{MAX}**(%)**
SSFL	-4.67	-26.2	+37.5	-10.12	-26.2	+49.4
SG 0.5	-0.74	-13.9	+33.7	-3.63	-18.0	+36.5
SG 1.1513	-0.44	-13.9	+30.3	-5.39	-22.1	+41.2
SG 2.5	-0.39	-13.9	+29.2	-6.74	-22.1	+45.9
SG 10	-0.57	-13.9	+31.8	-4.97	-18.0	+40.0
OC	-1.33	-18.0	+29.8	-3.67	-18.0	+38.5
SC	-0.9	-18.0	+34.9	-4.97	-18.0	+41.2
SRS	-0.41	-13.9	+30.4	-1.97	-13.9	+30.6
SR	-0.36	-13.9	+28.9	-1.10	-13.9	+27.0
SGHC 0.5	-2.52	-18.0	+38.0	-7.77	-22.1	+48.2
SGHC 1.1513	-0.44	-13.9	+29.2	-1.45	-9.8	+27.1
SGHC 2.5	N/A	N/A	N/A	+1.14	-1.6	+10.6
SGHC 10	N/A	N/A	N/A	N/A	N/A	N/A

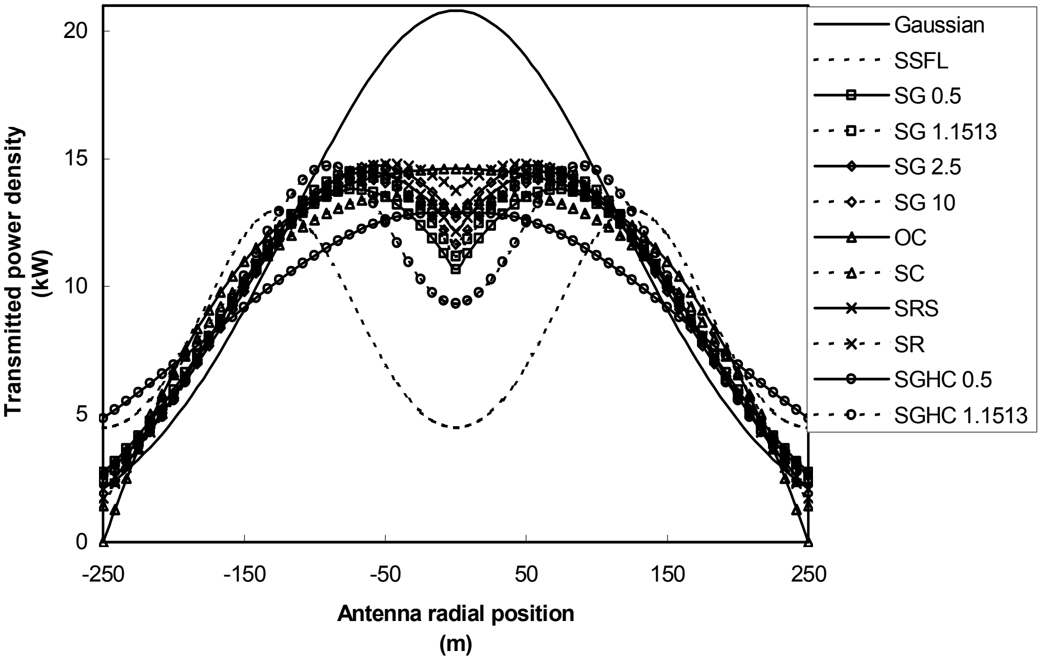

Fig. 2.30: Power density for 10 dB Gaussian and optimized tapers with radius of 250 m.

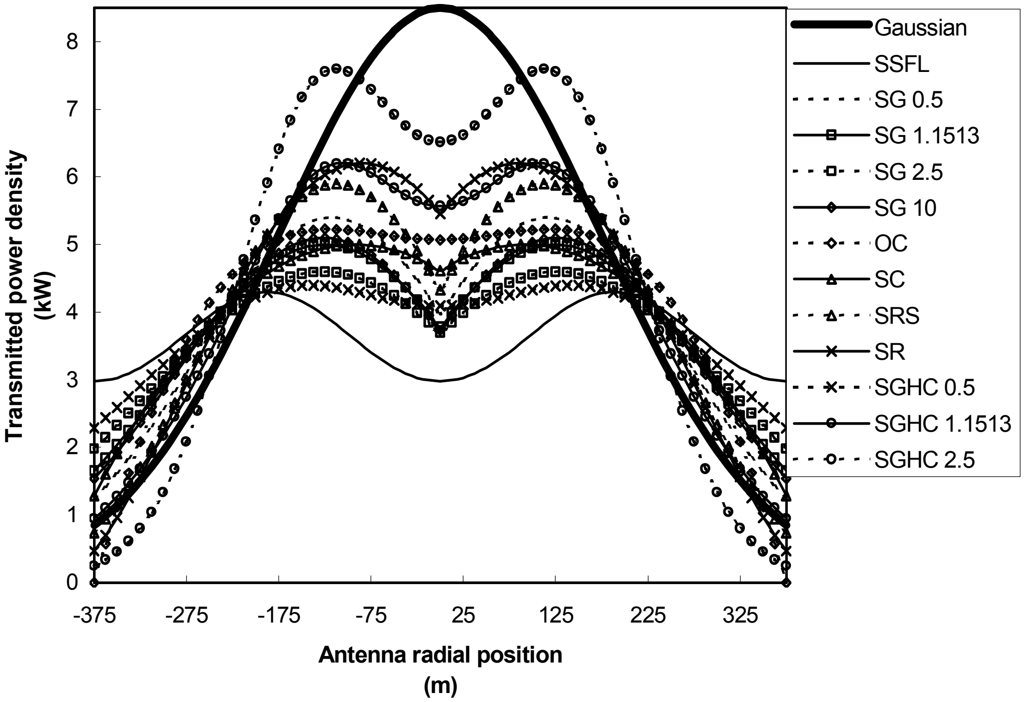

Fig. 2.31: Power density for 10 dB Gaussian and optimized tapers with radius of 375 m.

From the tapers' scores, one optimal taper is selected for each case of antenna radius. GUIWEFF displays the variation of performance entities such as η_c, SLL, and W_{MAX} over the specified range of a and b and presents the optimal taper with the highest score. Fig. 2.32 shows the results from GUIWEFF for the optimal taper SR in the case of an R_T of 250 m and Fig. 2.33 shows the results for the optimal taper OC in the case of 375 m. Appendix B shows results for all optimized tapers.

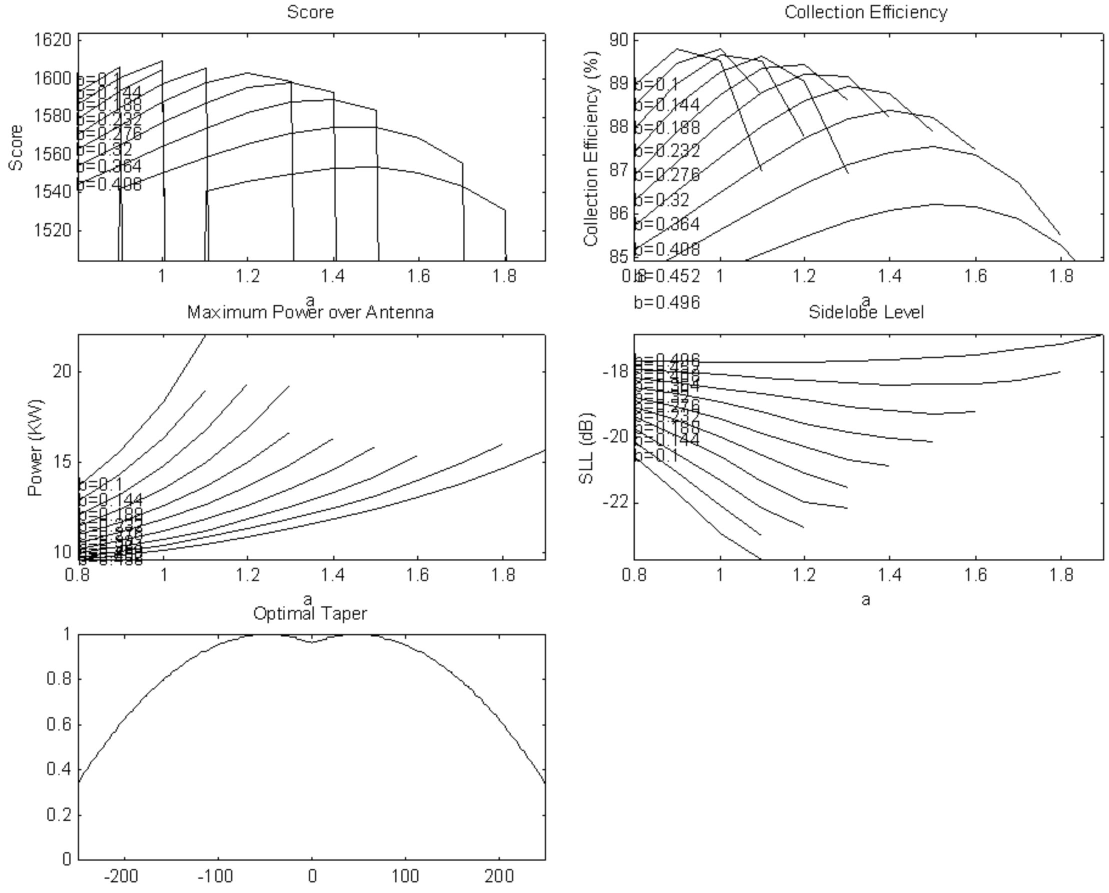

Fig. 2.32: Performance of best score optimal taper SR for R_T of 250 m.

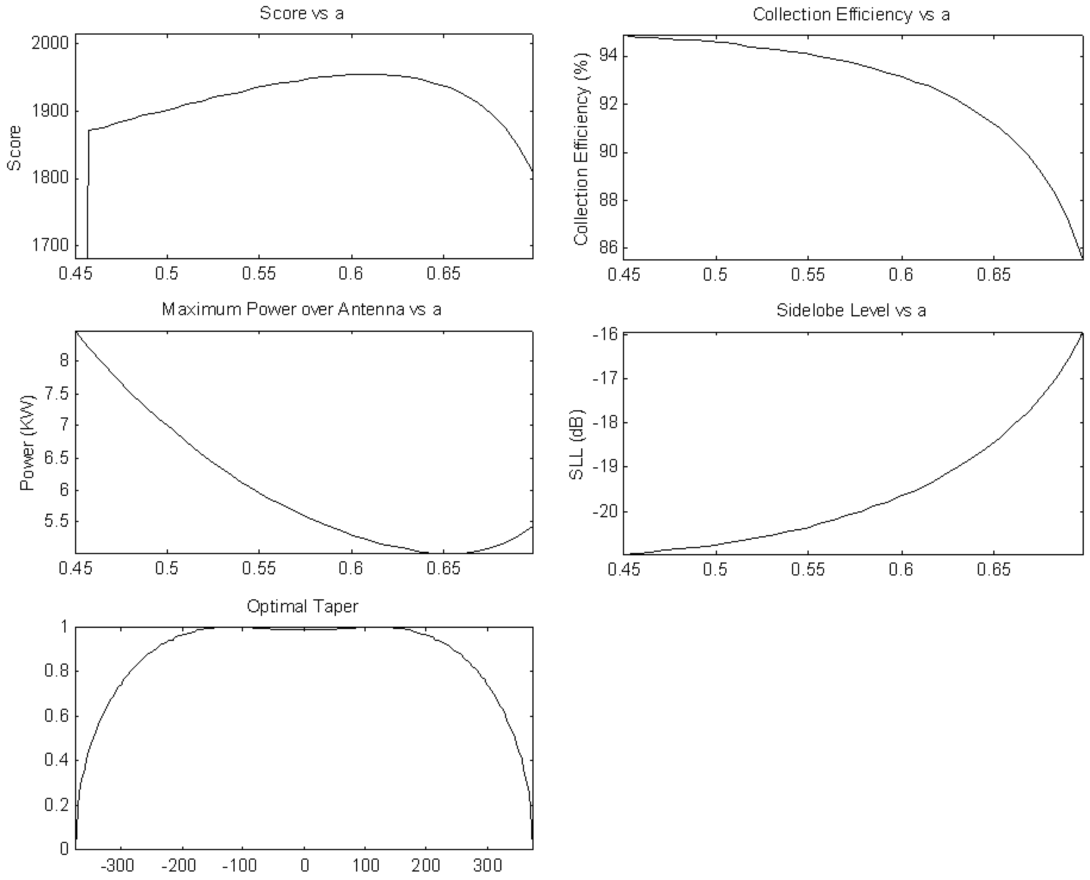

Fig. 2.33: Performance of best score optimal taper OC for R_T of 375 m.

From Fig. 2.32 and Fig. 2.33, one can observe the direct trade-off between the collection efficiency and the SLL or the W_{MAX}. SLL's are always maintained under a reasonable limit of -15 dB for all cases.

Fig. 2.34 illustrates a comparison between the power density for the 10dB Gaussian and the optimal Oval of Cassini tapers. It is clear that the Oval of Cassini taper exhibits a much lower W_{MAX}. It should be noted that although the total transmitted power is slightly lower for the 10 dB Gaussian taper (since its efficiency is higher), the area under the 10 dB Gaussian power density curve is not lower than the area under the Oval of Cassini power density curve. This is due to the fact that P_T is proportional to the power density integral in cylindrical (not rectangular) coordinates. The integrand consists of the normalized taper scaled over the antenna radius and multiplied by the corresponding radius position value at each integration point in cylindrical coordinates. Fig. 2.35 shows an example of this radially weighted integrand.

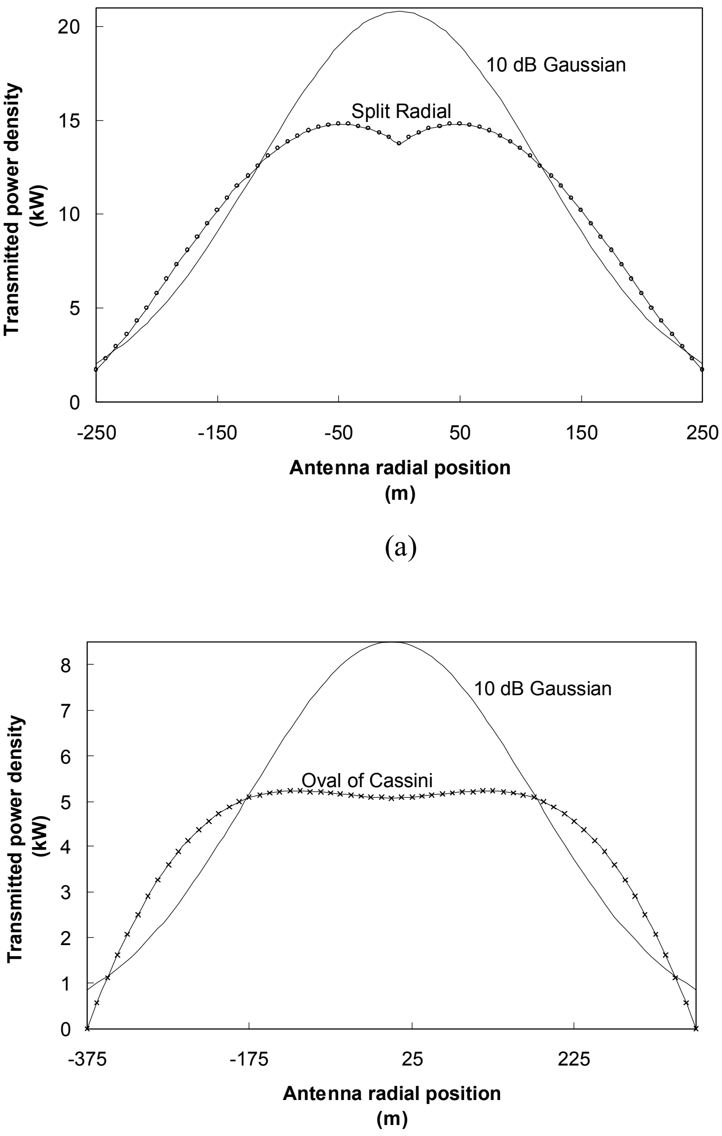

(a)

(b)

Fig. 2.34: Power density comparison of 10 dB Gaussian with optimal tapers. (a) Split Radial over antenna with radius of 250 m and (b) Oval of Cassini over antenna with radius of 375 m.

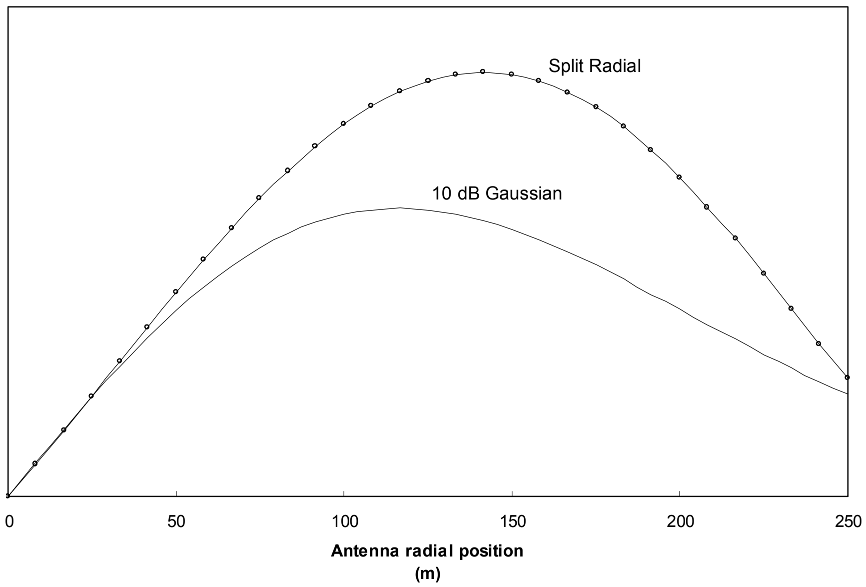

Fig. 2.35: Integrand for power integral. 10 dB Gaussian and optimal taper Split Radial for antenna radius of 250 m.

As seen in Fig. 2.35, the area under the Split Radial taper is larger than that of the 10 dB Gaussian as expected from the calculation of the maximum power density having the power integral in the denominator. The drop in maximum power density can therefore be appreciated from the increase in the power integral.

Fig. 2.36 illustrates the RF field pattern radiated by the transmitter for the 10 dB Gaussian, the optimal OC, and the optimal SR aperture tapers. As predicted by the level of smoothness in the taper edges, the 10 dB Gaussian has the lowest SLL and the OC has the highest SLL. All three levels are excellent in terms of interference and hazard minimization.

Table 2.16 summarizes the results for the two optimal tapers with different R_T. One can compare these with the 10 dB Gaussian characteristics given in Table 2.10 and conclude that with very similar efficiency and SLL, the distribution of the taper can be modified to reduce the concentration of energy at the center and ensure a lower W_{MAX} over the entire antenna surface. The reduction of the maximum power density with respect to the 10 dB Gaussian is of 29 % with the SR optimal taper for the 250-m case and of 39 % with the SR optimal taper for the 375-m case.

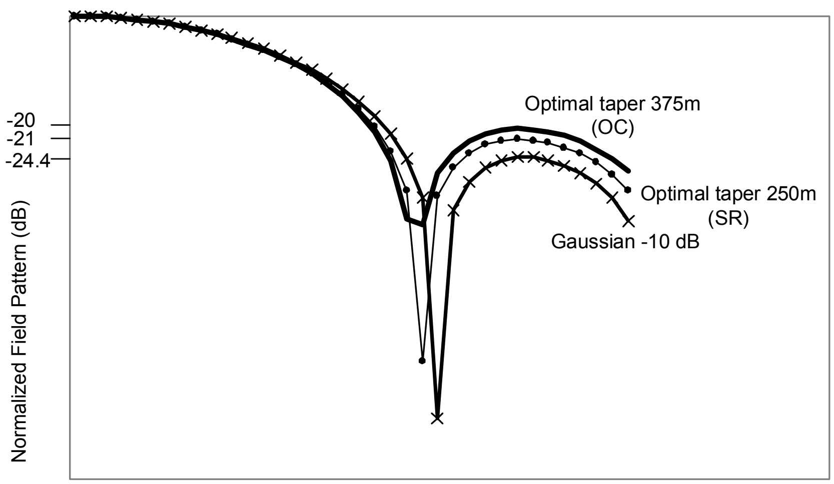

Fig. 2.36: Pattern comparison.

Table 2.16: Optimal tapers and their characteristics.

ρ (m)	Optimal Taper	Characteristic	Value
250	SR	*a*	1.0
		b	0.188
		c	N/A
		Efficiency	89.7%
		SLL	-21 dB
		Maximum power density	14.8 kW
375	OC	*a*	0.61
		b	N/A
		c	N/A
		Efficiency	93.0 %
		SLL	-20 dB
		Maximum power density	5.2 W

2.3.4 Discussion on optimal results

In this section, the optimal tapers were found to be the SR for the R_T of 250 m and the OC for the 375-m case with 29 % and 39 % of maximum power density reduction relative to the 10 dB Gaussian taper.

As seen from the results, the presented approach finds an optimal taper with high collection efficiency and low power density over the antenna area. The results also show that a split taper does not guarantee lower W_{MAX}; it depends on the level of distribution of power on the antenna surface. The trade-off between efficiency and power density needs to be adjusted with appropriate score weights in order to obtain successful optimization.

η_c is found to be higher for a larger antenna aperture due to the higher directivity. A larger radiation area also helps loosen the thermal constraints at the center of the antenna but imposes fabrication limitations for the antenna surface deployment.

Both split tapers can be realized using radial polarization through a slot antenna. In practice, a split taper with smooth center attenuation should result in the highest efficiency because of the expected agreement between the theoretical and fabricated discrete taper. Actually, the step function approximation may produce more significant errors than those resulting from theoretical efficiency differences between the 10 dB Gaussian and the optimal taper.

The directivity of the transmitted field for split beams was observed to be higher than that for a single beam in many cases. This effect needs to be further investigated but suggests that the former taper makes the aperture look larger given the dual beam. This is as if the aperture was viewed as an array of two subarrays.

Future improvements include the use of polynomial functions to define the tapers in GUIWEFF in order to add more flexibility into shaping the taper. Also, the user could choose to vary a physical parameter of the taper curve shape instead of the mathematical parameters a, b, and c. More options to customize the optimization goal (for example, find optimal W_{MAX} with efficiency > 92%) could also be easily implemented.

CHAPTER III

SYSTEM ANALYSIS FOR PHASED ARRAYS

Phased arrays are complex systems that necessitate careful choice of configuration, components and analysis approach. A phased array system consists mainly of an antenna array, which can focus its main beam towards a direction different from broadside (perpendicular to the array plane). The beam angle is controlled by the phase distribution on the element array. The phase is adjusted electronically (using electronic phase shifters with analog or digital control). Phase arrays are sometimes used as substitute for fixed antennas, allowing more flexibility on the shaping of the beam due to the large number of elements. However, in most cases, phased array systems are used to allow steering of the beam or to generate multiple beams. Study of the general phased array system focusing on the choice of configuration can be found in [7], [8], and [9]. Many additional publications are available on more specific phased array topics. Multi-beam systems (which date back to the beam formers introduced by Jesse Butler in the sixties [10]) radiate simultaneous beams at different angles. This allows for broad coverage and more flexibility in pattern shaping without the use of electrical or mechanical scanning of the main beam. Multi-beam systems have been used in electronic countermeasure, satellite communications, multiple-target radar, and adaptive nulling. The feed networks used for multi-beam systems include mainly the power divider beam former network (BFN), Butler matrix, Blass and Nolen matrices. The use of discrete phase shifters in these beam formers limits the system bandwidth, as these components are usually narrowband. They also contribute directly to the system cost as the number of radiating elements is increased. Moreover, Butler or Nolen matrices generally require complex and cumbersome power divider networks. We also have multi-beam systems using optical control. These are generally used for designs with large bandwidth requirements with true-time delay fiber-optics instead of phase shifters. They allow 2-dimensional (2D) scanning with linear array and offer very fast control for switch networks while keeping a low loss. Unfortunately, optically controlled multi-beams are also especially expensive.

The choice of components is a necessary step in the conceptual design of a phased array. Such components include the type of feed, phase shifter (analog vs. digital) [11], as well as radiating elements [12]. One also needs to predict the performance and level of errors for the preliminary system. The two main analysis methods are the statistical and the field analysis approaches [13], [14]. The former is used when the number of elements is over 10, and the later is more accurate for smaller arrays with stronger edge effects and mutual coupling. This chapter deals with the analysis methodology for the design of a small-scaled phased array. This will include details on the two main analysis approaches.

The research objectives of this section are to perform a preliminary analysis on a phased array system in order to determine its optimal configuration. The system was designed in the context of a group project at the EML (Electromagnetics Laboratory) of Texas A&M University and will be presented briefly with descriptions of the main components for clarity. The conceptual design was performed at high level and does not include the specific components design and their integration, which were realized by other team members. This high level design involves decisions at system level that are based, among others, on available test equipment and fabrication resources. Some of the options include the choice between a multibeam or scanned array, active or passive array, dual frequency transceiver or two separate arrays for receive and transmit functions, type of architecture to be used for the two-dimensional implementation, etc. Cost and reliability should also be included in this preliminary definition of the system. It should be noted that some decisions were also made as a group once the preliminary analysis has been realized and presented. Further design decisions were taken for the various components involved in the system such as choosing between commercially available digital phase shifters or designing a custom analog phase shifter. The analysis predicts the scan resolution, the phase quantization lobes, the beam pointing error, etc. It is also necessary to evaluate, for example, the scan loss (gain roll-off), the bandwidth, the half power beam width, as well as determine the number of elements and the optimal spacing with grating lobes and scan blindness considerations. This involves making tradeoffs between some performance parameters. The analysis was realized using the two most important methods: the field analysis and the statistical method. A comparative study between the efficiency of these two methods is newly introduced by using the statistical method to evaluate a small-scale array as a first order approximation.

3.1 Theoretical background

This section deals with the theoretical background required for the analysis and design of a phased array system. Large phased arrays (more than 10 elements) can be analyzed using closed-form statistical formulas. Those formulas are used to predict the behavior of the phased array under the effect of random errors. For smaller phased arrays, a field analysis and mutual coupling considerations are usually appropriate for accurate prediction of performance.

3.1.1 Important phased array concepts

Table 3.1 presents the most important symbols used throughout the section. If symbols are occasionally used or the same symbols are used for different physical entities, these are specified accordingly at each occurrence.

Table 3.1: List of symbols in phased arrays.

Symbol	**Definition**
N	Number of elements
η	Aperture efficiency
M	Number of phase shifter bits
D	Predicted directivity with errors
D_0	Total directivity without errors
θ_{HP}	Half power beamwidth
d	Distance between 2 radiators
λ	Wavelength in free space
θ_0	Scan angle
ϕ	Progressive phase shift (or interelement phase shift)

3.1.1.1 Distance between radiators

In order to avoid grating lobes, one has to separate the radiating elements by a nominal distance of $\lambda/2$. For an active array, the network loss ε_L (fraction of power reaching the receiver) that affects passive arrays is compensated for with the integration of gain amplifiers. One can compute the active array size with [14]:

$$G = D_0\left(1 - |\Gamma|^2\right) \tag{3.1}$$

$$D_0 = ND_{cell} \tag{3.2}$$

$$D_{cell} = \frac{4\pi}{\lambda^2}\left(d_x d_y\right)\cos\theta_0 \tag{3.3}$$

where G is the gain of the array, Γ is the reflection coefficient, d_x and d_y are the distances between 2 radiators in x and y respectively, and D_{cell} is the directivity of one cell. This is valid for large arrays so that each element sees the same reflection coefficient. For passive arrays, we have

$$G = D_0\varepsilon_L\left(1 - |\Gamma|^2\right) \tag{3.4}$$

3.1.1.2 Grating lobes criteria

Grating lobes are sidelobes with amplitude as high as the main lobe. We want to avoid these grating lobes to ensure a single mode of propagation and to maintain a high efficiency. A spacing of $\lambda/2$ (half wavelength) along the 2 rectangular axes is sufficient to exclude grating lobes for all scanning angles θ_0. This is an upper limit of the lattice spacing. In fact, if we have a maximum scan of $\theta_0 = \theta_{\max}$, there will be no grating lobes within a radius of λ/d in the direction cosine plane [13] equal to

$$1 + \sin\theta_{\max} \tag{3.5}$$

If the lattice of antenna elements is square,

$$\frac{\lambda}{d_x} = \frac{\lambda}{d_y} = 1 + \sin\theta_{\max} \tag{3.6}$$

θ_0 cannot be higher than 90°. In this case, sin 90° = 1 and λ/d is equal to 2. Therefore, the lowest limiting spacing for d_x and d_y is $\lambda/2$ and guarantees no grating lobes, as said previously, for any angle between 0° and 90° in elevation. Fig. 3.1 explains this phenomenon.

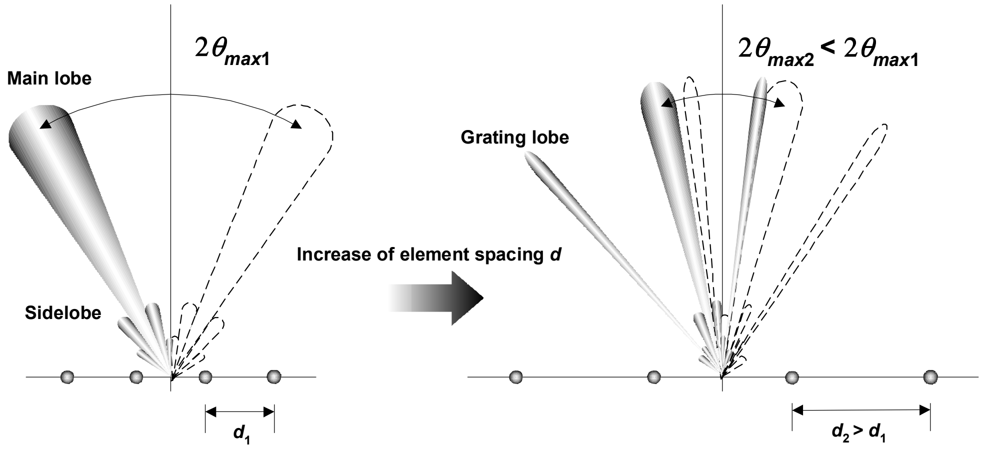

Fig. 3.1: Grating lobes criteria.

The main lobe and grating lobes will be located at [7]:

$$\sin\theta\cos\phi - \sin\theta_0\cos\varphi_0 = \pm\frac{m\lambda}{d_x} \qquad 3.7$$

$$\sin\theta\sin\phi - \sin\theta_0\sin\varphi_0 = \pm\frac{n\lambda}{d_y} \qquad 3.8$$

where θ_0, φ_0 indicate the steering angle (in elevation and azimuth from spherical coordinates) and θ, φ represent any other angle. For m=n=0 we get the position of the main beam. If array spacing is sufficiently large, scanning to any angle may produce one or more grating lobes. The grating lobes can be tolerated for receive-only applications or wide-band operation.

3.1.1.3 Steering angle relation

Fig. 3.2 and the following development explain the steering angle relation. The total phase from the sum of the electric phase introduced by the phase shifter, $(n\text{-}1)\phi$, and the propagation phase βl_n, n=1,2,3,… is a constant as given in equation 3.9.

$$\begin{aligned}\beta l_1 &= \beta l_2 + \phi \\ &= \beta l_3 + 2\phi \\ &\vdots \\ &= \beta l_{N-1} + (N-2)\phi \\ &= (N-1)\phi\end{aligned} \tag{3.9}$$

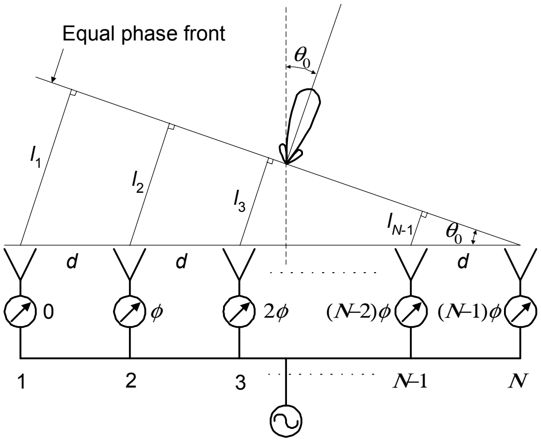

Fig. 3.2: Steering angle.

By substracting the two last expressions, $\beta l_{N\text{-}1} = \phi$ is obtained. Using this identity along with the geometry, the following steering angle relation results

$$\begin{aligned}&\phi = \beta d \sin\theta_0 \\ &\text{or} \\ &\theta_0 = \sin^{-1}\left(\frac{\phi}{\beta d}\right)\end{aligned} \tag{3.10}$$

3.1.1.4 Steering fractional bandwidth

For an array scanned by phase, the fractional bandwidth $BW = (f_2 - f_1)/f_0$ is expressed as [7]:

$$BW \cong \theta_{HP} / \sin\theta_0 \qquad 3.11$$

where θ_{HP} is in radians. If we are scanning in one of the principal planes, the half power beamwidth is given by [8]:

$$\theta_{HP} = \sin^{-1}\left(\sin\theta_0 + 0.4429\frac{\lambda}{Nd}\right) - \sin^{-1}\left(\sin\theta_0 - 0.4429\frac{\lambda}{Nd}\right) \qquad 3.12$$

For large arrays (high N), θ_{HP} can also be approximated by

$$\theta_{HP} \cong \frac{\lambda}{L} \qquad 3.13$$

L being the aperture size of the array.

3.1.1.5 Gain at broadside versus roll-off at scan

For a phased array design, we must consider the effect of the gain roll-off produced by the $(\cos\theta)^n$ factor when scanning at larger angles, n being the power of the cosine that provides the best fit between this function and the antenna element pattern. The radiation pattern can be expressed as the product of the array factor (summation of contributions from each element excitation amplitudes and phases, assuming isotropic antennas) and the element pattern (pattern of a single element used in the array). $(\cos\theta)^n$ is a good approximation of the normalized element pattern. The array factor directivity (or gain not counting the effect of the individual element) is approximated by 10 log N. This is what mainly determines the overall gain of the array. The individual element gain can be added (in dB) but does not have a major influence.

Our beam power is optimized considering the element pattern when scanning at the largest angle, not broadside. The theoretical directivity D_{pred} is inversely proportional to beamwidth as expressed by the following formula for a planar array having non-lossy isotropic elements:

$$D_{pred} = \frac{32000\cos\theta_0}{\theta_{xHP}\theta_{yHP}} \tag{3.14}$$

This means that as we scan, we loose a factor of $\cos\theta_0$.

For example, the element pattern of a high-gain horn presents a directivity that is much higher at broadside given the very sharp beam (since $\cos\theta_0 = 1$) but experiences a significant roll-off (or loss) as it is scanned to larger angles. This drop is of the order of the factor $\cos\theta$ elevated to some power n. The gain roll-off with scanning is shown in Fig. 3.3.

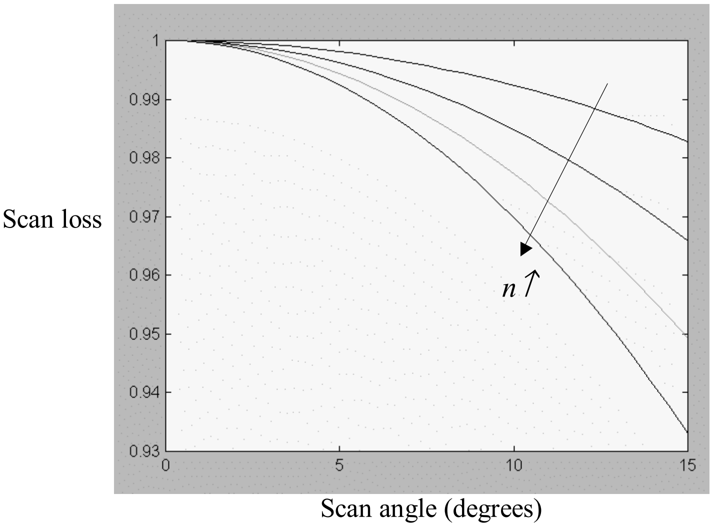

Fig. 3.3: Typical scan loss curves from $(\cos\theta)^n$.

Summarizing, the main contributor to the overall gain is the array factor and the maximum value will be at boresight. The gain roll-off must be calculated at the scan angle.

3.1.1.6 Analysis methodologies

As mentioned in the introduction of this chapter, two main analysis methods are used in the design of phased array systems. The most popular is the statistical analysis, which is used to predict the behavior of phased arrays under random errors when the number of elements exceeds at least 10. For a small phased array, this analysis gives less accurate results. A field analysis of the phased array computes the overall error by adding the individual contribution from each element. This is more adequate for a small array. The mathematical details of these methods are provided in sections 3.2.3 and 3.2.4.

3.1.2 Main components

The phased array system includes several important components. In general, the phased array is composed of a source, power divider, amplifier stages (low noise amplifiers for the receiver and high power amplifiers for a transmitter), phase shifters, and radiating elements.

The power divider is used to distribute the power from one or several sources to the elements. Unless otherwise specified, the power divider is preferably broadband and low loss. An example of broadband design is given in Fig. 3.4 [41].

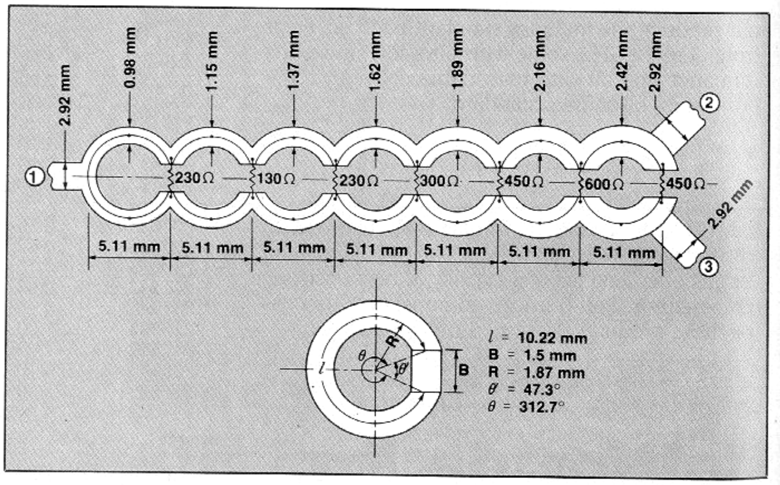

Fig. 3.4: 3 dB circular multisection Wilkinson power divider at 9 GHz with BW of 75 %. [41]

Devices that produce a phase shift are called phasers or phase shifters [13]. These are essential components for phased array operation. Discrete phase shifters provide only discrete differential phase shift (for each bit i), $\Delta\phi_i$, such as 180°, 90°, 45°, 22.5° and 11.25°. The number of possible phase shift values is 2^M. At the limit, as the number of bits is increased, the number of phase values increases and the steering approaches that of an analog phase shifter with continuous scanning. The use of true time-delay technology helps increase the bandwidth. Unfortunately as M increases, the insertion loss (IL) and the cost increase.

The phase least significant bit (LSB) is the smallest differential phase shift. An M bit phaser gives the following differential phase shifts for each bit:

$$\Delta\phi_i = \frac{2\pi}{2^i}, \quad i = 1\ldots M \tag{3.15}$$

So the phase LSB is given by $2\pi/2^M$ and the largest possible differential phase shift is π. For example, in the case of a 5 bits phase shifter, the following differential phase shifts are possible as seen in Fig. 3.5. This gives $2^5 = 32$ phase values as shown in Table 3.2.

180° 90° 45° 22.5° 11.25° $\longleftarrow$ $\Delta\phi_i = \frac{2\pi}{2_i}, \; i = 1,\ldots,5$

bit 1 bit 2 bit 3 bit 4 bit 5 $\longleftarrow$ bit i

Fig. 3.5: Differential phase shifts for a 5-bit phase shifter.

Table 3.2: Possible phase values with a 5-bit phase shifter.

1	0°	9	90°	17	180°	25	270°
2	11.25°	10	101.25°	18	191.25°	26	281.25°
3	22.5°	11	112.5°	19	202.5°	27	292.5°
4	33.75°	12	123.75°	20	213.75°	28	303.75°
5	45°	13	135°	21	225°	29	315°
6	56.25°	14	146.25°	22	236.25°	30	326.25°
7	67.5°	15	157.5°	23	247.5°	31	337.5°
8	78.75°	16	168.75°	24	258.75°	32	348.75°

As an example, the steering resolution is calculated here using a spacing of $d = 0.73\lambda$ that will be presented in section 3.2.2.

$$\theta_{inc} = \sin^{-1}\left(\frac{\pi/16}{2\pi/\lambda \cdot 0.73\lambda}\right)$$
$$\theta_{inc} = 2.45^{\circ} \qquad 3.16$$

But as ϕ is increased, the scanning increment will increase in a nonlinear fashion. (For smaller ϕ, $\theta_0 \approx k\phi$ where k is a constant.) Table 3.3 presents the possible scan angles with the required phase shifts and corresponding progressive phase shift. The use of discrete phase shifters produces phase quantization errors due to the discrete phase steps as illustrated in Fig. 3.6.

Table 3.3: Possible scan angles θ_0 with corresponding progressive phase shift ϕ for $d = 0.73\lambda$.

ϕ	**Phs 1**	**Phs 2**	**Phs 3**	**Phs 4**	**θ_0**
11.25°	0°	11.25°	22.5°	33.75°	2.45°
22.5°	0°	22.5°	45°	67.5°	4.91°
33.75°	0°	33.75°	67.5°	101.25°	7.38°
45°	0°	45°	90°	135°	9.86°
56.25°	0°	56.25°	112.5°	168.75°	12.36°
67.5°	0°	67.5°	135°	202.5°	14.88°
78.75°	0°	78.75°	157.5°	236.25°	17.44°

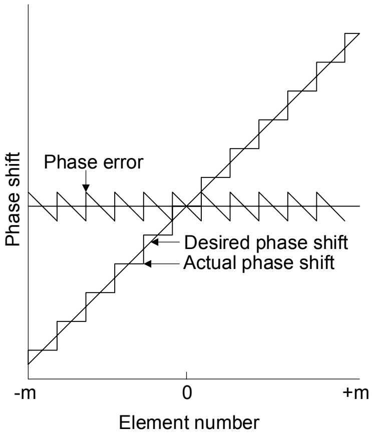

Fig. 3.6: Phase quantization errors.

This is what causes phase quantization lobes [13]. The average sidelobe level due to this quantization error is given by

$$\sigma_q^{\ 2} = \frac{1}{3M}\frac{\pi^2}{2^{2M}} \qquad 3.17$$

So as the number of bits M is increased, the sidelobe level drops. For example, if $M = 4$ bits, the average sidelobe level due to quantization error is

$$\sigma_q^{\ 2} = \frac{1}{3\times 4}\frac{\pi^2}{2^{2\times 4}} = 0.00321 \text{ or } -25\,\text{dB} \qquad 3.18$$

3.1.3 Practical considerations

One needs to consider practical aspects in designing a phased array system. Also, some theoretical design results require adjustments for worst case prediction.

3.1.3.1 Cost

The overall cost depends on the feed network, the phase shifters with drivers and the beam steering control in the circuitry [42].

To reduce the cost, we need to:

- Provide simpler feed
- Decrease the cost or the number of phase shifters
- Use simpler beam-steering control

To reduce the number of phase shifters from (n x m) to (n + m), where n is the number of columns and m is the number of rows, one can use a bulk phase-shifting. This is a row-column steering approach that implies a reduction of the number of phase shifters drivers and controls. The control of the phase would then be made over an entire row or column meaning the amplitude and phase of individual radiating element cannot be controlled. This will limit the level of sidelobes that can be achieved and limits the error correction possibilities. However, if ultralow sidelobes are not required, the row-column phase control can be used to reduce the cost.

3.1.3.2 Reliability

An active phased array requires providing control and DC/RF power to the T/R modules in clusters for reduction of cost. However, we want small clusters to increase the mean time between failures (MTBF). Therefore, there is a trade-off between MTBF, cost, and size. It should also be noted that the sidelobe level is improved with smaller size clusters. If we compare active antennas versus passive antennas, they offer [43]:

- higher reliability
- lower life cycle cost
- excellent anticlutter performance
- lower weight
- lower transmit and receive loss
- flexibility
- wider bandwidth

Most of the advantages are mainly obtained by distributing the transmit and receive functions at the aperture. Moreover, the impact of passive components on reliability is very small since they rarely fail.

In general, the reliability increases as the number of elements increases. A figure of merit of reliability is the MTBF. The MTBF is lower when the phased array fails in large clusters.

$$MTBF \propto \frac{1}{\text{size of cluster of failing elements}} \qquad 3.19$$

One way to increase the reliability is to use a large number of power supplies for all T/R modules as shown in Fig. 3.7. This would make the components redundant to eliminate the contributions to the MTBF.

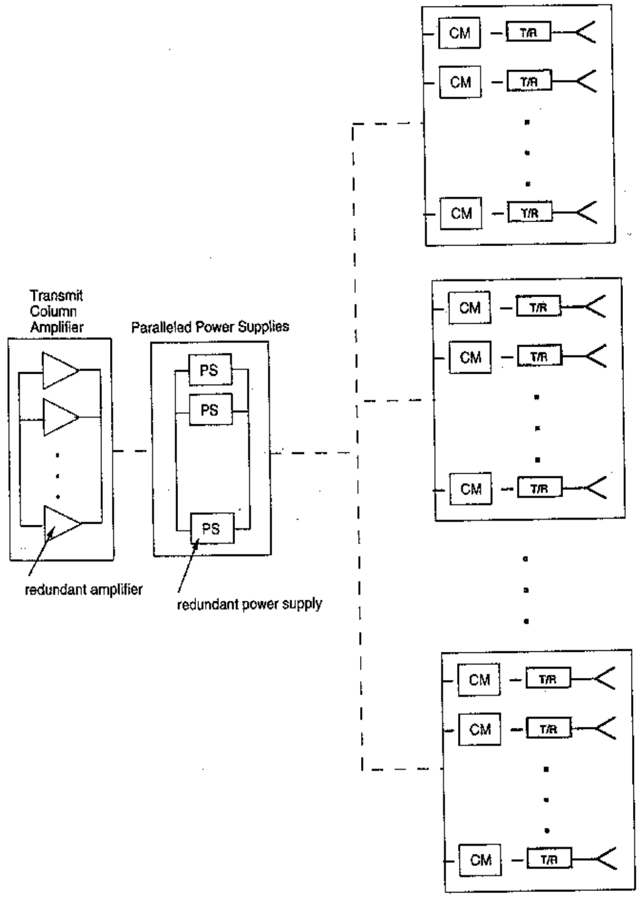

Fig. 3.7: Large number of power supplies in parallel for high MTBF. [43]

3.1.3.3 Element spacing

We want to use the maximum lattice size permitted to reduce the number of elements for a given scanning angle. However, the lattice is limited to a maximum value to avoid grating lobes and should be reduced even further to improve the mismatch. In practice, the elements spacing is reduced by 5% to 10% to avoid pattern deterioration from mutual coupling effects.

Also, a triangular lattice of elements is more economical since less T/R modules are required given the element spacing. A square lattice provides maximum power aperture products but at higher cost and more serious heat dissipation problems.

3.2 Planning and analysis methodology of the phased array system

To predict the phased array system performance and select the optimal design parameters and appropriate phased array implementation (for example, passive versus active), a study of the numerous considerations involved such as the available test setup equipment, the necessary circuits and fixtures fabrication procedures, and the research budget, is required. A statistical analysis will be realized even though the number of elements will be small. This will provide an approximate evaluation of the performance of the system using simple well-established equations to rapidly investigate the effects of design parameters in the configuration. For increased accuracy, a field analysis will also be conducted.

3.2.1 Survey of phased array techniques and considerations

The decision of the system composition was based on a study of the existing architectures and design approaches of phased arrays. These suggestions are based on available resources and fabrication technologies at the laboratory and are not intended to represent an exhaustive list.

3.2.1.1 Phased array architectures

The use of a planar array allows a scan in 2 dimensions and provides a higher gain. For the planar array, two configurations can be used: the brick architecture and the tile architecture, as show in Fig. 3.8 and Fig. 3.9, respectively. The brick architecture is not designed to present coupling between the vertical planes as opposed to the tile layout where the signal is coupled from one horizontal plane to the next. The brick architecture can be implemented using corporate fed power divider with shared T/R modules as illustrated in Fig. 3.8 or using T/R modules to individually drive each antenna element as shown in Fig. 3.10.

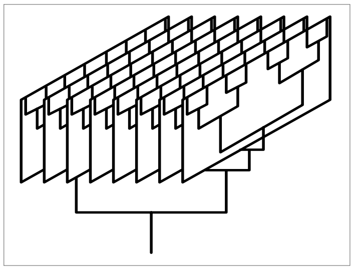

Fig. 3.8: Brick architecture.

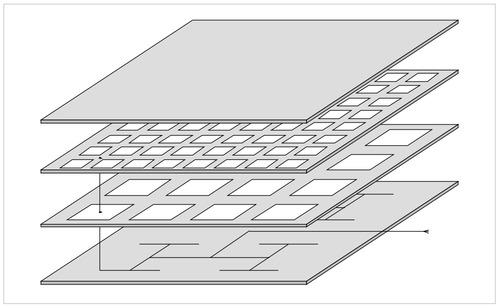

Fig. 3.9: Tile architecture.

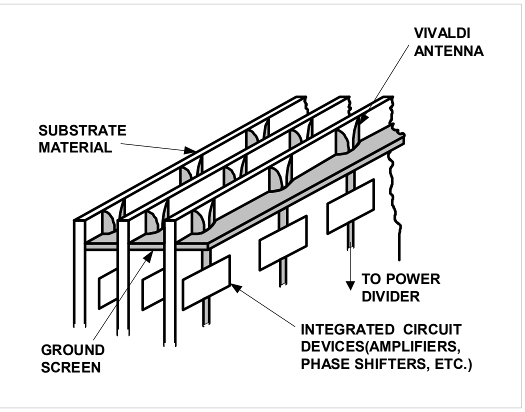

Fig. 3.10: T/R module at each element.

3.2.1.2 Active phased arrays

The EML Laboratory at Texas A&M University has had very innovative research activities these past years concerning the technology of active antennas [44]. The later is therefore a good candidate in the design approach of the phase array due to the extensive experience.

Using waveguide Gunn oscillators as sources and aperture antennas, we observe that the resonance frequency of the pattern (maximum gain) can be swept if coupled to other elements. This phenomenon is illustrated in Fig. 3.11 using the hand to vary the received signal resonance measured on the spectrum analyzer.

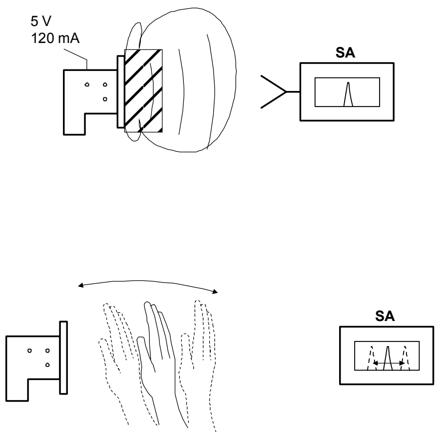

Fig. 3.11: Frequency sweep with coupling.

By varying the voltage V of the Gunn oscillators or the distance D between them, we can tune the mutual (or direct) coupling to transmit an injection locked signal, as shown in Fig. 3.12. The injection locking can also be achieved by an external stable source. Therefore, the scanning of a phased array beam is realized from spatial power combining by controlling the voltage at each element. The resulting scanned pattern is more difficult to predict than by using phase shifting devices.

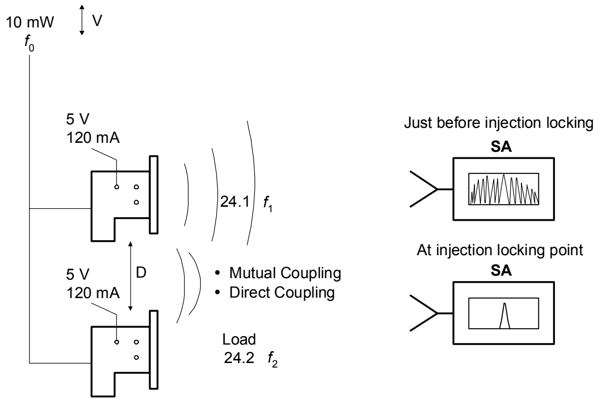

Fig. 3.12: Injection locking phenomenon through mutual coupling.

3.2.1.3 General considerations

If a square lattice is considered for a planar array, then it requires that $d_x = d_y = d$. In the case where the array is a portable unit, we can fix ψ_0, azimuth scanning angle (angle from spherical coordinates between the x axis and the projection in the z=0 plane of the line drawn from the origin to the point) perpendicular to the elevation scanning angle θ_0, to define one of the principal planes (along one of the lengths of the array, i.e. $\psi_0 = 0°$ or 90°). If we choose $\psi_0 = 0°$ for example, then the phase shifters will have a progressive phase shift along x only, which produces a steering across the x-axis. The chosen antenna for the planar array should not produce a θ_{HP} that is lower than a certain value because a sharpening of the beam will produce a great drop at scanning angle.

Another consideration is the effect of spacing between elements. The maximum steering angle, θ_{max}, will increase as the distance or separation between two elements decreases. This results in a densely packed array. As the spacing is decreased, the grating lobes are also avoided. If a small spacing is difficult to achieve in practice, one could also adjust the spacing to its limit so that the grating lobe amplitude is equal to that of the allowed sidelobe level at the edge of the visible space but this approach makes the visible portion of the grating lobe very sensitive to the spacing, so tight fabrication tolerances would be required. A null pattern could also be placed at the grating lobe position. However, one needs to be careful in not decreasing the spacing too much since the radiation pattern will show some nulls in certain directions for some values of d within the total field of view (FOV) of the array [7]. The occurrence of nulls in the pattern is referred as scan blindness. These considerations need to be addressed when designing the system.

3.2.2 System and specifications

The specifications for the phased array system under study for satellite communications are a minimum of 30° scan (±15°), two transmit (Tx) frequencies at 10 and 19 GHz, two receive (Rx) frequencies at 12 and 21 GHz, and an overall gain of 40 dB.

In order to calculate the spacing between elements, the grating lobes criteria is used. For the phased array system, $\theta_{max} = \pm 15°$. Using 3.6:

$$1+\sin(15^\circ)=1.26$$

$$d_x=d_y=\frac{\lambda}{1.26}=0.79\lambda \qquad 3.20$$

The highest frequency, 21 GHz (Rx operating frequency), will determine the maximum spacing necessary to avoid grating lobes for all cases. Therefore, in order to cover the entire band without any grating lobes, the spacing should be

$$d_x \le d_y \le 11.3\,\text{mm or } 445\,\text{mil} \qquad 3.21$$

It is good practice to reduce this maximum limit by a small percentage, about 5% to 10% less. However, this conservative spacing, which is around 0.73λ or for the highest operating frequency, 10.4 mm, is also more limiting due to practical constrains in the connection and integration of components. Due to mechanical restrictions, the required physical element spacing at earlier design stage needed to be at least d = 0.88 λ (or 12.5mm at 21 GHz). Using this spacing of 12.5 mm, the grating lobe criteria is met at all frequencies, except for 21 GHz. After optimization in the design, a spacing of 10 mm was physically possible between antenna elements. One can use Fig. 3.13 to decide on the spacing with the appearance of grating lobes at given directions in the FOV.

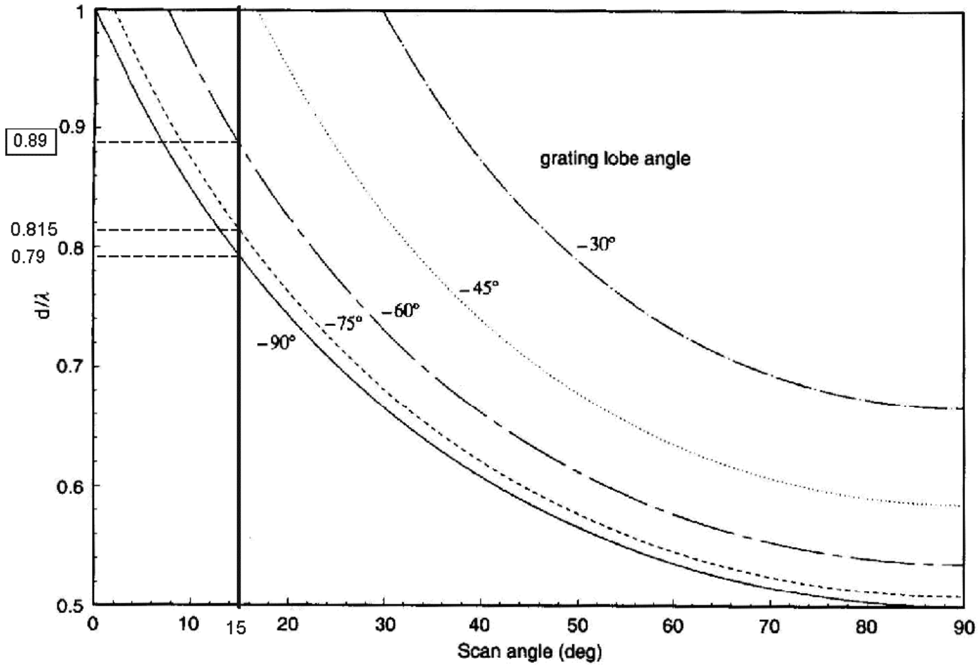

Fig. 3.13: Maximum spacing for grating lobe criteria given a scan angle. [13]

An overall gain of 40 dB was specified, which would require around 10,000 elements in total or a 100 x 100 array (refer to section 3.1.1.5). Obviously, this is not within the available budget and resources. The design considerations previously considered dictate a small array design (less than 10 elements). Therefore, a reasonable array size would be a 4x4 array. However, with only 16 elements, a gain of 12 dB is predicted. Moreover, the element gain cannot compensate for the remaining 28 dB to meet the specifications. Therefore, we compensate for the missing gain level using amplifier stages and for the losses from circuit connections, lines, and roll-off factor (10 log $(\cos\theta)^n$), etc.

This phased array is designed for a ground portable phased array unit, which can be orientated in order to scan only in elevation from -15° to 15 ° across a fixed, constant ψ_0. If using a 2D array with increased gain with respect to a linear array, the scan can still be done in one dimension as shown in Fig. 3.14. For a 4x4 brick architecture, only 4 different phase shift values would be needed using 4 discrete phase shifters with 4 or 5 bits.

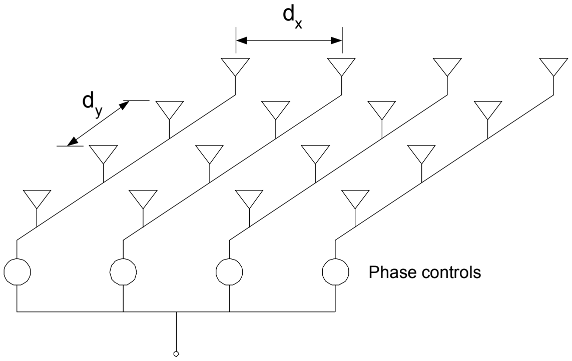

Fig. 3.14: Planar array to scan in one dimension.

Although the gain is higher using a planar array, due to cost and simplicity factors, a preliminary 4x1 linear subarray was ultimately favored to a more elaborated 2D array. Also, a passive array was preferred to the active array again for simplicity in a first prototype design, even if the active array presented many advantages (as seen in section 3.1.3.2 on Reliability) which are more apparent with a larger array.

After measuring the limited bandwidth in commercially available digital phase shifters, a broadband custom design was needed. A teammate, Tae-Yeoul Yun, developed an innovative analog phase shifter using piezoloectric material. This piezoelectric transducer (PET) induced a linear phase variation to the array elements and the scan could vary in a continuous manner. Fig. 3.15 illustrates this new phase shifter

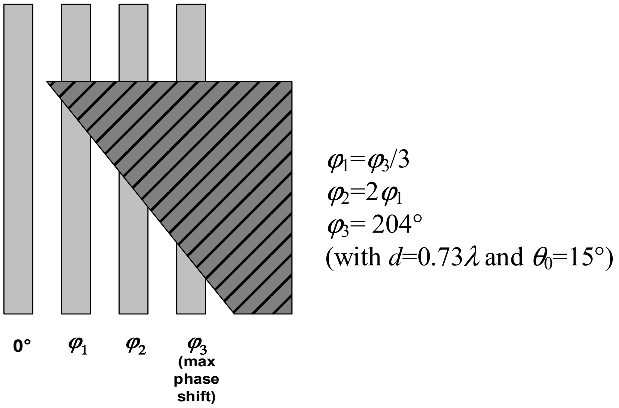

Fig. 3.15: PET providing linear phase variation.

Since the analog phase shifter provides a continuous progressive phase shift, the steering resolution should be very high, theoretically infinite.

Fig. 3.16 presents the scanning capability that can be reached given a maximum phase shift (at the end element). This graph is produced assuming a constant progressive phase shift between each pair of adjacent phase shifter. For a scan of ±15° as specified for this system and a spacing of 0.73λ, the required maximum phase is φ = 204°.

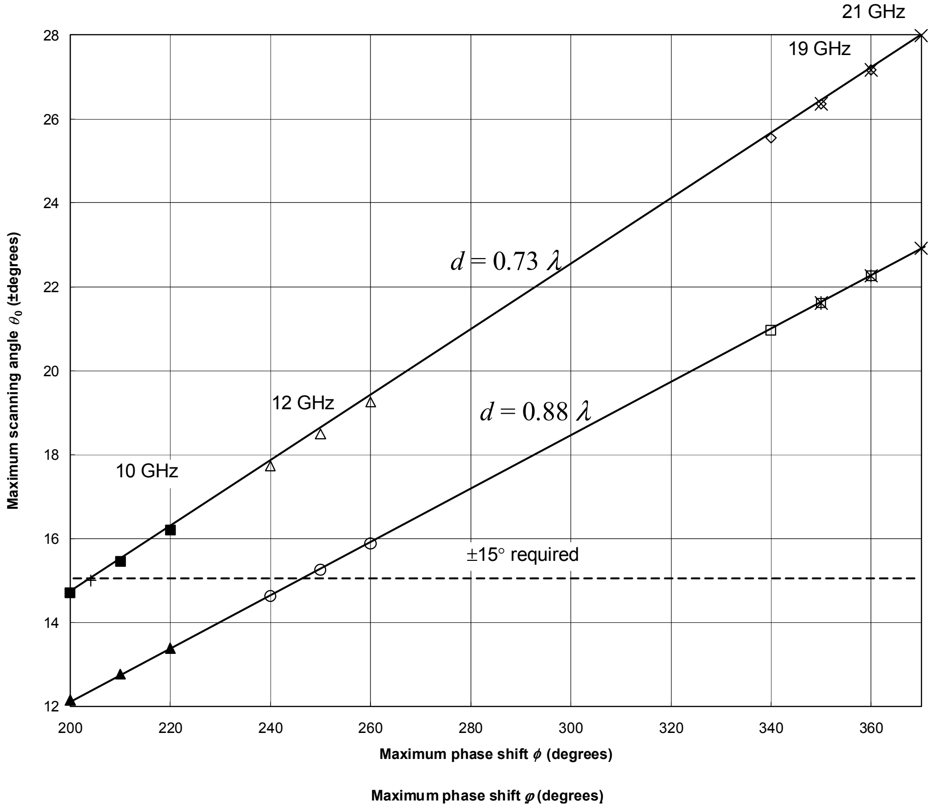

Fig. 3.16: Maximum scanning versus maximum phase shift.

Good isolation and simplification of bandwidth requirements for channel frequencies would easily be achieved using two arrays (one for transmitting and the other for receiving). For compactness, it was decided that all the functions would be integrated into a single array. Also, to loosen the design requirements, one could filter the frequencies in two larger bandpass instead of four narrow bandpass as shown in Fig. 3.17. The challenge of filtering four frequencies with good isolation between channels was successfully surpassed by Mr. Chunlei Wang with his very efficient broadband microstrip filter design.

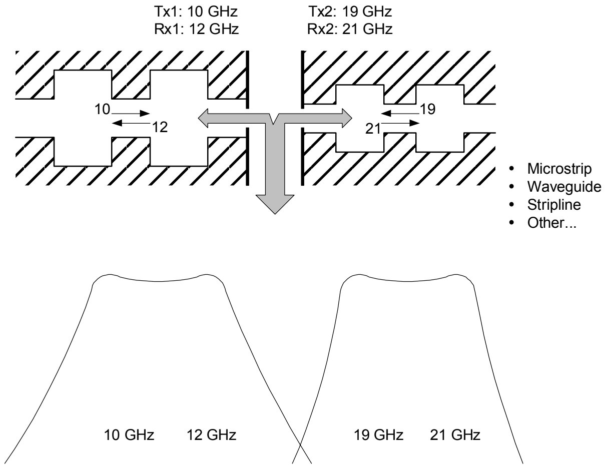

Fig. 3.17: Bandpass filtering for frequency specifications.

The type of antenna used is the Vivaldi antenna because of its broadband characteristics and for its endfire radiation to reduce spacing restrictions. This antenna should not be too long (antenna of traveling wave type) to avoid excessive scan loss as shown in Fig. 3.18.

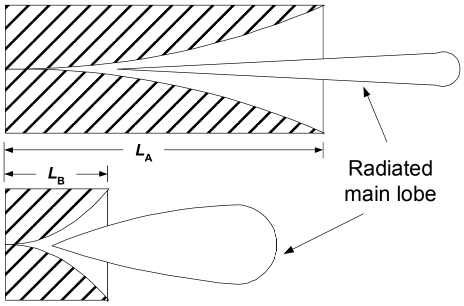

Fig. 3.18: Beamwidth versus length of antenna.

The calculation of the fractional bandwidth using equation 3.11 allows us to verify if our system will cover the required frequency band given the specifications on dimensions and scan angle. For this, the following condition must be satisfied:

$$\begin{aligned}&BW = \frac{f_2 - f_1}{f_0} \le \frac{\lambda / L}{\sin 15^\circ} \\ &\frac{22-9}{15.5} \le \frac{3 \cdot 10^8}{15.5 \cdot 10^9 \times 0.0485 \times \sin 15^\circ} \\ &0.839 < 1.542\end{aligned} \tag{3.22}$$

A frequency range of 9 to 22 GHz was used to ensure that the desired frequency range of 10 to 21 GHz would be covered without any gain loss. Therefore, the systems configuration is good since it provides a bandwidth larger than the specified fractional bandwidth of 0.839.

In summary, the phased array system blocks include a broadband power divider, the PET phase shifter, the broadband diplexers for channel frequency filtering, the amplifier stages, and finally the four Vivaldi antennas. Fig. 3.19 presents a block diagram of the system along with the main specifications.

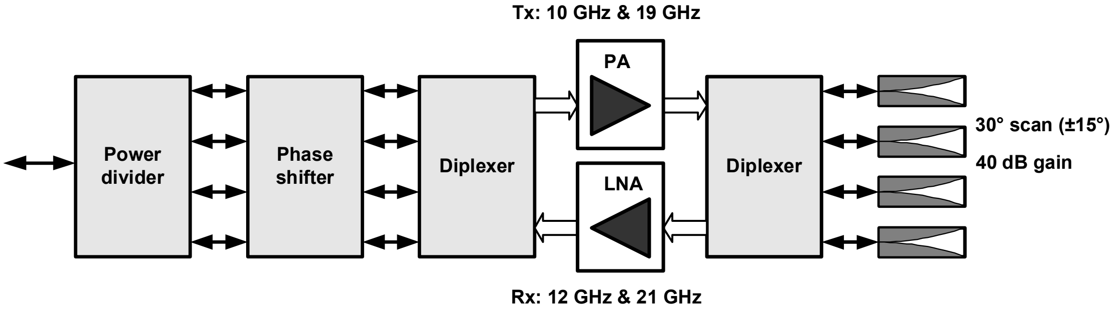

Fig. 3.19: System block diagram with specifications.

3.2.3 Statistical analysis method

The statistical method is accurate for large arrays (N>10) and for small amplitude and phase errors or imbalances of the output field (S_{12}) to the antennas. This method is widely used to predict the behaviour of phased array systems under some range of error. For the studied phased array, these formulas are approximate since they assume a sufficiently large array so that the central limit theorem applies (generally the number of elements be desirably above 20) and relatively small errors.

The errors of random type are uncorrelated errors subject to statistical manipulations. Random phase and amplitude errors in phased arrays affect their performance by reducing the directivity, raising the sidelobe level, and changing the main beam pointing and sometimes the beam shape. These effects are quantified by using the following statistical formulas [13]. ϕ_{ps} is the phase error in ± degrees, a is the amplitude limits in ± dB, P is the probability of survival of one element and other symbols are defined in Table 3.1.

RMS phase error (radians):

$$\sigma_{\phi_{ps}} = \frac{\phi_{ps}}{\sqrt{3}} \qquad 3.23$$

Phase error variance due to phase shifter quantization:

$$\sigma_{\phi_q}{}^2 = \frac{\pi^2}{3 \cdot 2^{2M}} \qquad 3.24$$

Total mean square phase error :

$$\sigma_{\phi}{}^2 = \sigma_{\phi_{ps}}{}^2 + \sigma_{\phi_q}{}^2 \qquad 3.25$$

RMS amplitude error (V):

$$\sigma_a = \frac{10^{\frac{a}{20}} + 10^{-\frac{a}{20}}}{2\sqrt{3}} \qquad 3.26$$

Average power sidelobe:

$$\sigma^2 = \frac{(1-P) + \sigma_a{}^2 + P\sigma_{\phi}{}^2}{N_T P \eta (1 - \sigma_{\phi}{}^2 - \sigma_a{}^2)} \qquad 3.27$$

Directivity loss:

$$\frac{D}{D_0} = \frac{P}{1 + \sigma_\phi^{\ 2} + \sigma_a^{\ 2}} \tag{3.28}$$

Beam pointing error as a fraction of θ_{HP}:

$$\frac{\sigma_\theta}{\theta_{HP}} = \frac{1}{0.88\pi}\sqrt{\frac{3(\sigma_\phi^{\ 2} + \sigma_a^{\ 2})}{N_T}} \tag{3.29}$$

The range of amplitude error from a given set of 4 measured excitation amplitudes at each element is the maximum error between the actual amplitudes and their average. For the phase error, in the broadside case, the calculation is as that for the amplitude since the ideal reference phase is constant for a progressive phase of zero. In the steering case, the maximum error between the measured values and a straight line best-fit is used.

In order to efficiently analyze the system and compilate the results, a spreadsheet was developped integrating the input parameters and all statistical formulas as shown in Fig. 3.20 and Fig. 3.21.

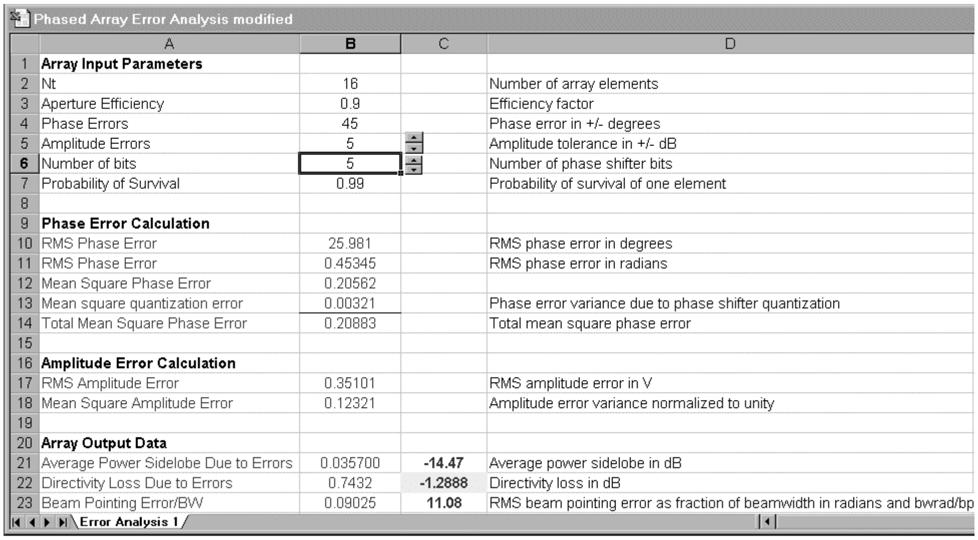

	A	B	C	D
1	**Array Input Parameters**			
2	Nt	16		Number of array elements
3	Aperture Efficiency	0.9		Efficiency factor
4	Phase Errors	45		Phase error in +/- degrees
5	Amplitude Errors	5		Amplitude tolerance in +/- dB
6	Number of bits	5		Number of phase shifter bits
7	Probability of Survival	0.99		Probability of survival of one element
8				
9	**Phase Error Calculation**			
10	RMS Phase Error	25.981		RMS phase error in degrees
11	RMS Phase Error	0.45345		RMS phase error in radians
12	Mean Square Phase Error	0.20562		
13	Mean square quantization error	0.00321		Phase error variance due to phase shifter quantization
14	Total Mean Square Phase Error	0.20883		Total mean square phase error
15				
16	**Amplitude Error Calculation**			
17	RMS Amplitude Error	0.35101		RMS amplitude error in V
18	Mean Square Amplitude Error	0.12321		Amplitude error variance normalized to unity
19				
20	**Array Output Data**			
21	Average Power Sidelobe Due to Errors	0.035700	**-14.47**	Average power sidelobe in dB
22	Directivity Loss Due to Errors	0.7432	**-1.2888**	Directivity loss in dB
23	Beam Pointing Error/BW	0.09025	**11.08**	RMS beam pointing error as fraction of beamwidth in radians and bwrad/bp

Fig. 3.20: Spreadsheet used for statistical error analysis.

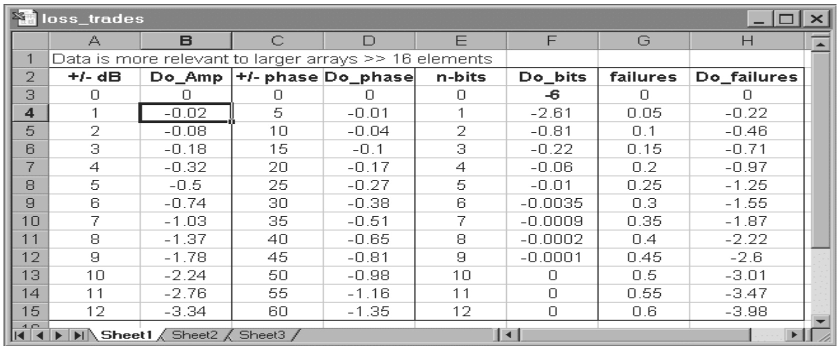

	A	B	C	D	E	F	G	H
1	Data is more relevant to larger arrays >> 16 elements							
2	**+/- dB**	**Do_Amp**	**+/- phase**	**Do_phase**	**n-bits**	**Do_bits**	**failures**	**Do_failures**
3	0	0	0	0	0	-6	0	0
4	1	-0.02	5	-0.01	1	-2.61	0.05	-0.22
5	2	-0.08	10	-0.04	2	-0.81	0.1	-0.46
6	3	-0.18	15	-0.1	3	-0.22	0.15	-0.71
7	4	-0.32	20	-0.17	4	-0.06	0.2	-0.97
8	5	-0.5	25	-0.27	5	-0.01	0.25	-1.25
9	6	-0.74	30	-0.38	6	-0.0035	0.3	-1.55
10	7	-1.03	35	-0.51	7	-0.0009	0.35	-1.87
11	8	-1.37	40	-0.65	8	-0.0002	0.4	-2.22
12	9	-1.78	45	-0.81	9	-0.0001	0.45	-2.6
13	10	-2.24	50	-0.98	10	0	0.5	-3.01
14	11	-2.76	55	-1.16	11	0	0.55	-3.47
15	12	-3.34	60	-1.35	12	0	0.6	-3.98

Fig. 3.21: Spreadsheet used for loss trades analysis.

The following graphs present the predicted performance of the phased array using the statistical method given the amplitude and phase error. These can be used as guide charts for first level design. Fig. 3.22, Fig. 3.23, and Fig. 3.24 present the predicted SLL, the directivity loss, and the beam pointing error as a function of the amplitude error with the maximum measured phase error. Fig. 3.25, Fig. 3.26, and Fig. 3.27 give the predicted SLL, the directivity loss, and the beam pointing error as a function of the phase error with the maximum measured amplitude error. It should be noted that the graphs were produced using the measured maximum phase and amplitude errors from a previous set different to the one used to predict the measured patterns.

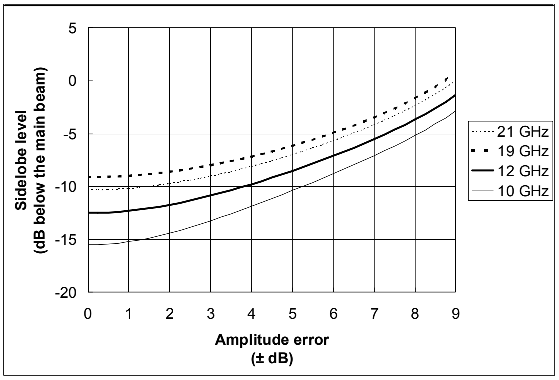

Fig. 3.22: Sidelobe level due to amplitude error with maximum phase error.

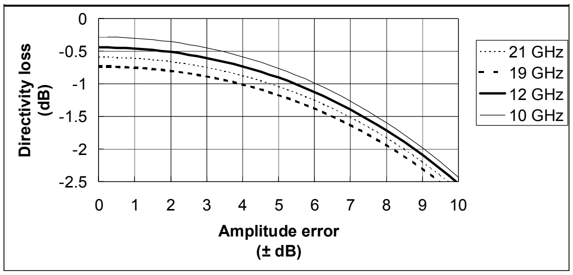

Fig. 3.23: Directivity loss due to amplitude error with maximum phase error.

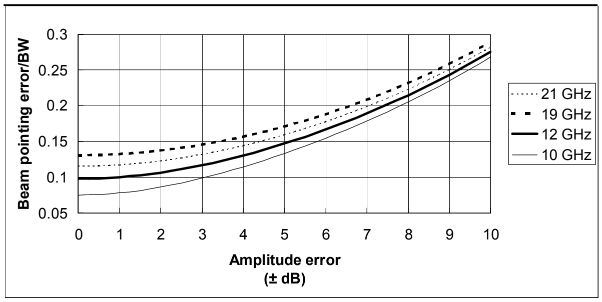

Fig. 3.24: Beam pointing error/BW due to amplitude error with maximum phase error.

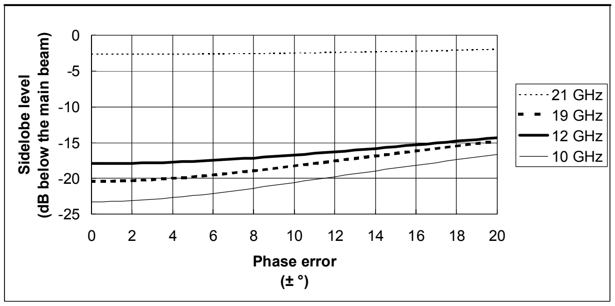

Fig. 3.25: Sidelobe level due to phase error with maximum amplitude error.

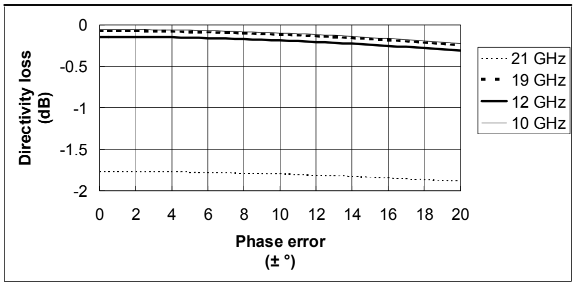

Fig. 3.26: Directivity loss due to phase error with maximum amplitude error.

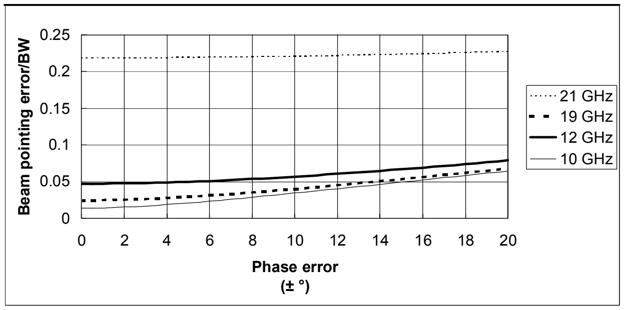

Fig. 3.27: Beam pointing error/BW due to phase error with maximum amplitude error.

From the previous results, the most critical error is the amplitude with the steepest slope on the performance charts. The noticeable separation between the 21 GHz curve and the other lower frequencies for the variation of the phase error is due to the large difference between the maximum amplitude error at 21 GHz (±8.9 dB) and at 10, 12 and 19 GHz (from ±0.6 to ±2.25 dB).

3.2.4 Field analysis method

For the small number of elements in the 1 x 4 phased array, a field analysis, calculating the overall error by adding the individual contribution from each element is more adequate than the statistical method. For simplification purposes, the mutual coupling between elements is neglected. The later will not be included to avoid the complexity of the measurement setup and procedures, but a first-order evaluation of its effect on the accuracy of the analysis will be conducted.

For a set of normalized excitation amplitudes (a_1 to a_4) and phases (β_1 to β_4) at each element both with imbalances, the far field pattern of the array can be calculated by

$$E(\theta) = \sum_{n=1}^{4} a_n \cdot e^{j\left[(n-1)\cdot k_0 \cdot d \cdot \sin\left(\frac{\pi \cdot \theta}{180}\right) - \beta_n\right]} \tag{3.30}$$

where β_n is the difference in phase for each element with respect to a reference element (line #4, set to 0°). To create the predicted pattern, one multiplies this array factor with the corresponding measured element pattern at each frequency. The measured element pattern is preferred to the approximation by a power of cosine since the goal of the analysis is to predict as closely as possible the performance of a phased array composed of antennas already known and characterized. Also, the measured pattern is sometimes non-symmetrical with a maximum that is not centered at 0° due to design and experimental errors. Therefore, once multiplied with the array factor the resulting maximum will not necessarily be at 0° as predicted in the broadside case, contributing to some beam pointing error. The details on the field prediction calculations are given in Appendix C with the MathCAD listing.

3.3 Correlation between predicted and measured data

This section presents the results from both analytical methods and measurements for comparison purposes. The needed input data is specified, the resulting patterns are displayed, and the performance parameters are summarized.

3.3.1 Input parameters

The input parameters required by the field and statistical analysis are given in this section. Table 3.4 presents some input data used in the statistical method calculations. The aperture efficiency needed in the calculation of the average power sidelobe (σ^2) is obtained from $\eta = \lambda^2 D/(4\pi A)$ where A is the physical area of the array. This assumes a uniform distribution of amplitudes and no conductor, matching or polarization match losses. The array directivity D is calculated using

Kraus approximation formula $D \approx 52{,}525/[\theta_{xHP} \cdot \theta_{yHP}]$ for patterns with a main lobe of elliptical cross-section. The θ_{HP}'s are in degrees and have been evaluated taking into account the scan angle using equation 3.12.

Table 3.4: Input data for statistical method calculation.

		N	4		
		***P* (%)**	0.99		
		***A* (mm^2)**	1,295.4		
		Frequency (GHz)			
		10	**12**	**19**	**21**
Broadside	***D* (dB)**	15.5	17.2	21.2	22.0
	η	1.93	1.95	1.98	1.99
Negative scan	***D* (dB)**	14.7	16.6	18.9	19.8
	η	1.61	1.68	1.17	1.18
Positive scan	***D* (dB)**	14.3	16.1	19.9	21.0
	η	1.46	1.51	1.47	1.58

Table 3.5, Table 3.6, and Table 3.7 give the measured amplitude and phase values of the output field at each element for each frequency used for broadside, negative scan, and positive scan radiation respectively. These values are needed for both the statistical and field analysis methods. The measured amplitudes and phases at the antenna input include the contribution of the phase shifter, diplexers and active modules. The amplitude distribution is not uniform and phase is unbalanced. If the phase varied linearly versus frequency, the beam scanning angle would be the same as in the ideal case at different frequencies for transmit and receive. In reality, this full-duplex function was not completely accomplished due to many reasons: non-perfect alignment of multi-line PET phase shifter, phase imbalances for four modules at each frequency, etc. Frequencies used in measurement, 10.04, 12.185, 19.14, and 21.025 GHz, are very close to the specified frequencies.

Table 3.5: Measured amplitude and phase of S_{12} for field analysis at broadside.

Channel number	**Frequency (GHz)**			
	10	**12**	**19**	**21**
1	$1.58\angle 144.5^\circ$	$4.68\angle 112.4^\circ$	$1.22\angle 202.7^\circ$	$1.05\angle 52.3^\circ$
2	$2.09\angle 104.8^\circ$	$2.16\angle 120.7^\circ$	$2.11\angle 160.3^\circ$	$1.51\angle 76.9^\circ$
3	$0.27\angle 212.2^\circ$	$0.32\angle 78.9^\circ$	$0.21\angle 201.2^\circ$	$0.19\angle 171.2^\circ$
4	$0.76\angle 151.3^\circ$	$4.68\angle 88.6^\circ$	$1.41\angle 145.2^\circ$	$1.02\angle 67.5^\circ$

Table 3.6: Measured amplitude and phase of S_{12} for field analysis at negative scan.

Channel number	**Frequency (GHz)**			
	10	**12**	**19**	**21**
1	$1.70\angle 251.0^\circ$	$3.31\angle 255.0^\circ$	$0.98\angle 332.7^\circ$	$0.78\angle 279.6^\circ$
2	$1.00\angle 152.4^\circ$	$4.03\angle 177.9^\circ$	$2.16\angle 223.1^\circ$	$0.95\angle 202.5^\circ$
3	$0.32\angle 208.5^\circ$	$0.25\angle 76.4^\circ$	$0.31\angle 204.2^\circ$	$0.46\angle 47.4^\circ$
4	$1.86\angle 83.0^\circ$	$2.24\angle 346.4^\circ$	$1.04\angle 70.1^\circ$	$0.77\angle 168.3^\circ$

Table 3.7: Measured amplitude and phase of S_{12} for field analysis at positive scan.

Channel number	**Frequency (GHz)**			
	10	**12**	**19**	**21**
1	$1.53\angle 96.1^\circ$	$2.07\angle 11.4^\circ$	$0.89\angle 63.8^\circ$	$1.02\angle 307.4^\circ$
2	$0.96\angle 72.0^\circ$	$2.99\angle 99.2^\circ$	$0.57\angle 135.8^\circ$	$1.35\angle 55.8^\circ$
3	$0.32\angle 267.3^\circ$	$0.47\angle 142.6^\circ$	$0.41\angle 311.3^\circ$	$0.21\angle 202.8^\circ$
4	$1.07\angle 210.5^\circ$	$3.31\angle 239.5^\circ$	$2.11\angle 348.4^\circ$	$0.98\angle 273.3^\circ$

3.3.2 Patterns

Fig. 3.28 to Fig. 3.31 present the measured patterns at broadside superposed by the predicted patterns using the field analysis method. The measured patterns are displayed in a solid black line and the predicted patterns in a dashed gray line. These patterns will be used to extract some performance parameters that will be presented in the following subsections. The difference in fitting at 19 GHz (mostly angular position of main beam) is partly due to the fact that the measured pattern was available only at 25 V (not at 20 V as was set for the amplitudes and phases measurements). This 5V difference represents a scanning effect of the PET, which explains the small separation between the beams. Following are Fig. 3.32 to Fig. 3.35 that present the measured patterns at a negative scan angle with their corresponding predicted patterns obtained from the field analysis. Fig. 3.36 to Fig. 3.39 show the fitting results for the measured patterns at a positive scan angle. It should be noted that the element pattern used for the fit of all array patterns at 21 GHz was that measured at 20 GHz because the one at 21 GHz was erroneous (it was the only single element pattern that felt 15 dB under the level of all others measured at 3.5 to 8 dB of maximum gain at frequencies ranging from 8 to 26.5 GHz). This could also contribute to some fitting differences. Other causes of fitting discrepancies will be explained in the discussion (section 3.4). Considering these problems in measurements, the agreement between the predicted and measured results is fairly good.

The field analysis performance parameters will be compared with the statistical results (with reference to the measured results). These parameters are the sidelobe level (SLL), the directivity loss (D_{LOSS}), and the beam pointing error (BPE/BW). A last section also evaluates the gain loss prediction accuracy using the cosine approximation. All results are summarized in Table 3.8 to Table 3.11 in section 3.3.3.

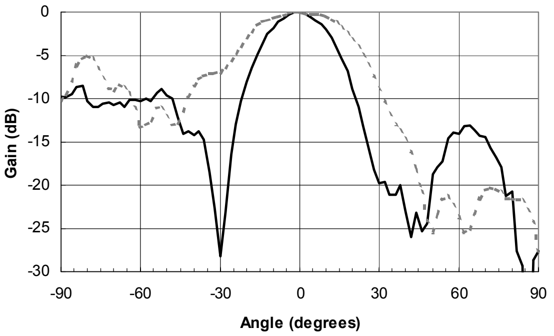

Fig. 3.28: H-plane broadside radiation pattern at 10 GHz.

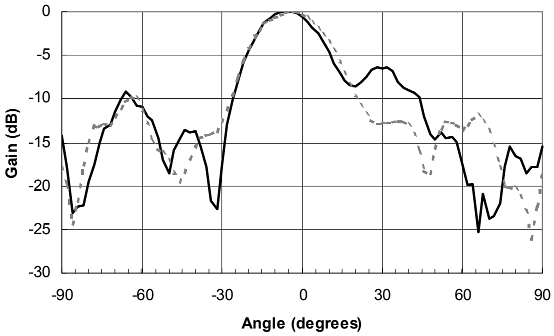

Fig. 3.29: H-plane broadside radiation pattern at 12 GHz.

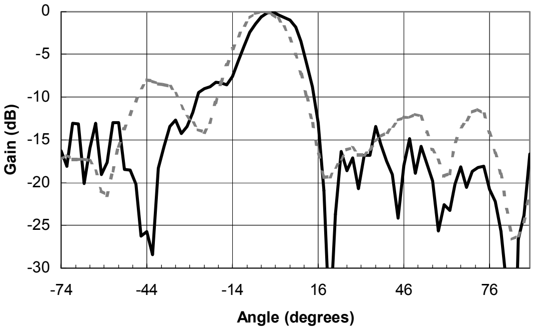

Fig. 3.30: H-plane broadside radiation pattern at 19 GHz.

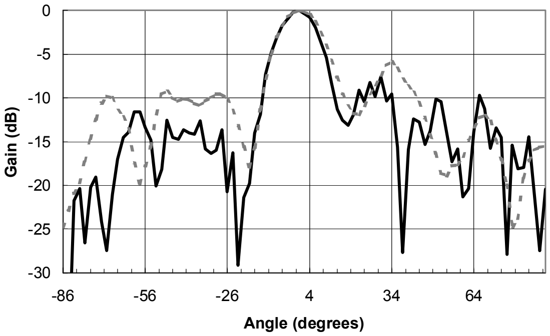

Fig. 3.31: H-plane broadside radiation pattern at 21 GHz.

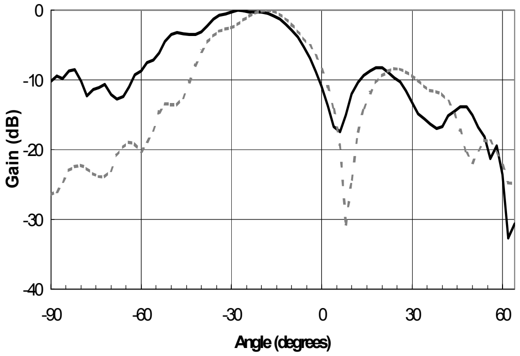

Fig. 3.32: H-plane radiation pattern with negative scan angle at 10 GHz.

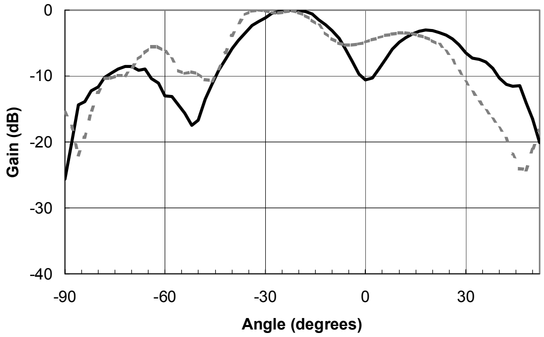

Fig. 3.33: H-plane radiation pattern with negative scan angle at 12 GHz.

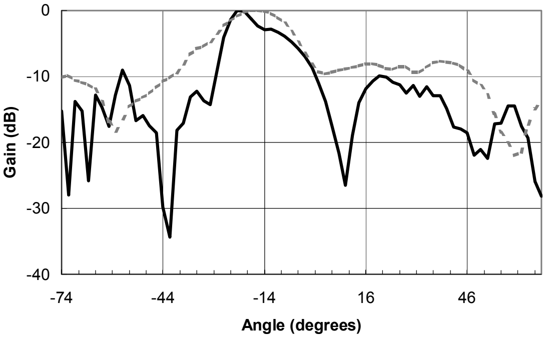

Fig. 3.34: H-plane radiation pattern with negative scan angle at 19 GHz.

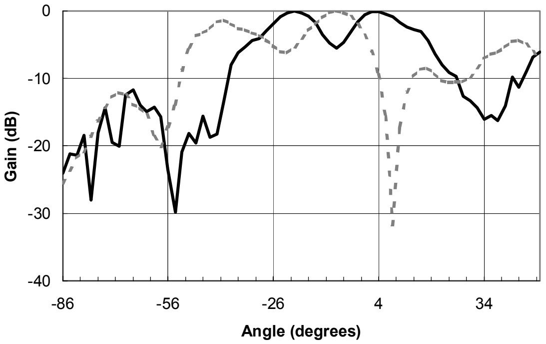

Fig. 3.35: H-plane radiation pattern with negative scan angle at 21 GHz.

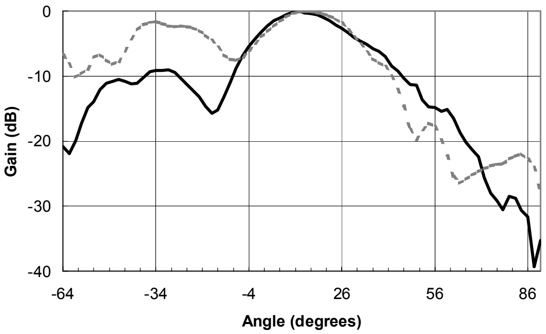

Fig. 3.36: H-plane radiation pattern with positive scan angle at 10 GHz.

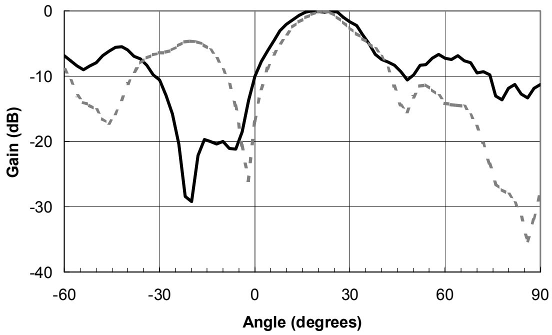

Fig. 3.37: H-plane radiation pattern with positive scan angle at 12 GHz.

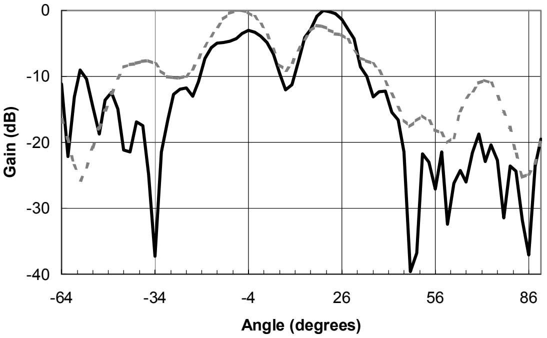

Fig. 3.38: H-plane radiation pattern with positive scan angle at 19 GHz.

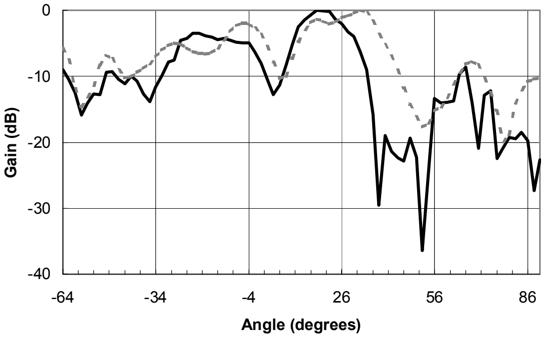

Fig. 3.39: H-plane radiation pattern with positive scan angle at 21 GHz.

3.3.2.1 Sidelobe levels (SLL)

An approximate prediction of the sidelobe levels was done using the statistical equation 3.27 (σ^2). Some input parameters are needed to solve this equation. These can be found in Table 3.4 to Table 3.7. The SLL values from the statistical method are by definition the average values of all predicted SLLs at one frequency.

The SLL prediction using the field analysis can be extracted from the theoretical field pattern as seen in Fig. 3.28 to Fig. 3.39. The measured SLL can also be read from the same figures. The maximum measured SLL is compared to the corresponding SLL in the field prediction, with maximum amplitude on the same side of the main beam. This is not necessarily the maximum

SLL of the field pattern as observed in the case of broadside radiation at 12 GHz in Fig. 3.29. As mentioned previously, all read values are summarized in section 3.3.3.

3.3.2.2 Directivity loss (D_{LOSS}*)*

The directivity loss calculated by the field analysis is obtained from the difference between the ideal predicted maximum gain (AF_field_idealxEP) and the predicted maximum gain with errors (AF_field_realxEP). AF_field_realxEP is calculated using measured amplitudes and phases with errors (non-uniform amplitude and non-linear phase variations) given in Table 3.5 to Table 3.7. AF_field_idealxEP is obtained using a uniform set of amplitudes corresponding to the maximum amplitude value. This choice was based on the fact that a design goal is to minimize components losses, therefore an optimal amplitude is the highest possible. A phase vector without errors is also used. For the broadside case, all phases are equal to 0° or any constant to give a progressive phase equal to zero. For the steering cases, the phases are obtained from a straight line best-fit of the measured phases. The predicted main beams using amplitudes and phases with errors are not necessarily centered at the ideal scan angle. For the directivity loss calculation, the maximum gain is considered even if the beam is slightly deviated. The beam pointing error will characterize this angular deviation. The predicted directivity losses for the broadside case are 4.1, 5.5, 4.4, and 2 dB at 10, 12, 19, and 21 GHz, respectively. For the negative scan patterns, the directivity losses are 5.1, 4.3, 6.2, and 3.1 dB and for the positive scan angle, 5, 3.8, 4.5, and 4, dB at 10, 12, 19, and 21 GHz, respectively.

The statistical method uses equations 3.23, 3.26, and 3.28 with the input parameters found in Table 3.4 to Table 3.7. The calculated directivity losses are 3.3, 5.1, 4.1, and 4.4 dB for the broadside case, 3, 6.7, 2.3, and 1 dB for the negative scan angle, and 3.2, 3.1, 2.1, and 2.9 dB for the positive scan angle at 10, 12, 19, and 21 GHz, respectively.

The measured directivity loss was evaluated by subtracting the measured maximum gain from AF_field_ideal multiplied by the element pattern. The measured directivity losses are 7.4, 7.3, 14, and 4.9 dB for the broadside case, 9, 5.9, 10.4, and 2.7 dB for the negative scan, and 3.4, 3.9, 8.3, and 3.6 dB for the positive scan at 10, 12, 19, and 21 GHz, respectively.

3.3.2.3 Beam pointing error (BPE/BW)

The beam pointing error is referenced to the θ_{HP} in order to appreciate its effect on the phase array performance. For example, by observing the patterns one can see that the beamwidth is relatively broad which makes the beam error less relevant.

For the broadside radiation, the deviation of the main beam is evaluated with respect to 0°. From the steered measured and field predicted patterns, one can calculate the deviation of the scan angle with respect to the ideal scan angle obtained from equation 3.10 using the progressive phase shift that results from a straight line best-fit phase distribution with respect to the measured phases. The beam pointing error predicted by field analysis is 0.05, 0.15, 0.22, and 0 for the broadside case, 0.15, 0.24, 0.22, and 0.74 for the negative scan, and 0.48, 0.39, 0.53, and 0.24 for the positive scan at 10, 12, 19, and 21 GHz, respectively. For the statistical analysis, again using the input parameters in Table 3.4 and Table 3.5 to Table 3.7, and equation 3.29, the values obtained for broadside are 0.33, 0.47, 0.39, and 0.41; 0.31, 0.59, 0.26, and 0.15 for negative scan, and 0.32, 0.32, 0.24, and 0.3 for positive scan at 10, 12, 19, and 21 GHz, respectively. Finally, the measured beam pointing error gives 0, 0.16, 0, and 0 at broadside, 0.19, 0.65, 0.07, and 1.21 at negative scan, and 0.51, 0.19, 0.5, and 0.54 at positive scan for 10, 12, 19, and 21 GHz, respectively.

3.3.2.4 Gain (or scan) loss

The scan loss of an array of taper slot antennas can be evaluated from calculations of mutual coupling parameters or approximated by the measured element pattern. A cosine function elevated to some power can be used to fit the element pattern and predict the scan loss. For example, empirical data for a patch antenna show that the roll-off factor can be approximated by $(\cos \theta)^{0.55}$. Fig. 3.40 to Fig. 3.43 present the single element patterns measured at all four frequencies with their corresponding approximation cosine function elevated to the appropriate power (for best fit) n equal to 2.3, 3, 4.7, and 5.6 for 10, 12, 19, and 21 GHz, respectively. The element pattern used for scan loss prediction at 21 GHz was taken at 20 GHz instead, for the reasons given previously. Fig. 3.44 to Fig. 3.47 show the scanned array patterns for scan loss reading from their maximum gain values. In order to calculate the accuracy of the scan loss prediction (indicated by "Max. error" in Table 3.11, section 3.3.3), the difference between the predicted loss at the measured scan angle and the corresponding measured loss is compared to the maximum measured loss at our specified maximum scan angle of 15°.

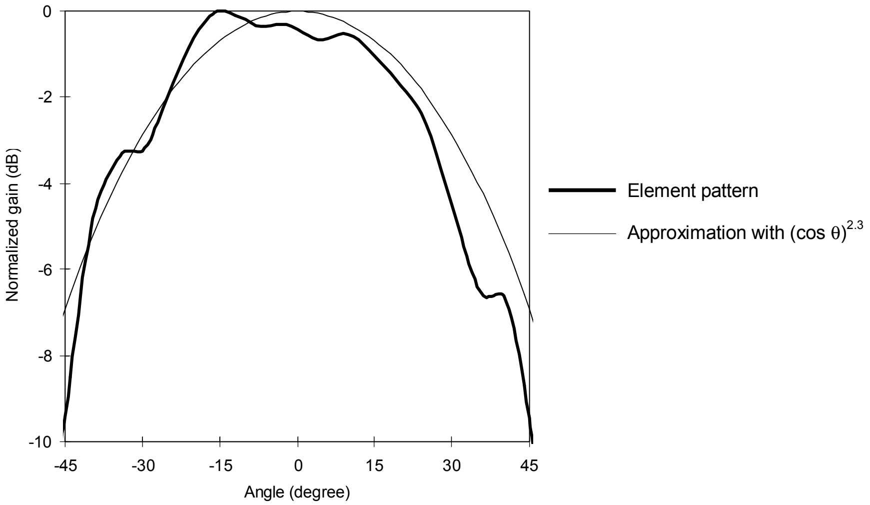

Fig. 3.40: Element pattern and $(\cos\theta)^{2.3}$ for scan roll-off approximation at 10 GHz.

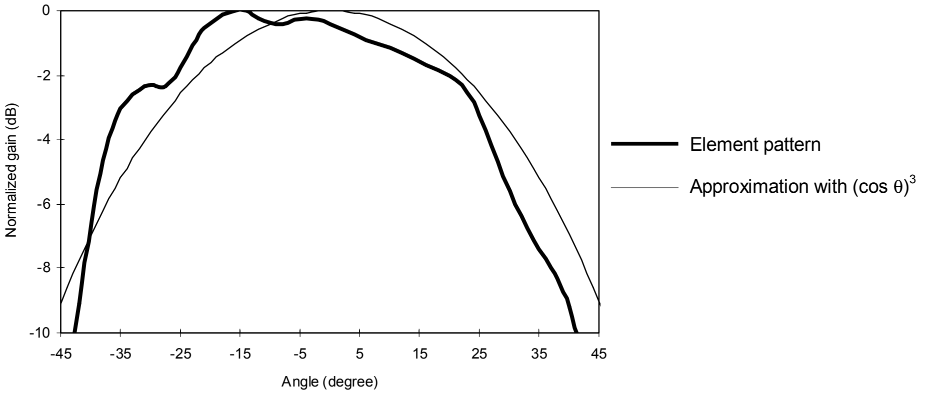

Fig. 3.41: Element pattern and $(\cos\theta)^3$ for scan roll-off approximation at 12 GHz.

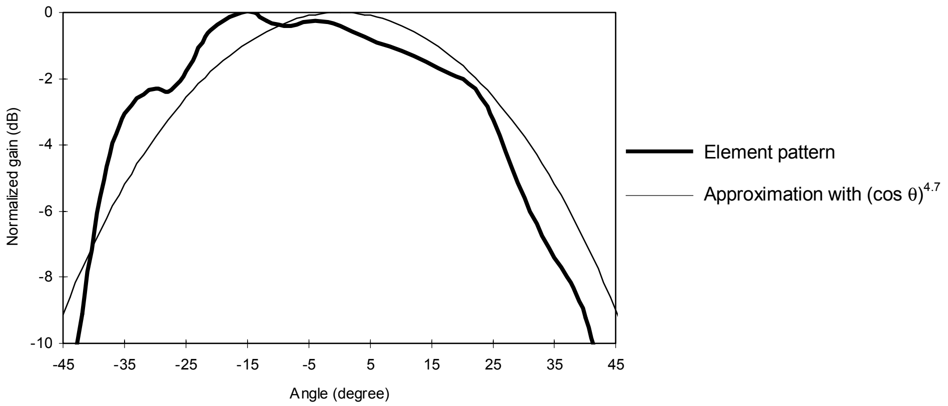

Fig. 3.42: Element pattern and $(\cos\theta)^{4.7}$ for scan roll-off approximation at 19 GHz.

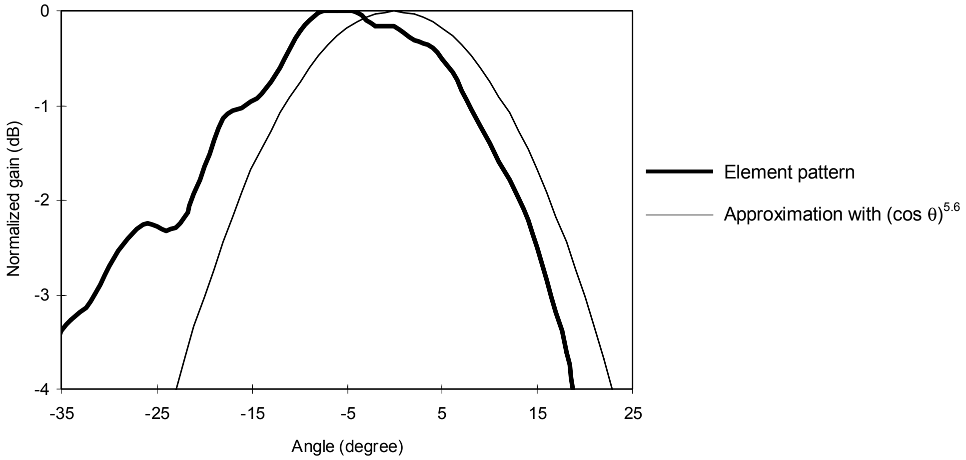

Fig. 3.43: Element pattern and $(\cos\theta)^{5.6}$ for scan roll-off approximation at 20 GHz.

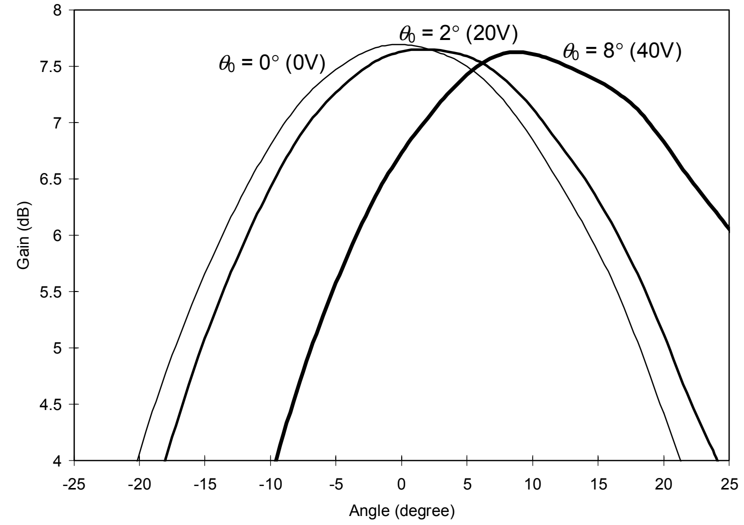

Fig. 3.44: Scanning of main lobe with scan loss at 10 GHz.

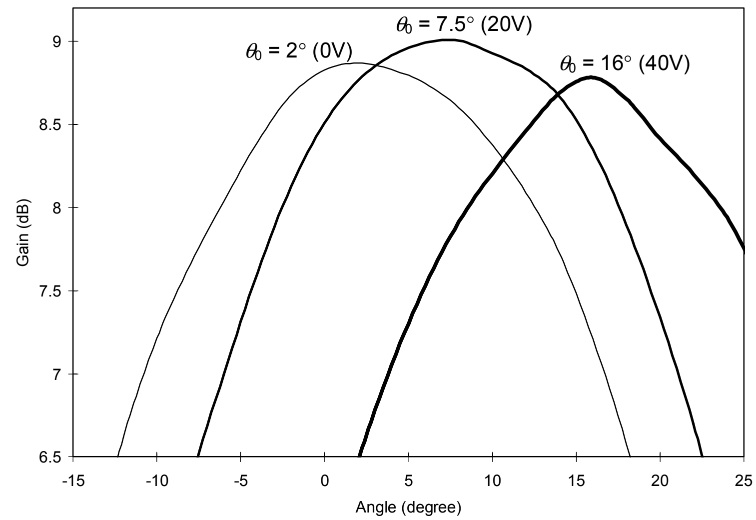

Fig. 3.45: Scanning of main lobe with scan loss at 12 GHz.

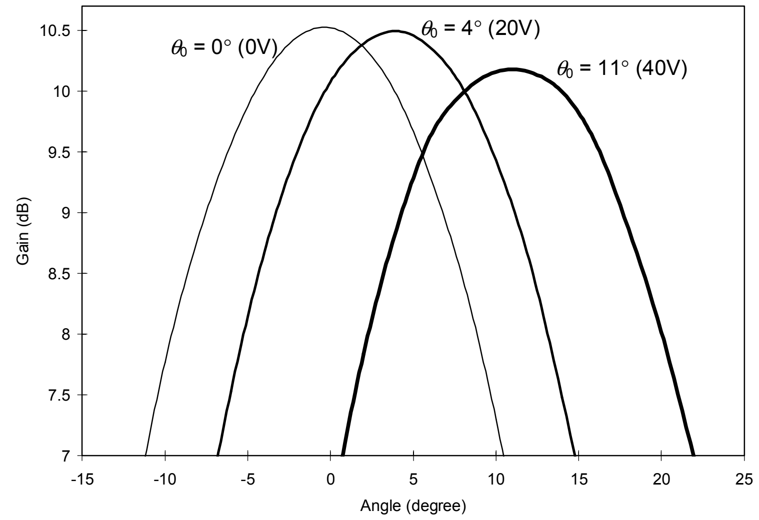

Fig. 3.46: Scanning of main lobe with scan loss at 19 GHz.

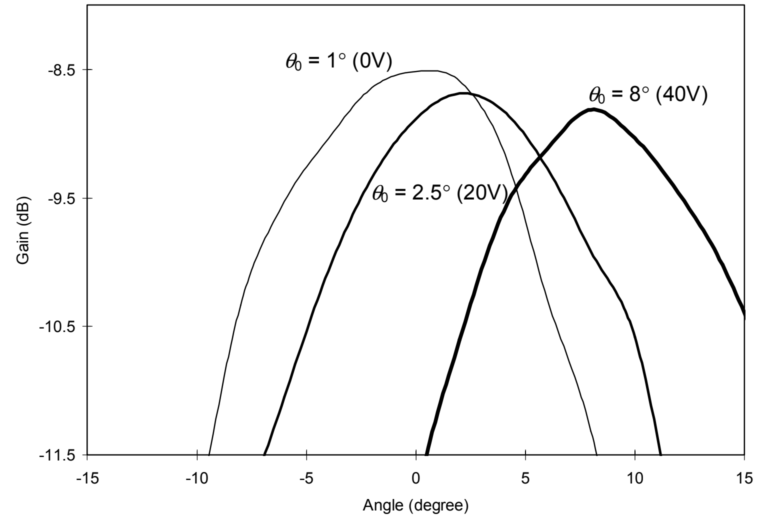

Fig. 3.47: Scanning of main lobe with scan loss at 21 GHz.

3.3.3 Summary

Table 3.8, Table 3.9, and Table 3.10 summarize the results calculated in the previous sections on performance parameters for the phased array system. Table 3.11 presents the results for the gain roll-off study.

Table 3.8: Comparison of two error analysis methods for broadside case.

	Frequency (GHz)	**SLL (dB)**	**D_{LOSS} (dB)**	**BPE/BW**
Predicted results with field analysis	**10**	5.0	4.1	0.05
	12	12.0	5.5	0.15
	19	8.0	4.4	0.22
	21	5.8	2.0	0.0
Predicted results with statistical method	**10**	N/A	3.3	0.33
	12	N/A	5.1	0.47
	19	N/A	4.1	0.39
	21	N/A	4.4	0.41
Measured results	**10**	8.5	7.4	0.0
	12	6.4	7.3	0.16
	19	8.3	14.0	0.0
	21	7.6	4.9	0.0

Table 3.9: Comparison of two error analysis methods for negative scan angle case.

	Frequency (GHz)	**SLL (dB)**	**D_{LOSS} (dB)**	**BPE/BW**
Predicted results with field analysis	**10**	8.4	5.1	0.15
	12	3.5	4.3	0.24
	19	9.9	6.2	0.22
	21	1.4>main lobe	3.1	0.74
Predicted results with statistical method	**10**	8.3>main lobe	3.0	0.31
	12	N/A	6.7	0.59
	19	3.1	2.3	0.26
	21	11.4	1.0	0.15
Measured results	**10**	8.3	9.0	0.19
	12	3.1	5.9	0.65
	19	9.0	10.4	0.07
	21	0.1	2.7	1.21

Table 3.10: Comparison of two error analysis methods for positive scan angle case.

	Frequency (GHz)	**SLL (dB)**	**D_{LOSS} (dB)**	**BPE/BW**
Predicted results with field analysis	**10**	1.6	5.0	0.48
	12	4.6	3.8	0.39
	19	2.3 >main lobe	4.5	0.53
	21	2.0	4.0	0.24
Predicted results with statistical method	**10**	N/A	3.2	0.32
	12	N/A	3.1	0.32
	19	5.6	2.1	0.24
	21	3.2>main lobe	2.9	0.30
Measured results	**10**	9.0	3.4	0.51
	12	5.5	3.9	0.19
	19	3.0	8.3	0.50
	21	3.5	3.6	0.54

Table 3.11: Measured and predicted scan roll-off.

10 GHz			12 GHz			19 GHz			21 GHz		
Angle (°)	Meas. (dB)	Pred. (dB)	Angle (°)	Meas. (dB)	Pred. (dB)	Angle (°)	Meas. (dB)	Pred. (dB)	Angle (°)	Meas. (dB)	Pred. (dB)
2	0.046	0.012	7.5	0.149	0.306	4	0.026	0.106	2.5	0.17	0.03
8	0.077	0.195	-	-	-	11	0.365	0.76	8	0.297	0.476
Max. at 15° (dB)		0.695	**Max. at 15° (dB)**		1.235	**Max. at 15° (dB)**		1.5	**Max. at 15° (dB)**		1.7
Max. error (%)		16	**Max. error (%)**		13	**Max. error (%)**		26	**Max. error (%)**		11

3.4 Discussion and recommendations

The high level of sidelobes in the phased array is primarily caused by the phase and magnitude imbalance between the four modules. If the modules imbalances were lower, the predicted and measured data would have been more similar. When the measurements were performed, interconnection loss, some substrate damage loss caused by many soldering trials, integration mismatch, and other unknown losses occurred and could not be predicted [45]. Also, the aperture efficiency is less significant for a small number of elements or with thin antennas (not large effective aperture area for endfire antennas).

The indication of "N/A" for SLLs at some frequencies in the statistical method results (from Table 3.8 to Table 3.10) signifies that the statistical formula used for calculation of average power of SLL is not valid for the given amplitude (a) and phase errors (ϕ_{ps}) at the antennas. As was mentioned previously, the statistical method is valid for small ranges of errors or imbalances. From equation 3.27, one can see that the sum of mean square phase and amplitude errors, σ_{ϕ}^2 and σ_a^2 respectively, should not be higher than 1 for the absolute value of SLL to be positive. From this condition, the maximum a that is acceptable with $\phi_{ps} = 0$ is ±11.45 dB. Inversely, with $a = 0$, the maximum ϕ_{ps} is limited to ±99°. The maximum amplitude and phase errors that were measured are ±16.5 dB and ±79°, respectively. Therefore, there is at least one case for which a is beyond the limit for the SLL statistical formula to be valid, even for $\phi_{ps} = 0$ (which is not the case for any measurement at any frequency or scan angle). Obviously, a combination of large amplitude and phase errors, each under their limit, can still lead to $\sigma_{\phi}^2 + \sigma_a^2 > 1$. Fig. 3.48 shows the value of $\sigma_{\phi}^2 + \sigma_a^2$ with respect to the amplitude error for different phase errors. As seen, the validity of the statistical formula for SLL is much more sensitive on the amplitude error than the phase error.

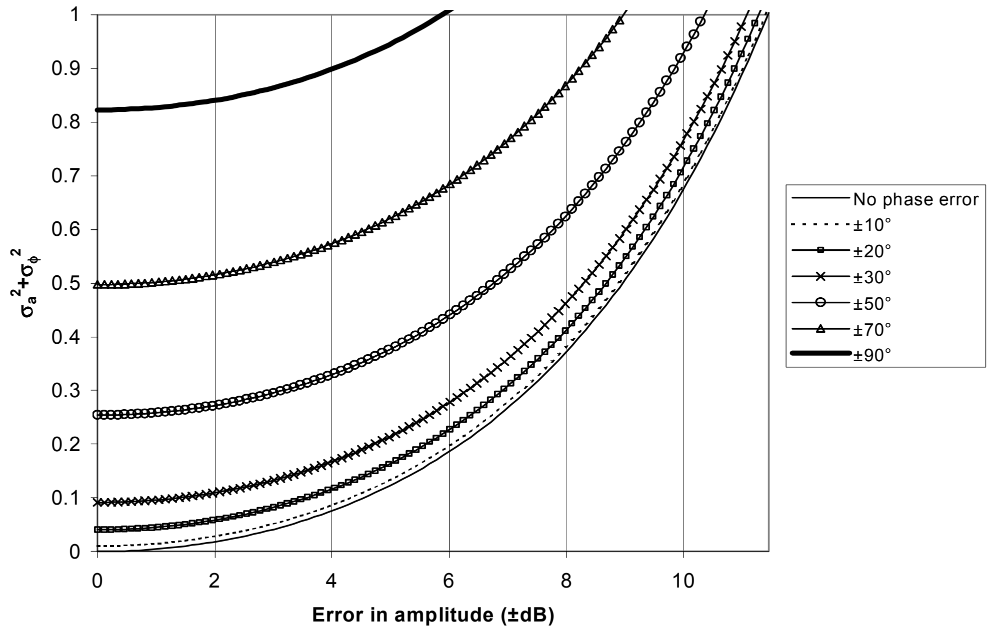

Fig. 3.48: Validity of statistical calculation of SLL for given amplitude and phase errors.

The directivity losses present some differences between the three methods. The difference between the statistical method and the two others can be explained by the fact that the former method assumes a large number of elements and therefore predicts a more optimistic result than the later methods. The difference between the measured directivity loss and the one predicted by the field analysis is directly related to the fact that the mutual coupling effects are neglected in the prediction calculations. Also the edge effects and other experimental losses can simply not be predicted. The contribution of these undesirable effects can be quantified by the difference between the predicted gain from the field analysis with unbalanced amplitudes and phases, and the measured gain. The predicted gain is calculated using the vector of non-normalized amplitudes and phases with errors. The value obtained corresponds to the difference between the measured directivity loss and the one predicted with the field analysis. In other words, if the mutual coupling effects had been integrated into the field analysis method, the directivity losses for the field analysis and the measured results would have been almost the same.

In some cases, the predicted performance is worst than the measured one. For example, in Fig. 3.30, the predicted SLL is higher than the measured one, or even worst, in Fig. 3.38, the predicted SLL is above the main beam. These unexpected predicted performances with respect to the measured results can be attributed to fine tuning during the antenna measurements that cannot be enforced when measuring the amplitude and phase at the elements. Since the later is a transmission type of measurement, one needs a different setup, which can cause some slight mechanical variations in the PET position for the same voltage, and hence, differences between the measured amplitudes and phases with respect to the ones used during the antenna measurement. The only available element pattern data used for the field predicted pattern was measured several months before the final tuning of the system and although the same basic design was kept for the antenna, it was constantly being optimized to improve the results as needed throughout the project. Therefore, the more recent measured array patterns used here for comparison were produced with antenna elements that were slightly different to those that served to generate the element pattern data.

Overall, the measured and predicted patterns compare well. Since the field analysis did not include the mutual coupling effects which contributes in great part to the degradation of the pattern (as will be explained later, mostly in a small array), and other experimental errors, one can observe some differences in the lobes positions. Also, one should note that the accuracy of the beam pointing error evaluation is directly dependent on the number of data points available to create the patterns. To calculate this precision, the angle step used is divided by the smallest beamwidth. The step of the measured data is 0.5° and that of the predicted pattern is of 2° corresponding to that of the available single element pattern data. The smallest measured beamwith is 12.3° and the minimum predicted beamwidth is 17°. This gives a beam pointing error accuracy of ±0.02 for the measured patterns and of ±0.06 for the predicted patterns.

The predicted results from the statistical error formulas are approximated since the array counts only 4 elements with relatively large phase and amplitude errors. Still, this statistical analysis of random errors for our phased array gave us a good preliminary idea of the performance tendency. In general, the field analysis predicts more accurately the measured results. This method can predict asymmetries in the radiation pattern and is more suited for analyzing small arrays. The differences can be attributed to the mutual coupling and uniform excitation approximations.

In order to have a closer match between the predicted and measured responses, two options are possible:

- Model the array with a Method of Moment (MoM) program to include the mutual coupling;
- Measure the active element pattern (only one element driven, all others matched) and use this instead of the isolated element pattern as was done.

The first option is very long to develop. This type of analysis could also have been realized with a commercial full-wave simulator such as Zeland's, IE3D® but it would not have been efficient for optimization of the 4x1 array since it is very long to simulate.

The second option is less accurate than the MoM and would have required some pattern measurements of the phased array with one element driven and the others matched. Unfortunately, this was not possible due to the fact that the system had already been dismounted after the last phased array measurement.

Therefore, the mutual coupling was measured between different pairs of elements in the passive 4x1 array of Vivaldi antennas, as shown in Fig. 3.49, to provide a qualitative discussion on its effect over the performance of the phase array system. As can be seen in Fig. 3.49, the coupling coefficients between elements decrease at higher frequencies and with elements separation. Therefore, the highest coupling levels were -12dB and -14.5 dB, observed between element #1 and #2, and between element #2 and #3 respectively at channel frequency of 10 GHz. At 12 GHz, all coupling coefficients are under –15 dB and at 19 GHz and 21 GHz, they can be neglected (under –32 dB).

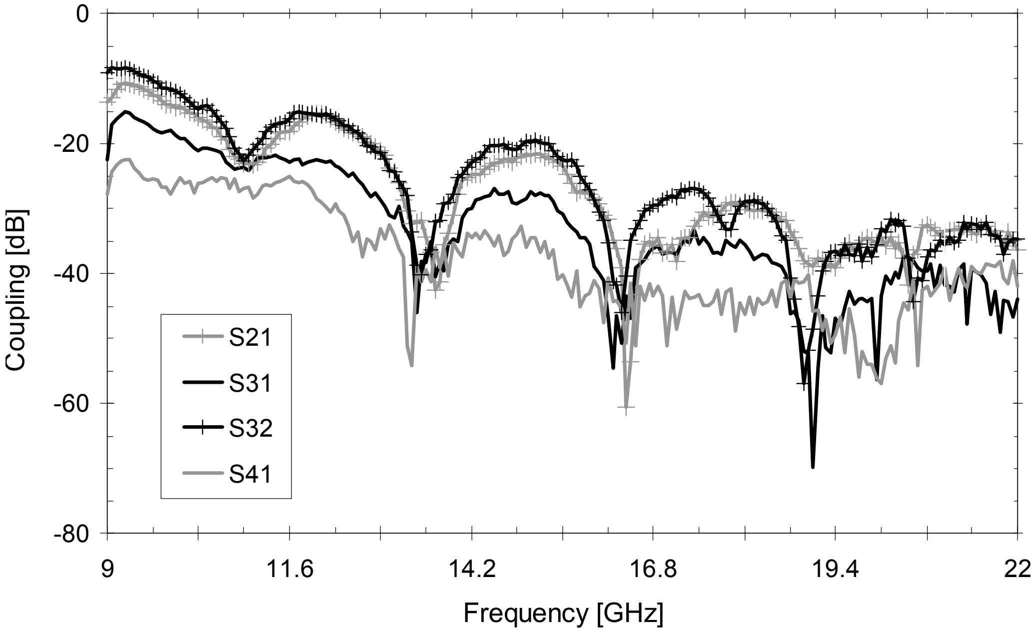

Fig. 3.49: Mutual coupling measured between elements of 4x1 array of Vivaldi antennas.

It can be concluded that the mutual coupling and the resulting sidelobes found in a small array are higher due to the finite size and edge effects. The performance could be improved by using a larger array as an increase in the number of elements gives lower sidelobe levels but new trade-offs would need to be considered for the design optimization such as prevention of scan blindness (which is generally not observable in a small array) or higher system complexity and cost.

CHAPTER IV

MICROWAVE COMPONENTS

Large antenna systems as in power transmission applications or as phased arrays require careful design at the components level to ensure high efficiency and low cost. Many specifications are met after optimization of individual units or components in the system and are rather independent on the interaction with other blocks. In the past 50 years, microwave components have progressed towards higher performance and frequency, thanks to new solid-state devices, increased precision in fabrication and compact layout techniques (such as micro-machined and multi-layer circuits), as well as faster design iterations with more accurate models. Among the numerous and most important microwave components that have been used for diverse wireless applications are the transitions that integrate two blocks using different media without sacrificing the matching. Many mass-produced and low-cost commercial applications such as intruder detectors, doppler radars (both at K-band) and collision avoidance radar (at W-band) involve the use of transitions between waveguide media and Microwave Integrated Circuits (MICs). A compact and planar transition from waveguide to microstrip antenna array, which can be doubly-conformal, need to be designed for short distance detection applications such as those enumerated above. Doubly-conformal antennas may be required within curved mounting surfaces such as automobile body. Other essential microwave components are the filters units. For bandpass operations, a certain number of resonators are required to provide a selective response. This results in large planar circuit area to accommodate the necessary resonators. The use of a multilayer configuration provides improved compactness by stacking the same number of resonators. At the same time, broadside coupling is added between resonators bringing in more design flexibility. In the next sections, the design of an efficient transition, the study of a multilayer filter and the modeling of a high-speed switch will be covered.

4.1 Design of transition for microstrip patch antenna array at W- and K-band

Characteristics such as low loss and high-power handling have promoted the widespread use of waveguides. As alternatives, microwave integrated circuits (MICs) and monolithic microwave integrated circuits (MMICs) were developed to improve reproducibility and reliability while reducing the size and cost of components and systems [15]. Trade-offs to develop a low-cost, marketable product may require the use of MICs, MMICs, waveguides or a combination of these technologies. The integration of waveguide and planar technologies requires the use of efficient transitions such as the loop transition. Two-dimensional arrays of loop transitions have been used for many past applications as antenna feeders for rectangular or circular waveguide radiators [16] and measurements have been limited to the S-band [17] and X-band [18].

In this section, the use of a rectangular waveguide feeding a microstrip patch array through two types of loop transition at K-band is demonstrated. The distribution of energy from the single feed input is realized in a planar series feeding configuration. Simulation results for the loop are obtained from a three-dimensional full-wave simulator. The antenna array is designed and optimized at 24.125 GHz. The theoretical results and the overall efficiency are verified with measurements on a K-band 8×8 planar microstrip patch antenna array. The use of a rectangular waveguide feeding through a loop transition to a microstrip patch array with series feeding configuration at W-band is also demonstrated. The loop performance optimization is based on available models [17]. The planar microstrip patch antenna array measured performance at W-band validates the theoretical results.

4.1.1 Waveguide-to-coaxial-to-microstrip transitions

The integration of waveguide and planar technologies requires the use of several types of efficient transitions such as apertures [46], probes [47] and loops [17], [18], and [48]. In this paper, a loop transition was selected to route energy from a waveguide to a planar antenna array. The choice is based on its performance and its end-launching feature. Fig. 4.1 illustrates the three different waveguide-to-coaxial transitions.

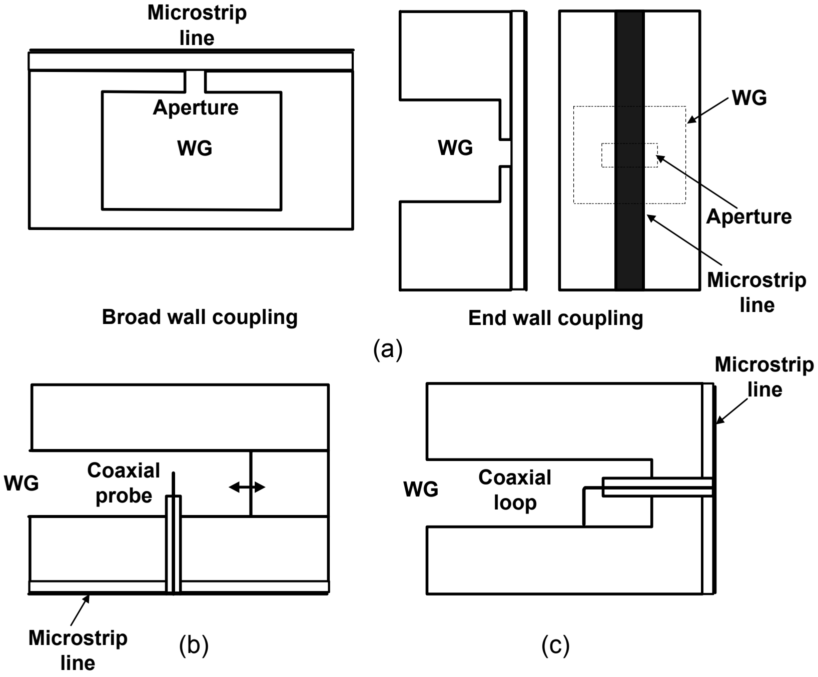

Fig. 4.1: Configuration of three types of waveguide-to-coaxial-to-microstrip transitions. (a) Aperture coupled transition; (b) electric field probe; (c) magnetic field loop.

Aperture transition requires backside registration and etching of the slot and microstrip line plus accurate alignment with the waveguide interface. The well-known electric field probe requires an E-plane waveguide bend to mate up to the waveguide in the conventional configuration. The loop provides an alternative to the slot in an aperture transition for an end-launch without the need for backside etching. As illustrated in Fig. 4.1 (c), the loop can be used to couple to microstrip in an in-line fashion from a rectangular waveguide. This optimal arrangement is particularly useful in applications where severe space restrictions from dense packaging of waveguide circuitry are imposed. Various analyses have been completed on the loop transition and some equivalent circuits have been suggested [17]. From these references, the equivalent circuit of the in-line loop transition can be found as shown in Fig. 4.2.

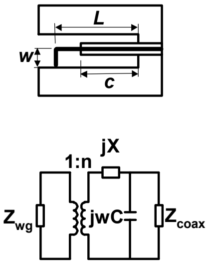

Fig. 4.2: Loop equivalent circuits.

4.1.2 Loop transitions theoretical design

In this section, the design of efficient loop transitions is described. The design steps and final dimensions for the loops at K-band and W-band are listed, and the simulation results with optimum performances are provided.

4.1.2.1 K-band loop transition

Two loop transitions, as illustrated in Fig. 4.3, are designed at 24.125 GHz using Zeland's Fidelity®, a 3-dimensionnal full-wave electromagnetic simulator.

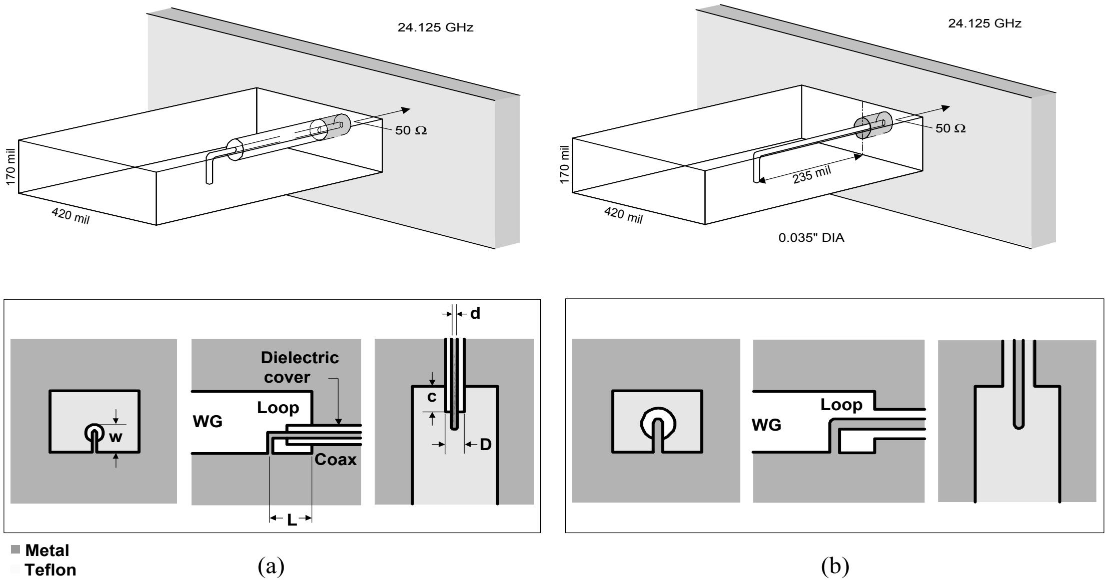

(a) (b)

Fig. 4.3: Loop configurations. (a) Loop A; (b) loop B.

The symbols used for the different dimensions are as illustrated in Fig. 4.3. a and b are the dimensions of the waveguide large and narrow walls respectively. The loop in Fig. 4.3 (a) is called loop A and uses a dielectric covered coaxial line with Teflon inserted in a WR-42 waveguide with dimensions of a = 420 mil and b = 170 mm. Loop A is difficult to mass-produce due to the small hole diameter (where the coaxial line is inserted) needed for good matching. Another more convenient loop version called B features a line without dielectric cover using the same WR-42 waveguide as seen in Fig. 4.3 (b). This loop is very easily mass manufactured because the dimensions are larger compared to loop A and since not using a dielectric cover, it can be injection-molded. The matching of the loops is achieved by varying the dimensions of the loops as given in Fig. 4.3 based on the loop transition equivalent circuit [17], [18] (see Fig. 4.2). A 50 Ω commercially available UT-47 coaxial line is used for loop A with d = 12 mil and D = 38 mil, and the outer conductor from a UT-34 is used for loop B with d = 35 mil and D = 80 mil.

4.1.2.2 W-band loop transition

The design specification is to provide a good matching of the transition at 76.5 GHz. The loop uses a dielectric covered coaxial line as illustrated in Fig. 4.3 (a) inserted in a WR-10 waveguide with dimensions of 100 mil × 50 mil. The matching is tuned by varying L, w, and c (see Fig. 4.3). The dielectric cover is necessary for mechanical support of the center conductor, which features a very small diameter at W-band frequencies. The dimensions of a commercially available 50 Ω Teflon covered coaxial line at 76.5 GHz are d = 0.11 mm for the diameter of the inner conductor and D = 0.58 mm for the inner diameter of the outer conductor.

4.1.2.3 Simulated results and observations

The optimization of the return loss (RL) was realized using Fidelity®. In order to optimize the RL at midband, different parameters can be varied on the transition structure. The tuning was done by trial and error investigating the variation of S_{11} on the Smith Chart as the dimensions and position of the loop were changed. For the K-band loop A and W-band loop transitions, the matching was tuned by varying the length of the dielectric cover. For all three loop transitions, the length and the width of the loop were tuned as well as the lateral position with respect to the waveguide center axis.

By tuning only the length of the three loop transitions while maintaining all other parameters constant (on-axis position with width of loop equal to half of narrow wall), a fairly acceptable RL for the W-band loop was achieved with 14.62 dB but more than 10 % of reflection in loop A was observed with RL = 9.535 dB. Therefore, an additional tuning dimension such as the length of the dielectric cover was varied to further improve the return loss for loop A and W-band loop. By optimizing a minimal length loop, a lower insertion loss (IL) results since there is less metallic loss but once fabricated, it is more difficult to manipulate for assembly, especially for the W-band loop. From the position of simulated RL on the Smith Chart and the equivalent circuit (see Fig. 4.2), one can fine-tune the matching by adding the required inductances and capacitances. The length of the loop mainly determines the series inductance contributing to the reactance jX of the equivalent circuit in Fig. 4.2. The shunt capacitance C varies mainly with the loop width and slightly with the dielectric cover length.

In the following sub-sections, the optimal results for K-band loop A and B, and W-band loop are shown. A summary table is also provided.

a) K-band loops

The simulated $|S_{11}|$ and $|S_{21}|$ are shown in Fig. 4.4 (a) and Fig. 4.4 (b) for loop A and B, respectively.

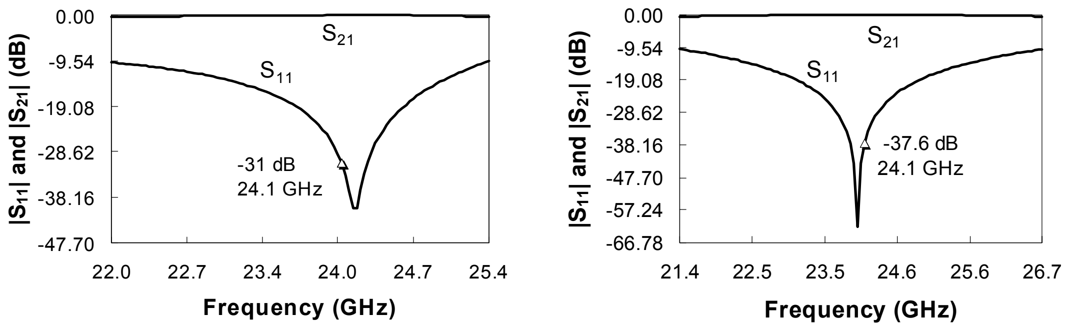

(a) (b)

Fig. 4.4: Simulated loop performance. (a) Loop A; (b) loop B.

b) W-band loop

The simulated and optimized $|S_{11}|$ and $|S_{21}|$ are shown in Fig. 4.5. At the design frequency of 76.5 GHz, the simulated return loss is 26.2 dB and the insertion loss is negligible.

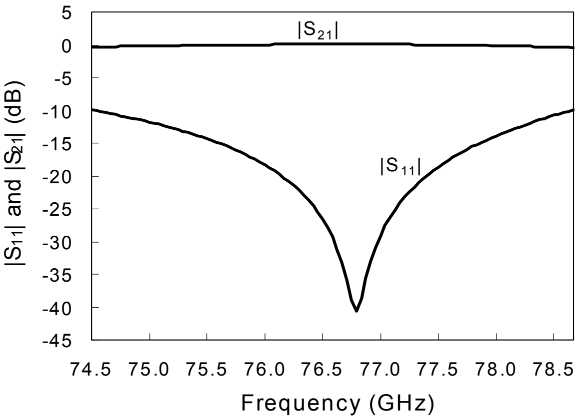

Fig. 4.5: S-parameter simulation results for the loop transition.

c) Summary

The final dimensions for all loops and optimized results are listed in Table 4.1.

Table 4.1: Dimensions and simulation results for loop A and B.

		Loop A	**Loop B**	**W-band**
Dimensions (mil)	***d***	12	35	4
	D	38	80	23
	L	209	102	94
	w	73	104	38
	c	126	-	19
Max. Insertion Loss (dB)		0.4	0.4	0.4
2:1 VSWR bandwidth (GHz)		22 to 25.4	21.4 to 26.7	74.5 to 78.5

4.1.3 Microstrip patch antenna array design and integration

A simple 64-element planar microstrip array has been designed and built by Omni-Patch Designs Inc. to be tested for the 24.125 GHz applications. The antenna operating bandwidth is from 24 to 24.250 GHz. The elements are arranged in a rectangular lattice as seen in Fig. 4.6 with a nominal spacing of 360 mil. The overall array aperture dimensions are 2.8 inches square. The distribution network feeds the array using a series-parallel configuration as shown in Fig. 4.6. The distribution network is designed to present a 25 dB taylor weighting over the face of the array. The expected half-power beamwidth in the E- and H-planes is approximately 10.8 degrees. The calculated directivity of the array is about 25 dB. The array design was etched on a 10 mil thick Rogers 5880 substrate with half-ounce rolled copper. The minimum line on the entire array is approximately 6 mil. The loop transition uses the waveguide as the feeder to the microstrip patch array. The loop center conductor feeds each half of the array symmetrically. The loop center conductor is shown in Fig. 4.6 from the antenna side. A low-cost, commercially available waveguide Gunn diode transceiver can be coupled to the planar microstrip patch antenna array through the loop transition.

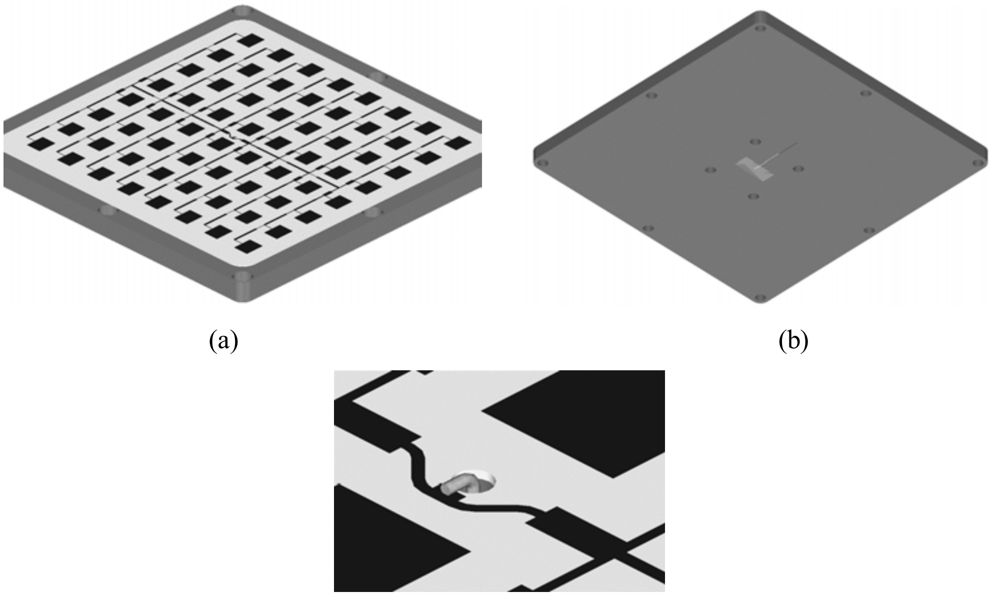

(a) (b)

(c)

Fig. 4.6: 8x8 microstrip patch antenna array fed through loop transition. (a) Top view; (b) back view; (c) detail of coaxial feed.

The complete antenna system at W-band operation is illustrated in Fig. 4.7. The patch antennas were fabricated on RT Duroid substrate 5880 with a thickness of 5 mil and $\varepsilon_r = 2.2$. The same distribution network design used for K-band operation was implemented at W-band.

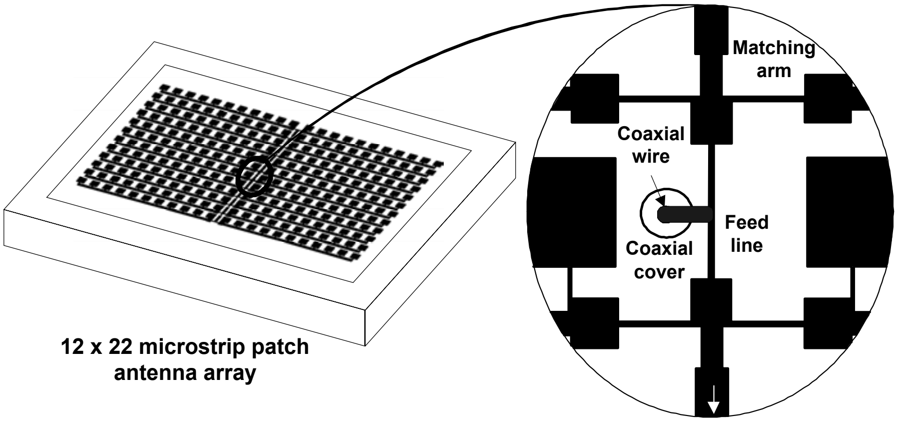

Fig. 4.7: Patch antenna array configuration.

4.1.4 Experimental results

The transition loss was measured using a back-to-back transition for loop A. The performance of the complete system was tested for the K- and W-band applications.

4.1.4.1 Transition characterization

A back-to-back loop A transition, as shown in Fig. 4.8 (back of structure), was used to measure the loss of the loop transition. A microstrip line is etched on a substrate that is grounded to the base plate. Two commercially available waveguide-to-coaxial transitions are connected to the back of the plate. These transitions were calibrated off before the measurements to exclude their loss. The measurement results are shown in Fig. 4.9. A total IL of 1.1 dB was measured. To extract a single loop transition loss, one needs to substract the microstrip line attenuation, α_c, and divide by 2 since the measurement was realized on two mirror loops. Therefore, the loop A transition loss is equal to $(|S_{21}| - \alpha_c)/2 = (1.1 - 0.35)/2 = 0.38$ dB. This loss includes the radiation leakage loss. Therefore, the designed loop is very efficient.

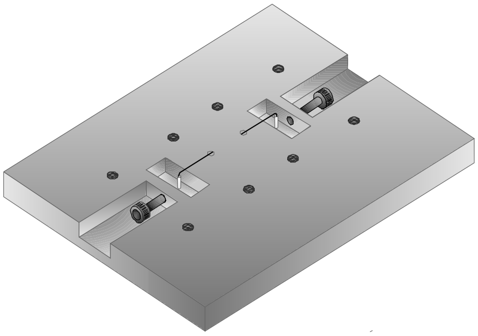

Fig. 4.8: Back-to-back fixture used to measure loss on loop A transition.

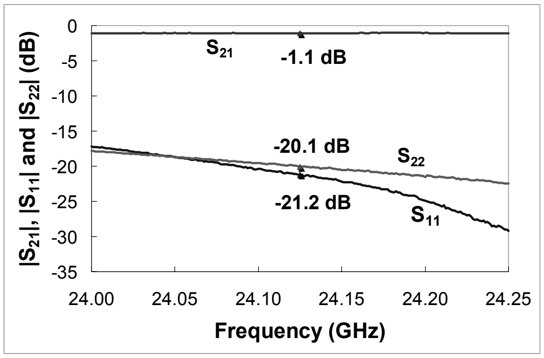

Fig. 4.9: Transition efficiency measurement.

4.1.4.2 System performance

Two antenna measurements were realized to evaluate the overall performance of the integrated system with designed loop transitions at K- and W-band.

a) K-band array

The K-band pattern measurements are performed in an anechoic chamber designed for measurements up to Ka-band antenna measurements. The array return loss is measured using a network analyzer HP8510B®. Satisfying patterns and return loss levels are obtained using loop A as illustrated in Fig. 4.10. Loop B was only studied theoretically due to the mechanical difficulties involved in fabrication to maintain the coaxial conductor suspended and centered in the drilled hole without the support of a dielectric cover. The measured system gain over frequency is above 21.5 dB from 23.7 to 24.3 with a peak of 21.6 dB at 24.1 GHz. The half-power beamwidths measure approximately 11.5 degrees in both principal planes. The good performance confirms the high efficiency of the designed loop A transition.

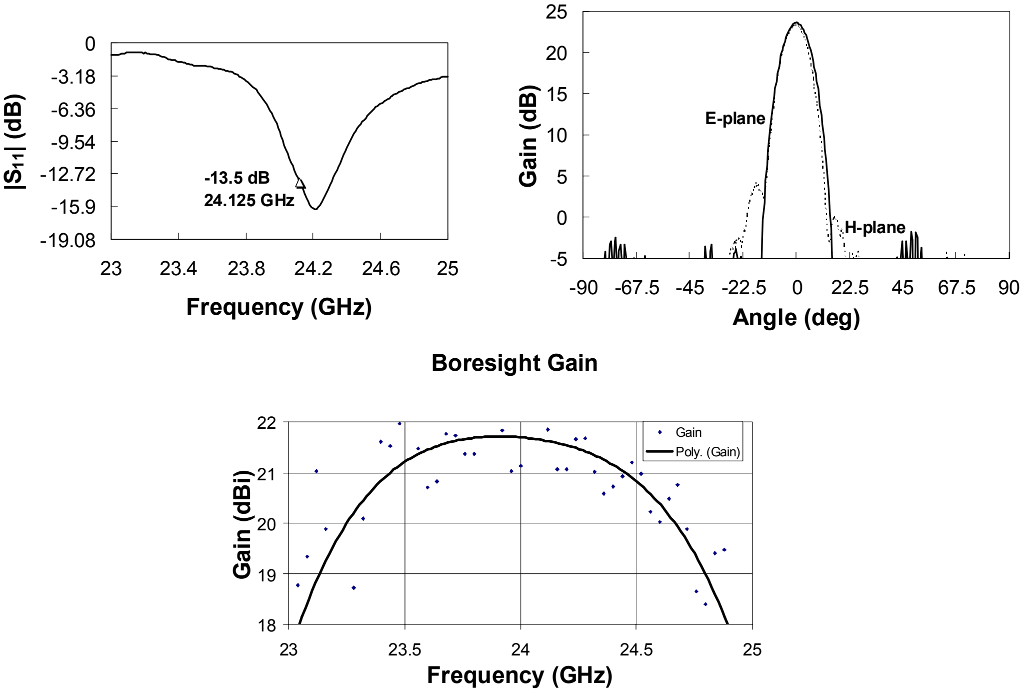

Fig. 4.10: Antenna $|S_{11}|$ and radiation patterns for loop A.

b) W-band array

For the W-band measurements of the microstrip patch antenna array, a mm-wave extension was used to multiply the frequency range of the HP8510B® test set. The gain pattern presents a maximum gain of 25 dB and the return loss is less than 12 dB from 75.1 GHz to 77.3 GHz with 22.2 dB return loss at 76.5 GHz (see Fig. 4.11). The satisfying experimental results confirm the efficiency of the loop transition and validate the simulated design.

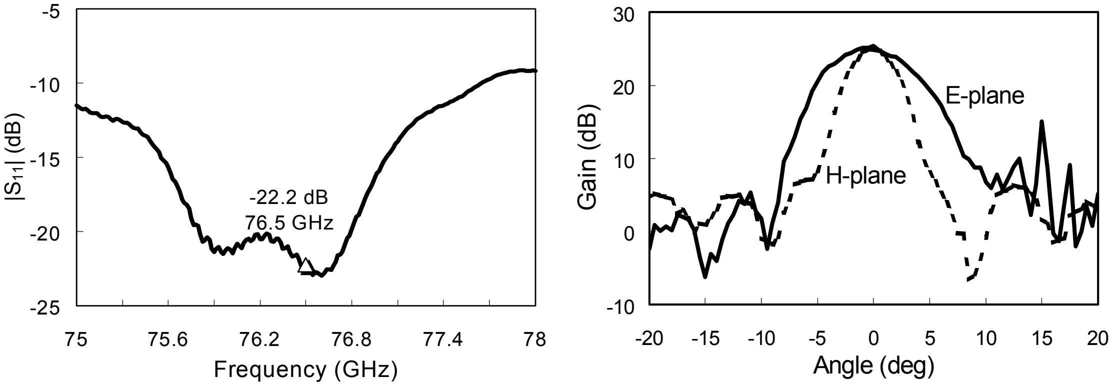

Fig. 4.11: Performance of overall system at W-band.

c) Summary of performance results

The previous experimental results are listed in Table 4.2.

Table 4.2: System performance results for K-band and W-band array.

	K-band	W-band
Broadside gain (dB)	21.6	25
2:1 VSWR bandwidth (GHz)	23.7 to 24.3	75.1 to 77.3

4.1.5 Loss budget

There is a small difference between the predicted directivity and the peak gain of the measured pattern. To explain this difference, Omni-Patch Design Inc. has provided the data in Table 4.3 with the losses involved in the K-band system that amount to the gain difference. The calculated directivity was 25 dB and the measured peak gain is 22.6 dB. In the table, the Taylor taper loss is caused by the weighted average distribution of energy used to feed to the elements. The beam broadening is calculated from the difference between the maximum gain obtained from Kraus formula for directivity in planar arrays 41,253/[$\text{HPBW}_H \cdot \text{HPBW}_E$] ($\text{HPBW}_H$ and HPBW_E are the

H- and E-plane half-power beamwidth, respectively, in degrees) with predicted and measured HPBW's. As seen from the table, the loss budget has correctly evaluated the measured gain and calculates an efficiency of 45% to the entire K-band system.

Table 4.3: Loss budget calculation.

Directivity calculation	25.1 dB	calculation
Taylor taper loss	-0.5 dB	calculation
Antenna efficiency	-0.5 dB	references, assume 90%
Line loss	-0.36 dB	calculation for microstrip lines
Loop transition	-0.38 dB	measured
Manufact. Errors	-0.3 dB	calculation
Beam broadening	-1.4 dB	approximated from measurements/calculation
Total	21.7 dB	
Efficiency	44.52%	

4.1.6 Conclusion

The demonstrated transitions provide an efficient, compact and low-cost alternative to other coupling approaches currently in use. The transitions also lend themselves well to many mass-production approaches such as casting and molding for lower per-unit costs. A K-band and W-band antenna array application was used to demonstrate the success of this approach.

4.2 Design of compact bandpass filter at 5.8 GHz

Multilayer circuits present many advantages such as broader bandwidth, high level of quality factor and compactness compared to their two-dimensional counterparts. For complex microstrip structures, multilayer media adds more versatility to the design. In filters, higher coupling between resonators gives a broader bandwidth. The broadside coupling in multilayer filters defines a strong capacitance in the equivalent circuit, which helps tune the circuit filtering characteristics.

Many types of multilayer filters have been studied in the past. For example, aperture coupled resonators that were traditionally implemented in cavities or using dielectric resonators have recently been realized using multilayer microstrip or stripline circuits [19]. When using dual-mode patch or ring resonators, the aperture allows the tuning of the coupling between the two modes by varying the length of the orthogonal slots, as seen in Fig. 4.12 (a). This design presents a large loss that is probably due to the weaker coupling between the separated resonators by the added aperture layer, as opposed to a direct broadside coupling. There is also the multilayer version of the end-coupled bandpass filter which overlaps the half-wave resonators edges with coupling resonators on other layers [20] as illustrated in Fig. 4.12 (b). This adds more poles in the stopband and zeros in the passband. The design is more compact when compared to its planar counterpart but still extends considerably in the propagation direction compared to the stacked patch or ring resonators. A folded coupled line filter as been reported in the literature that uses folded half wavelength resonators for compactness [21], as shown in Fig. 4.12 (c). Vertical metallizations are needed to connect the two coupled lines which complicates the fabrication process.

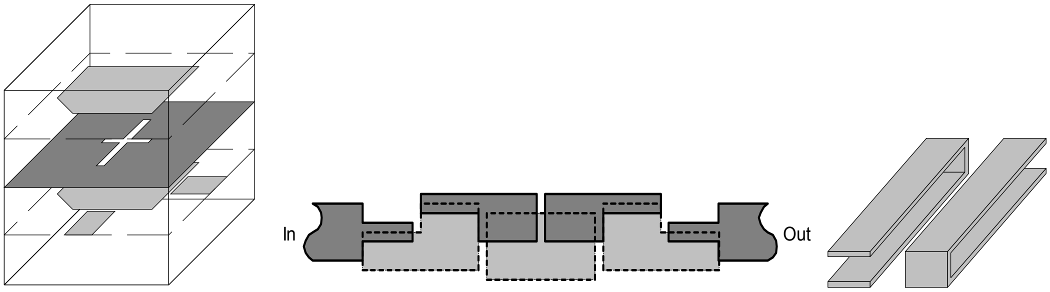

(a) (b) (c)

Fig. 4.12: Review of different multilayer filter structures. (a) Aperture coupled stripline dual-mode resonators; (b) overlap end-coupled bandpass filter; (c) broadside and edge coupled folded half-wavelength resonators.

The analysis of multilayer filters have been realized in the frequency domain using quasi-static Spectral Domain Approach (SDA) which is a full wave (and therefore very accurate) method. One drawback is that the formulation is very dependent on the geometry of the problem, which makes it less versatile [22]. The analysis has also been reported to be less accurate for gaps and open-ends in open structures such as multilayer microstrip (non-shielded). Finite Element Method (FEM) has also been used to analyze multilayer structures. A hybrid analysis based on FEM improved the conventional method to a full-wave precision and allows the calculation of the total characteristic impedance of the multilayer structure [22].

The first attempt in this study was to observe the differences between a two-dimensional two-stage square ring resonator and a multilayer stacked ring resonator implementation with same ring size and resonant frequency. Since there were no available gap-coupled square ring resonators design in the literature at the time, a custom configuration was optimized to serve as a reference for the two-layer stacked ring resonators. Then a modified multilayer folded line structure was studied and presents potential in ultra-band performance.

4.2.1 Design specifications

Besides being as small as possible, the filter had to meet several minimal performance specifications, listed as follows:

- Filter characteristics:
- Size < 19 mm x 19 mm
- Substrate material : ceramic package
- Passband: 7.25 GHz to 7.75 GHz
- Insertion loss < 3 dB
- Stopband : 7.9 GHz
- Rejection > 12 dB
- Return loss in band < 10 dB

Ceramic lamination technique allows for very thin (in the order of 0.5 mm) dielectric layer stacked filters. The choice of copper cladding should be a very thin metal strip to prevent gaps between the stacked layer. Once fabricated, the use of soft duroid on a top layer allows the filling of the gap around the metal strips by applying some pressure on it. A design with central frequency operation at 5.8 GHz will be realized while covering of the specified passband (at least from 7.25 GHz to 7.75 GHz). This frequency is used in wireless LAN, radio base station and cordless telephone.

The goals are to improve the rejection band with a deeper attenuation level, a steeper slope (, and a larger bandwidth using a larger number of stacked resonators with respect to a two-dimensional ring resonator. A larger IL should be expected due to metallization losses between different layers. Extending through the third dimension allows for a more compact design in the horizontal plane.

4.2.2 Square ring resonator

The square ring resonator as illustrated in Fig. 4.13 is studied as a basic filter block due to its geometrical simplicity and hence speed of simulation. Once the planar circuit is characterized, a planar two-stage and stacked version are investigated for comparison.

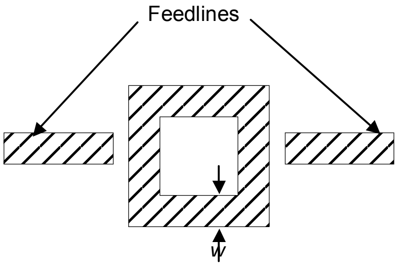

Fig. 4.13: Gap-fed square ring resonator.

4.2.2.1 Observations from a planar gap-fed single square ring resonator

To operate at a designed resonant frequency f_0, the ring resonator needs a mean perimeter of λ_g, transmission line guided wavelength. Microstrip transmission line was used for the planar version. A soft duroid substrate of dielectric constant of ε_r = 10.2 was chosen to best approximate the ceramic media (ε_r = 9.9) The square ring resonator was used to speed the simulation process with a full wave simulator (Zeland's IE3D® or Sonnet Software®) using rectangular meshing. As seen in Fig. 4.14, it was noticed that the coupling increases and the IL decreases by increasing the feedline width gap-coupled to the ring resonator. This requires an increase of the substrate thickness to preserve the *w*/*h* ratio for proper matching, where *w* is the microstrip line width and *h*, the height of susbstrate.

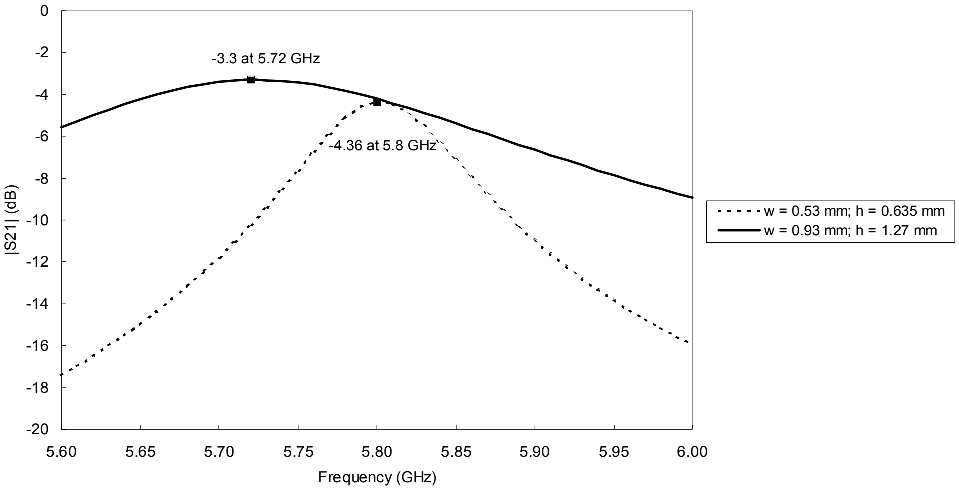

Fig. 4.14: Effect of coupling width between the feedline and the ring resonator.

When the coupling gap length (g) is increased as shown in Fig. 4.15, the IL increases, the resonant frequency (f_R)gets closer to the predicted resonance (f_0) since the ring resonator is less perturbed by the adjacent coupling and the quality factor (Q) increases. As g decreases, the IL improves and f_R becomes smaller than the resonance due to loading effect of nearby feeds. The quality factor decreases as well. Therefore there is a tradeoff between the IL, and the desired resonant frequency and Q.

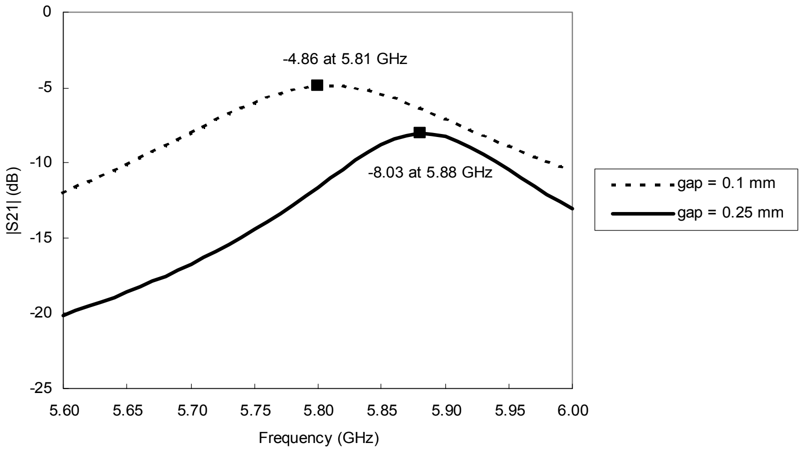

Fig. 4.15: Effect of gap between the feedline and the ring resonator.

The effect of an increase in feedlines length (fl) is a decrease of the IL, of the f_R (higher than f_0) and a decrease of Q, as seen in Fig. 4.16. By including extra feedline length, some inductance is added to tune S_{11} closer to a 50 Ω match. In this case, there is a tradeoff between the matching and IL versus the designed f_0 and quality factor.

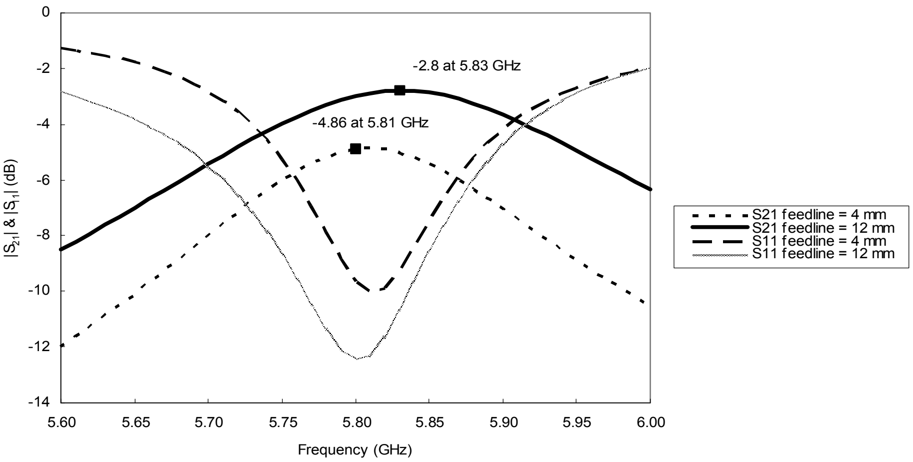

Fig. 4.16: Effect of feedline lengths on coupling and return loss.

We also noticed that with a low dielectric constant, IL degrades since there is more radiation leakage (antenna effect).

4.2.2.2 Observations from two-stage ring resonators

To improve the coupling and selectivity of the filter, a double resonator approach was used. This was realized by connecting two square ring resonators in series, as seen in Fig. 4.17. As the separation between the two coupled rings (g_r) is increased, the two resonance peaks get closer and the coupling is reduced. Ideally the gap between them should be as small as possible but we are limited by the etching tolerance of 0.1 mm. Fig. 4.18 illustrates the filter response ($|S_{21}|$ and $|S_{11}|$) with respect to the separation between the two square ring resonators.

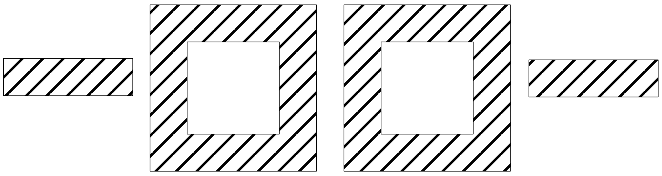

Fig. 4.17: Two-stage square ring resonator.

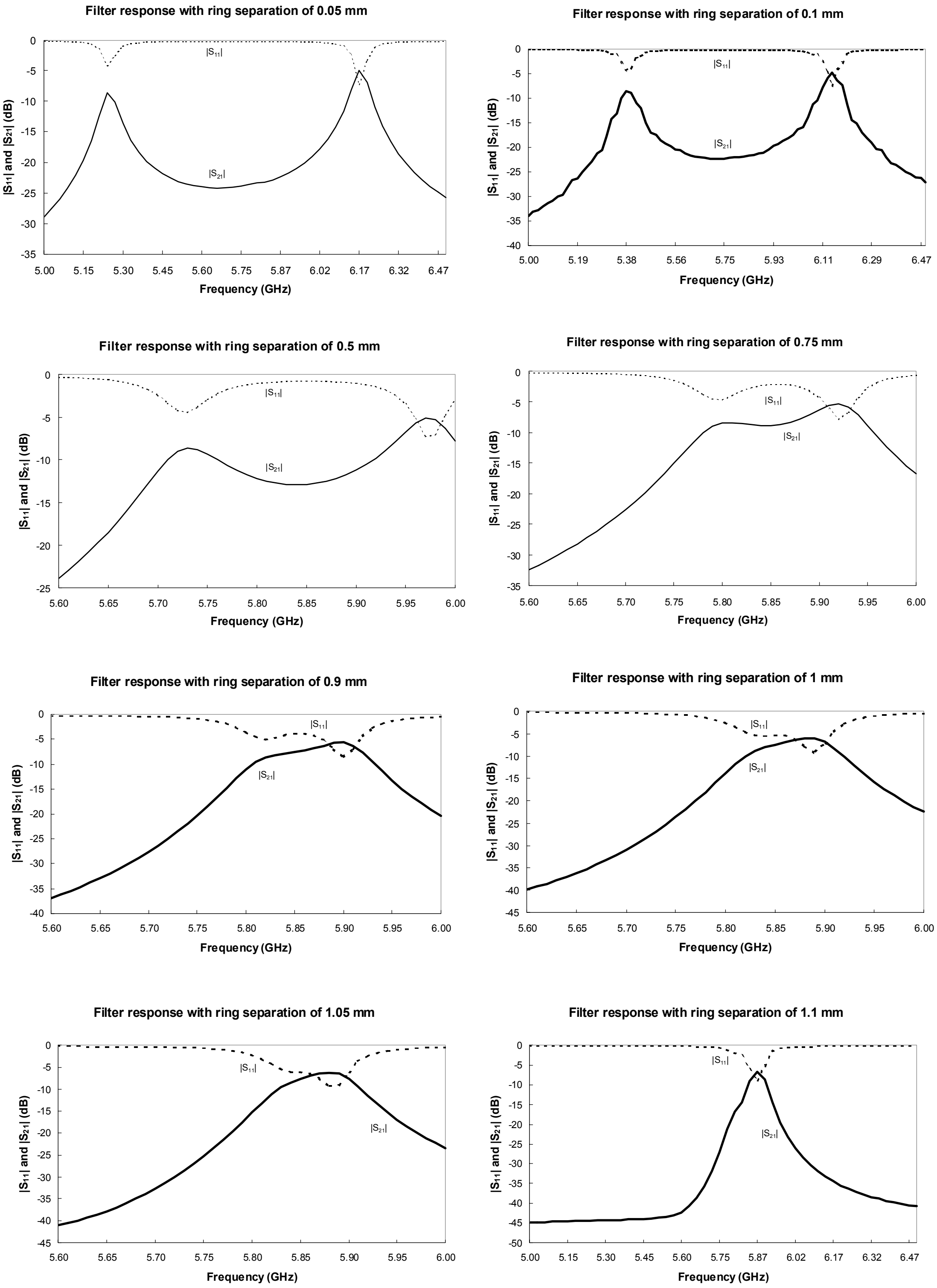

Fig. 4.18: Filter response of the two-stage square ring resonator with separation.

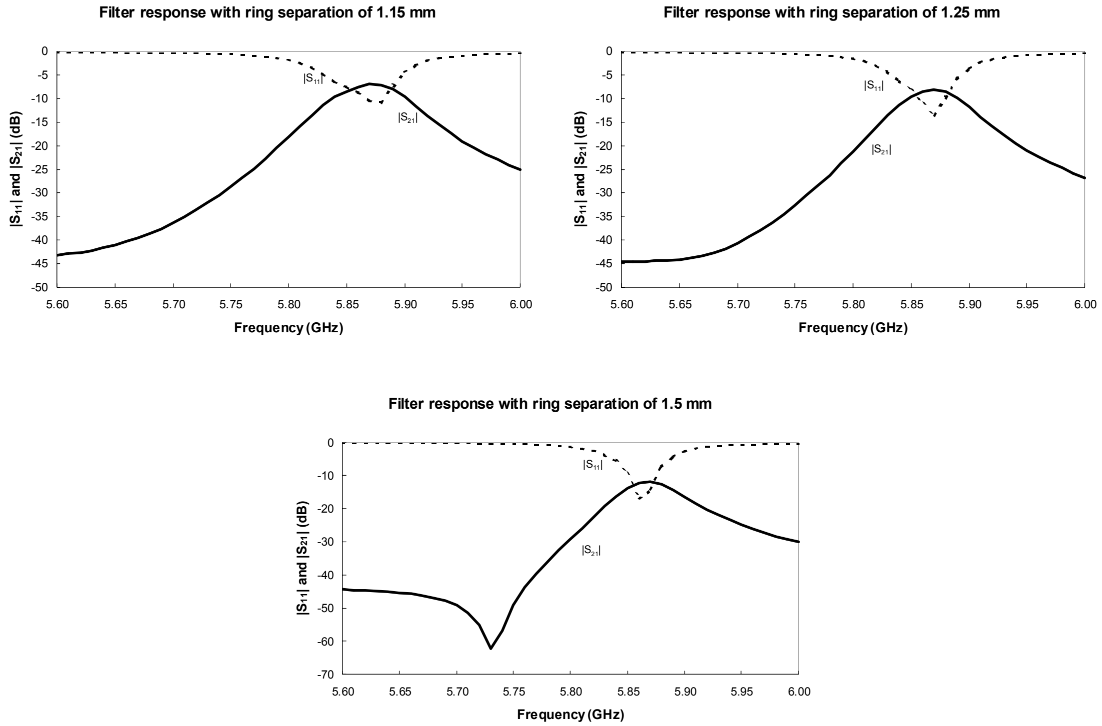

Fig. 4.18: (con't).

Also, when the spacing between resonators is very small, the resonance frequency decreases as if the ring had twice the length of the single resonator.

An optimized single square resonator with tuning stubs was developed by a member of our research group, Lung-Hwa Hsieh [49]. Two instances of this resonator has been used to implement a direct coupled two-stage filter (see Fig. 4.19). It was noticed that this filter presents a steeper slope than the single resonator version since a larger number of poles have been added by the second resonator (see Fig. 4.20). The sharpness of the knee can be improved by strategically locating the couple pole-zero around the inflexion point. The rejection band seems to have enlarged considerably by more than two times at a 20 dB attenuation level.

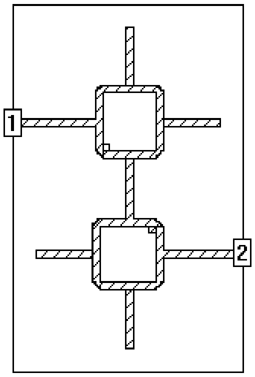

Fig. 4.19: Two-stage filter using an optimized square ring resonator.

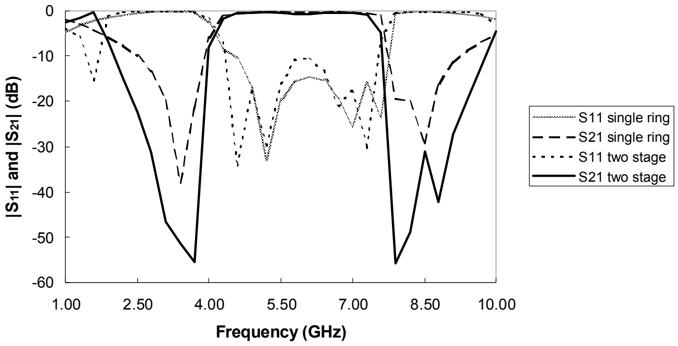

Fig. 4.20: Ring filter performance comparison.

Optimized single square ring resonator and two-stage direct coupled ring resonator filter.

4.2.2.3 Observations from multilayer filters simulations

Stacking two square ring resonators will require that the matching be tuned since it does not correspond exactly to a microstrip line mode. When stacked without any offset, the resulting IL will increase due to a loose coupling. When the top layer layer is shifted laterally, more capacitances are added providing a higher degree of coupling as seen on Fig. 4.21. The corresponding frequency response is also shown in Fig. 4.21.

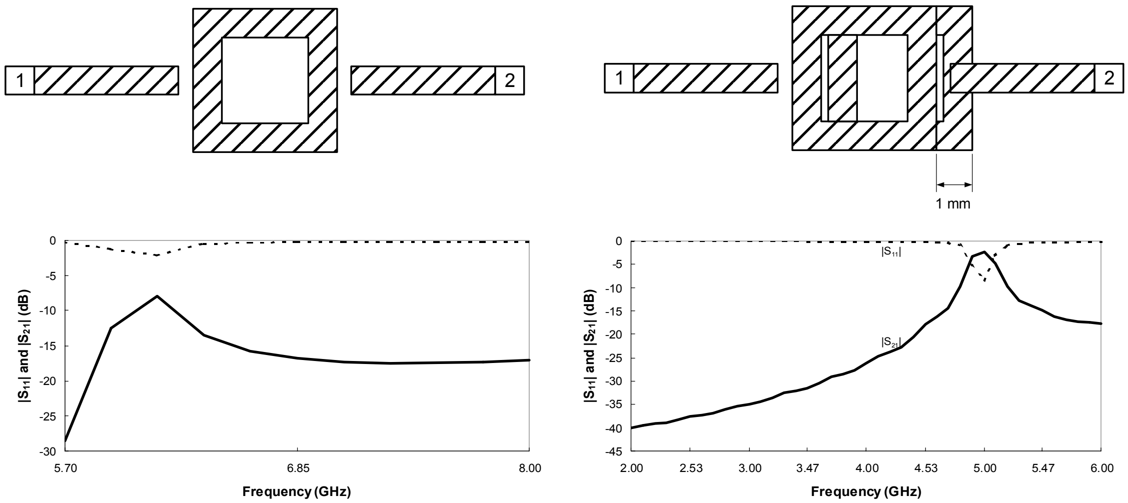

(a) (b)

Fig. 4.21: Two stacked ring resonators and corresponding filter response. (a) Without lateral offset, (b) with lateral offset.

Using the same dielectric constant for both layers fixed at 10.8 and varying the height, it was found that for both layers with same height of 0.635 mm, a good coupling was achieved at a value slightly higher than the predicted resonance frequency. Also, for a smaller second layer height (h_2), the coupling is higher and the resonance frequency gets closer to the predicted value. By further reducing the thickness of the second layer, the coupling continues to increase but the frequency start decreasing from the resonance value. So there is a threshold for the optimum thickness of the coupling layer. As we reduce the coupling layer's height, the IL and RL improve, and the bandwidth (BW) increases (see Fig. 4.22 for a comparison of the frequency responses).

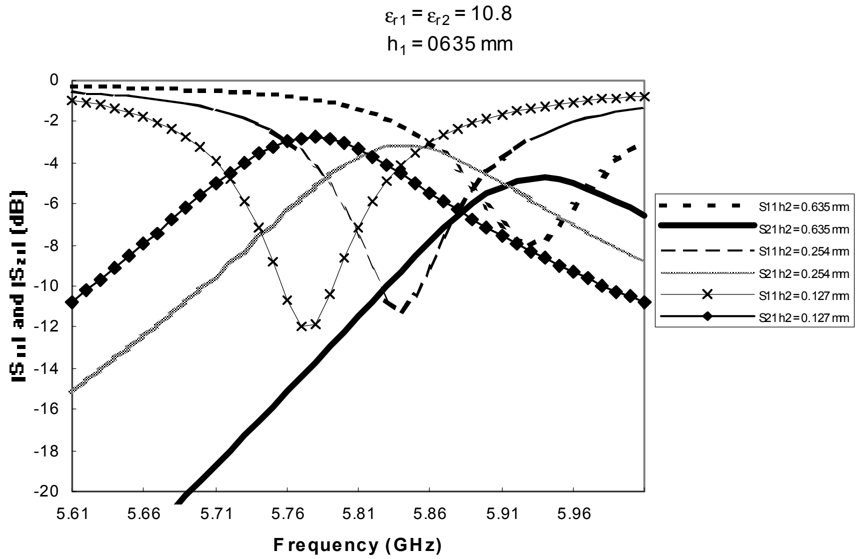

Fig. 4.22: Comparison between stacked ring resonators using different substrate heights.

By using a low dielectric constant for the coupling layer (ε_{r2}) with the same height for both layers, the same level of coupling as that with a thinner coupling layer is obtained. However, the resonance frequency is closer to the predicted value with the thinner coupling layer (see Fig. 4.23).

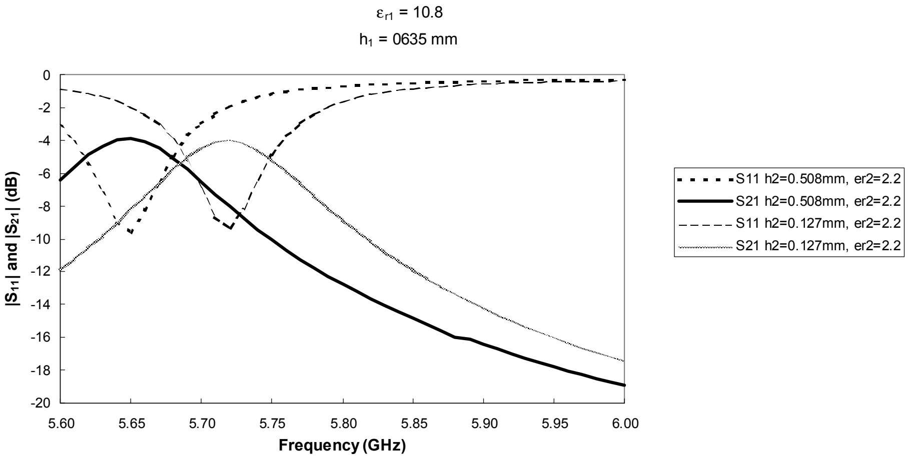

Fig. 4.23: Stacked ring resonators for different substrate heights and dielectric constants.

When using three layers instead of two, the coupling is similar to that obtained with a two-layer filter but the resonant frequency for the three-layer filter is closer to the predicted value. The bandwidths are comparable (see Fig. 4.24).

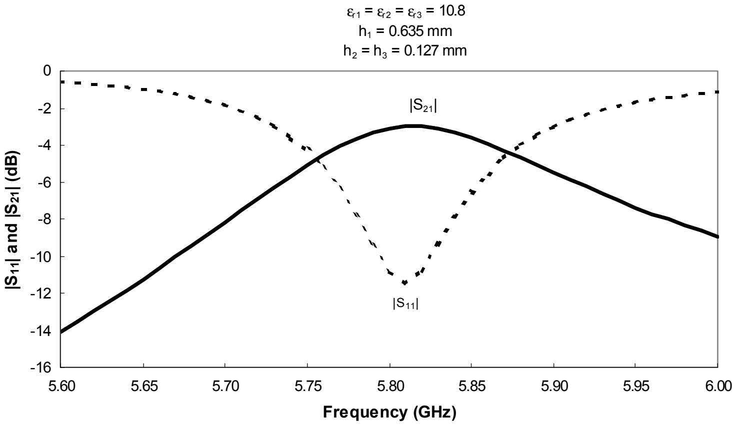

Fig. 4.24: Filter response for three stacked ring resonators.

Measurements on stacked ring resonators were realized to study the effect of adding a number of layers on the filter performance. Up to 5 layers were stacked using a substrate with $\varepsilon_r = 2.2$ and $h = 20$ mil over the first layer with feedlines and $\varepsilon_r = 10.2$ and $h = 50$ mil. The measurements were very sensible to applied pressure on the stacked pile and on the alignment of coupled resonators. Fig. 4.25 shows the measured frequency response of stacked ring resonators with a varying number of layers.

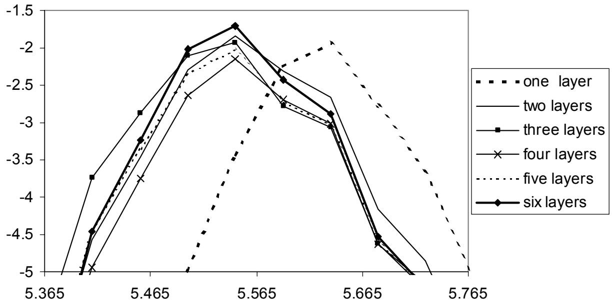

(a)

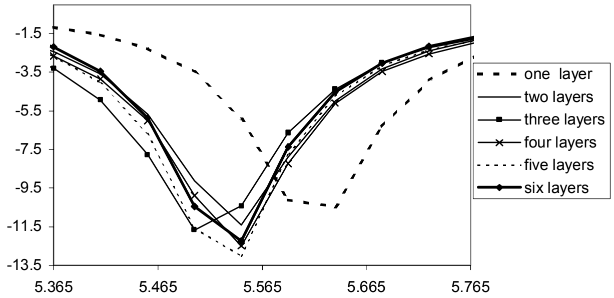

(b)

Fig. 4.25: Frequency response of stacked square ring resonators vs. number of layers. (a) IL; (b) RL.

These measurements compare well with the previous theoretical simulations. As the layers are stacked up to four, the IL decreases, as was predicted in Fig. 4.21 (a). However, an improvement in the IL is observed when stacking five and six layers. More coupling is observed with a slight increase in bandwidth as the layers get stacked. A lower dielectric constant and smaller height were used for the stacked layers to facilitate the coupling between resonators. This change in substrate characteristics with respect to the first layer caused a shift in the resonant frequency is observed. This is due to the mismatch created by the discontinuity in the propagation media. The same effect was reported in the simulation result of Fig. 4.23.

The optimized single square resonator (see Fig. 4.19) was stacked to compare performances, as shown in Fig. 4.26. It was found that by adding a second layer, the passband starts splitting when the height of the coupling layer is decreased. This is caused by the addition of a pole at the break point. The height and dielectric constant of the coupling layer can be varied to move the location of the pole towards the end of the passband. By increasing the thickness of the coupling layer (thus reducing the coupling shunt capacitance), the pole moves to higher frequencies as expected for a small pole value (see Fig. 4.27).

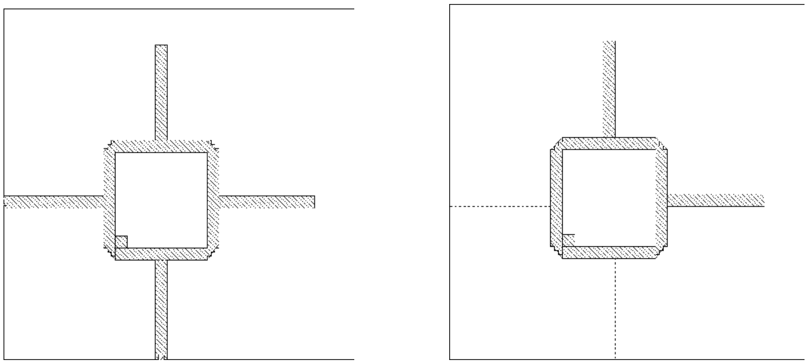

(a) (b)

Fig. 4.26: 3D configuration of stacked optimized square ring resonator. (a) First layer; (b) second layer.

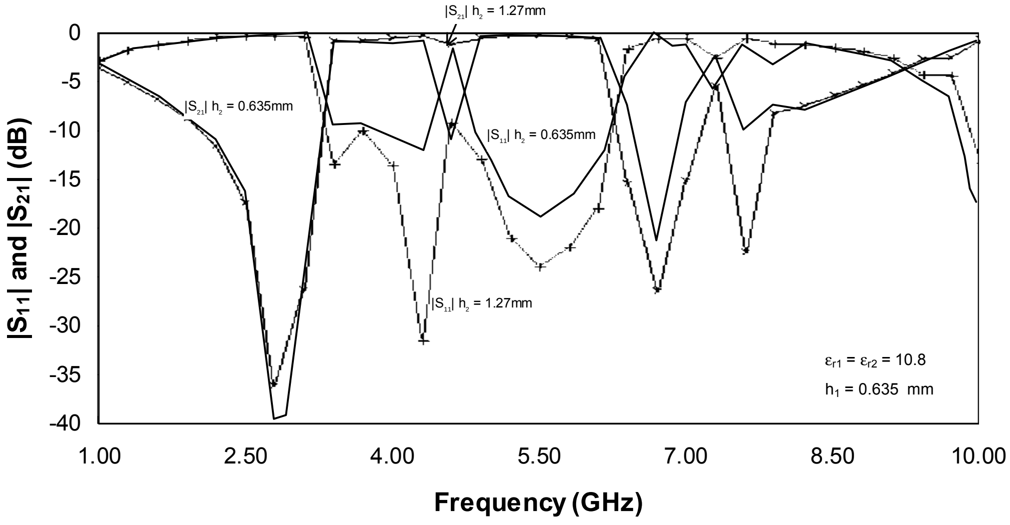

Fig. 4.27: Comparison between two stacked ring resonators with different coupling heights.

Although this design has not been optimized (the substrate and square rings parameters would need to be tuned and their effects studied), it can be seen that by adding a broadside coupling, the inflexion point at the passband ends is sharper than for the 2D design (see Fig. 4.28).

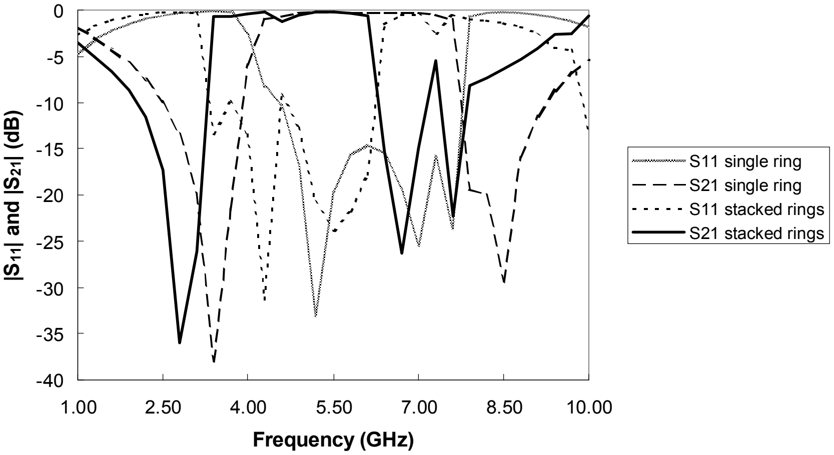

Fig. 4.28: Planar vs. 3D ring filter performance comparison.

Optimized single square ring resonator and two-layer stacked ring resonator filter.

Table 4.4 summarizes the first order effects of the geometrical parameters of the ring on the frequency response that have been describes in this section.

4.2.3 Multilayer folded line filter design

The multilayer folded line filter as shown in the two-layer layout of Fig. 4.29 is based on the half-wavelength coupled line filter. To reduce the length of a high degree filter (large number of resonators), broadside coupling and folded lines can be used. By keeping the total resonator length equal to a half wavelength, the resonance frequency is predictable and the number of resonators can be increase in the vertical direction to prevent the filter area from expanding. This configuration translates into a complex equivalent circuit, which allows more flexibility for the tuning of the passband parameters.

Table 4.4: Effects of geometrical parameters of ring resonators filters.

	Single square ring	**Two-stage ring filter**	**Multilayer filter**
IL ↓	w ↑ g ↓ fl ↑ ε_r ↑	g_r ↓	offset ↑ h_2 ↓ ε_{r2} ↓
BW ↑	w ↑ g ↓ fl ↑	Need to adjust poles to optimal position	h_2 ↓ ε_{r2} ↓
$\boldsymbol{f_R \approx f_0}$	g ↑	g_r ↑ to optimal value	h_2 ↓ to optimal value

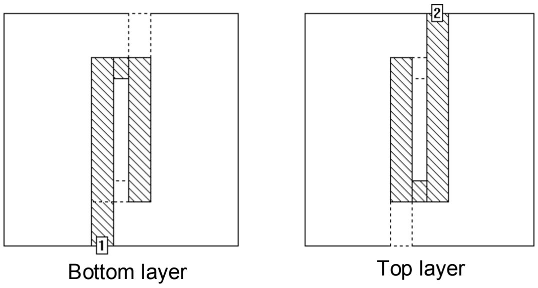

Fig. 4.29: 3D configuration of multilayer folded line filter.

The multilayer folded line filter was fabricated using $\varepsilon_r = 2.2$, and $h_1 = h_3 = 20$ mil (top and bottom substrates) and $h_2 = 10$ mil (center substrate) with top and bottom ground planes. The measured results are shown in Fig. 4.30. The multilayer design is more compact in area because of the folding. The bandwidth also broadens considerably from 2.5 to 7.5 GHz.

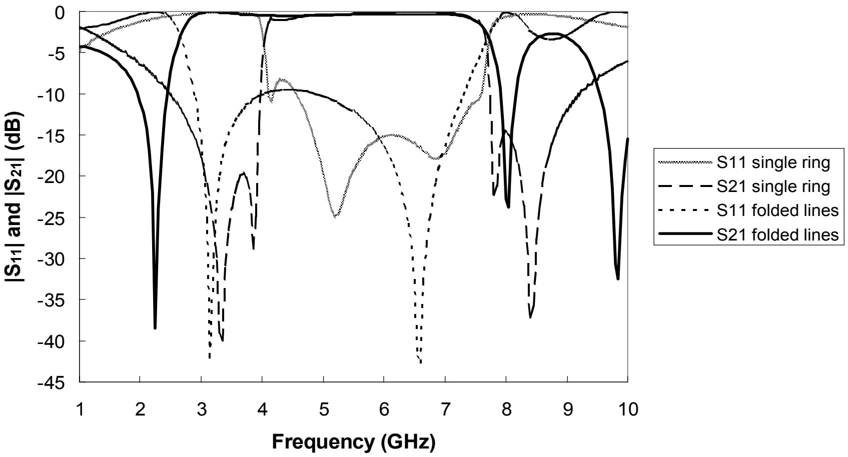

Fig. 4.30: Planar ring vs. 3D folded line filter performance comparison. Optimized single square ring resonator and two-layer folded line filter.

As a future optimization step, the rejection band would need to be enlarged and the inflexion point sharpened. One solution would be to enclose the printed circuits filters since those present a better out-of band rejection. Transmission zeros strategically located contribute to improve the rejection. In the next section, a model for the folded line is proposed to help optimize the filter characteristics.

4.2.4 Suggested model for multilayer folded line

The location of the poles and zeros provided by the shunt capacitances (and series inductances of the transmission line lengths) and series capacitances respectively controls the width of the band, the sharpness of the knee and the steepness of the slope. Fig. 4.31 shows the layout of a non-folded two-layer end-coupled filter with the corresponding cross section and equivalent circuit.

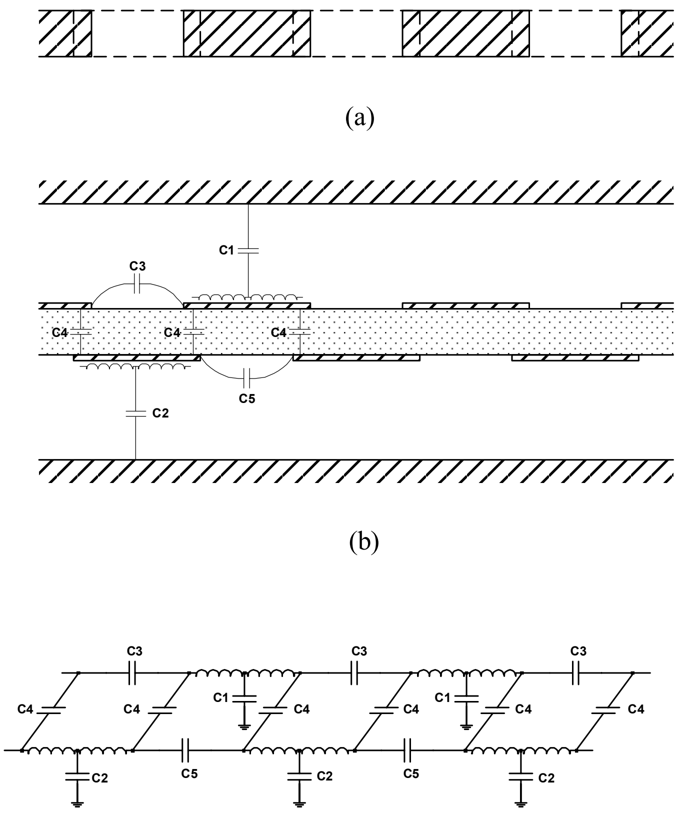

(a)

(b)

(c)

Fig. 4.31: Two-layer end-coupled half-wavelength resonators. (a) Layout; (b) cross section; (c) equivalent circuit.

From the equivalent circuit schematic, C1 and C2 are poles, and C3 and C5 are transmission zeros. C4 controls the coupling between the two layers and contributes in making the slope steeper. C4 is a combination of edge fringing capacitances and a plate capacitance from the overlapped region. For a sharper knee, a pole-zero couple needs to be placed strategically around the inflexion region. For a large rejection band, a couple of zeros with close values are located at the beginning of the rejection band and another zero is placed very far to define a large attenuation band. The zeros are mainly controlled by the coupling gaps between the resonators and the widths of the lines. In order to place a zero at the high end of the rejection band, the gaps need to be increased so that C3 and C5 are lowered. To increase the coupling between the two layers and thus increase C4, high dielectric constant values need to be chosen as well as small substrate heights. The coupling area also enhances C4 but this would perturb the frequency and the matching of the filter due to the fixed dimensions of the resonance length and the width of the lines.

For the location of the poles, the dielectric constant and height of substrates between the metallic traces and the top/bottom ground planes of the enclosed box can be varied. In general, thick substrates and high dielectric constants are used to confine the electromagnetic fields inside the substrate. However, the dielectric constant is restricted to a value close to the ceramic dielectric constant of 9.9 (required in the specifications). Fig. 4.32 presents the implemented folded line filter and Fig. 4.33 shows the equivalent circuit using a combination of transmission lines and lumped elements.

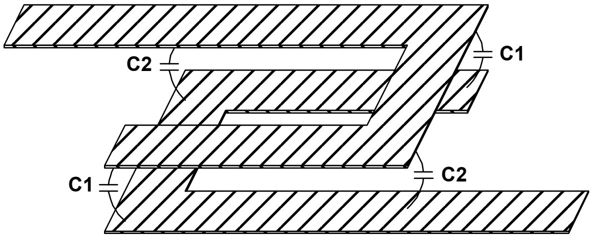

Fig. 4.32: Folded line filter with equivalent shunt capacitances.

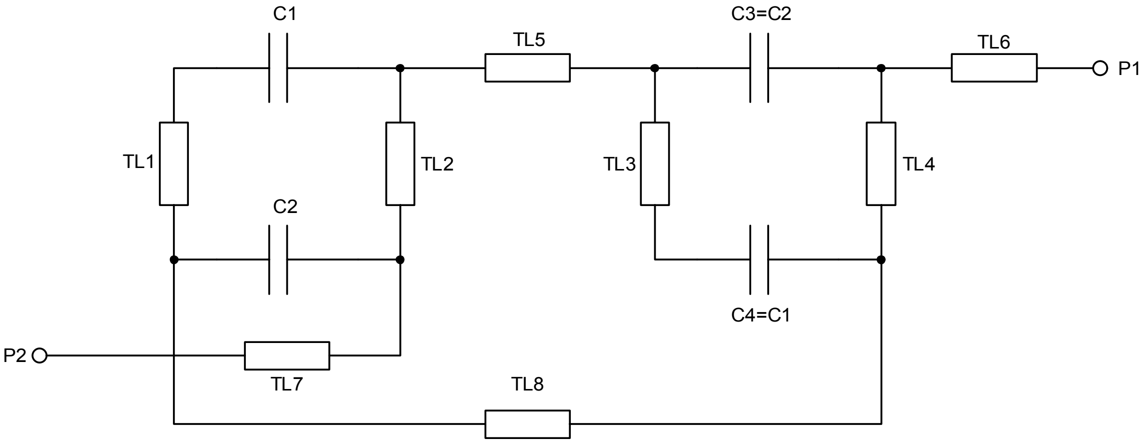

Fig. 4.33: Equivalent circuit of the folded line filter.

4.2.4.1 Study of geometrical parameter effect

Fig. 4.34 presents the layout of the folded line with its cross-section. The dimensions shown will be varied to study the effect of the geometrical parameters on the frequency response. Table 4.5 lists the dominant effects of important geometrical parameters for the understanding of the model behaviour. The "+" sign indicates that a large variation of the corresponding dimension is needed to observe an appreciable effect on the response. L_T represents the total length of the folded line taken at the center of the width.

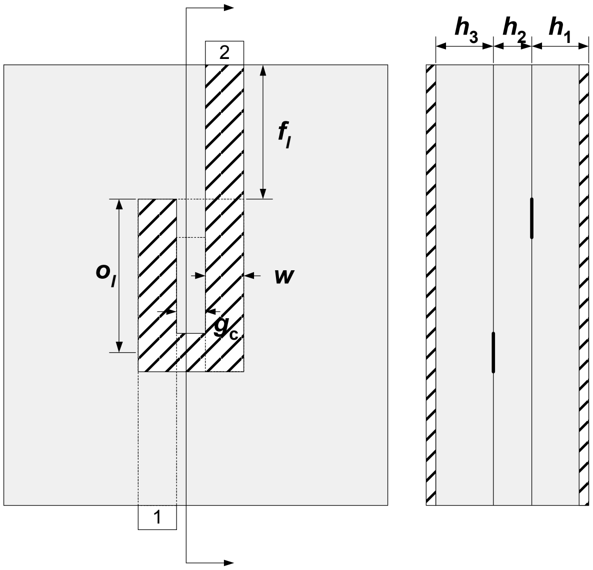

Fig. 4.34: Layout and cross-section of two-stacked folded line filter.

Table 4.5: Dominant effects of geometrical parameters of folded line filter.

	BW	**IL**	f_R	**Rej. band**	**Rejection**	**Selectivity**
$f_l \downarrow$		$\downarrow (\uparrow^+)$				$\downarrow^+$
$f_l \uparrow$		$\uparrow$		$\downarrow$	$\downarrow$	
$g_c \downarrow$ **or** $\uparrow$			$\uparrow$			
$h_1 (= h_3) \downarrow$	$\downarrow$	$\uparrow$		$\uparrow$		
$h_1 (= h_3) \uparrow$	$\uparrow^+$					
$h_2 \downarrow$	$\uparrow$				$\downarrow$	
$h_2 \uparrow$	$\downarrow$	$\uparrow$			$\uparrow$	
$o_c \downarrow$	$\uparrow^+$		$\uparrow$			
$w \downarrow$ (L_T **cst,** $g_c \uparrow$)	$\downarrow$				$\downarrow$	$\downarrow$
$w \uparrow$		$\uparrow$	$\uparrow$			
$b_w \downarrow$				$\uparrow$		

The last parameter in Table 4.5, b_w, signifies the width of the bend as shown in Fig. 4.35. It can be a smooth or straight-line variation.

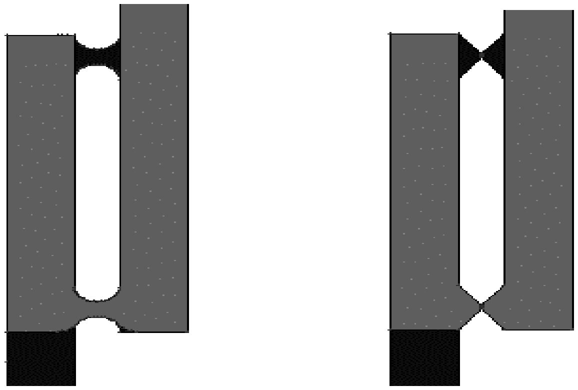
(a) (b)

Fig. 4.35: Reduction of bend width, b_w. (a) Rounded; (b) straight-line variation.

The decrease in f_l, produces less metallic loss but can be realized to a limit to which there is not enough length for the EM signal to stabilize (as a rule-of-thumb, length of couple of wavelengths is safe). The change of height has also been studied by setting different variations for h_1 and h_3. It was found that if h_3 is set to a very large value to reduce the effect of the top ground plane, the BW increased and rejection band decreased if h_1 increase in a very marked way. An optimal h_1 would be needed to meet the two specifications.

4.2.4.2 Optimization of folded line frequency response

In this section, the tuning of the frequency response was realized in order to mainly increase the rejection band and the selectivity at the high end while maintaining a large bandwidth, low IL high rejection level in the stopband.

a) Modified shaped of the folded line configuration

Different alternate versions of the folded line filter layout were simulated to study the effect of the configurations on the performance. For example, it was observed that some shape changes had almost no effect on the performance such as mitering the corners around the bend of the folded line to reduce the fringing parasitical effect. On the other hand, create a gap discontinuity in the bend, as small as could be was very detrimental to the frequency response. A very degraded response was also generated when placing the two feed lines on the same plane. These two last versions of folded line were discarded since they did not present some potential for further optimization.

Orthogonal feeds were also studied. The resulting performance was a function of the coupling area. Fig. 4.36 and Fig. 4.37 show the studied configurations with a small level of broadside coupling and a larger level of coupling. The broadside coupling regions are circled. As seen, a larger coupling is required for bandwidth enlargement. The response illustrated in Fig. 4.37 is still not very selective, mostly at the low-end and would require more optimization.

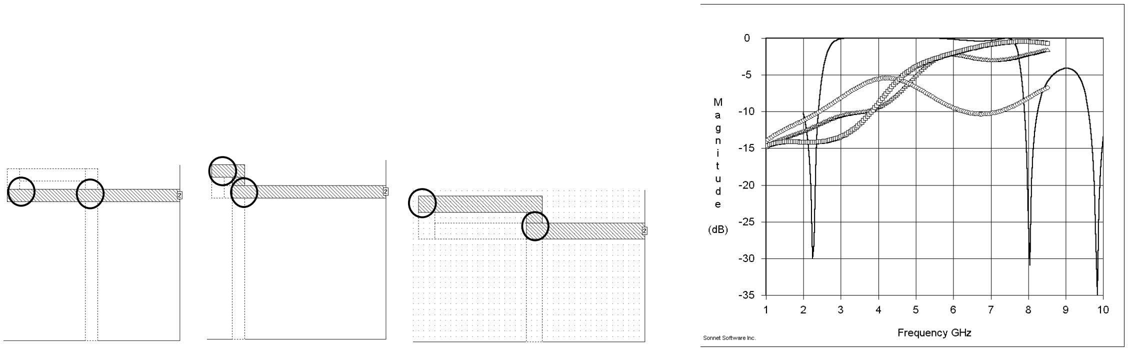

Fig. 4.36: Orthogonal feeds configuration with low broadside coupling and poor performance.

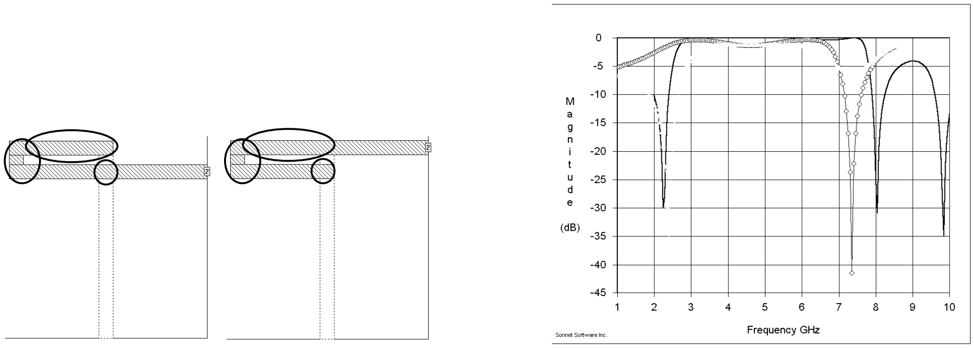

Fig. 4.37: Orthogonal feeds with larger broadside coupling and improved performance.

b) Improvement of frequency response by addition of stages to unit folded line cell

To increase the selectivity on both sides of the frequency response, a two-stage folded line configuration was simulated, as shown in Fig. 4.38 with corresponding frequency response. Some tuning was done by varying the separation between the two resonators. The bandwidth is maintained with a second stage and a larger rejection band and selectivity is obtained on both ends as predicted. Some optimization is needed to increase the level of rejection in the stopband region. Fig. 4.39 and Fig. 4.40 present the layouts and performances of a folded line filter with harmonic suppression on the high end using a low-pass filter at one end and two low-pass filters at each end. The version with only one low-pass filter at one end present a lower IL since less conductor metallization is included. All three of these modified versions of the folded line basic unit present potential for optimization and characterization.

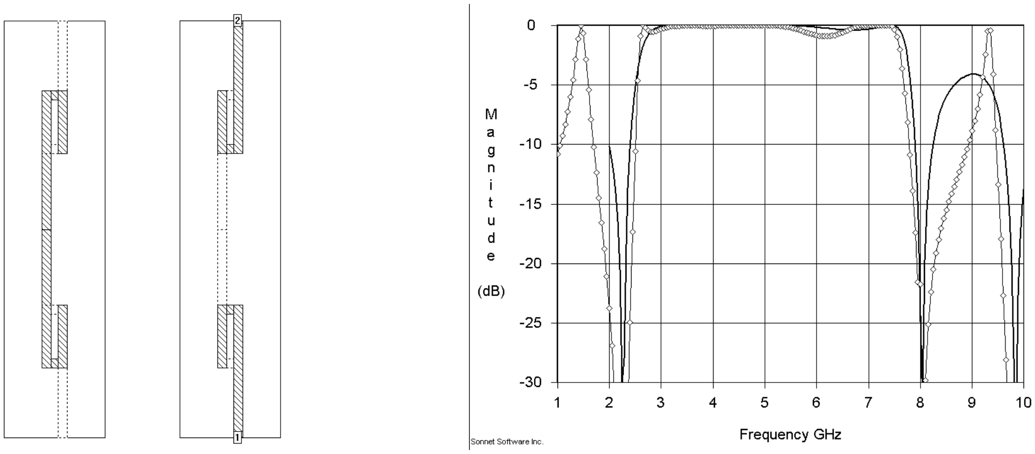

Fig. 4.38: Two-stage folded line filter layout.

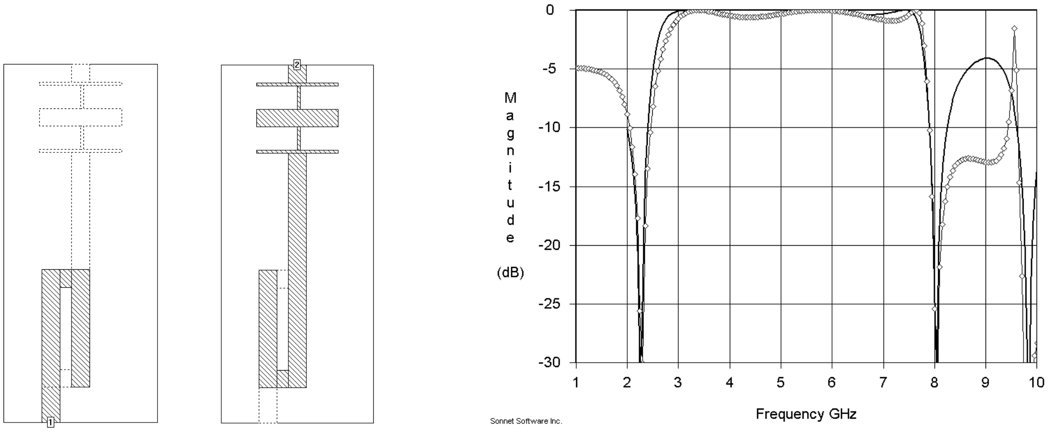

Fig. 4.39: Low-pass filter added to one end of folded line filter.

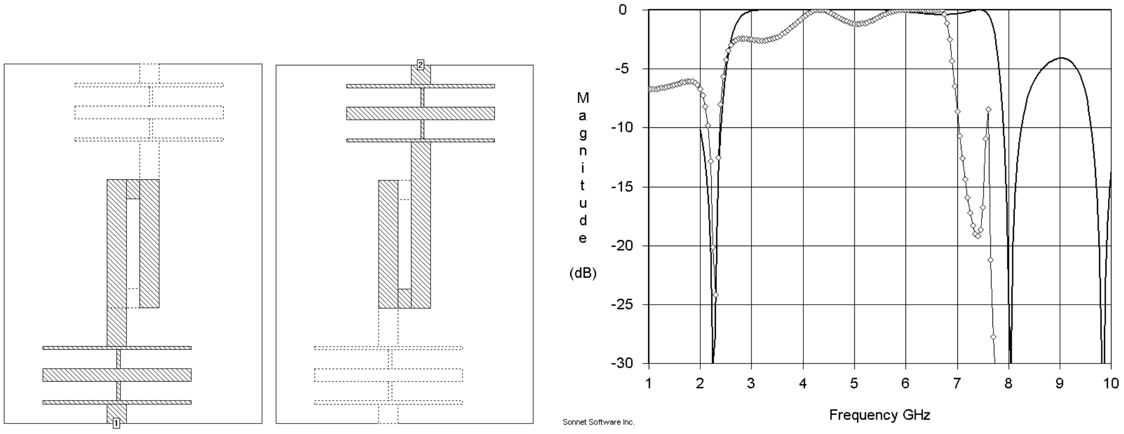

Fig. 4.40: Low-pass filter added to two ends of folded line filter.

Other configurations were simulated to supress the out-of-band harmonic levels such as a Photonic Bandgap (PBG) ground for the low-end improvement. Unfortunately, due to the large amount of meshing involved with this layout simulation (periodic holes in the ground with printed area of folded lines on top), the optimization run-time was not practical. Therefore, this configuration was dropped.

4.2.5 Conclusions

From the study of the effects of stacking square ring resonators in a vertical direction, many general trends have been observed, as listed in Table 4.4. However, multilayer design is complex due to the large number of parameters involved, which allows more versatility in the tuning for performance optimization. It was found that by adding harmonic suppression stages to the folded line resonator, the rejection band and selectivity were improved while maintaining a large bandwidth and a low IL.

4.3 Study and optimization of symmetrical three-terminal FET switch model

The design of digital phase shifters for high frequency phased array systems requires accurate switch models over a broadband range. The FET switch follows conventional layout rules for GaAs integrated circuits [23]. A model can be created from carefully studying the layout topology. In order to obtain initial values for the model parameters, one needs to use theoretical analysis in conjunction with empirical data [24]. The main objective of this research is to optimize the fitting and simplify the preliminary model for a three-terminal intrinsic FET switch. Feed models should be created for each terminal in the switch. The original three port switch model with physical line lengths defining the FET intrinsic length was documented for 18 different FET sizes. A symmetrical equivalent circuit was used to model odd number of fingers FET. This allows a reduction in the number of variables since the drain and source parameters become equal. The physical line length consists of half of the FET length on the drain and source port for symmetry. Since the purpose of the switch is to be used in a phase shifter application, the phase of S_{21} is the most important parameter to fit. The desired characteristics of the model are a large scalability and broadband fitting. The goal is to obtain a phase fitting error of less than ±2° over the entire range of frequencies and scaling. Moreover, the magnitude fitting error for S_{21} should be kept under 5%.

4.3.1 General optimization approach

The development of an accurate and scalable model requires a methodical approach. A spreadsheet was created to calculate the scaled parameters used as starting values for a new FET size optimization and to evaluate the errors between scaled and fit values. For each FET size, the errors from the scaled model and fitted model were compared. This provided insight on the sensitive model parameters. It also made apparent the need for an improved model configuration for better phase fitting, which was mainly realized by adding transmission line lengths at the drain and source ports. A second step was to optimize this improved model with starting FET size of 3x100. Then, all the other switch sizes were incrementally scaled from the 3x100 and optimized. More details about the scaling methodology will be provided in section 4.3.6. The third step was to generate new models with much simpler configuration by eliminating the non-sensitive parameters identified from the previous scaling study. After each model was optimized in Libra, their performance metrics were extracted and compiled into summary graphs.

4.3.2 Switch and feed networks models definition

Fig. 4.41 illustrates the three terminal symmetrical switch model using physical line lengths on the drain and source ports of half the FET intrinsic length. All the parameters used in this section are as illustrated in Fig. 4.41.

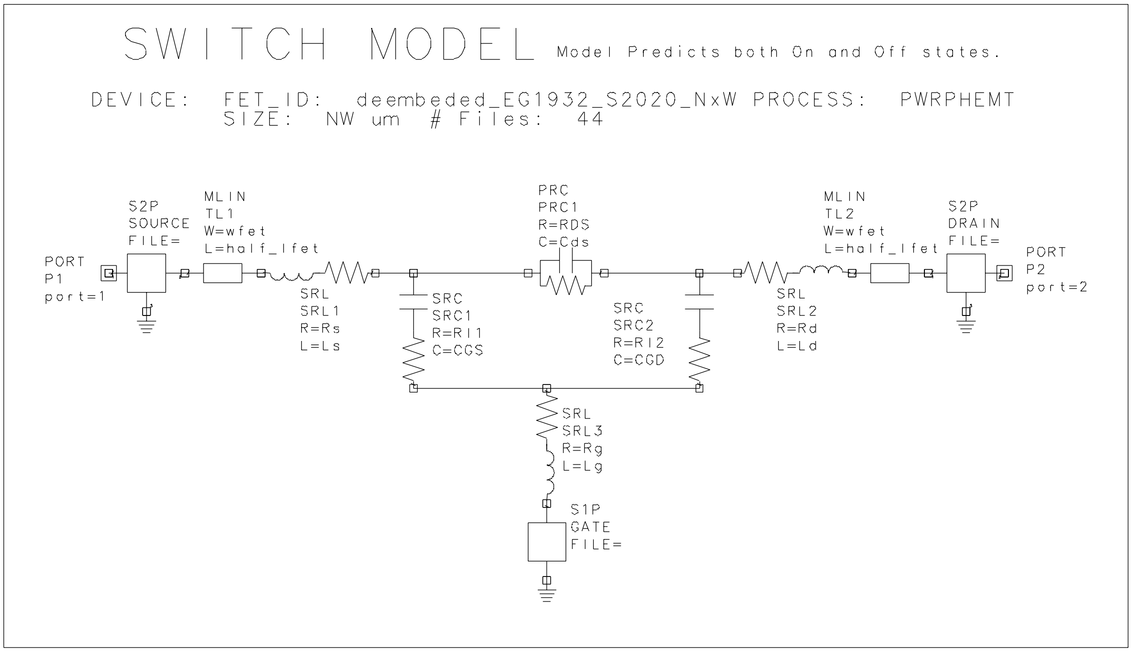

Fig. 4.41: Switch three terminal symmetrical model.

The common state (ON and OFF) parameters are Rg and Rs (or Rd). The bias dependent parameters are Cg, Ri, Rds and Cds. The feed networks (before the data deembedding for the drain and source ports) were modeled for each FET size from its layout. In Fig. 4.42, Fig. 4.43, and Fig. 4.44, the feed networks models are given for the 3x100 case. As seen in Fig. 4.44, a gate finger bus was added in parallel to the input port on the gate feed network to improve the fit for larger FETs in particular. The results were compared to the case without a second gate bus. The model with a second gate bus provides a more physical description. The second bus to the gate feed did not produce a very large difference, except for S_{21}_on magnitude and phase. The dimensions were taken from the layout of an actual wafer, which is shown in Fig. 4.45.

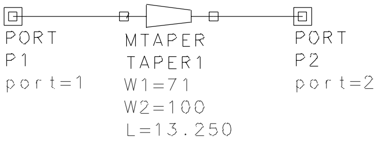

Fig. 4.42: Source feed network.

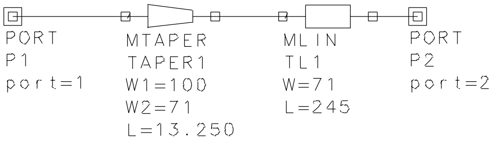

Fig. 4.43: Drain feed network.

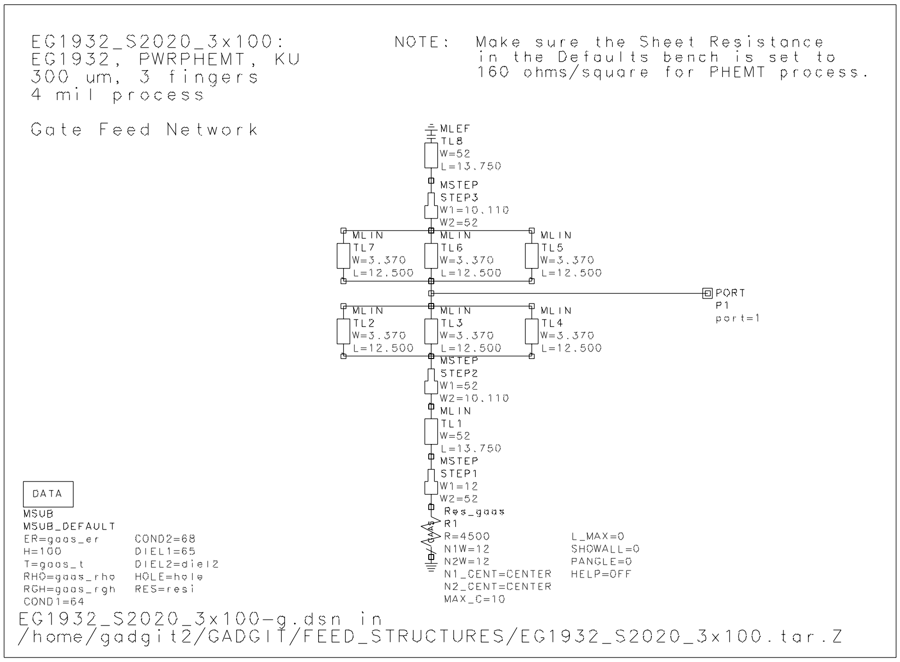

Fig. 4.44: Gate feed network.

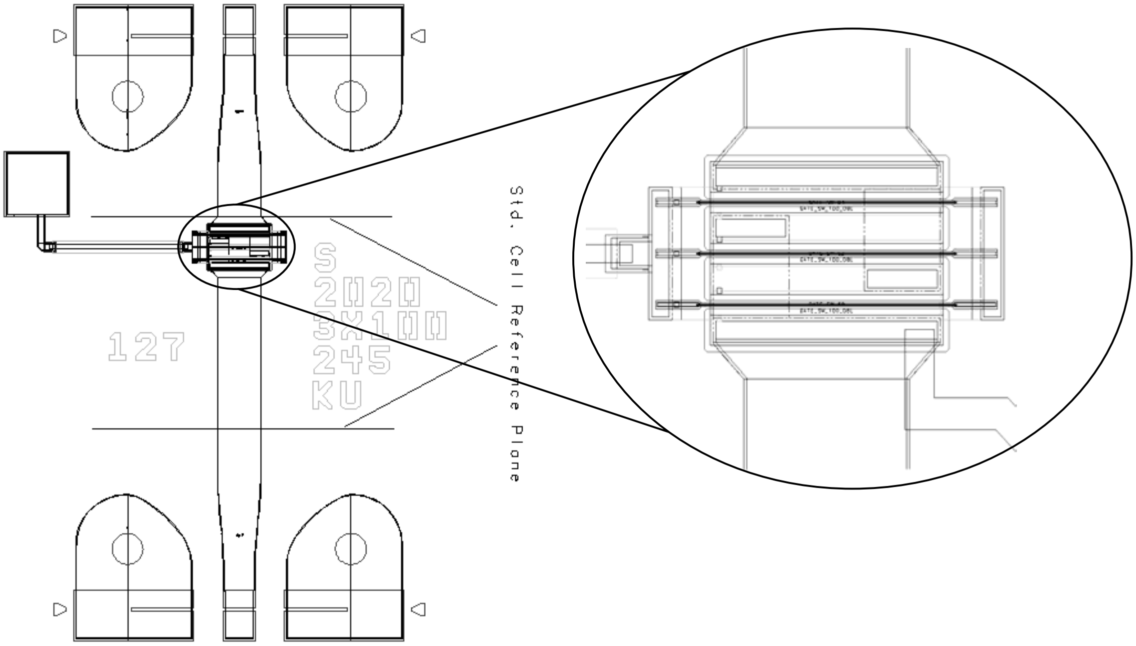

Fig. 4.45: 3x100 layout.

4.3.3 Libra simulation setup

Fig. 4.46 provides the entered equations for calculation of fitting errors of various performance parameters. These parameters will be used for the definition of optimization weights. In order to use the gradient optimizer with unconstrained variables, it is necessary to have the values made positive using absolute values.

To automatically optimize the parameters for each FET size, a customized feature for Libra developped by TriQuint called Handtune was used. In order to update the optimized parameters in each data file, the original scripts from the switch project directory were modified to consider a symmetrical model. The Cds parameter bias was made dependent to improve the simultaneous fit of S_{21} for the ON and OFF states. Some Perl scripts were modified to take into account the change in Cds.

```
Zin_meas_on=(1+(measure1\S11))/(1-(measure1\S11))
Zin_mod_on=(1+(model1\S11))/(1-(model1\S11))
Zout_meas_on=(1+(measure1\S22))/(1-(measure1\S22))
Zout_mod_on=(1+(model1\S22))/(1-(model1\S22))
z11meas2=(1+(measure2\S11))/(1-(measure2\S11))
z11mod2=(1+(model2\S11))/(1-(model2\S11))
z22meas2=(1+(measure2\S22))/(1-(measure2\S22))
z22mod2=(1+(model2\S22))/(1-(model2\S22))
phase_on_s11=(model1\S11)/(measure1\S11)
phase_on_z11=(Zin_mod_on)/(Zin_meas_on)
phase_on_s12=(model1\S12)/(measure1\S12)
phase_on_s21=(model1\S21)/(measure1\S21)
phase_on_s22=(model1\S22)/(measure1\S22)
phase_on_z22=Zout_mod_on/Zout_meas_on
mag_on_s11=100*(mag(model1\S11)-mag(measure1\S11))/(mag(measure1\S11))
mag_on_z11=100*(mag(Zin_mod_on)-mag(Zin_meas_on))/(mag(Zin_meas_on))
mag_on_s12=100*(mag(model1\S12)-mag(measure1\S12))/(mag(measure1\S12))
mag_on_s21=100*(mag(model1\S21)-mag(measure1\S21))/(mag(measure1\S21))
mag_on_s22=100*(mag(model1\S22)-mag(measure1\S22))/(mag(measure1\S22))
mag_on_z22=100*(mag(Zout_mod_on)-mag(Zout_meas_on))/(mag(Zout_meas_on))
opt_err1_Z11=mag(((Zin_mod_on)-(Zin_meas_on))/(Zin_meas_on))
perc_err1_Z11=100*opt_err1_Z11
opt_err1_s11=mag(((model1\S11)-(measure1\S11))/(measure1\S11))
opt_err1_s12=mag(((model1\S12)-(measure1\S12))/(measure1\S12))
opt_err1_s21=mag(((model1\S21)-(measure1\S21))/(measure1\S21))
opt_err1_Z22=mag((Zout_mod_on-Zout_meas_on)/Zout_meas_on)
perc_err1_Z22=100*opt_err1_Z22
opt_err1_s22=mag(((model1\S22)-(measure1\S22))/(measure1\S22))
phase_off_s11=(model2\S11)/(measure2\S11)
phase_off_s12=(model2\S12)/(measure2\S12)
phase_off_s21=(model2\S21)/(measure2\S21)
phase_off_s22=(model2\S22)/(measure2\S22)
mag_off_s11=100*(mag(model2\S11)-mag(measure2\S11))/(mag(measure2\S11)
mag_off_s12=100*(mag(model2\S12)-mag(measure2\S12))/(mag(measure2\S12)
mag_off_s21=100*(mag(model2\S21)-mag(measure2\S21))/(mag(measure2\S21)
mag_off_s22=100*(mag(model2\S22)-mag(measure2\S22))/(mag(measure2\S22)
opt_err2_Z11=mag(((Zin_mod_off)-(Zin_meas_off))/(Zin_meas_off))
perc_err2_Z11=100*opt_err2_Z11
opt_err2_s11=mag(((model2\S11)-(measure2\S11))/(measure2\S11))
opt_err2_s12=mag(((model2\S12)-(measure2\S12))/(measure2\S12))
opt_err2_s21=mag(((model2\S21)-(measure2\S21))/(measure2\S21))
opt_err2_Z22=mag((Zout_mod_off-Zout_meas_off)/Zout_meas_off)
perc_err2_Z22=100*opt_err2_Z22
opt_err2_s22=mag(((model2\S22)-(measure2\S22))/(measure2\S22))
```

Fig. 4.46: Equations for calculation of fitting errors of various performance parameters.

4.3.4 Effect of parameters on model fit

Table 4.6 summarizes the observations drawn for the switch parameters from the numerous optimizations. The relative level of effect of each parameter on the fit is measured by fixing all other parameters. The most sensitive parameters have been highlighted. It was found that Rg, Ri_on, Ri_off and Rds_off had no significant effect on the model fit.

Table 4.6: Effect of parameters on switch model fitting.

Model parameter	**On state**				**Off state**			
	Re(Z_{11})**	**Im(Z_{11})**	**|S_{21}|*****	**$\angle S_{21}$°**	**Re(Z_{11})**	**Im(Z_{11})**	**|S_{21}|**	**$\angle S_{21}$°**
Rg	N	N	N	N	N	N	N	M
Rs*	**L**	N	**L**	N	M	N	M	M
Ls*	N	**L**	N	**L**	N	M	N	M
Lg	N	N	N	N	N	N	N	N
Cg_on	N	**L**	**L**	**L**	N/A			
Ri_on	N	M	M	N				
Rds_on	N	N	**L**	N				
Cds_on	**L**	N	M	N				
Cg_off	N/A				N	N	N	N
Ri_off					N	N	N	N
Rds_off					N	N	M	M
Cds_off					N	N	M	**L**

L: large
M: moderate
N: negligible
*: Rd=Rs and Ld=Ls for this symmetrical model with odd number of fingers FET.
**: Z_{22}=Z_{11} since symmetrical input/output ports after deembedding drain line.
***: S_{12}=S_{21} because using reciprocal switch model.

The most probable reason for the negligible effect of Rg is that it is absorbed by the large resistor of 4500 ohms in the gate feed network. As Rg increases significantly (to the order of magnitude of the gate feed resistor), the phase of S_{21}_off starts to be affected.

The optimized value of Rs tends to be very small. It mainly affects the level of $|S_{21(12)}|$. An increase in Rs lowers the magnitude level of $S_{21(12)}$ and vice-versa. This effect is not as apparent for S_{21}_off since Rds_off dominates. Rs seems to help slightly once all S-parameters have been optimized to fit the magnitude of S_{21}_off. A small effect is also observed on the phase of S_{21}_on (as Rs decreases, better fit at higher frequency). As Rs increases, the phase of S_{21}_off degrades (changes in slope) but the effect is small. Rs also helps in fitting the real part of S_{11}, S_{22}. Rs does not really affect the phase of S_{11}, S_{22} since a reactive element would be required to contribute to the imaginary part of S_{11}, S_{22}. When Rs is fixed to 0, a very large trade-off between the real part of $S_{11}(_{22})$ and the level of the magnitude of S_{21}_on is observed. Since Rs is very sensitive to the magnitude of S_{21}_on, it needs to be constrained in a tight range.

Ls (or Ld) affects the phase of S_{21} in the opposite direction of that of S_{11}. A trade-off exists also between the curvature of the magnitude and the phase of S_{21}_on as Ls is varied. The phase of S_{21}_off is affected moderately by this inductance. Ls and Ld vary with opposite signs and reach relatively small values. By fixing Ld equal to Ls for the symmetrical switch model, the value tends to be close to 0. If Ls is close to 0 then it might not affect the fit that much. When Ls is set to 0, the fitting results are very similar to those obtained with a finite value of Ls, mostly for the transmission parameters. The elimination of this parameter is to be considered since it does not scale appropriately with any revised scaling method. Lg does not seem to affect anything in the fit so it can be forced to be 0.

Cg_on is a very sensitive parameter. It controls the slope of $|S_{21}|$ and, to a smaller degree, the phase of S_{21}_on in opposite direction. A decrease causes the slope of $|S_{21}|$ to flatten. Cg_on affects the imaginary part of Z_{11}, Z_{22}_on within a range of values.

Ri_on controls the magnitude of S_{21}_on in a very slight manner. Ri_on also affects moderately the slope of $|S_{21}\text{\_on}|$ when it reaches large values. As Ri_on increases, the slope of $|S_{21}\text{\_on}|$ becomes steeper. Ri_on also affects the imaginary part of S_{11} and S_{22}_on when increased within a range of relatively large values. As Ri_on decreases, the slope of the magnitude of S_{21}_on decreases as if Cg_on was decreasing. This can be explained by a distributive effect of Cg that starts to appear at higher frequencies as Ri is shorted.

Rds_on mostly controls the magnitude of S_{21} and S_{12}_on as does Rs. An increase of Rds_on greatly affects the real part of $S_{11\ (22)}$. (as it increases, it moves S_{11} to off state I/O parameters location).

Cds_on has almost no effect on S_{21}_on. In order for it to be effective as in the off state, Ri_on needs to be very large or Rds_on needs to increase but then the level of $|S_{21}|$ decreases. A large Rg also helps making Cds_on more sensitive. Cds_on affects Z_{11} as well. When Cds_on is increased within a certain range, the real part of S_{11} increases as shown in Fig. 4.47.

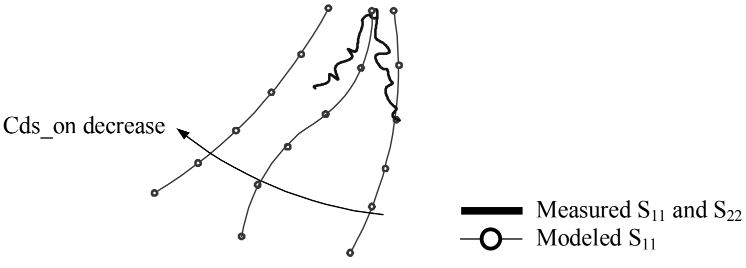

Fig. 4.47: Effect of Cds_on on S_{11}_on.

By reducing Cds_on below the range of effective values, the fit error does not change. However, if Cds_on is increased beyond these values, the fit degrades. By making Cds a bias dependent parameter, some improvement is noticed for the magnitude of S21_on (at least 1% less error mostly at 50 GHz) while maintaining the same fit for the other s-parameter.

Cg_off is sensitive and affects the slope of the magnitude and the phase of S_{21}_off. An increase worsens S_{11}_off. When decreased the phase improves slightly, mostly at high frequency. Lower values of Ri_off help to ground the input signal for the off state but the effect is not very noticeable.

Rds_off always seems to reach higher than necessary. This is why we leave it unconstrained so that it will not hit the upper limit of a constrained range while using the optimization routines. This neutral behavior after it has reached a certain threshold value allows it to be easily scaled.

When Rds_off is close to an open circuit, reactive components such as Ls, Ld, and Cds are the ones that mostly affect the fit. Rds_off affects the phase of S_{21}_off when less than about 50 k ohms (for a 3x100). In the OFF state, whenever Rds_off goes on a tangent towards very high values, it was noticed that Ri_off decreased to extremely low values. As was mentioned previously, this tendency seems to be the result of an 'over-optimization' since Ri_off is not very sensitive to the OFF state parameters.

Cds_off mostly affects the S_{21}_off phase in a very sensitive manner. The level (or shape) of S_{21}_off can also be changed by varying Cds_off. As Cds_off increases, it gives more transmission and less loss mostly at higher frequency.

The parasitic inductances tend to reach very small values and are difficult to scale. With parasitic inductances included in the model, the microstrip line length does not vary that much from the specified half of the FET width. Without the inductances, the physical length increases. As this length increases, the imaginary part of S_{11}_on increases. The microstrip line length tends to reach a value of about 45 um (instead of the specified nominal value of 36 um half width of the 3x100) and helps provide a good fit for S_{21}_on and S_{11}_on simultaneously. Tentative models will be presented without inductances and as will be seen, still give a good fit to measured data.

4.3.5 Optimization trade-offs

Many trade-offs were observed between different s-parameter fits during the optimization. This implies that some fits be sacrificed in favor of the most important ones that ensure a proper performance of the FET switch. A tolerated maximum error in the fit needs to be determined and the weight distribution for the fit of different s-parameters has to be adjusted accordingly.

Among the trade-offs observed, S_{21}_on was one parameter that had difficulty converging simultaneously for the phase and the magnitude fit. This conflict is accentuated in the off state for smaller FETs such as the 1x25. Even a reciprocity problem between the phase of S_{21}_on and S_{12}_on was observed for the 1x25. Despite the distribution of some model parameters into ON and OFF state elements there is still a small trade-off between the fit of the ON and OFF s-parameters probably because of a small bias dependence of the common state parameters. This trade-off becomes more dominant with larger FETs.

For all FET sizes, the largest trade-off was between the input/output parameters (S_{11} and S_{22}) and the transmission parameters (S_{21}, S_{12}) fits for both states. Two cases of weight distributions were compared to study this trade-off. The first case uses all the weights on S_{11}/S_{22} (ON/OFF) leaving all other parameters without any weights. The second case uses an optimized weight distribution. The starting values for the model were those from the optimized 3x100 FET and the range of optimization was set from 5 to 40 GHz. The two cases corresponding fitting and error graphs are seen in Fig. 4.48 to Fig. 4.53. All graphs in rectangular coordinates have a frequency scale division of 10 GHz/division and the Smith Charts show data variation from 1 to 50 GHz. The cartesian graphs for modeled and measured S_{21}_on(off) have a magnitude scale in dB on the left axis and a phase scale in degrees on the right axis. The chart labeled C1 located to the left corresponds to the first case of optimization (as described previously) and the chart labeled C2 located to the right corresponds to the second case. Table 4.7 provides a legend for the symbols used in the graphs. These symbols are to be used by default in any fitting result, unless otherwise specified. Following are Table 4.8 that presents the weight distributions, Table 4.9 with the maximum errors observed after optimization, and Table 4.10 with the resulting circuit parameters.

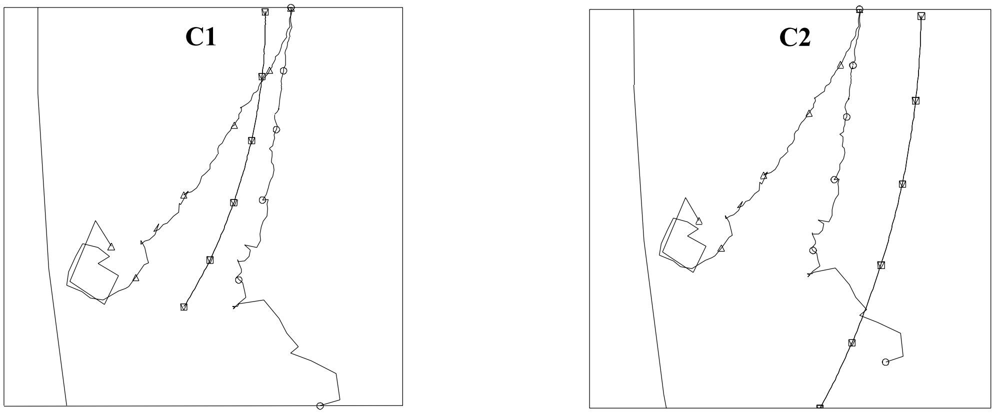

Fig. 4.48: Fitting of phasor S_{11}/S_{22}_on.

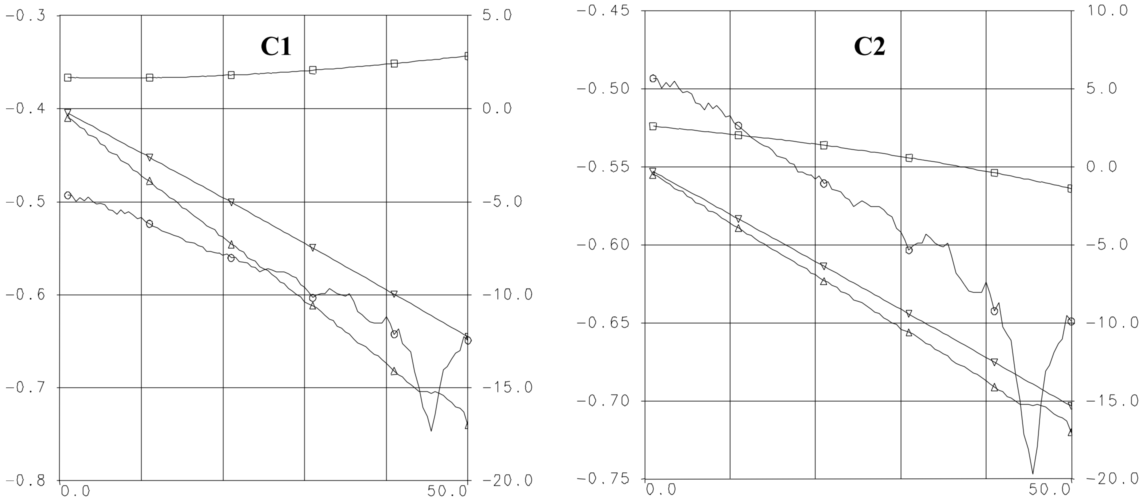

Fig. 4.49: Fitting of S_{21}_on.

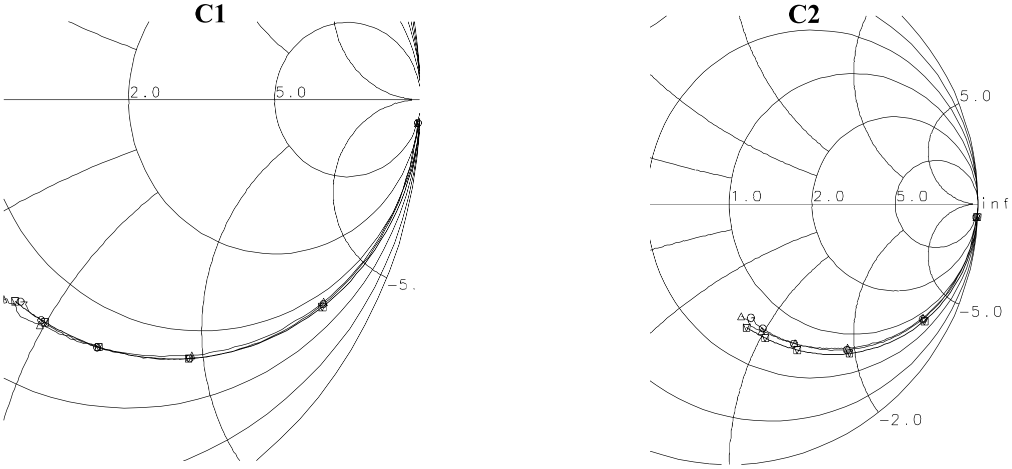

Fig. 4.50: Fitting of S_{11}/S_{22}_off.

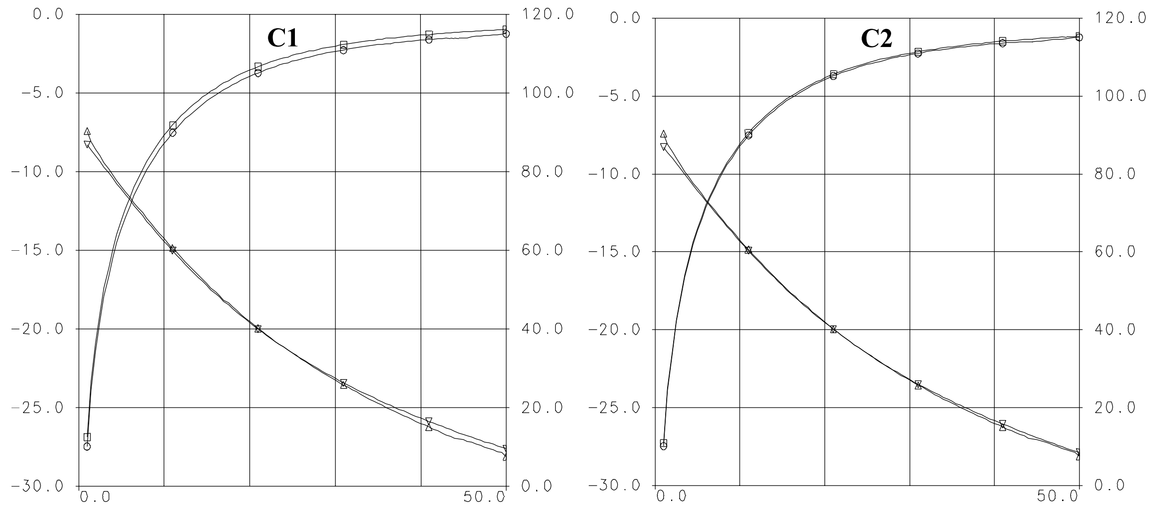

Fig. 4.51: Fitting of S_{21}_off.

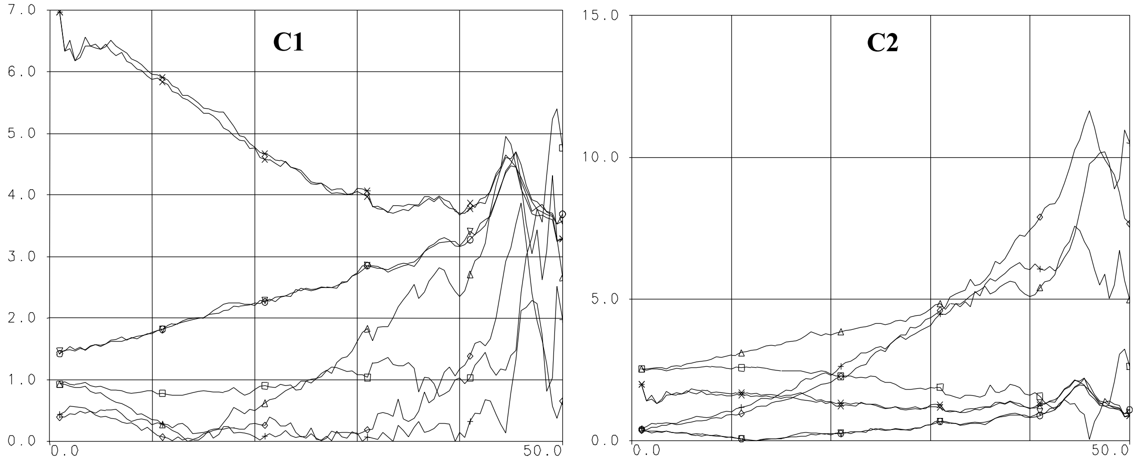

Fig. 4.52: Magnitude error of performance parameters.

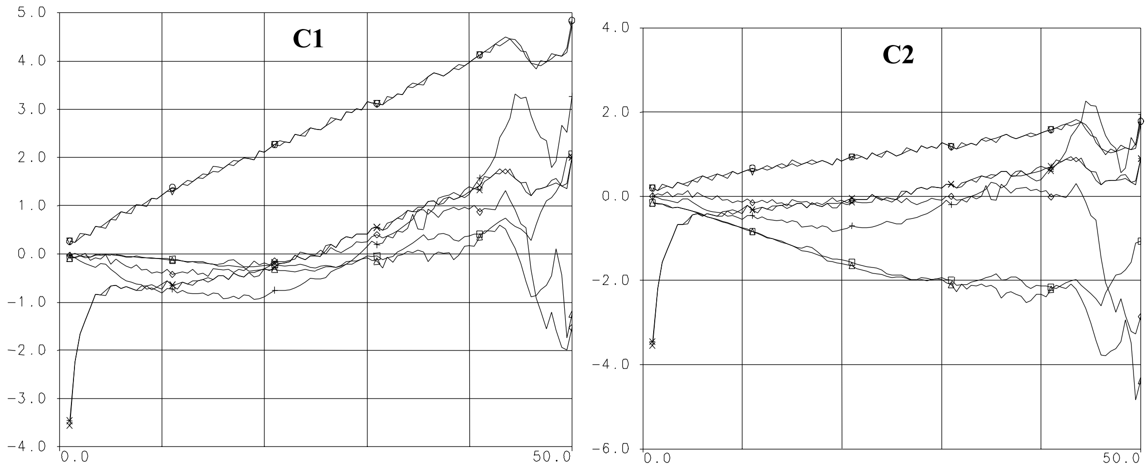

Fig. 4.53: Phase error of performance parameters.

Table 4.7: Legend for symbols used in Fig. 4.48 to Fig. 4.53.

Symbol	**S_{21}_on(off)**	**S_{11}_on(off)**	**Magnitude error**	**Phase error**
□	Magnitude of S_{21} from model data (dB)	Phasor S_{11} from model simulation	Fitting error on magnitude of S_{11}_on (%)	Fitting error on phase of S_{11}_on (%)
○	Magnitude of S_{21} from measured data (dB)	Phasor S_{11} from measured data	Fitting error on magnitude of S_{12}_on (%)	Fitting error on phase of S_{12}_on (%)
▽	Phase of S_{21} from model data (deg)	Phasor S_{22} from model simulation	Fitting error on magnitude of S_{21}_on (%)	Fitting error on phase of S_{21}_on (%)
△	Phase of S_{21} from measured data (deg)	Phasor S_{22} from measured data	Fitting error on magnitude of S_{22}_on (%)	Fitting error on phase of S_{22}_on (%)
◇	N/A	N/A	Fitting error on magnitude of S_{11}_off (%)	Fitting error on phase of S_{11}_off (%)
✳			Fitting error on magnitude of S_{12}_off (%)	Fitting error on phase of S_{12}_off (%)
╳			Fitting error on magnitude of S_{21}_off (%)	Fitting error on phase of S_{21}_off (%)
+			Fitting error on magnitude of S_{22}_off (%)	Fitting error on phase of S_{22}_off (%)

Table 4.8: Weight distribution on optimization goals for two cases.

Optimization goal	**Z_{11}/Z_{22} on/off optimized**	**Optimized distribution**
Opt_err1_Z_{11}	50	50
Opt_err1_S_{12}	0	1
Opt_err1_S_{21}	0	1
Opt_err1_Z_{22}	50	50
Opt_err2_Z_{11}	50	50
Opt_err2_S_{12}	0	1
Opt_err2_S_{21}	0	1
Opt_err2_Z_{22}	50	50
Phase_on_S_{12}	0	0.025
Phase_on_S_{21}	0	0.025
Phase_off_S_{12}	0	0.1
Phase_off_S_{21}	0	0.1
Mag_on_S_{12}	0	0.1
Mag_on_S_{21}	0	0.1
Mag_off_S_{12}	0	0.01
Mag_off_S_{21}	0	0.01

Table 4.9: Maximum error in magnitude and phase performance parameters for two cases.

Performance parameter	**Z_{11}/Z_{22} on/off optimized**		**Optimized distribution**	
	Mag error (%)	**Phase error (±deg)**	**Mag error (%)**	**Phase error (±deg)**
Z_{11}_on	1.37	0.43	2.6	2.2
Z_{22}_on	2.81	0.37	5.6	2.5
Z_{11}_off	1.21	1.27	7.4	0.3
Z_{22}_off	0.51	0.96	6.3	0.8
S_{21}_on	3.31	4.0	1	1.5
S_{21}_off	6.5	1.38	1.9	0.7

Table 4.10: Optimized model parameter for two cases.

Model parameter	**Z_{11}/$Z_2$2 on/off optimized**	**Optimized distribution**
VAR RG	0.0282	0.24
VAR RS	0	0
VAR RD	0	0
VAR LG	0	0
VAR LS	0	0
VAR LD	0	0
VAR CGS_ON	$1.864 \cdot 10^{-6}$	0.00277
VAR RI1_ON	0.0102	0.0296
VAR RDS_ON	4.304	6.205
VAR CGD_ON	$1.864 \cdot 10^{-6}$	0.00277
VAR RI2_ON	0.0102	0.0296
VAR CDS_ON	0.26	9.381e-06
VAR CGS_OFF	0.00098	0.00352
VAR RI1_OFF	0.0121	0.0325
VAR RDS_OFF	544932	419622
VAR CGD_OFF	0.00098	0.00352
VAR RI2_OFF	0.0121	0.0325
VAR CDS_OFF	0.0723	0.0688
VAR ERROR_ON	6.256	5.058
VAR ERROR_OFF	4.320	4.862

As can be seen from the weight distribution required for a reasonable fit of all parameters, the weights on the transmission parameters have a much more pronounced effect than those on Z_{11}/Z_{22}. In fact, the magnitude of S_{21}_off is probably the main trade-off to Z_{11}. As explained in section 4.3.4 (Effect of parameters on model fit), reactive components such as Ls and Cg affect the imaginary part of Z_{11} and S_{21} in opposite directions. Also, the resistive components such as Rs or Rds affect the real part in the same way. It seems that when Rs is fixed to 0 and only Rds serves as the path resistance, a larger trade-off appears between the real part of Z_{11} and S_{21}.

4.3.6 Scaling methodology

The scaling method from an internal modeling document from TriQuint was chosen as the most appropriate for the switch model because of its simplicity and the fact that there is no dependence on previously optimized parameters from a reference FET, which can have a different layout configuration from the switch. The scaling method used is based on a physically intuitive approach: the capacitance values increase while the resistance values decrease proportionally as the FET width increases. The scaling formulas used are as follow:

- W1: Total gate periphery of the known FET
- W2: Total gate periphery of the desired FET
- WG1: Individual gate width (finger length) of the known FET
- WG2: Individual gate width (finger length) of the desired FET
- N1: Number of gate fingers of the known FET
- N2: Number of gate fingers of the desired FET
- K1 = W2/W1
- K2 = WG2/WG1
- K3 = N2/N1
- C_{gs}, C_{gd}, C_{ds}: Multiply by K1
- R_i, R_s, R_{ds}, R_d: Divide by K1
- R_g: Multiply by K2 and divide by K3
- L_g, L_d: These parameters do not scale directly, as a significant portion of each merely absorbs errors in creation of date- or drain-feed networks.

Two cases of optimization over the full range of FET sizes (from 1x25 to 9x100) with odd number of gate fingers have been completed. The scaling for the first case was done using the 3x100 as the reference. For the second case, a sequential scaling was used as described in Fig. 4.54.

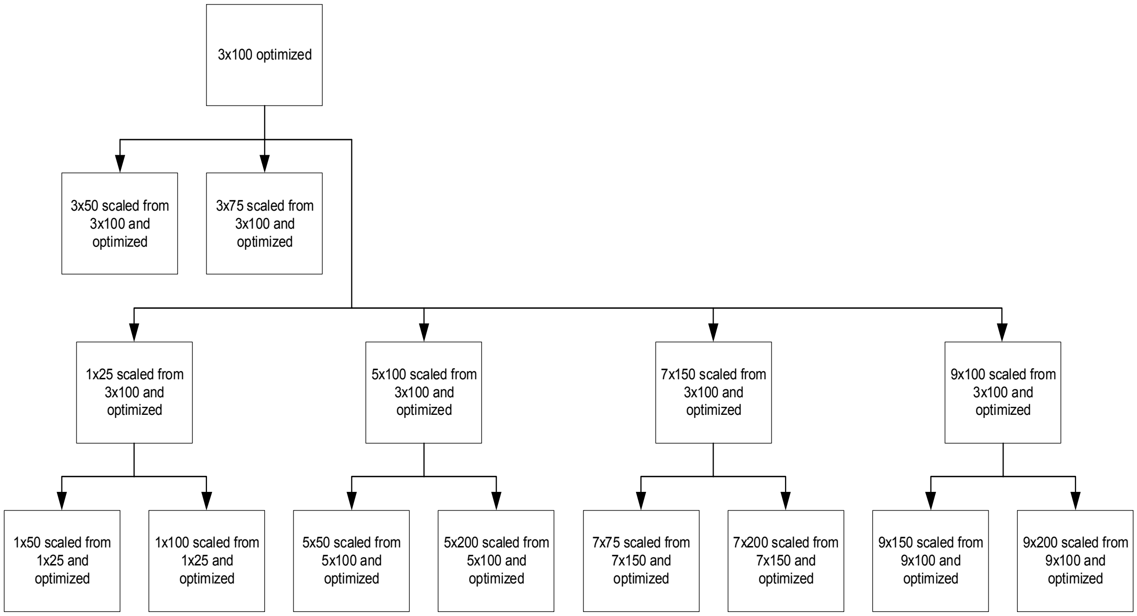

Fig. 4.54: Scaling for the second case of optimization over the full range of FET sizes

4.3.7 Measurements and optimization considerations

In this section, a description of the measured results, errors and choice of optimization range is provided. The determination of proper starting values, variables range, optimizers, and weights is also covered among other observations.

4.3.7.1 Optimization range

The optimization frequency range had to be adjusted according to the validity of measurements of the FET considered due to calibration and equipment limitations. In general, the smaller FETs present a more degraded measured response at lower frequency and the larger switch FETs cannot perform properly at higher frequencies. For instance, S_{21}_off does not fit well at low frequencies for the 1x25. This may be due to a measurement limitation since, as we reduce the size of the FET, the isolation becomes larger (C decreases and R increases) and the sensitivity of the network analyzer may not be large enough to ensure an accurate measurement of such a low signal as S_{21}_off.

Another possible measurement degradation common to all FET sizes and more pronounced for the smaller ones was the phase of S_{21}_off at low frequencies which deviates quite largely from the model response in a very local frequency region. This is clearly apparent in the numerous phase error graphs that present a tip of large phase error for the OFF state S_{21} below about 5 GHz. This is why we chose to set our lower frequency range limit to 5 GHz. Also the magnitude of S21_on measured at higher frequency presents larger oscillation from about 40 GHz and above. In particular, a peak of about 0.1 dB down for the magnitude and a small deviation in the phase (0.5° to 1°) are observed in all the measurement data files for the 3x100 at 41.5 GHz. This being said, the optimization was done over a relatively broad range from 5 to 40 GHz for moderate size FETs such as the 3x100.

The phase in the OFF state seems to degrade after ~25 GHz for larger FET sizes (from 5x100 and above). This suggests a limitation in the optimization upper frequency for large FETs to 26 GHz. Three cases of optimization range were investigated for the 7 and 9 fingers FETs, namely, from 1 to 40 GHz, from 5 to 40 GHz, and from 1 to 26 GHz, and errors were compared. The optimization over the range from 1 to 26 GHz helped improve the magnitude of S_{21}_off in all cases. A very small difference was observed between the errors from the optimization up to 40 GHz and the optimization up to 26 GHz for the 9x200. Only a small improvement in the magnitude of S_{21}_on is obtained (0.3% instead of 0.5%) by optimizing up to 26 GHz. However, the total error in the ON state is larger for the range 1-26 GHz than for 1-40 GHz which means the error for S_{11}/S_{22} is probably much larger.

As the FET size increases, the values for the optimum parameters are closer from one measurement data file to the other. This implies that the measured data is very repeatable. This allows a valid averaging of all optimized parameters over the entire set of data for the scaling of these larger FETs.

4.3.7.2 Variables range, optimizers, and weights

The optimization of all files was initially conducted using unconstrained parameters with the 3x100 switch model parameter values available from the GADGIT library as starting values. The random optimizer is used in the first runs of optimization with a large number of iterations for each. Once the fit gets close to the desired level, the gradient optimizer is used to further reduce the error. The random optimizer helps reduce the error for the level of the magnitude of S_{21}_on very quickly but the slope of the magnitude of S_{21}_on does not converge easily to the measured one. The resistive elements mostly affecting the level of $|S_{21}$_on$|$ are less sensitive than the Cg element controlling the slope of $|S_{21}$_on$|$. This is why a random optimization is less effective in finding the optimum value for Cg requiring very small trial increments unless it is constrained within a very tight range around the optimum value. The gradient optimizer efficiently finds the optimum Cg. Since the optimization goals of zero errors are rarely met, the criterion to stop the optimization is whenever the gradient optimization is terminated by a zero gradient.

A gradient optimization is therefore needed at the end of an optimization routine to refine the fit. However, if an unconstrained variable is optimized with the gradient optimizer using a starting value relatively close to zero, the gradient optimization may find negative optimum values which are not physical switch parameters. To avoid getting negative values while gradient optimizing over an unconstrained range, the variables were forced positive by using an absolute value or square root function. Some already available Perl scripts were modified to integrate the absolute value feature. After better understanding how the gradient optimizer was finding the optimum values, it was decided to eliminate the absolute value feature. This is because whenever a negative value was found as an optimum, it was kept as an optimum if the fit would stay the same having been forced to be positive. This meant that the gradient optimizer was finding two equal minima instead of the smallest possible one.

Later in the project, it was decided to remove the absolute value feature from the unconstrained parameters since the gradient may find two minimas simultaneously whenever a negative value is forced positive. The constrained range should be chosen carefully and the parameters that tend to increase hitting any specified upper boundary need to be lowered manually while maintaining a good fit.

Therefore, the variables were constrained within a reasonable range around a possible optimum (determined after a few random optimizations). Only Rds_off was left unconstrained in order for it not to hit the upper bound in the constrained range, as it seemed to do for any specified range. This would not cause a negative value problem with the gradient optimizer since the starting value was set to a very large number (around 100k ohms).

After noticing the large trade-off between Z_{11} and S_{21} as described in section 4.3.5 (Optimization trade-offs), a need for an optimum weight (W) distribution was felt in order to have reasonable error levels for both parameters. A number of weight combination trials were tested and compared to obtain the best weight values. Fig. 4.55 to Fig. 4.61 present the fit for different weight distributions cases. Table 4.11 gives the corresponding optimum model parameters.

4.3.8 Fitting results and scaling errors

This section gathers the fitting results and corresponding scaling errors of optimized parameters for three main cases of optimization. The first case was as a preliminary optimization study to get familiar with the effects of the switch parameters over the fit. The two other cases list the optimization results for the entire range of FET sizes with optimization settings as described in sections 4.3.8.2 and 4.3.8.3.

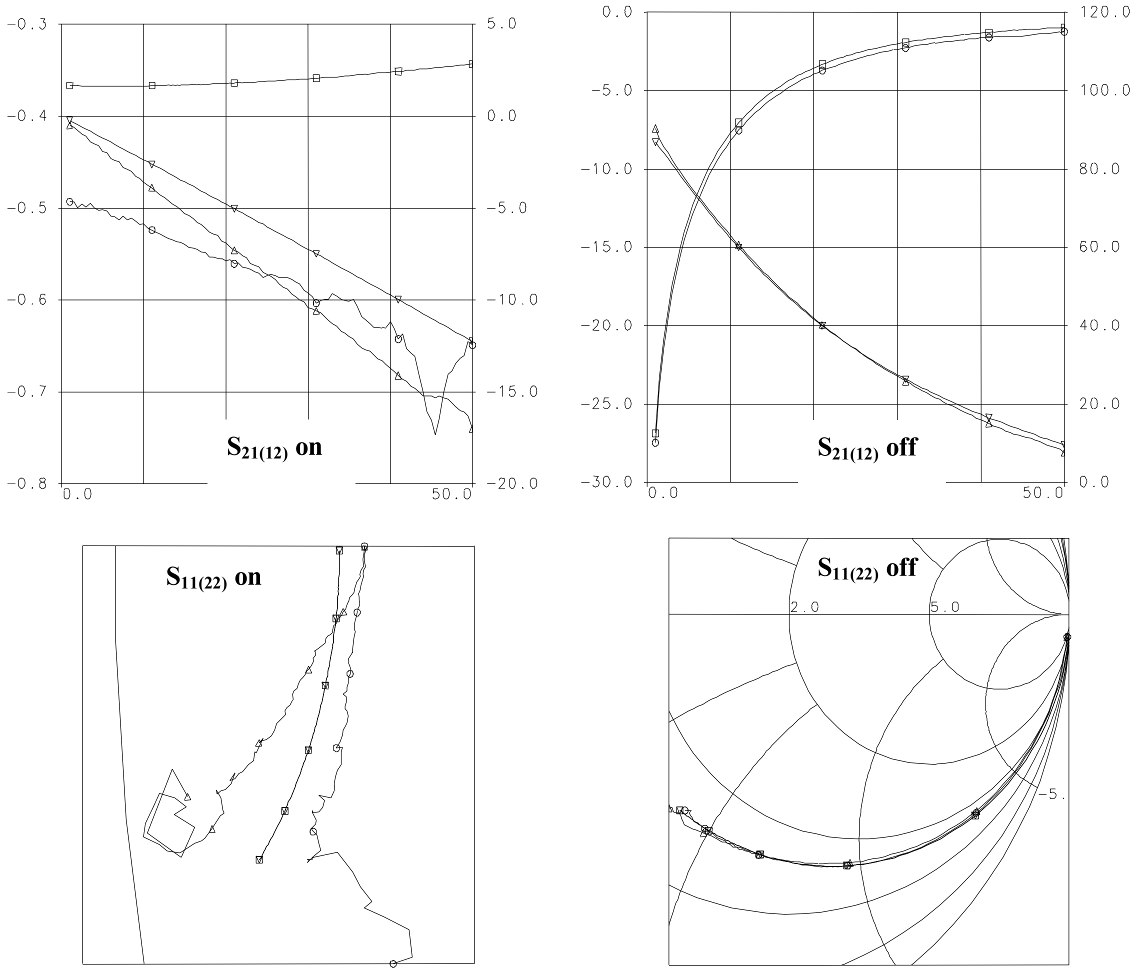

$S_{21(12)}$ on

$S_{21(12)}$ off

$S_{11(22)}$ on

$S_{11(22)}$ off

Fig. 4.55: Results for Case 1 of weights. W=50 for $Z_{11(22)}$ on(off) and W=0 for S_{21} on(off), mag/phase.

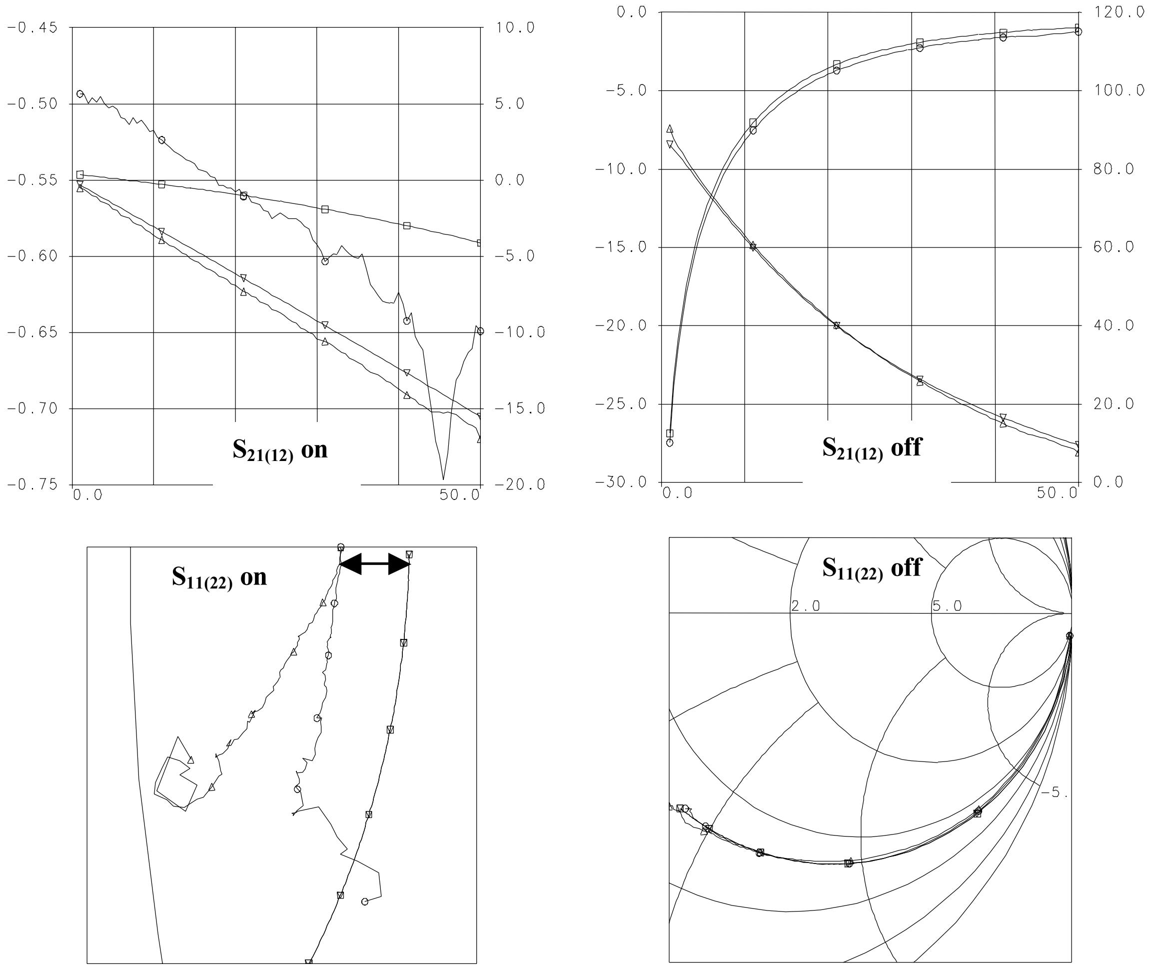

Fig. 4.56: Results for Case 2 of weights. W=50 for $Z_{11(22)}$_on(off), W=1 for S_{21}_on magnitude, and W=0 for remaining.

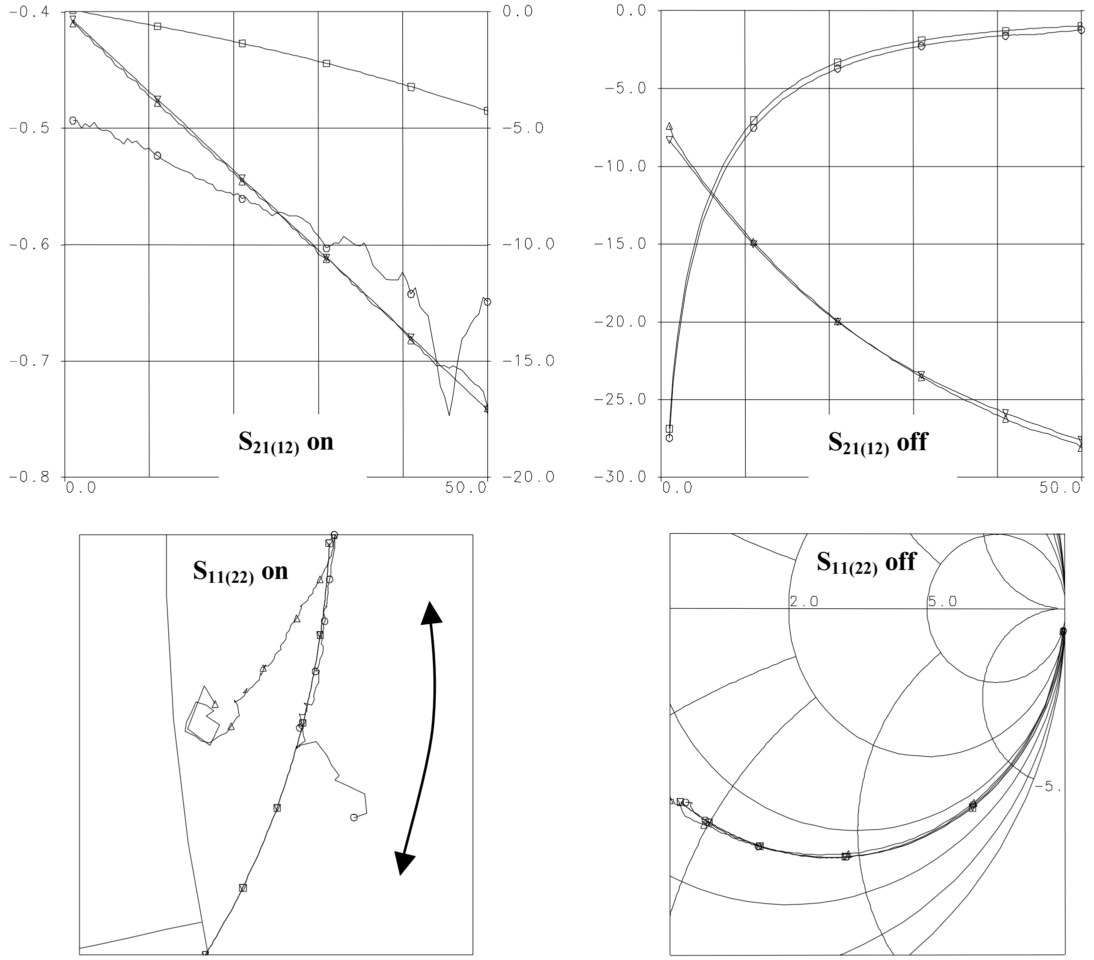

Fig. 4.57: Results for Case 3 of weights. W=50 for $Z_{11(22)}$_on(off), W=1 for S_{21}_on phase, and W=0 for remaining.

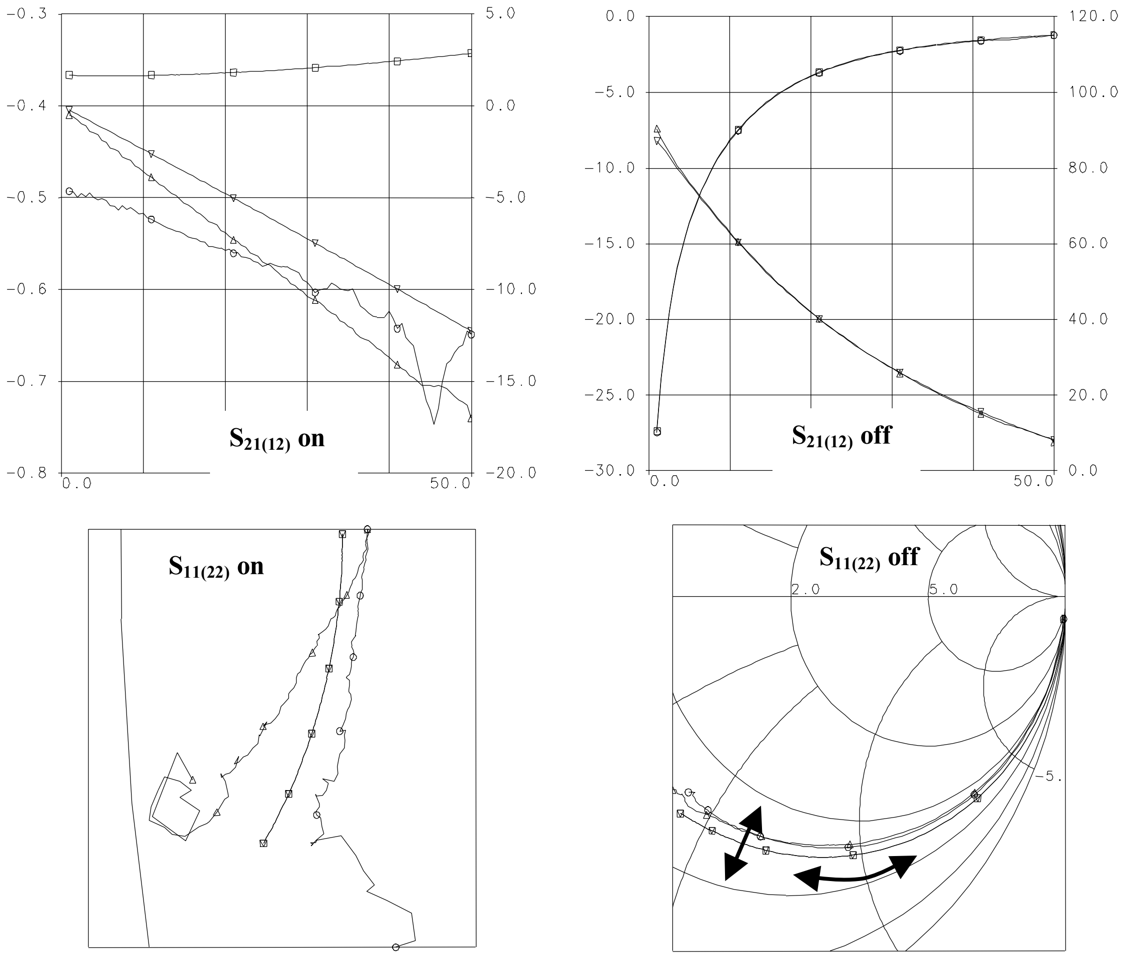

Fig. 4.58: Results for Case 4 of weights: W=50 for $Z_{11(22)}$ on(off), W=1 for S_{21} off phase, and W=0 for remaining.

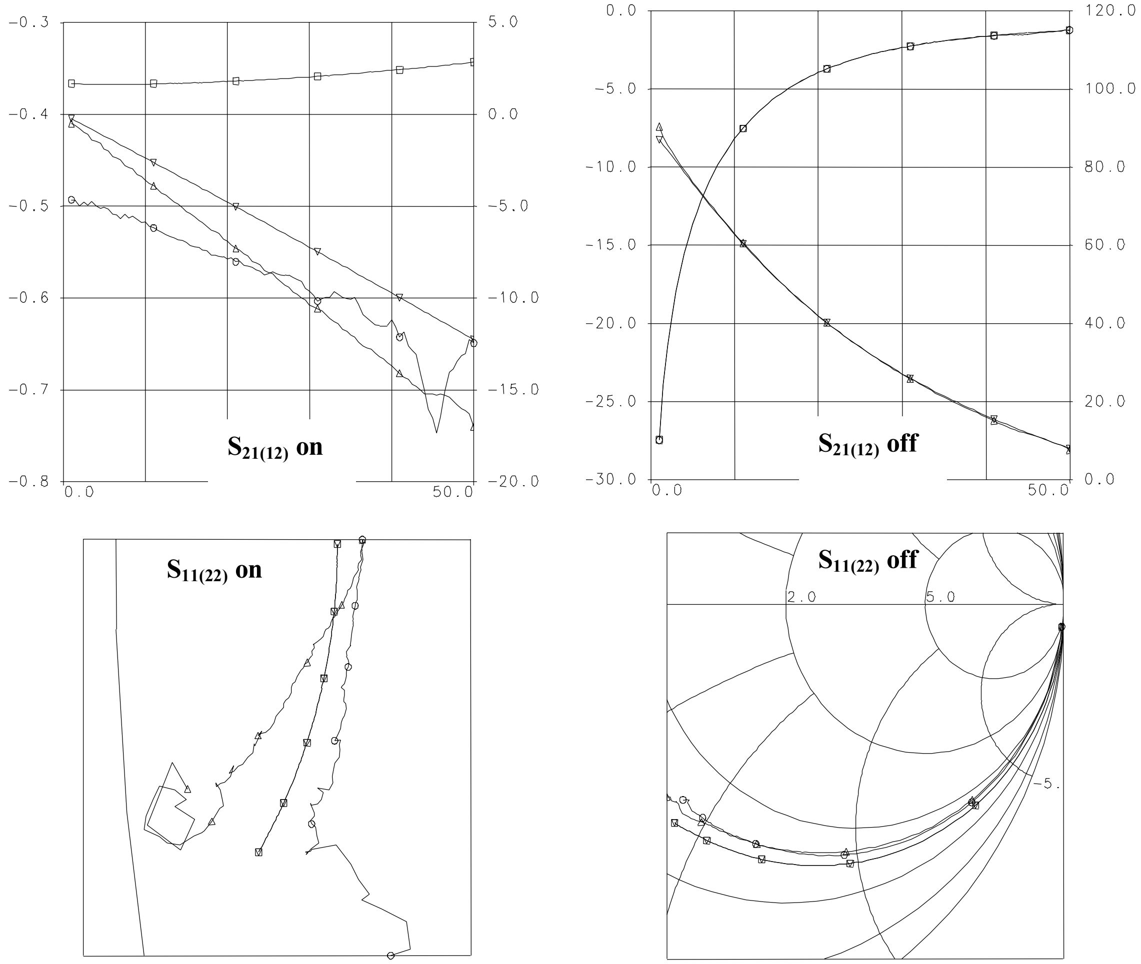

Fig. 4.59: Results for Case 5 of weights. W=50 for $Z_{11(22)}$ on(off),

W=1 for S_{21} off magnitude, and W=0 for remaining.

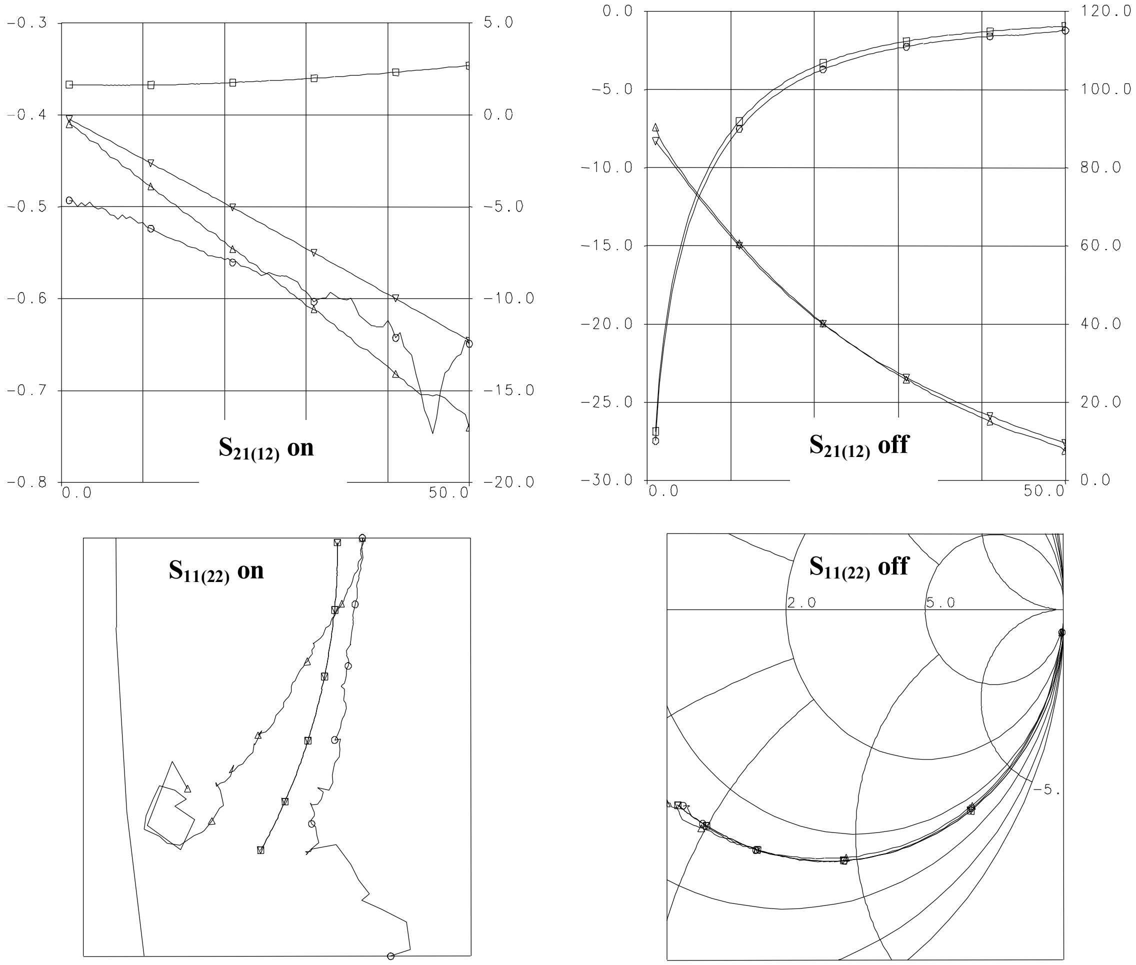

Fig. 4.60: Results for Case 6 of weights. W=50 for $Z_{11(22)}$ on(off), W=1 for opt_err1_S_{21} (combines magnitude and phase error for the ON state), and W=0 for remaining.

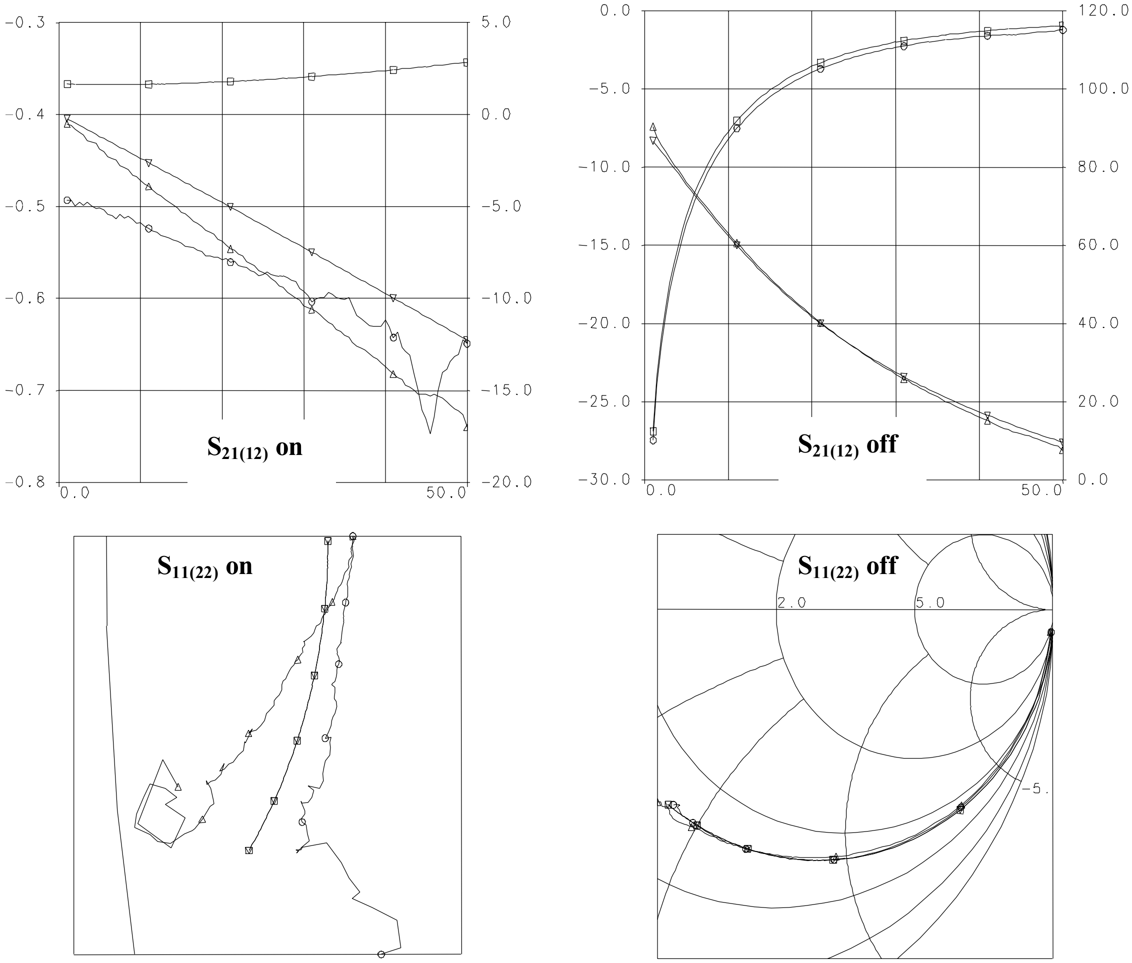

Fig. 4.61: Results for Case 7 of weights. W=50 for $Z_{11(22)}$ on(off), W=1 for opt_err2_S_{21} (combines magnitude and phase error for the off state), and W=0 for remaining.

Table 4.11: Optimized parameter values for Case 1 to Case 7 of weight distribution.

Optimized parameter	**Case 1**	**Case 2**	**Case 3**	**Case 4**	**Case 5**	**Case 6**	**Case 7**
RG	0.0282	2.036	0.0332	0.00056	0.0327	0.0404	0.0516
CGS_ON	$1.86\cdot10^{-6}$	0.00303	0.00586	$6.18\cdot10^{-9}$	$1.87\cdot10^{-10}$	$1.89\cdot10^{-6}$	$2.61\cdot10^{-6}$
CGS_OFF	0.00098	0.001	0.00098	0.00435	0.00476	0.00098	0.00102
RS	0	0	0	0	0	0	0
RI1_ON	0.0102	0.3	0.0272	0.0102	0.0102	0.0102	0.0102
RI1_OFF	0.0121	0.0674	0.0164	0.0606	0.0146	0.0178	0.0253
RD	0	0	0	0	0	0	0
RDS_ON	4.304	6.48	4.674	4.305	4.304	4.309	4.305
RDS_OFF	544933	141729	441247	1388519	487899	423860	336381
LG	0	0	0	0	0	0	0
CGD_ON	$1.86\cdot10^{-6}$	0.00303	0.00586	$6.18\cdot10^{-9}$	$1.87\cdot10^{-10}$	$1.89\cdot10^{-6}$	$2.61\cdot10^{-6}$
CGD_OFF	0.00098	0.001	0.00098	0.00435	0.00476	0.00098	0.00102
LS	0	0	0	0	0	0	0
RI2_ON	0.0102	0.3	0.0272	0.0102	0.0102	0.0102	0.0102
RI2_OFF	0.0121	0.0674	0.0164	0.0606	0.0146	0.0178	0.0253
LD	0	0	0	0	0	0	0
CDS_ON	0.26	$3.18\cdot10^{-5}$	0.00338	0.261	0.259	0.249	0.261
CDS_OFF	0.0723	0.0723	0.0723	0.068	0.0674	0.0723	0.0722

4.3.8.1 Preliminary optimization study

A first run of optimization without yet deembedding the drain and source port was conducted on three cases namely, the 3x50, 3x100, and 9x100. The 3x100 parameter values were taken as the reference to scale from for the two other FETs. The variables setting is as follows: all inductances are set to 0 (the microstrip line length adds some inductance to our advantage since Ls (or Ld) is difficult to scale); Rs=Rd for a symmetrical model; the frequency range for the optimization is from 0.5 to 50 GHz for smaller FETs (such as 3x50 and 3x100), and from 0.5 to 26 GHz for the larger FET (9x100); Cds is not yet bias dependent. Fig. 4.62 presents the average scaling error and the standard deviation from the three previous cases (3x50, 3x100 and 9x100) for each model parameter.

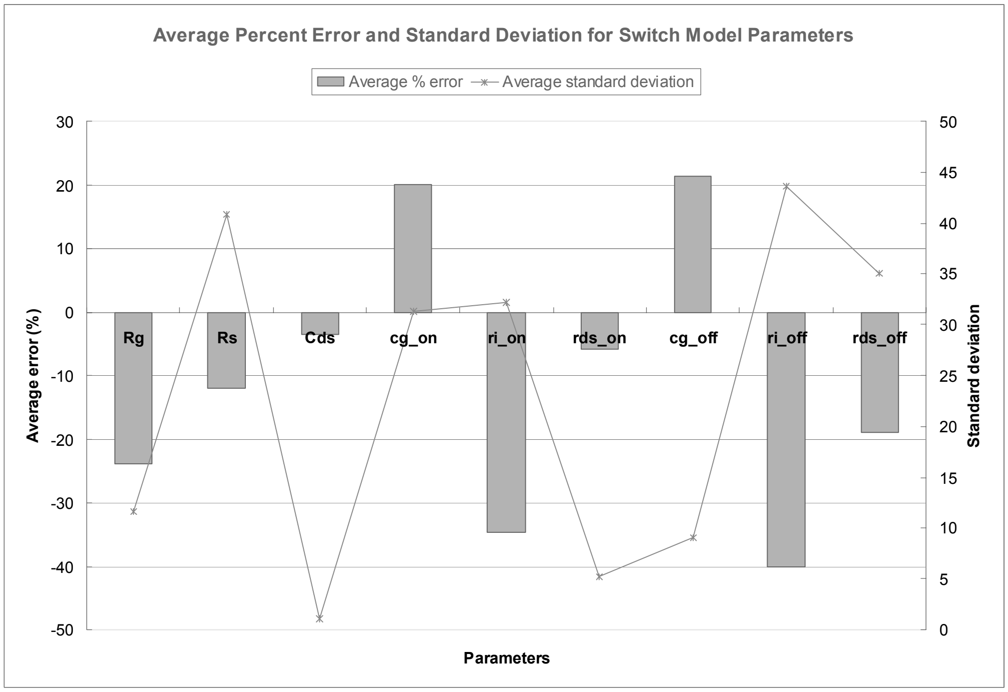

Fig. 4.62: Average percent error and standard deviation for the model parameters.

4.3.8.2 Optimization over entire range of FET size using constrained parameters

This optimization was done over the frequency range from 1 to 50 GHz for all FETs and the parameters were constrained within a reasonable range. The scaling was calculated using the

3x100 as the scaling reference. The measured data is deembedded at the drain and source ports up to the intrinsic region. This was done since the Z_{11} and Z_{22} responses were not superimposed on the Smith chart due to an extra microstrip line on the drain feedline. Once feedlines are deembedded, a similar behavior between Z_{11} and Z_{22} for both the ON and OFF state is observed. In this case, the feed networks needed not be used anymore for the drain and source ports. Cds is defined as a bias dependent parameter. The corresponding scaling errors for the previous fitting results are shown in Fig. 4.63.

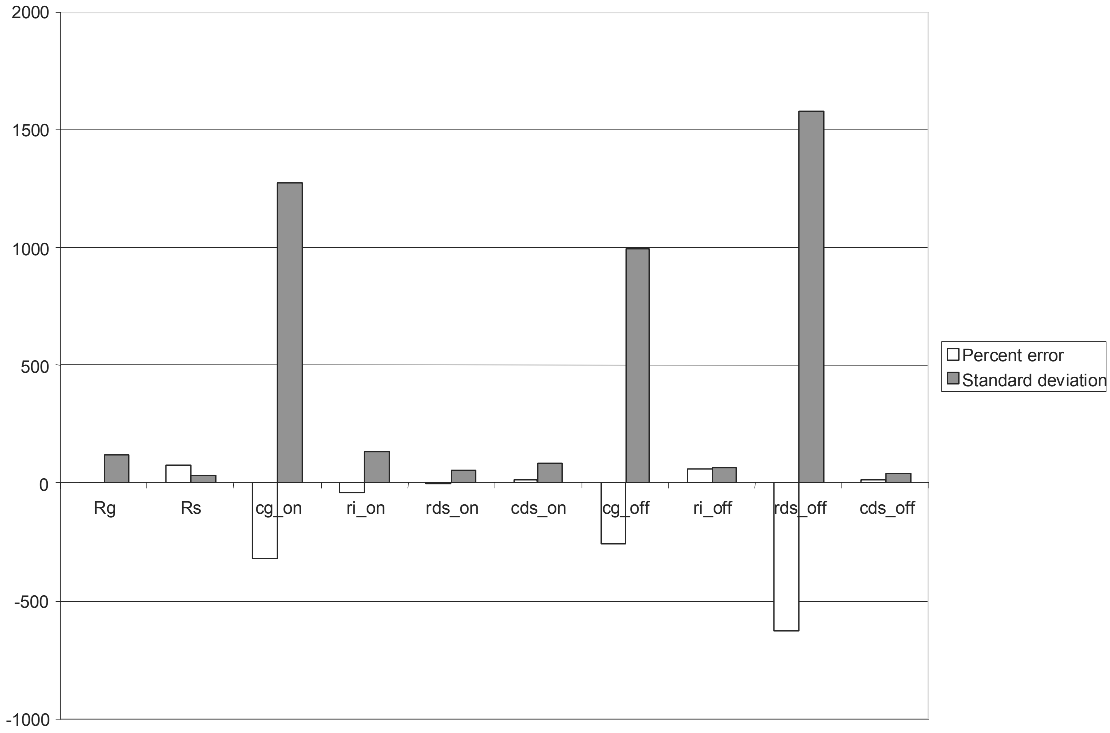

Fig. 4.63: Scaling errors in percentage and standard deviation for fitting results.

4.3.8.3 Optimization over entire range of FET sizes using unconstrained parameters

This optimization was done over the frequency range from 10 to 40 GHz for the 1x25, from 5 to 40 GHz for moderate size FETs, and from 1 to 26 GHz and from 1 to 35 GHz for larger FETs. All the parameters were left unconstrained using an absolute value feature to avoid negative non-physical parameter values. The 3x100 was used as the scaling reference for the 3x50 and 3x75, as well as one FET size from a certain number of gate fingers set as shown in Fig. 4.54. The measured data is also deembedded at the drain and source ports up to the intrinsic region and Cds is defined as a bias dependent parameter. The scaling error for each parameter is given in Fig. 4.64.

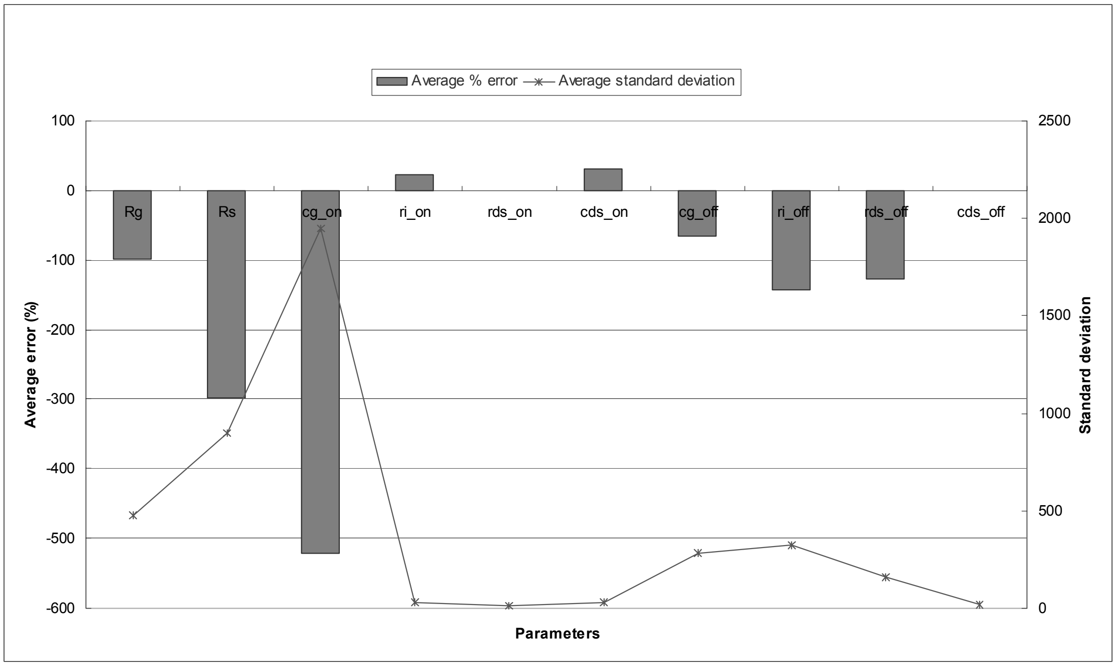

Fig. 4.64: Average percent error and standard deviation for switch model parameters.

The variation of each parameter versus different size factors (FET width, number of fingers, or total area) corresponding to the previous fitting results have been extensively simulated. The general tendency is that as the area increases, the R's decrease in an exponential way and that the C's increase in a linear way.

4.3.9 Study cases

In this section, we study some cases to have a better understanding of the effect of the parameters as summarized in section 4.3.4 (Effect of parameters on model fit). The cases studied include the effect of the model parameters on Z_{11} (Z_{22})_on, the trade between the two path resistances Rs and Rds, the determination of the non-sensitive model parameters and a search for optimum models.

4.3.9.1 Case study 1: effect of parameters on Z_{11} (Z_{22})_on

This study was realized using the optimized values for the 3x100 as starting values. The objective is to improve the fit of the Z_{11} and Z_{22} parameters for the ON state, mainly the imaginary part. As was explained in section 4.3.4, only Cg_on and Ri_on seem to affect the imaginary part of Z_{11}, and Rds or Rs position the real part on the Smith chart. We intend to investigate how Cg_on and Ri_on affect the imaginary part of Z_{11}. Fig. 4.65 illustrates the fitting results for Z_{11} (Z_{22})_on using the starting values of Cg_on=0.0078 and Ri_on=69 from the previously optimized 3x100. As we optimize both parameters from 0 to 1,000,000 using the gradient optimizer, we get Cg_on=500,000 and Ri_on=500,000. Every time the upper limit of the range is adjusted to a very high value (for instance to 1,000,000,000), the optimized value is always exactly half of the range (hence 500,000,000). Although the imaginary part fit is satisfactory as shown in Fig. 4.66 and Fig. 4.67, these optimum parameters are non-physical values.

Fig. 4.65: Fitting result for Z_{11}_on using starting values of Cg_on=0.0078 and Ri_on =69

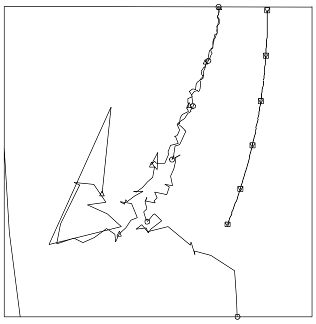

Fig. 4.66: Optimized fit with values of Cg_on=ri_on=$5x10^5$ for a range limit of $1x10^6$.

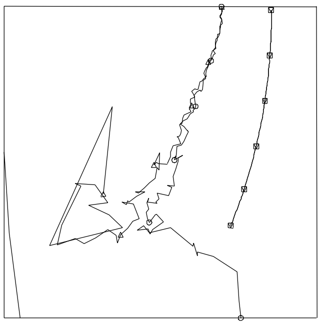

Fig. 4.67: Optimized fit with values of Cg_on=ri_on=$5x10^8$ for a range limit of $1x10^9$.

Cg_on is constrained up to 0.01 and Ri_on up to 200. The optimized realistic values and the fit are given on Fig. 4.68. Optimizing only on Cg_on (with Ri_on constant), we get Cg_on=0.0008 as shown in Fig. 4.69. Optimizing only on Ri_on (with Cg_on constant) with a range from 1 to 1,000,000, we get Ri_on=2772 as shown in Fig. 4.70. We notice that Ri_on increases to very high values but the imaginary part of Z_{11} fit is worse than with Cg_on.

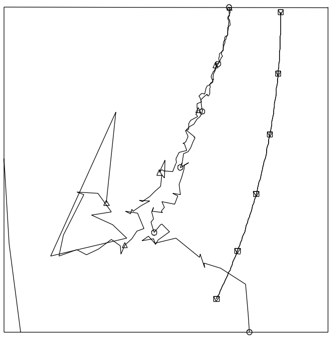

Fig. 4.68: Fitting result for a smaller optimization range. Cg_on=0.009 and Ri_on=195.9.

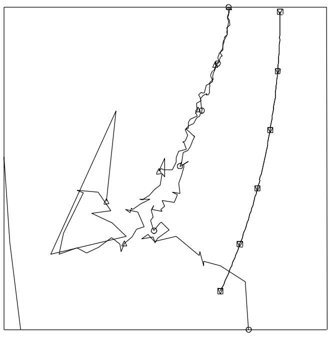

Fig. 4.69: Fitting results optimizing only on Cg_on with optimum at 0.008.

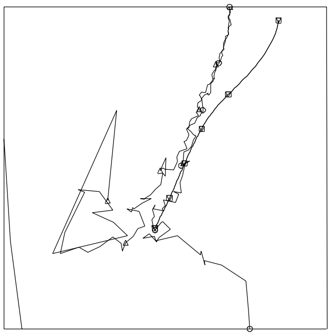

Fig. 4.70: Fitting results optimizing only on Ri_on with optimum at 2772.

Using an optimization range from 0 to 1000, Cg=0.0026 and Ri_on=999.9. If left unconstrained, Cg=0.024 and Ri=2797.9. The fitting results are shown respectively in Fig. 4.71 and Fig. 4.72.

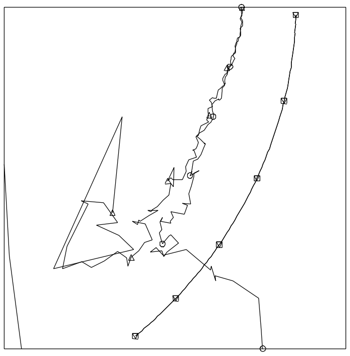

Fig. 4.71: Fitting result using an optimization range up to 1000. Cg_on=0.0026 and Ri_on=999.9.

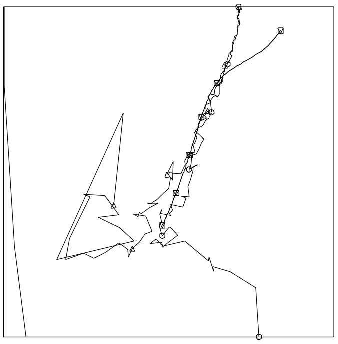

Fig. 4.72: Fitting result using an unconstrained optimization range. Cg=0.024 and Ri=2797.9.

The graph of S_{21}_on shown in Fig. 4.73 has the following sequence of Cg_on with Ri_on left constant: Cg=0.0068, Cg=0.0058, Cg=0.0048, Cg=0.0038, Cg=0.0028, Cg=0.0018, Cg=0.0008, and finally the optimum Cg=0.008054. Keeping Cg_on constant, the variation of S_{21}_on shown in Fig. 4.74 is observed with the following sequence for Ri_on: Ri=400, Ri=800, Ri=1200, Ri=1600, Ri=2000, Ri=2400, and the optimum Ri=2771.97. The corresponding graphs for Z_{11}, Z_{22}_on for the two previous sequences are given in Fig. 4.75 and Fig. 4.76, respectively.

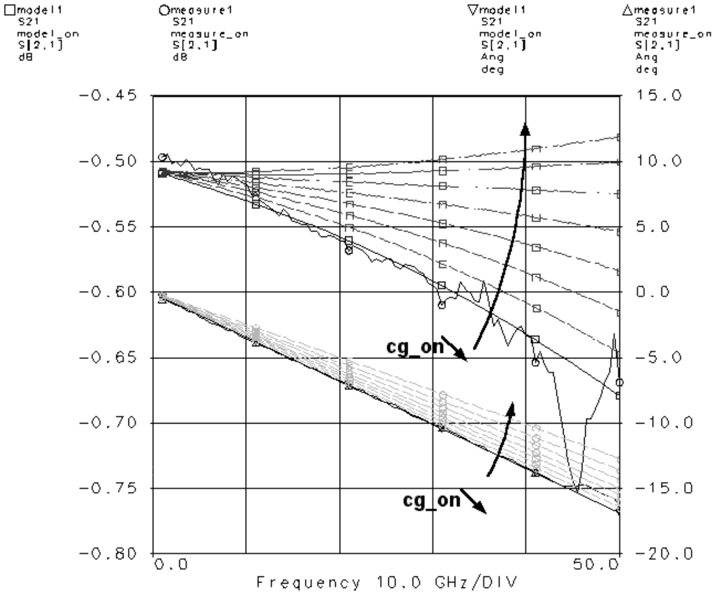

Fig. 4.73: Effect of variation of Cg_on on S_{21}_on for an optimum Z_{11}_on.

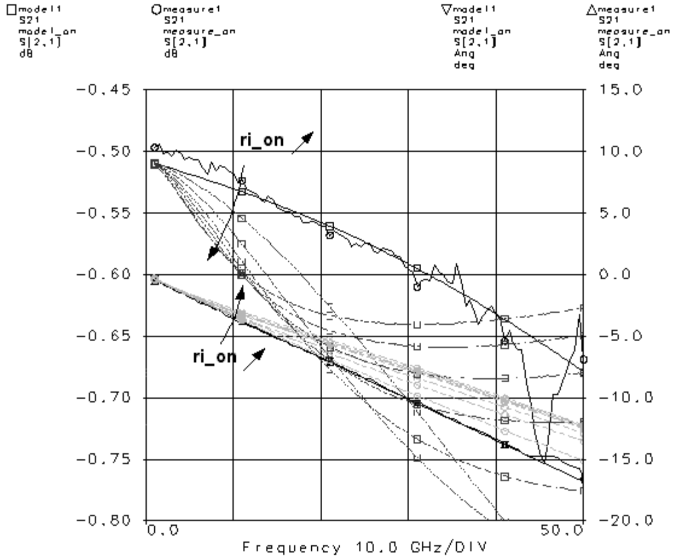

Fig. 4.74: Effect of variation of Ri_on on S_{21}_on for an optimum Z_{11}_on

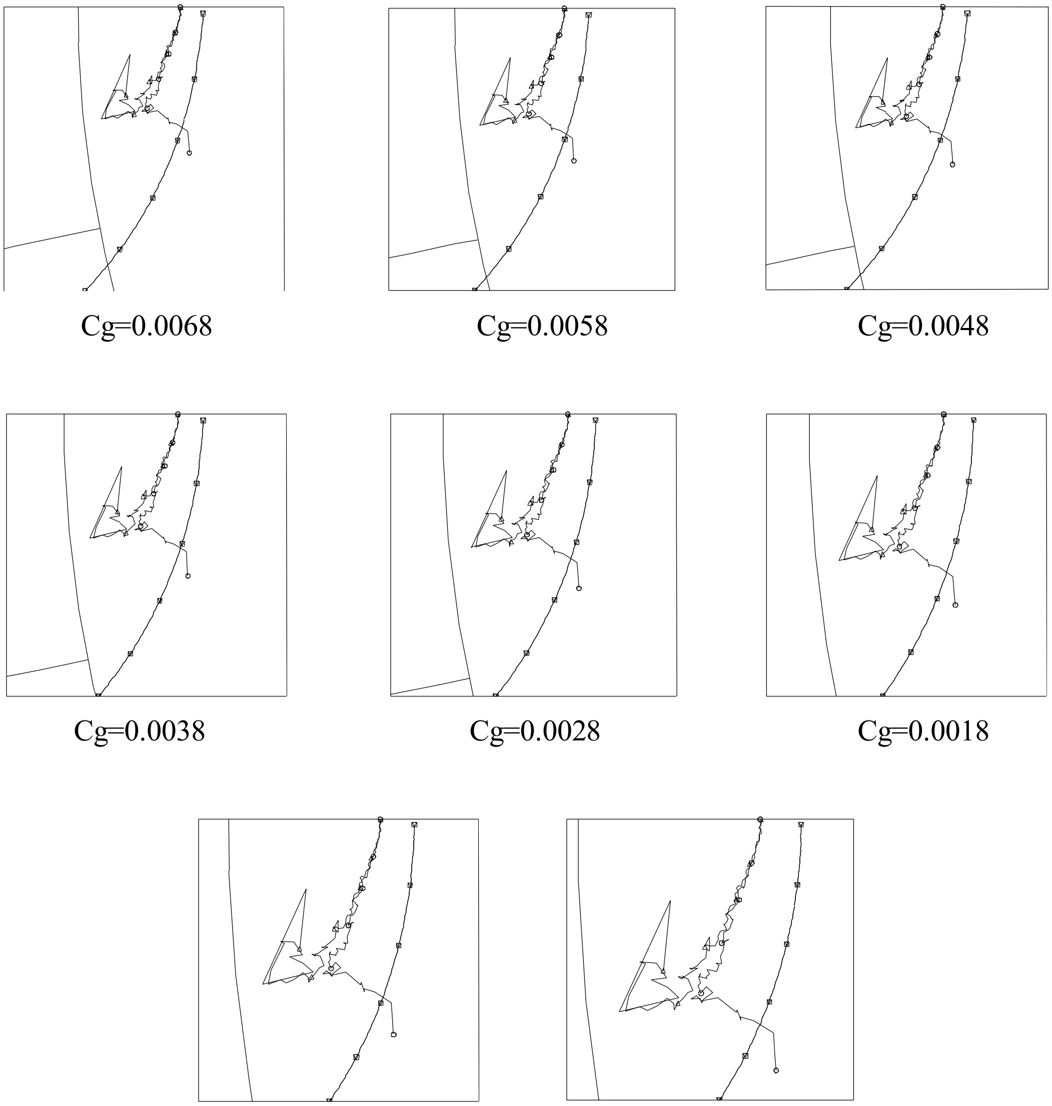

Cg=0.0068 Cg=0.0058 Cg=0.0048

Cg=0.0038 Cg=0.0028 Cg=0.0018

Cg=0.0008 Cg=0.008054

Fig. 4.75: Effect of variation of Cg_on on Z_{11}_on for an optimum Z_{11}_on.

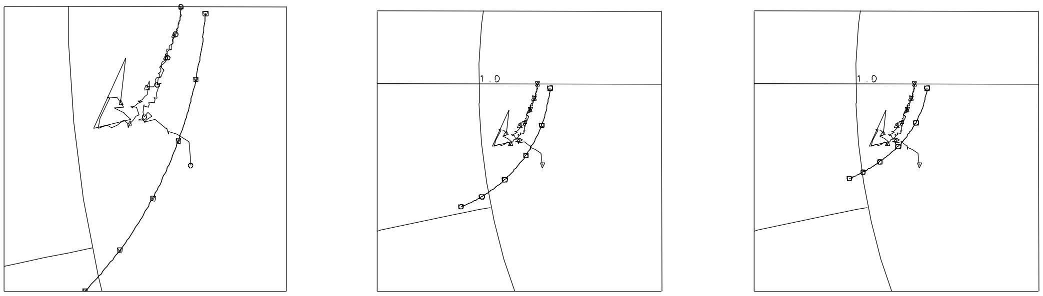

Ri=69 Ri=400 Ri=800

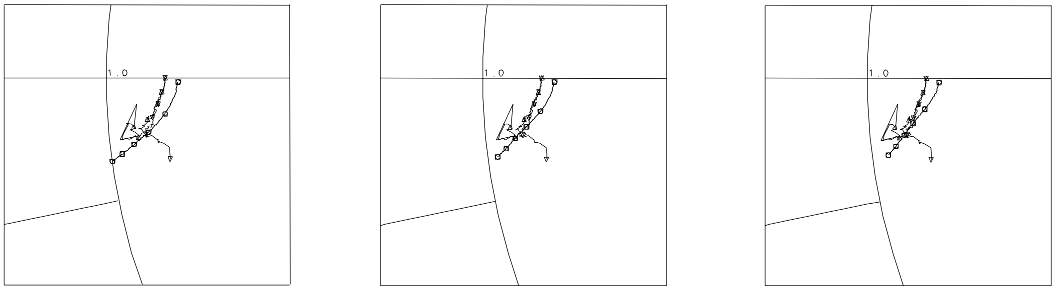

Ri=1200 Ri=1600 Ri=2000

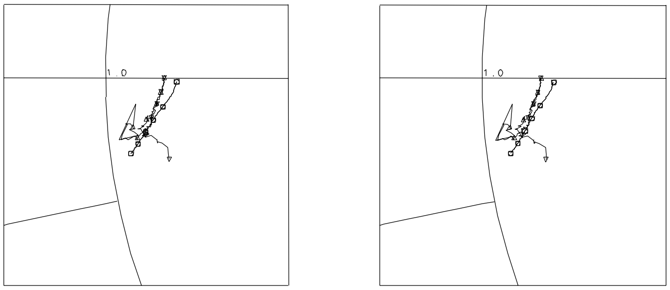

Ri=2400 Ri=2771.97

Fig. 4.76: Effect of variation of Ri_on on Z_{11}_on for an optimum Z_{11}_on.

In order to center the modeled Z_{11} and Z_{22}_on between the measured Z_{11}_on and Z_{22}_on, a combination of optimum Rsod, Ls and Cg_on must be found. Without Ls, the modeled Z_{11} and Z_{22}_on branch cannot bend as needed to improve the fit. On the other hand, Ls optimized individually cannot provide the necessary tilt of Z_{11}_on. This requires the contribution from Rsod, Cg_on and Ls. Fig. 4.77 explains this phenomenon for the 3x100. It was also found that a combination of a variable microstrip line length at the drain (or source) terminal with Cg_on and

Rds_on helped center the Z_{11}_on branch to improve the fit. However Ls proves to be more effective than the microstrip line parameter in fitting Z_{11}_on (faster optimization and smaller fit error).

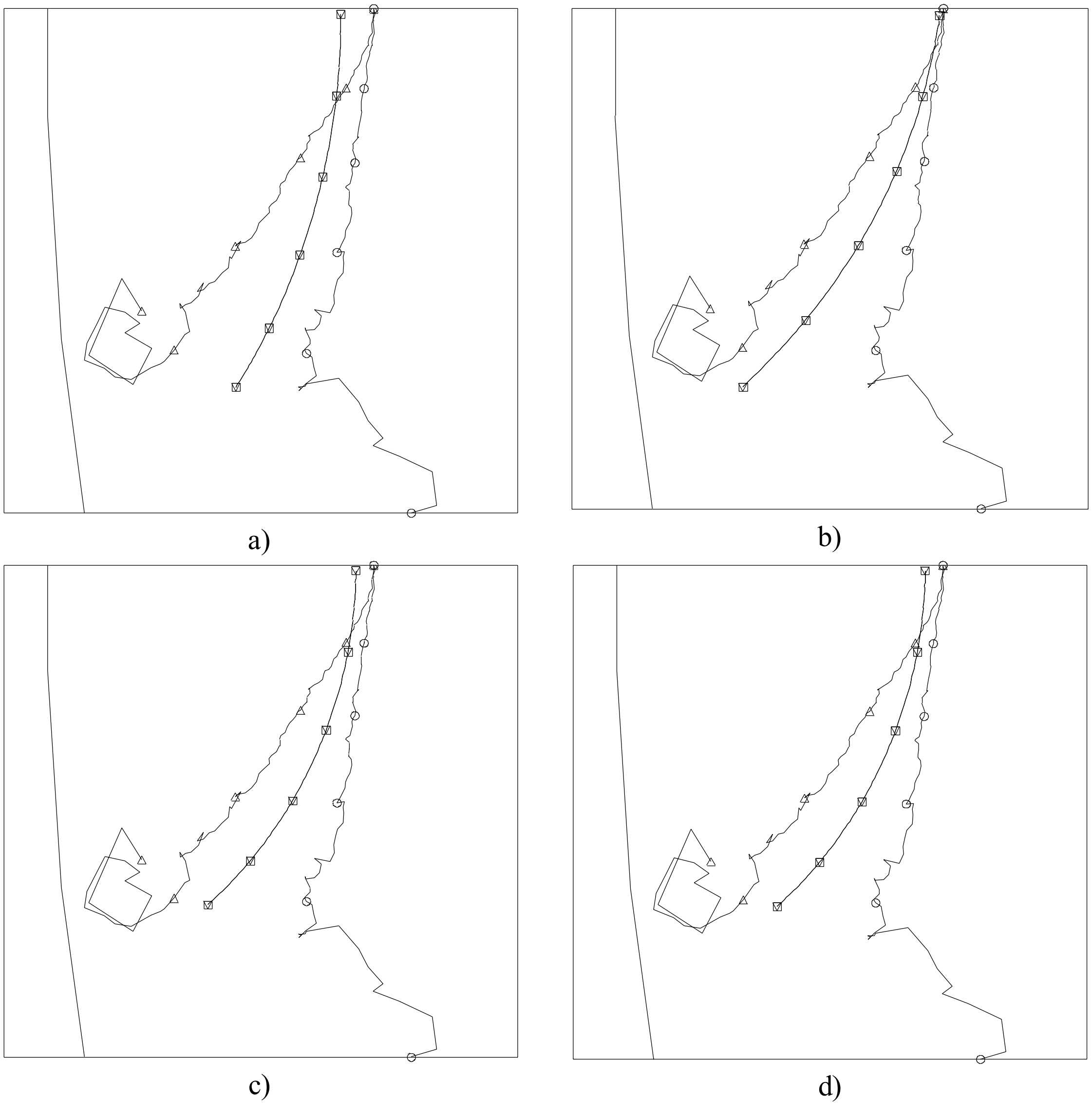
a) b) c) d)

Fig. 4.77: Optimization of Z_{11}_on. a) Without inductances, b) with inductances, c) with inductances leaving only Rs, Cg_on, Rds_on, and the inductances variable (parameters values as previously optimized model), d) with inductances leaving only Rg, Rs,_on parameters, and the inductances variable (parameters values as previously optimized model).

4.3.9.2 Case study 2: trade-off between Rs and Rds_on

A trend study was conducted to verify if Rs and Rds_on could be combined into a single resistance. Again, the 3x100 measured data was used for the fit.

The three following cases use the previously optimized parameters for the 3x100 as starting values. The optimum Rs and Rds_on are as given:

1) Rs is fixed to 0 and all other parameters are kept constant: Rds_on=5.9466.
2) The optimization range is from 0 to 10 for Rs and Rds_on, and all other variables are kept constant: Rds_on=5.9458 and Rs=8.062x10^{-6}.
3) The optimization range is from 0 to 10 and all variables are left variable: Rds_on=5.957796566547 and Rs=2.248x10^{-5}.

As seen from the previous results, setting Rs to 0 does not seem to affect the fit. The following cases use the measured data from the 3x100 except that the starting values for all parameters are 0:

4) Rds_off is constrained from 800,000 to 5,000,000: Rds_on=5.8066 and Rs=0.022 .
5) More random optimizations than case 4) alternating with gradient optimizations with Rds_off constrained from 0 to 5,000,000: Rds_on=5.7735, Rs=6.411x10^{-5}.

Since smaller FETs present higher a resistivity, the previous 5 cases were repeated for the 1 gate finger FET 1x25 as a worst case for the sensitivity to Rs:

1) Rds_on=69.6627 and Rs=0 (fixed). The fit for the magnitude of S_{21}_on is not as good.
2a) Rds_on=60.0794 and Rs=2.935 (all other parameters are fixed).
2b) Rds_on=67.4572 and Rs=0 (Rs and all other parameters are fixed). The phase and magnitude_on do not look very good for S_{21}.
3) Rds_on=63.4015 and Rs=3.155. The fit on the magnitude of S_{21}_on is not very good.
4) Rds_on=55.799 and Rs=4.967.

The sum of Rds_on and Rs is not a constant for smaller FETs (such as 1x25) with high resistance values. If Rs varies and Rds_on is kept fixed to 0 with all other parameters fixed to their previously optimized values, then Rs=30. In this case, the fit suffers enormously for the ON and OFF phase.

Two other cases comparable to case 3) were studied for the 1x25. All the parameters are left to vary from the optimized values and Rs is set to 0: a) Rds_on=66.0441 (rds_on is optimized from the starting value of 67.4572 from the previously optimized case; b) Rds_on=66.0575 (rds_on starting value is 0).

A good fit is obtained for these two last cases since the other parameters could adjust to improve the fit despite Rs being fixed to 0. Also, now the Rds_on compares well with the sum of Rds_on and Rs from case 3) (about 66) suggesting a possible combination of Rds_on and Rs into a single resistance in the model.

The effect of Rs and Rds_on on Z_{11} and Z_{22} is shown in the following figures. Fig. 4.78 illustrates the fit from setting Rs equal to 0 and letting Rds_on be finite. Fig. 4.79 presents the errors in Z_{11} and Z_{22} for a finite optimized Rs and Rds_on equal to 0.

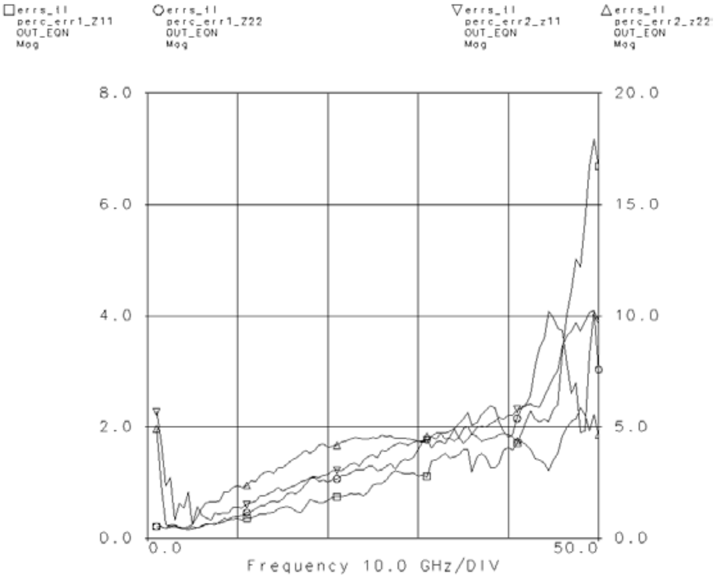

Fig. 4.78: Errors in Z_{11} and Z_{22} with Rs equal to 0 and Rds_on optimized to a finite value.

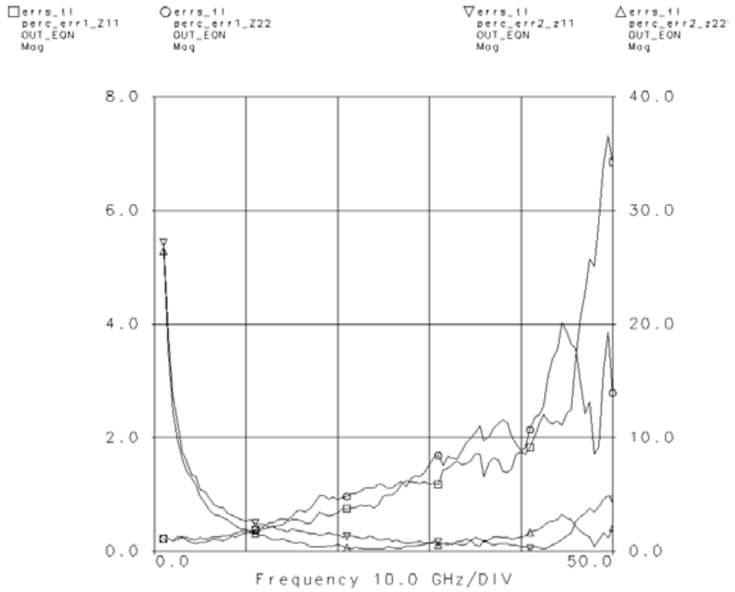

Fig. 4.79: Errors in Z_{11} and Z_{22} with Rds_on equal to 0 and Rs optimized to a finite value.

4.3.9.3 Case study 3: non-sensitive parameters and optimum weight distribution

The previous study case suggests that Rs is not a sensitive parameter even for the smaller FETs. Following this trend a third study was conducted using Rs=0 for the 3 fingers FET set in order to eliminate other non-sensitive parameters and find an optimum weight distribution to fit Z_{11} and S_{21}. The following conditions are set for this study: the starting values are previously optimized values for each FET size and the optimization range is from 5 to 40 GHz. Also, Rds_off is left unconstrained from a small starting value of 100,000. All other parameters are first constrained within reasonable limits using the random optimization first (250 iterations at a time) then the gradient optimization (15 iterations the first time and 30 the following runs). The parameters are then made unconstrained and the gradient optimizer (30 iterations) alternates with the random optimizer (100 iterations) until the gradient optimizer is "terminated with zero gradient".

As was shown in section 4.3.7.2 (Variables range, optimizers, and weights), the weights on S_{21}_on magnitude and phase is a trade-off to Z_{11}, Z_{22}_on. The weight on the magnitude of S_{21}_on affects the real and imaginary parts of Z_{11}, Z_{22}_on. The weight on the phase of S_{21}_on affects mostly the imaginary part of Z_{11}, Z_{22}_on. After setting a weight of 1 for opt_err1_S21, opt_err2_S21, phase_off_S21 and mag_off_S21 (see section 4.3.3 Libra simulation setup for a description of these optimization goals), the magnitude and phase of S_{21}_on is not affected but Z_{11}, Z_{22}_off is. Leaving weights of 1 only on opt_err1(or 2)_S21, no degradation of Z_{11}, Z_{22}_on or _off is noticed. The weights for Z_{11}, Z_{22}_on and _off are set to 50 and opt_err1(or 2)_S21 are fixed to 1, leaving the magnitude and phase ON and OFF of S_{21} to be determined.

From the available documentation at the company where the project was conducted, 5% of magnitude error and ±2° of phase are tolerated for an acceptable fit of the model. This error should be better for smaller devices and worse on large ones. We can also sacrifice for other parameters to fit better the most important ones. Knowing that the S_{21} parameters are very important (mostly the phase) for the switch performance, the errors should be minimal on these transmission parameters compared to the input/output parameters. Also, measurements of S_{11}, S_{22} (mostly for the ON state) degrade after about 30 GHz and show non-symmetric behavior (S_{11} response is not superimposed on S_{22} even if both the drain and source have been deembedded up to the intrinsic region), which limits the optimization range and the error discrimination.

Having specified the maximum tolerated error over a limited frequency range of optimization, the following optimum weight distribution is found from many trials:

Opt_err1_Z11 = 50
Opt_err1_S12 = 1
Opt_err1_S21 = 1
Opt_err1_Z22 = 50
Opt_err2_Z11 = 50
Opt_err2_S12 = 1
Opt_err2_S21 = 1
Opt_err2_Z22 = 50

Phase_on_S12 = 0.025
Phase_on_S21 = 0.025
Phase_off_S12 = 0.1
Phase_off_S21 = 0.1
Mag_on_S12 = 0.1
Mag_on_S21 = 0.1
Mag_off_S12 = 0.01
Mag_off_S21 = 0.01

Z_{11}, Z_{22}_off is mostly affected by a weight on the magnitude of S_{21}_off and Z_{11}, Z_{22}_on is affected mainly by a weight on the phase of S_{21}_on.

Using the optimized weights, two cases are studied for the 3 finger set: in the first case, non-sensitive parameters, namely, Rg, all inductances, Ri_on, Cds_on, and Ri_off are set to 0; in the second, only the inductances are zeroed. Fig. 4.80 and Fig. 4.81 show the scaling error using the 3x50 as the scaling reference for the two previous cases, respectively. Fig. 4.82 and Fig. 4.83 present the corresponding parameter values. As seen in the graphs, the scaling error is always below 24%.

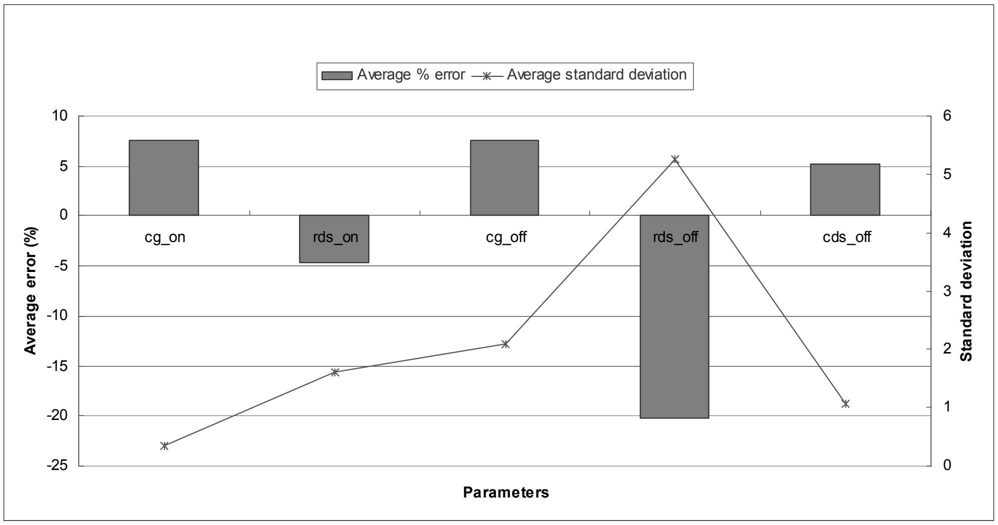

Fig. 4.80: Average percent scaling error and standard deviation for case 1.

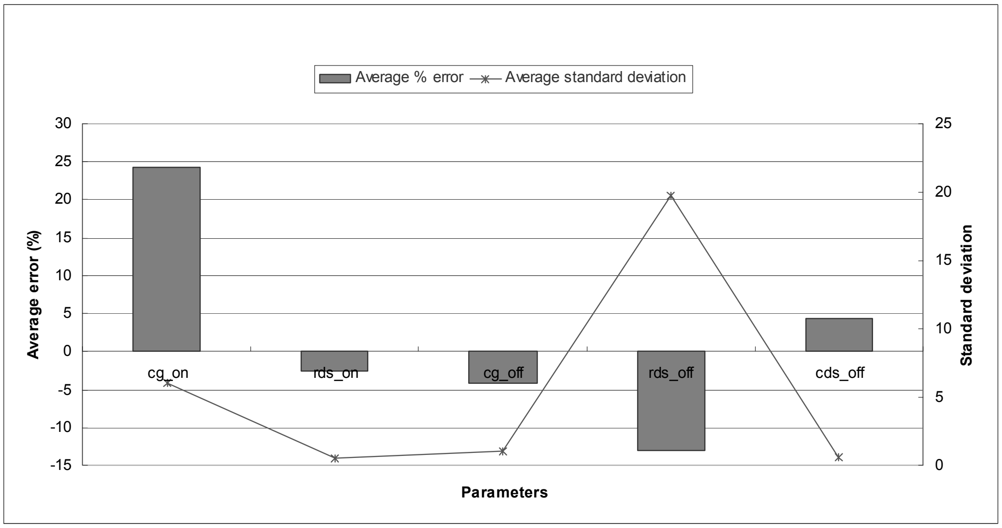

Fig. 4.81: Average percent scaling error and standard deviation for case 2.

3x50 **Scaled (reference)**		**Optimized**	
W2	150		
WG2	0.5		
N2	3		
K1		W1	150
K2		WG1	0.5
K3		N1	3
VAR RG =	0.00000000	RG =	0
VAR RS =	0.00000000	RS =	0
VAR RD =	0.00000000	RD =	0
VAR LG =	0.00000000	LG =	0
VAR LS =	0.00000000	LS =	0
VAR LD =	0.00000000	LD =	0
VAR CGS_ON =	0.00333324	CGS_ON =	0.003367658
VAR RI1_ON =	0.00000000	RI1_ON =	0
VAR RDS_ON =	11.86873585	RDS_ON =	11.86255724
VAR CGD_ON =	0.00333324	CGD_ON =	0.003367658
VAR RI2_ON =	0.00000000	RI2_ON =	0
VAR CDS_ON =	0.00000000	CDS_ON =	0
VAR CGS_OFF =	0.00267332	CGS_OFF =	0.002683892
VAR RI1_OFF =	0.00000000	RI1_OFF =	0
VAR RDS_OFF =	607650.800	RDS_OFF =	664805.8492
VAR CGD_OFF =	0.00267332	CGD_OFF =	0.002683892
VAR RI2_OFF =	0.00000000	RI2_OFF =	0
VAR CDS_OFF =	0.03584018	CDS_OFF =	0.035836247

a)

3x75 **Scaled**		**Optimized**	
W2	225		
WG2	0.5		
N2	3		
K1	1.50	W1	150
K2	1	WG1	0.5
K3	1.00	N1	3
VAR RG =	0.00000000	RG =	0
VAR RS =	0.00000000	RS =	0
VAR RD =	0.00000000	RD =	0
VAR LG =	0.00000000	LG =	0
VAR LS =	0.00000000	LS =	0
VAR LD =	0.00000000	LD =	0
VAR CGS_ON =	0.00505149	CGS_ON =	0.004680423
VAR RI1_ON =	0.00000000	RI1_ON =	0
VAR RDS_ON =	7.90837149	RDS_ON =	8.180395564
VAR CGD_ON =	0.00505149	CGD_ON =	0.004680423
VAR RI2_ON =	0.00000000	RI2_ON =	0
VAR CDS_ON =	0.00000000	CDS_ON =	0
VAR CGS_OFF =	0.00402584	CGS_OFF =	0.003783202
VAR RI1_OFF =	0.00000000	RI1_OFF =	0
VAR RDS_OFF =	443203.90	RDS_OFF =	549251.1812
VAR CGD_OFF =	0.00402584	CGD_OFF =	0.003783202
VAR RI2_OFF =	0.00000000	RI2_OFF =	0
VAR CDS_OFF =	0.05375437	CDS_OFF =	0.05134235

b)

3x100 **Scaled**		**Optimized**	
W2	300		
WG2	0.5		
N2	3		
K1	2.00	W1	300
K2	1	WG1	0.5
K3	1.00	N1	3
VAR RG =	0.00000000	RG =	0
VAR RS =	0.00000000	RS =	0
VAR RD =	0.00000000	RD =	0
VAR LG =	0.00000000	LG =	0
VAR LS =	0.00000000	LS =	0
VAR LD =	0.00000000	LD =	0
VAR CGS_ON =	0.00673532	CGS_ON =	0.006208429
VAR RI1_ON =	0.00000000	RI1_ON =	0
VAR RDS_ON =	5.93127862	RDS_ON =	6.270318246
VAR CGD_ON =	0.00673532	CGD_ON =	0.006208429
VAR RI2_ON =	0.00000000	RI2_ON =	0
VAR CDS_ON =	0.00000000	CDS_ON =	0
VAR CGS_OFF =	0.00536778	CGS_OFF =	0.004886299
VAR RI1_OFF =	0.00000000	RI1_OFF =	0
VAR RDS_OFF =	332402.92	RDS_OFF =	387180.4117
VAR CGD_OFF =	0.00536778	CGD_OFF =	0.004886299
VAR RI2_OFF =	0.00000000	RI2_OFF =	0
VAR CDS_OFF =	0.07167249	CDS_OFF =	0.06738199

c)

Fig. 4.82: Model parameters for the 3 finger FET set with non-sensitive parameters zeroed.

3x50 Scaled (reference)		Optimized	
W2	150		
WG2	0.5		
N2	3		
K1		W1	150
K2		WG1	0.5
K3		N1	3
VAR RG =	0.00000000	RG =	1.310766531
VAR RS =	0.00000000	RS =	1.369313155
VAR RD =	0.00000000	RD =	1.369313155
VAR LG =	0.00000000	LG =	0
VAR LS =	0.00000000	LS =	0
VAR LD =	0.00000000	LD =	0
VAR CGS_ON =	0.00333324	CGS_ON =	0.001945504
VAR RI1_ON =	0.00000000	RI1_ON =	1.327735677
VAR RDS_ON =	11.86873585	RDS_ON =	8.854655398
VAR CGD_ON =	0.00333324	CGD_ON =	0.001945504
VAR RI2_ON =	0.00000000	RI2_ON =	1.327735677
VAR CDS_ON =	0.00000000	CDS_ON =	2.90E-05
VAR CGS_OFF =	0.00267332	CGS_OFF =	0.001443546
VAR RI1_OFF =	0.00000000	RI1_OFF =	4.978930966
VAR RDS_OFF =	607650.800	RDS_OFF =	5272579.13
VAR CGD_OFF =	0.00267332	CGD_OFF =	0.001443546
VAR RI2_OFF =	0.00000000	RI2_OFF =	4.978930966
VAR CDS_OFF =	0.03584018	CDS_OFF =	0.036144542

a)

3x75 Scaled		Optimized	
W2	225		
WG2	0.5		
N2	3		
K1	1.50	W1	150
K2	1	WG1	0.5
K3	1.00	N1	3
VAR RG =	1.31076653	RG =	2.112161496
VAR RS =	0.91287544	RS =	0.954815913
VAR RD =	0.91287544	RD =	0.954815913
VAR LG =	0.00000000	LG =	0
VAR LS =	0.00000000	LS =	0
VAR LD =	0.00000000	LD =	0
VAR CGS_ON =	0.00291826	CGS_ON =	0.002333288
VAR RI1_ON =	0.88515712	RI1_ON =	3.121722134
VAR RDS_ON =	5.90310360	RDS_ON =	6.080143296
VAR CGD_ON =	0.00291826	CGD_ON =	0.002333288
VAR RI2_ON =	0.88515712	RI2_ON =	3.121722134
VAR CDS_ON =	0.00004347	CDS_ON =	6.00E-06
VAR CGS_OFF =	0.00216532	CGS_OFF =	0.002272286
VAR RI1_OFF =	3.31928731	RI1_OFF =	1.412273335
VAR RDS_OFF =	3515052.75	RDS_OFF =	4462638.885
VAR CGD_OFF =	0.00216532	CGD_OFF =	0.002272286
VAR RI2_OFF =	3.31928731	RI2_OFF =	1.412273335
VAR CDS_OFF =	0.05421681	CDS_OFF =	0.052045142

b)

3x100 Scaled		Optimized	
W2	300		
WG2	0.5		
N2	3		
K1	2.00	W1	300
K2	1	WG1	0.5
K3	1.00	N1	3
VAR RG =	1.31076653	RG =	0.084913092
VAR RS =	0.68465658	RS =	0.835837561
VAR RD =	0.68465658	RD =	0.835837561
VAR LG =	0.00000000	LG =	0
VAR LS =	0.00000000	LS =	0
VAR LD =	0.00000000	LD =	0
VAR CGS_ON =	0.00389101	CGS_ON =	0.002779235
VAR RI1_ON =	0.66386784	RI1_ON =	0.209508309
VAR RDS_ON =	4.42732770	RDS_ON =	4.527824765
VAR CGD_ON =	0.00389101	CGD_ON =	0.002779235
VAR RI2_ON =	0.66386784	RI2_ON =	0.209508309
VAR CDS_ON =	0.00005796	CDS_ON =	5.90E-08
VAR CGS_OFF =	0.00288709	CGS_OFF =	0.00298652
VAR RI1_OFF =	2.48946548	RI1_OFF =	0.052897558
VAR RDS_OFF =	2636289.56	RDS_OFF =	2609822.724
VAR CGD_OFF =	0.00288709	CGD_OFF =	0.00298652
VAR RI2_OFF =	2.48946548	RI2_OFF =	0.052897558
VAR CDS_OFF =	0.07228908	CDS_OFF =	0.068761185

c)

Fig. 4.83: Model parameters for the 3 finger FET set with inductance parameters zeroed.

4.3.9.4 Case study 4: search for optimum and simple models

In order to simplify the number of variables in the model and reduce the scaling and fitting errors, a study of different models was conducted using the 3x100 measured data to find an optimal configuration. The optimization setting was the following:

- All the model parameters are optimized from zero (except for Rds_off which starting value is equal to 500,000);

- The parameters are constrained within a reasonable range except for Rds_off, which is left unconstrained. The ranges are as follow: Rg: 0 to 5, Rs: 0 to 5, Ls: 0 to 0.1, Lg: 0 to 0.1, Cg_on: 0 to 0.1, Ri_on: 0 to 10, Rds_on: 0 to 10, Cds_on: 0 to 0.5, Cg_off: 0 to 1, Ri_off: 0 to 5, Cds_off: 0 to 1;
- The optimization is started with 250 iterations of random optimizer followed by 30 gradient iterations. Then, 100 random iterations alternating with 30 gradient and so on until the gradient optimizer is "terminated with zero gradient";
- The optimization weights follow the optimized distribution defined in section 4.3.8.3 (Non-sensitive parameters and optimum weight distribution);
- The optimization frequency range is from 5 to 40 GHz;
- The averaged ON and OFF measured data from the 3x100 is used.

In total, 25 different models were studied with varying configurations of topology and parameter values, while focusing on the simplification of the model. All of these circuits are included in Appendix D. After studying the effect of the parameters on the fit of the model, some of the non-sensitive parameters were eliminated to facilitate the scaling of other more sensitive parameters. The simplified models take less time to get optimized and the gradient optimizer is quickly "terminated with zero gradient". Fig. 4.84 to Fig. 4.88 present a compilation of each model's fitting performance. Selecting the optimal models from these graphs is then an easy task.

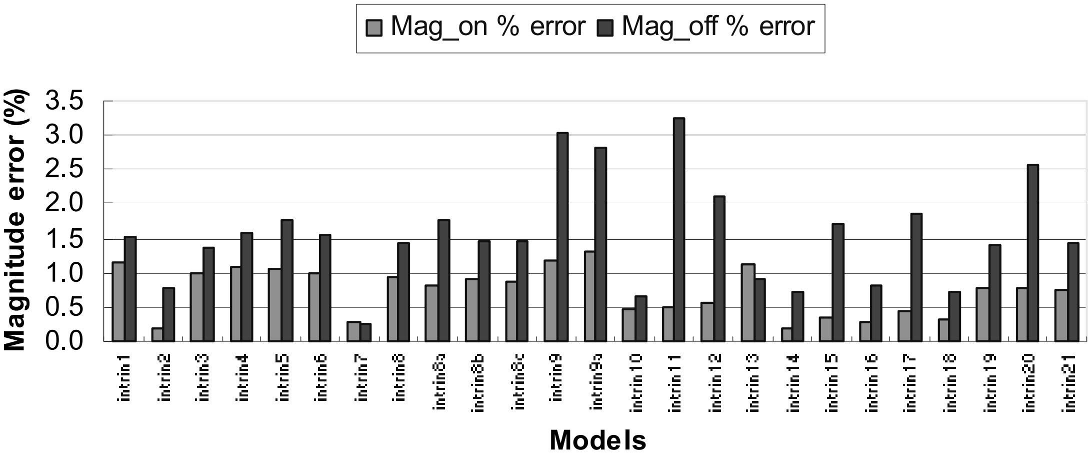

Fig. 4.84: Comparison of magnitude error.

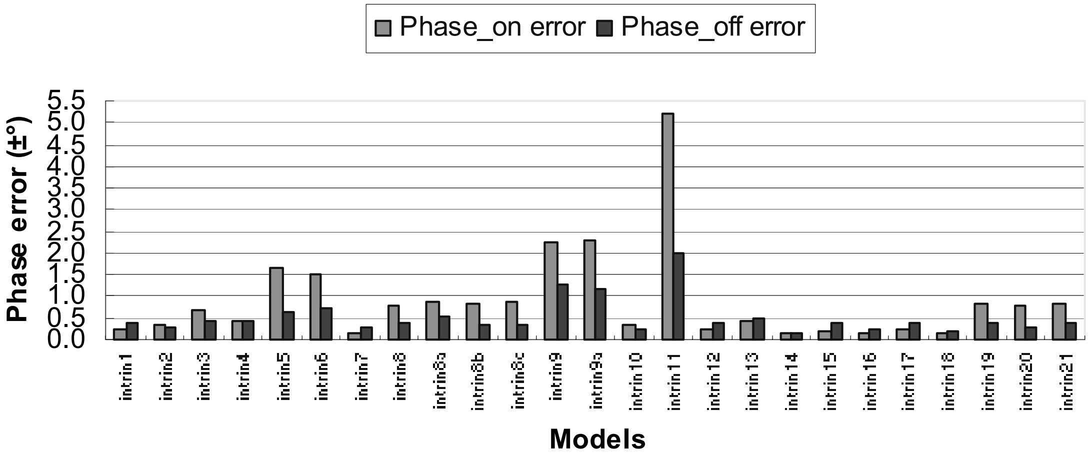

Fig. 4.85: Comparison of phase error.

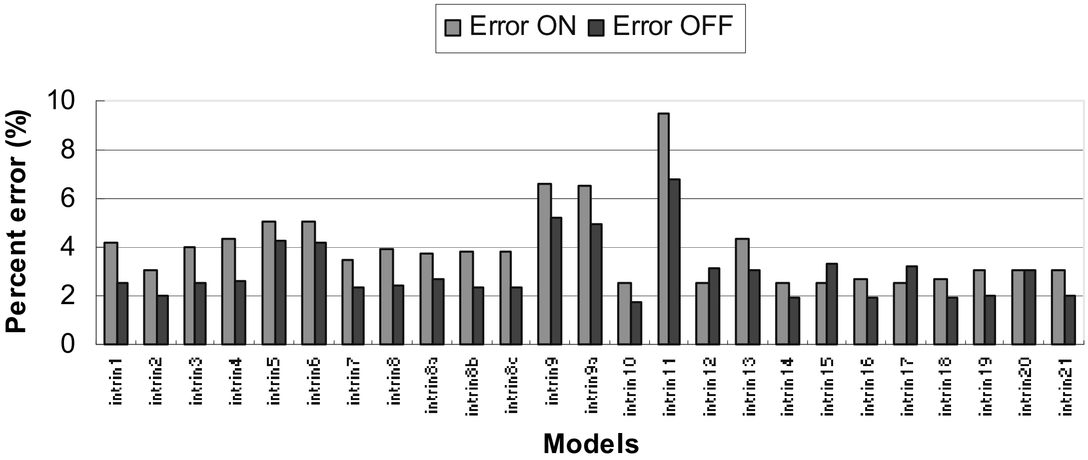

Fig. 4.86: Comparison of error ON and error OFF. This total error is to be considered as a total fitting error provided by the optimizer.

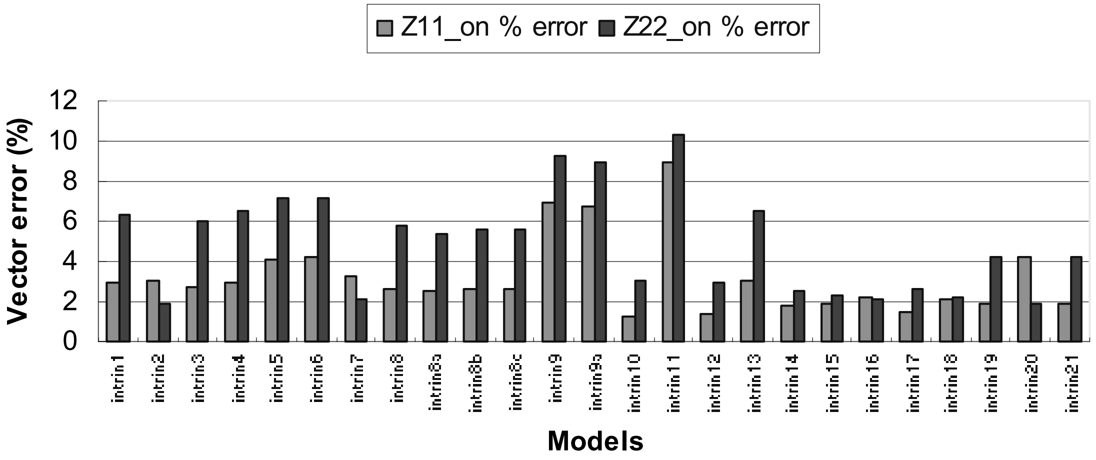

Fig. 4.87: Comparison of vector error ON state (matching).

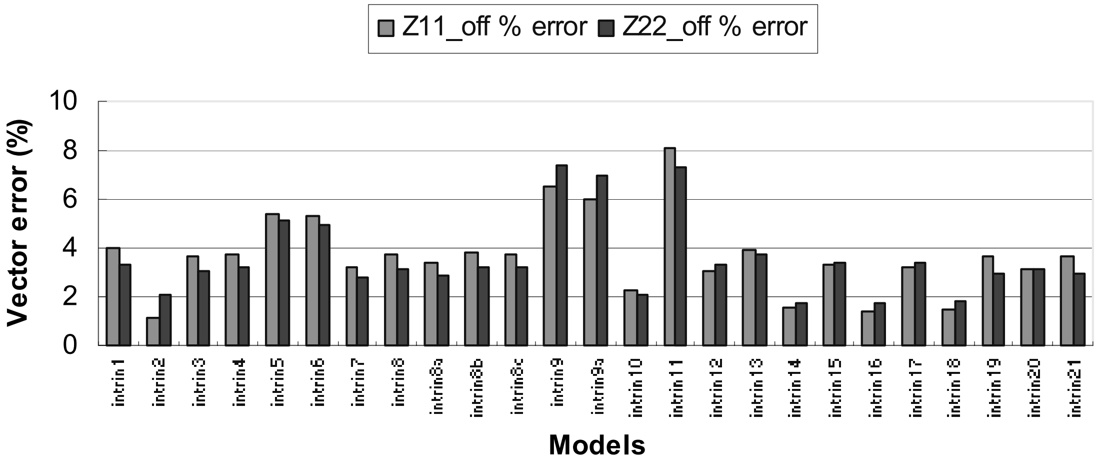

Fig. 4.88: Comparison of vector error OFF state (matching).

4.3.10 Summary and conclusions

In this project, a detailed method was used to investigate improved models for a FET switch with large scalability for broadband operation (5 to 40GHz). An existing model was used as a starting point. After defining an exhaustive modeling and scaling procedure, as well as observing the effect of each model parameter, four major cases were studied. The first case had for goal to improve the fit of the imaginary part for Z_{11} and Z_{22} ON state. This was achieved by optimizing the sensitive parameters, Cg_on and Ri_on for the 3x100 case using microstrip lines at the drain and source. Cg_on had a larger effect on the imaginary part and Rds_on helped improve the fit on the real part. Also, Ls was found to be more effective in the fit than the microstrip lengths.

In order to further simplify the model, a second study was conducted to determine the sensitivity to Rs for the 3x100 case. The study was repeated for a 1x25 as a worst case (since a smaller FET has a higher resistivity). A good fit was obtained with Rs=0, which suggests a possible combination of Rs and Rds_on.

In the third study, the goal was to eliminate other non-sensitive parameters and find an optimal weight distribution for the fit of Z_{11} and S21 in the three finger set. Two cases were studied. It was found that Rg, Ls, Rin_on, Cds_on, Ri_off did not have a large effect on the fit. The scaling error using a 3x25 for all dominant parameters was under 24% overall after setting the previous non-sensitive parameters to 0.

Finally, in the fourth study, an optimal weight distribution was determined to improve the fit for Z_{11} and Z_{22} while keeping a relatively good fit on the more important transmission parameters. Some of the non-sensitive parameters were eliminated from the model. This considerably decreased the error between the scaled and the fit values for the sensitive parameters (all scaling errors under 10 %). Different models have also been investigated in order to provide the best fit and reduce the number of variables.

It was found that a simpler model, if correctly optimized, can yield better matching and scaling for a given frequency range. From Fig. 4.84 to Fig. 4.88, the models presenting the lowest levels of total fitting errors for both states are Intrin10, Intrin14, Intrin16, and Intrin18. The circuits for these cases are shown in Fig. 4.89. All these models show an overall total error under 3%, and are simplified versions of the original three terminal switch model. Their magnitude errors are less than 8%, their phase errors less than $\pm 0.4^{o}$, their vector errors for the ON state less than 3% and their vector errors for the OFF state less than 2.2%. Intrin10 has the smallest errors, excludes the gate parameters and the intrinsic resistances Ri's. Intrin14 excludes all inductances, the gate parameters, and intrinsic resistances Ri's. Intrin16 excludes the gate parameters, the intrinsic resistances Ri's, and optimized the width and length of the drain and source microstrip lines. Intrin18 excludes the gate parameters, the intrinsic resistances Ri's, and only the length of the drain and source microstrip lines was variable (the width being fixed to the nominal 100 um). Also in Appendix D are shown the detailed fitting results for the four optimal models.

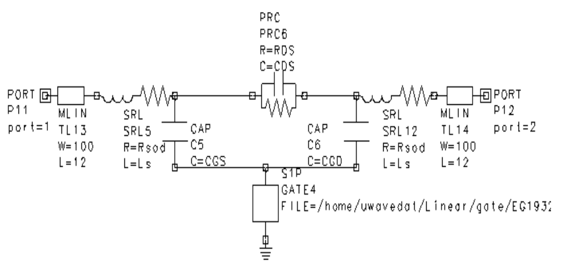

RG	0.000	RI2_ON	0.000
RS	0.920	CDS_ON	0.002
RD	0.920	CGS_OFF	0.013
LG	0.000	RI1_OFF	0.000
LS	0.015	RDS_OFF	4777.7K
LD	0.015	CGD_OFF	0.013
CGS_ON	0.016	RI2_OFF	0.000
RI1_ON	0.000	CDS_OFF	0.065
RDS_ON	3.903	ERROR_ON	2.552
CGD_ON	0.016	ERROR_OFF	1.751

a)

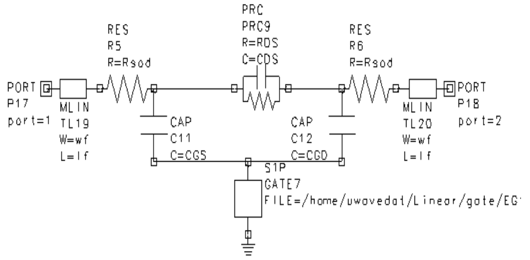

RG	0.000	RI2_ON	0.000
RS	0.722	CDS_ON	0.000
RD	0.722	CGS_OFF	0.018
LG	0.000	RI1_OFF	0.000
LS	0.000	RDS_OFF	103.1K
LD	0.000	CGD_OFF	0.018
CGS_ON	0.020	RI2_OFF	0.000
RI1_ON	0.000	CDS_OFF	0.064
RDS_ON	3.623	ERROR_ON	2.542
CGD_ON	0.020	ERROR_OFF	1.913

b)

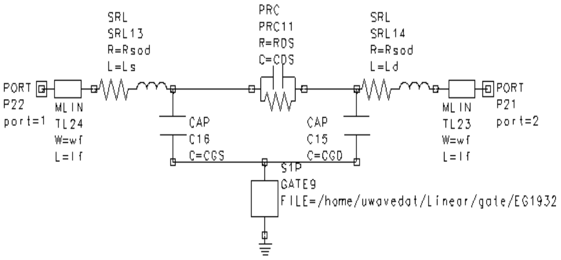

RG	0.000	RI2_ON	0.000
RS	1.031	CDS_ON	0.031
RD	1.031	CGS_OFF	0.019
LG	0.000	RI1_OFF	0.000
LS	0.020	RDS_OFF	114.8K
LD	0.020	CGD_OFF	0.019
CGS_ON	0.022	RI2_OFF	0.000
RI1_ON	0.000	CDS_OFF	0.063
RDS_ON	3.469	ERROR_ON	2.700
CGD_ON	0.022	ERROR_OFF	1.933

c)

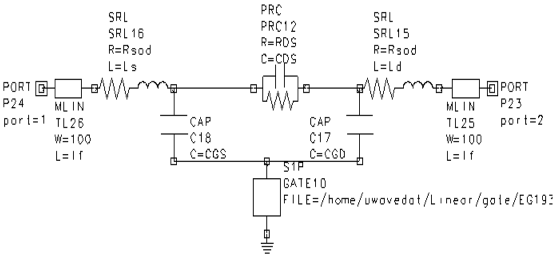

RG	0.000	RI2_ON	0.000
RS	1.023	CDS_ON	0.030
RD	1.023	CGS_OFF	0.019
LG	0.000	RI1_OFF	0.000
LS	0.018	RDS_OFF	156.6K
LD	0.018	CGD_OFF	0.019
CGS_ON	0.021	RI2_OFF	0.000
RI1_ON	0.000	CDS_OFF	0.064
RDS_ON	3.504	ERROR_ON	2.658
CGD_ON	0.021	ERROR_OFF	1.881

d)

Fig. 4.89: Optimal models. a) Intrin10, b) intrin14, c) intrin16, d) intrin18.

4.3.11 Future recommendations

The last four optimum models (Intrin10, Intrin14, Intrin16, and Intrin18) show promising features in the fitting and need to be validated for the scaling. As was shown in section 4.3.9.3 (Non-sensitive parameters and optimum weight distribution), the elimination of non-sensitive parameters from the full switch model helps in reducing the scaling error as far as the 3 finger set is concerned. This theory needs to be tested for the complete range of FET sizes from 1x25 to 9x200 to evaluate the scalability of the optimum models.

From the scaling errors charts, Rds_off usually shows the highest levels of error. Since this parameter is non-sensitive to the fit of the switch model after a minimum value, the model should be scaled using this minimum value or a fixed value above it. Leaving Rds_off unconstrained helps finding lower optimized values as opposed to leaving it constrained unless the upper boundary of the constrained range is relatively low. Otherwise, Rds_off tends to reach very high values that hit the upper limit of the constrained range. Sometimes the optimization process may take longer than necessary because of the increasing value of Rds_off. To prevent this optimization elongation, Rsd_off could be fixed to the minimum value and the other parameters left to vary.

The length of the microstrip line could be that of a single drain (or source) finger (for the 3x100 case, 12um) instead of half of the total FET length. Beyond the first drain finger delimitation, parasitic elements from air bridges and other metal layers add up and become part of the intrinsic model.

Finally, inductances may need to be reintegrated into the model to help the simultaneous fit of input/output and transmission parameters.

CHAPTER V

CONCLUSIONS

This dissertation presented the research involved for important microwave topics: WPT, phased array systems analysis, and components design and modeling. More specifically, the tasks realized were the conceptual design of a WPT system, a comparative study between two ISM frequencies, the optimization of thermally efficient split tapers for a sandwich array transmitter, the analysis of a small-scale phased array system, the design of efficient loop transitions and a multilayer filter, and the optimization of a switch model.

WPT systems are complex and require considerable documentation and in depth analysis of the numerous considerations involved. The performed study allowed the determination of the main design parameters that lead to an optimal overall DC (or AC) to DC efficiency using minimal antenna and rectenna size. The calculations were based on published charts from measured performances, design equations, and a software analysis program developed at Texas A&M University, WEFF, for the simulation of wireless power transmission. One megawatt of DC power is rectified from the efficiently collected (90%) RF power at the receiver end which is located one kilometer away from the emitter. The optimization routine used in this study to obtain the size and configuration for the transmitter and receiver was of theoretical nature and therefore constitutes a preliminary set of design values. These parameters need to be iteratively optimized experimentally with a scaled model to take into consideration second order effects that were neglected or approximated in the theoretical calculations.

It was seen that many items would affect the selection of the operating frequency in WPT systems. This useful frequency comparison shows that the majority of the considerations favor 2.45 GHz for the proposed ground-based wireless power transportation demonstration. For space to space applications, the atmospheric attenuation is no longer a consideration and the advantages of small size at 35 GHz might become more attractive. With the rectenna technology expanding in the higher frequencies for space applications, the component reliability will improve once research reaches certain maturity and components cost could significantly decrease according to market demand.

More recent sandwich array transmitters that present more compactness need to be carefully designed for thermal constraint issues. The main contributor to the overheating of electronics is the taper distribution at the antenna. Therefore, an optimized taper is an essential requirement in designing the transmitter. A study of the effects of important parameters for various aperture tapers on the collection efficiency and the sidelobe level (SLL) for safety and interference considerations was realized. The tapers considered in the study include the 10 dB Gaussian taper used as reference for the optimum collection efficiency and several split tapers that present low heat dissipation at the center. For each case, the results were calculated with WEFF, including the collection efficiency, which is expected to decrease with a split beam taper. The coefficients in the taper distribution formulas were varied in order to adjust the level of the SLL and the collection efficiency. This type of tuning was realized with GUIWEFF, a program that was developed as part of this project to help automate efficiently the optimization of the taper definition to suit the specifications. Optimal tapers were found in terms of thermal distribution and efficiency. The optimal tapers were found to be the SR for the R_T of 250 m and the OC for the 375-m case with 29 % and 39 % of maximum power density reduction relative to the 10 dB Gaussian taper as well as high collection efficiency, both above 89 %, and SLL's better than -20 dB. After analysis of the results, it can be concluded that the conventional 10 dB Gaussian taper is not optimal for WPT applications where thermal constraints must be considered.

As for WPT systems, a phased array system also requires extensive analysis before fabrication of the first prototype. Many design decisions were taken for the various components involved in the studied system. In order to choose an appropriate phased array implementation, the available test setup equipment, the necessary circuits and fixtures fabrication procedures, and the research budget were taken into account. These considerations imposed a small array design (less than 10 elements). Also, due to cost and simplicity factors, a preliminary 4x1 linear subarray was favored to a more elaborated planar array. To predict the phased array system performance and select the optimal design parameters, an in-depth study of the numerous considerations involved was realized. A statistical analysis was conducted even though the number of elements was small for an approximate evaluation of the performance of the system using simple well-established equations to rapidly investigate the effects of modifications in the configuration. For increased accuracy, a field analysis followed. Mutual coupling was not included in the analysis to avoid the complexity of the measurement setup and procedures, but a first-order evaluation of its effect on the accuracy of the analysis was done. The field analysis performance parameters were compared with the statistical results (with reference to the measured results). These parameters were the sidelobe level, the directivity loss, and the beam pointing error. The gain loss prediction accuracy using the cosine approximation was also evaluated. Overall, the measured and predicted patterns compare well.

A third problem addressed in this dissertation is the design and modeling of components that can be used in antenna arrays. Compact waveguide-to-(coax-to-)microstrip transitions that do not compromise a doubly-conformal antenna design were designed. A high-frequency end-launched loop transition was designed, simulated and tested at K-band and W-band for this purpose. This transition does not necessitate a 90° waveguide elbow since it is in-line with the feed propagation presenting a major advantage over other existing transitions. An additional advantage of the loop transition is the simplicity of construction with many mass-production approaches such as casting and molding for lower per-unit costs as opposed to other techniques that necessitate complex assembly steps. Therefore, the demonstrated transitions provide an efficient, compact and low-cost alternative to other coupling approaches currently in use. The theoretical transition efficiency was verified with measurements on a back-to-back loop transition fixture as well as on the complete system with the planar microstrip patch antenna array at K-band and W-band. The measured system gain over frequency is above 21.5 dB from 23.7 to 24.3 GHz with a peak of 21.6 dB at 24.1 GHz. The half-power beamwidths measure approximately 11.5 degrees in both principal planes. The good performance confirms the high efficiency of the designed loop. For the W-band measurements of the microstrip patch antenna array, a mm-wave extension was used to multiply the frequency range of the HP8510B® test set. The gain pattern presents a maximum gain of 25 dB and the return loss is less than 12 dB from 75.1 to 77.3 GHz with 22.2 dB return loss at 76.5 GHz. The satisfying experimental results confirm the efficiency of the loop transition and validate the simulated design.

Many wireless applications require a compact filter design featuring a sharp attenuation slope for high channel selectivity (elliptic or quasi-elliptic response). For compact design with the previous feature, a multilayer filter is preferred over a planar version. A study of the effects of stacking square ring resonators in a vertical direction was realized for a better insight of broadside coupling. From the overlap-end coupled configuration, the resonators were fold to further increase compactness. Because of the broadside coupling between the two stacked metallizations, additional poles from coupling capacitances result in a higher order filter and therefore allow sharper attenuation slopes in the frequency response. A preliminary equivalent circuit using lumped elements was obtained by inspection of the folded line filter. The circuit's geometrical parameters were varied to study their effects on the frequency response. An improved measured bandwidth from 2 to 7.5 GHz and IL of 1.2dB were obtained with the folded line filter operating at 2.45 GHz. The printed area is almost half of that of a planar ring resonator with similar response (the bandwidth is about 1.5 times larger for the folded line filter). Overall, the advantages observed in using a multilayer filter are more numerous that those found in using the planar version, mostly for applications that require high level of integration and compactness. The bottleneck is in the design and optimization since research in the characterization of multilayer configuration is still developing.

An accurate model with large scalability and broadband fitting to measured results is needed for high-speed switches applications such as high-frequency phased arrays. The research realized on the switch model was based on the existence of a preliminary, low-precision model of the FET switch. The fitting of the original three-terminal intrinsic switch model is acceptable for a frequency range of 1 to 20 GHz with an error of less than 5% for the magnitude of S_{21} and less than ±2° for the phase of S_{21}. Above 20 GHz, the phase fitting error starts to increase to an unacceptable level of ±6°. The scalability should cover a range of FET sizes (18 in total) from 1 finger x 25 μm up to 9 fingers x 200 μm. The switch frequency of operation ranges from 1 to 50 GHz. Dispersive effects at higher frequency have been taken into account and dictated the modification of the initial model by adding transmission lines. The automated optimization tools of Libra Touchstone® were used to fit the model to the corresponding measurement results. The first step was to characterize the effects of each component in the model on the performance of the switch with respect to the measurement results. The optimization process was repeated for each FET size until a satisfactory model was found for the whole frequency and scaling ranges. An optimal weight distribution was determined to improve the fit for Z_{11} and Z_{22} while keeping a relatively good fit on the more important transmission parameters. Some of the non-sensitive parameters were eliminated from the model. This considerably decreased the error between the scaled and the fit values for the sensitive parameters (all scaling errors under 10 %) since it loosen their optimization constraints. Different models have been investigated in order to provide the best fit and reduce the number of variables. The models presenting the lowest levels of total fitting errors for both states are Intrin10, Intrin14, Intrin16, and Intrin18. All these models show an overall total error under 3%, and are simplified versions of the original three terminal switch model. Their magnitude errors are less than 8%, their phase errors less than ±0.4^{o}, their vector errors for the ON state less than 3% and their vector errors for the OFF state less than 2.2%.

REFERENCES

[1] G. Pignolet, *Wireless Power Transportation*. Paris: Centre National d'Études Spatiales, Université de La Réunion, 1999.

[2] W. C. Brown, "The technology and application of free-space power transmission by microwave beam," *Proc. of the IEEE*, vol. 62, pp. 11-25, Jan. 1974.

[3] *Proceedings of Solar Power Satellite (SPS) Workshop on Microwave Power Transmission and Reception*. NASA contract NAS 1.55: 2141, Lyndon B. Johnson Space Center, Houston, Jan. 1980.

[4] G. J. Stern and R. S. Elliott, "Resonant length of longitudinal slots and validity of circuit representation: theory and experiment," *IEEE Trans. Antennas and Propagation*, vol. 33, pp. 1264-1271, Nov. 1985.

[5] W. C. Brown, "Satellite power system (SPS) magnetron tube assessment study," *NASA Contractor Report 3383*, Contract NAS8-33157, Feb. 1981.

[6] T. Yoo, "Experimental and theoretical study on 35 GHz RF-to-DC power conversion receiver for millimeter-wave beamed power transmission," Ph. D. Dissertation, Department of Electrical Engineering, Texas A&M University, 1993.

[7] N. Foukiris, *Phased Array-Based Systems and Applications*. New York: Wiley, 1997.

[8] R. J. Mailloux, "Antenna array architecture," *Proc. of the IEEE*, vol. 80, pp. 163-172, Jan. 1992.

[9] A. Agrawal, R. Clark, and J. Komiak, "T/R module architecture tradeoffs for phased array antennas," *IEEE MTT-S Int. Microwave Symp. Dig.*, San Francisco, CA, pp. 995-998, 1996.

[10] J. L. Butler and R. Lowe, "Beam forming matrix simplifies design of electronically scanned antennas," *Electronic Design*, vol. 9, pp. 170-173, April 1961.

[11] R. Tang and R. W. Burns, "Array technology," *Proc. of the IEEE*, vol. 80, pp. 173-182, Jan. 1992.

[12] D. H. Schaubert, "Wide-band phased arrays of vivaldi notch antennas," *Proc. of the 10th Int. Conf. on Ant. and Prop.*, Edinburgh, UK, pp. 1.6-1.12, 1997.

[13] R. C. Hansen, *Phased Array Antennas*. New York: Wiley, 1998.

[14] R. J. Mailloux, *Phased Array Antenna Handbook.* Norwood, MA: Artech House, 1994.

[15] I. Bahl and P. Bhartia, *Microwave Solid State Circuit Design*. New York: Wiley, 1988.

[16] K. K. Chan, R. Martin, and K. Chadwick, “A broadband end launched coaxial-to-waveguide transition for waveguide phased arrays,” *IEEE AP-S Int. Symp. Dig.*, Atlanta, GA, pp. 1390-1393, 1998.

[17] S. M. Saad, “A more accurate analysis and design of coaxial-to-rectangular waveguide end launcher,” *IEEE Trans. Microwave Theory Tech.*, vol. 38, pp. 129-134, Feb. 1990.

[18] M. D. Deshpande, B. N. Das, and G. S. Sanyal, “Analysis of an end launcher for an X-band rectangular waveguide,” *IEEE Trans. Microwave Theory Tech.*, vol. 27, pp. 731-735, Aug. 1979.

[19] J. A. Curtis and S. J. Fiedziuszko, “Multi-layered planar filters based on aperture coupled, dual mode microstrip or stripline resonators,” *IEEE MTT-S Int. Microwave Symp. Dig.*, Albuquerque, NM, pp. 1203-1206, 1992.

[20] M. Tran and C. Nguyen, “Modified broadside-coupled microstrip lines suitable for MIC and MMIC applications and a new class of broadside-coupled band-pass filters,” *IEEE Trans. Microwave Theory and Tech.*, vol. 41, pp. 1336-1342, Aug. 1993.

[21] R. K. Settaluri, A. Weisshaar, and V. K. Tripathi, “Compact multi-level folded-line bandpass filters,” *IEEE MTT-S Int. Microwave Symp. Dig.*, Boston, MA, pp. 311-314, 2000.

[22] M. S. Alam, M. Koshiba, K. Hirayama, and Y. Hayashi, “Hybrid-mode analysis of multilayered and multiconductor transmission lines,” *IEEE Trans. Microwave Theory and Tech.*, vol. 45, pp. 205-211, Feb. 1997.

[23] R. Williams, *Modern GaAs Processing Methods*. Boston, MA: Artech House, 1990.

[24] G. Dambrine, A. Cappy, F. Heliodore, and E. Playez, “A new method for determining the FET small-signal equivalent circuit,” *IEEE Trans. Microwave Theory and Tech.*, vol. 36, pp. 1151-1159, July 1988.

[25] G. Goubau and F. Schwering, *Microwave Power Engineering*. New York: Academic Press, vol. 1, pp. 241-255, 1968.

[26] G. D. Arndt and E. M. Kerwin, “Applications of low-earth-orbit power transmission,” *Space Power*, vol. 8, no. 3, pp. 137-155, 1986.

[27] W. C. Brown and E. E. Eves, “Beamed microwave power transmission and its application to space,” *IEEE Trans. Microwave Theory Tech.*, vol. 40, pp. 1239-1250, June 1992.

[28] A. M. Brown, "A systems engineering approach to the analyses of wireless power transmission systems," Master of Science Thesis, Department of Electrical Engineering, Texas A&M University, August 1993.

[29] W. C. Brown, "Experiments involving a microwave beam to power and position a helicopter," *IEEE Trans. Aerospace and Electronics Systems*, vol. 5, pp. 692-702, Sept. 1969.

[30] J. C. McCleary, J. O. McSpadden, and K. Chang, "WEFF: Computer simulation of wireless power transmission systems," Technical Report, Electromagnetics and Microwave Laboratory, Texas A&M University, 1991.

[31] J. C. McCleary, "Studies on beam propagation pertaining to beamed microwave power transmission and open resonator quasi-optics," Master of Science Thesis, Department of Electrical Engineering, Texas A&M University, 1991.

[32] J. A. Navarro and K. Chang, *Integrated Active Antennas and Spatial Power Combining*. New York: Wiley, 1996.

[33] J. O. McSpadden, T. Yoo, and K. Chang, "Theoretical and experimental investigation of a rectenna element for microwave power transmission," *IEEE Trans. Microwave Theory Tech.*, vol. 40, pp. 2359-2366, Dec. 1992.

[34] J. O. McSpadden and K. Chang, "Wireless power transmission demonstration at 5.8 GHz and 35 GHz," Technical Report, Electromagnetics and Microwave Laboratory, Texas A&M University.

[35] D. M. Pozar, *Microwave Engineering*. Addison-Wesley Publishing Company, New York, p. 2, 1993.

[36] R. M. Dickinson, "Issues in microwave power systems engineering," *IEEE AES Systems Magazine*, vol. 12, pp.10-14, May 1997.

[37] P. Koert and J. T. Cha, "Millimeter wave technology for space power beaming," *IEEE Trans. Microwave Theory Tech.*, vol. 40, pp. 1251-1258, June 1992.

[38] N. Fourikis, *Phased Array-Based Systems and Applications*. New York: Wiley, 1997.

[39] M. Abramowitz, *Handbook of Mathematical Functions, with Formulas, Graphs, and Mathematical Tables*. New York: Dover Publications, 1965.

[40] C. A. Balanis, *Antenna Theory: Analysis and Design*. New York: Wiley, 1997.

[41] C. Q. Li, S. H. Li, and R. G. Bosisio, "CAD/CAE design of an improved, wideband Wilkinson power divider," *Microwave J.*, vol. 27, pp. 125-135, Nov. 1984.

[42] J. B. L. Rao, G. V. Trunk, and D. P. Patel, "Two low-cost phased arrays", *IEEE Int. Symp. on Phase Array Systems and Technology*, Boston, MA, pp.119-124, 1996.

[43] A. K. Agrawal, "Active phased array architecture for high reliability", *IEEE Int. Symp. on Phase Array Systems and Technology*, Boston, MA, pp.159-162, 1996.

[44] J. A. Navarro and K. Chang, *Integrated Active Antennas and Spatial Power Combining*. New York: Wiley, 1996.

[45] H. E. Schrank, "Low sidelobe phased array antennas," *IEEE Ant. and Prop. Society Newsletter*, pp.5-9, April 1983.

[46] D. M. Pozar, "Aperture coupled waveguide feeds for microstrip antennas and microstrip couplers," *IEEE AP-S Int. Symp. Dig.*, Baltimore, MD, pp. 700-703, 1996.

[47] R. B. Keam and A. G. Williamson, "Broadband design of coaxial line/rectangular waveguide probe transition," *IEE Proc. Mic., Ant., and Prop.*, vol. 141, pp. 53-58, Feb. 1994.

[48] B. N. Das and G. S. Sanyal "Coaxial-to-waveguide transition (end-launcher type)," *Proc. IEE*, vol. 123, no. 10, pp. 984-986, 1976

[49] L.-H. Hsieh and K. Chang, "Compact dual-mode elliptic-function bandpass filter using a single ring resonator with one coupling gap," *Electronics Lett.*, vol. 36, pp. 1626-1627, Sept. 2000.

APPENDIX A

DETAILED ALGORITHM OF GUIWEFF

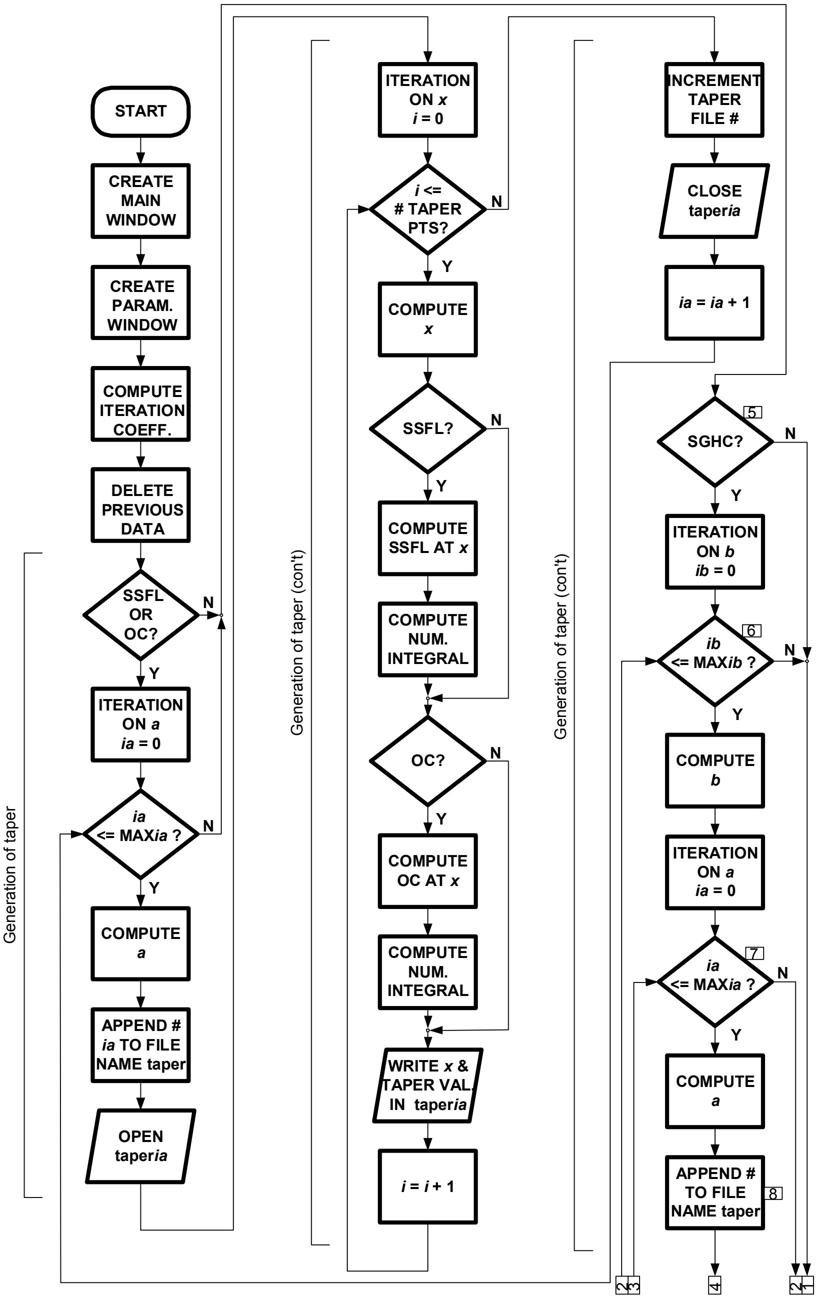

Fig. A.1: Detailed algorithm of GUIWEFF.

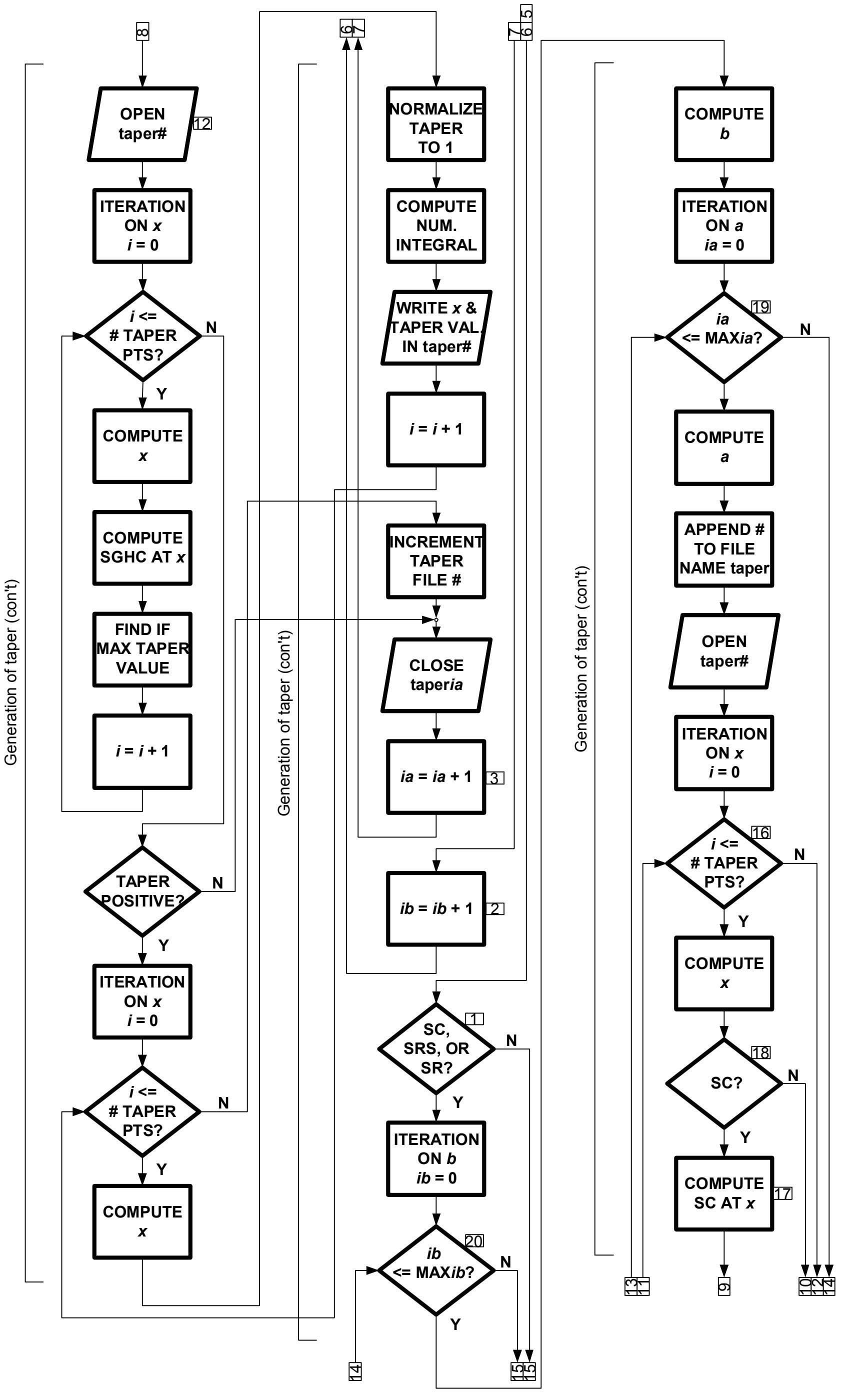

Fig. A.1: (Continued).

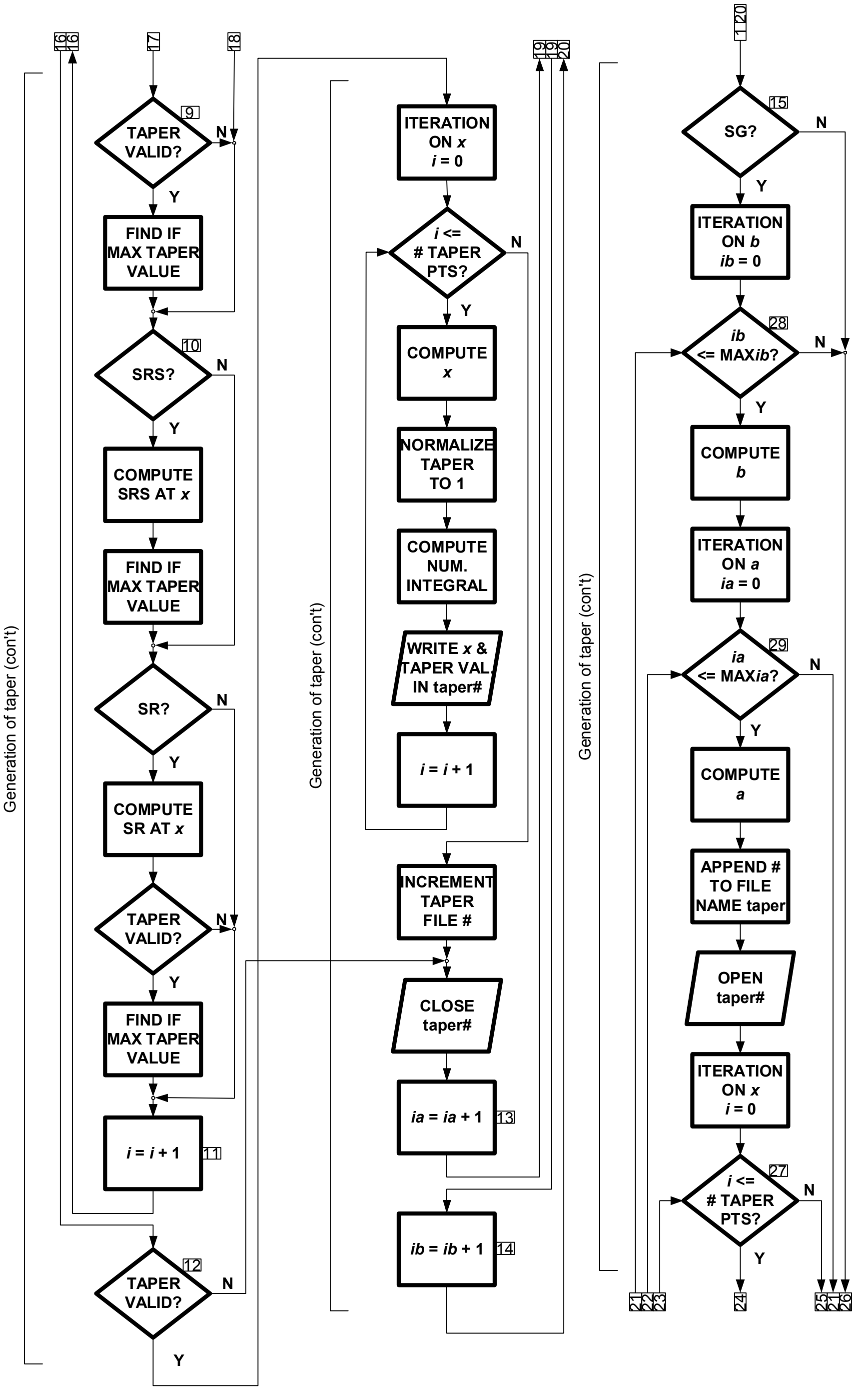

Fig. A.1: (Continued).

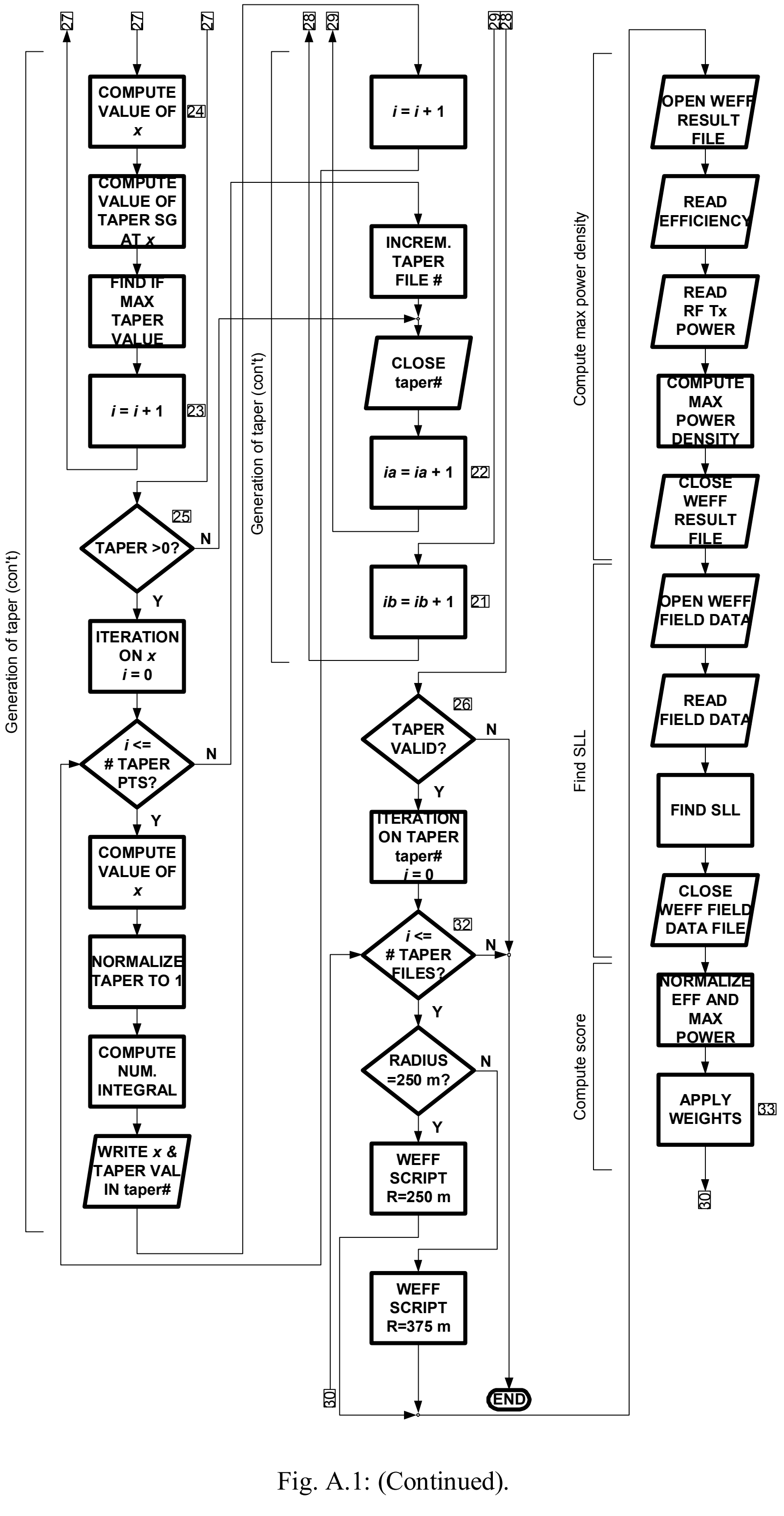

Fig. A.1: (Continued).

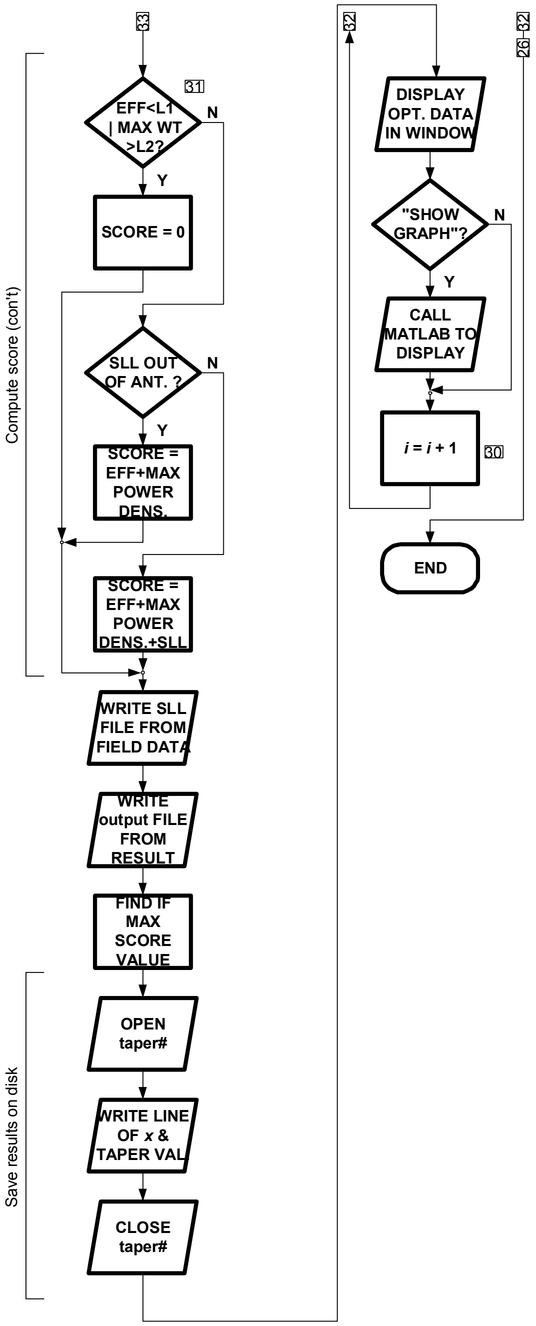

Fig. A.1: (Continued).

APPENDIX B

RESULTS FROM GUIWEFF FOR OPTIMIZED TAPERS

Fig. B.1 to Fig. B.10 show optimized tapers results for R_T= 250 m. Also, Fig. B.11 to Fig. B.21 show optimized tapers results for R_T= 375 m.

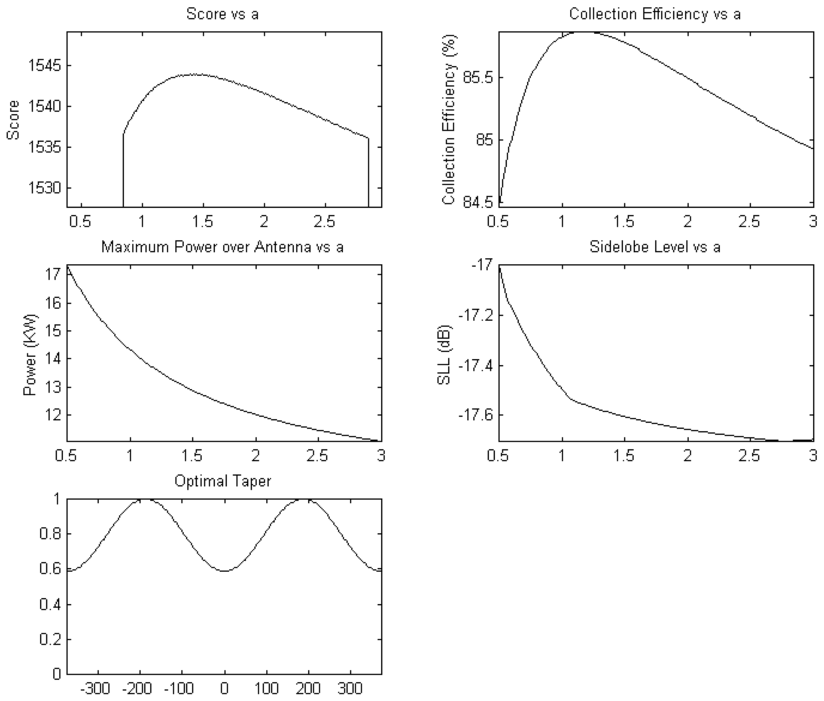

Fig. B.1: Results from GUIWEFF for the case of SSFL with optimized taper and antenna radius of 250m.

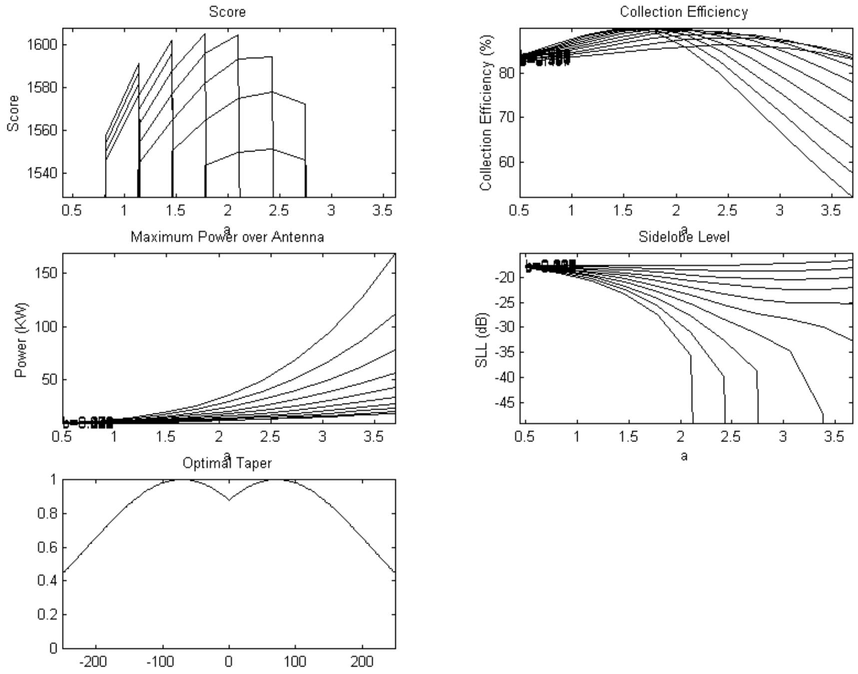

Fig. B.2: Results from GUIWEFF for the case of SG0.5, optimized taper and antenna radius of 250m.

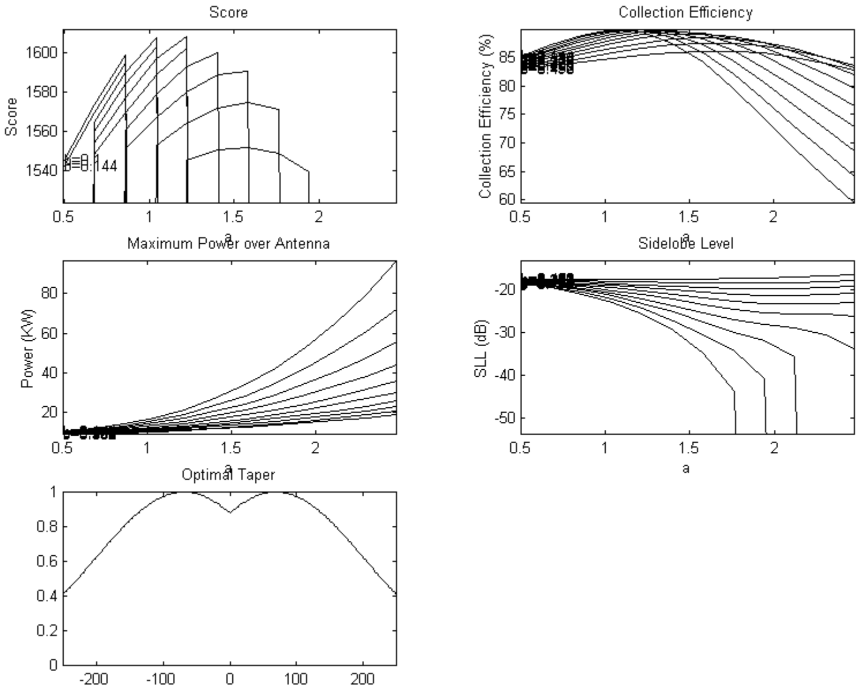

Fig. B.3: Results from GUIWEFF for the case of SG1.1513, optimized taper and antenna radius of 250m.

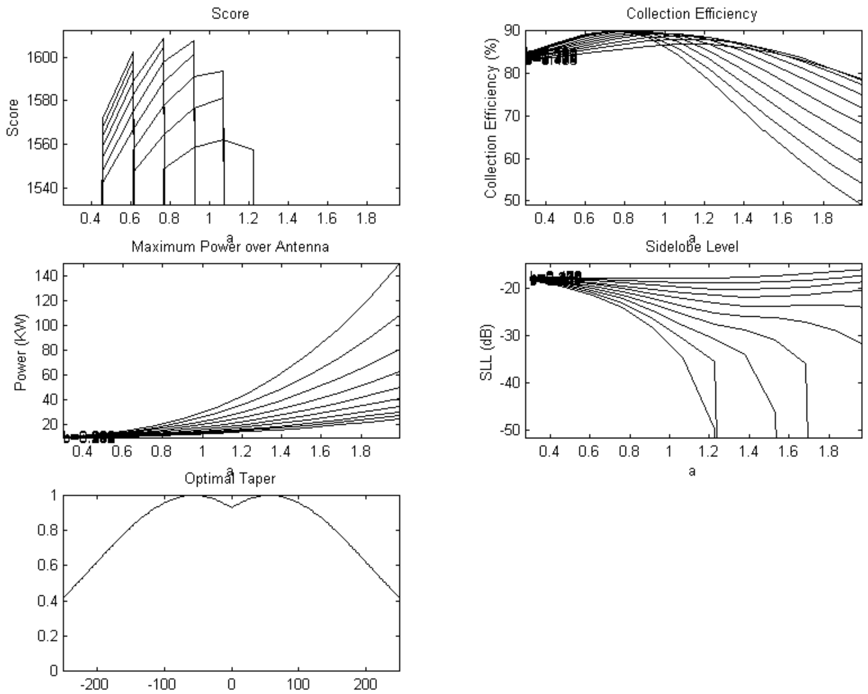

Fig. B.4: Results from GUIWEFF for the case of SG2.5, optimized taper and antenna radius of 250m.

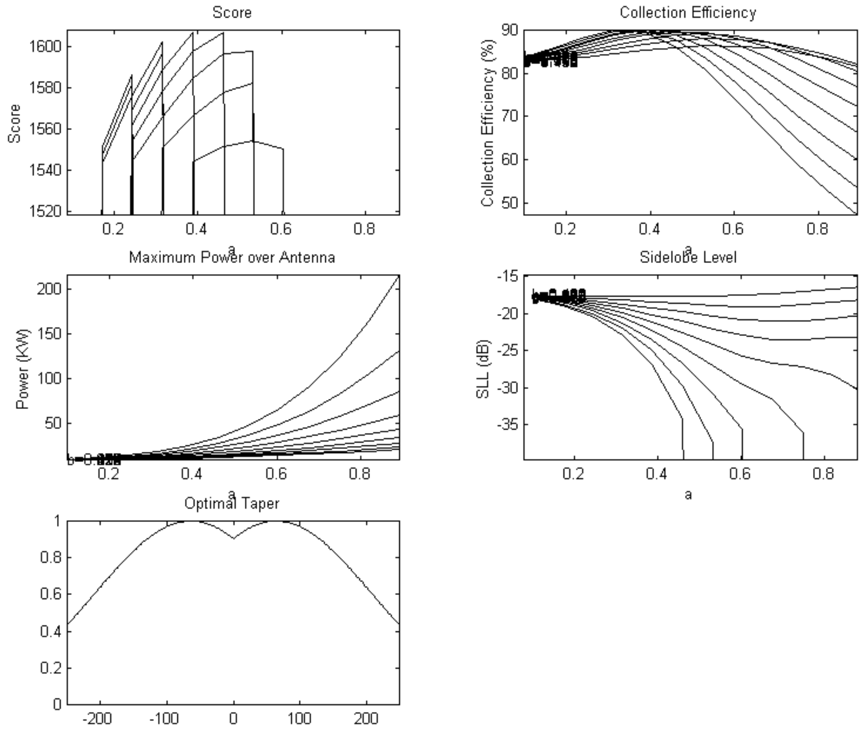

Fig. B.5: Results from GUIWEFF for the case of SG10, optimized taper and antenna radius of 250m.

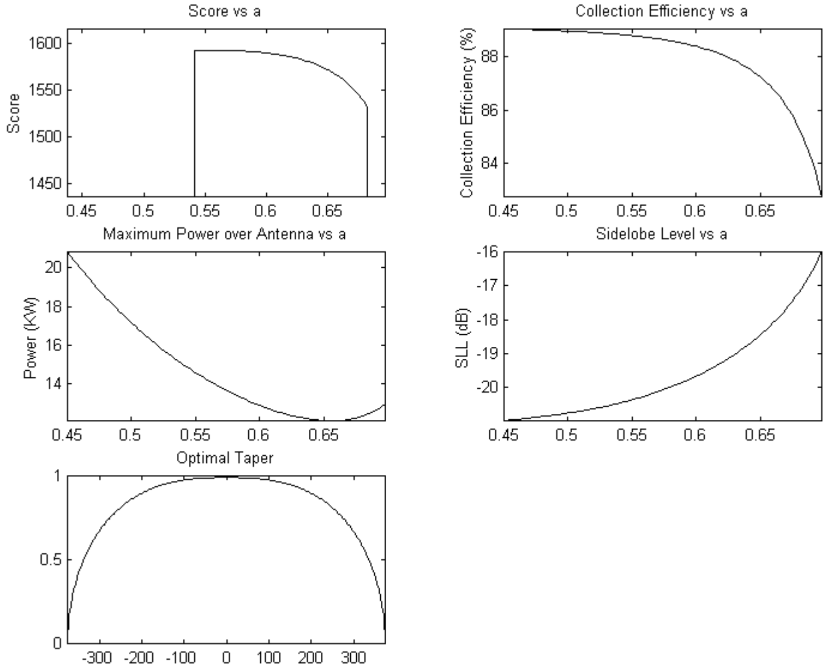

Fig. B.6: Results from GUIWEFF for the case of OC with optimized taper and antenna radius of 250m.

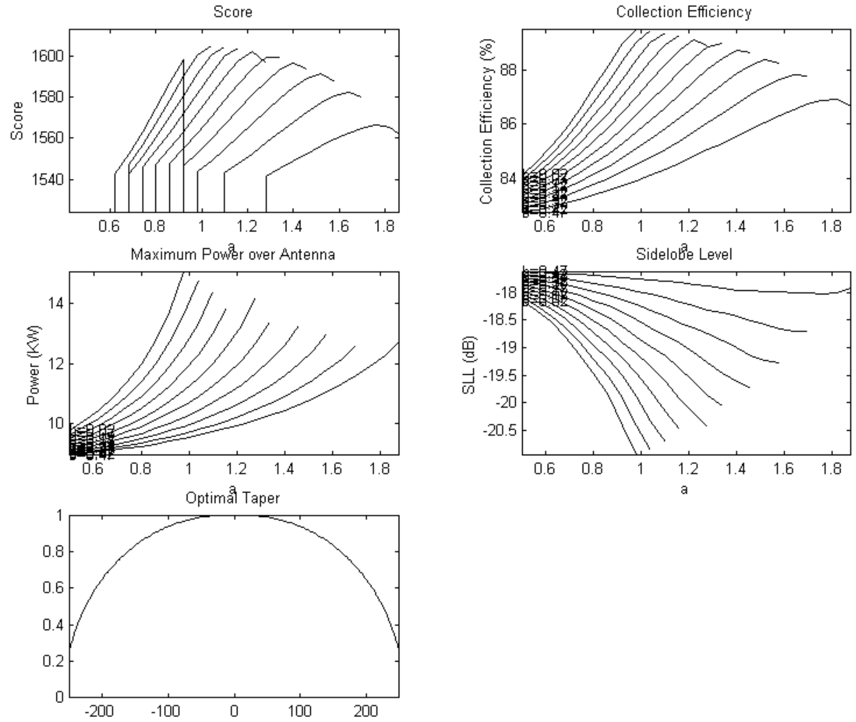

Fig. B.7: Results from GUIWEFF for the case of SC with optimized taper and antenna radius of 250m.

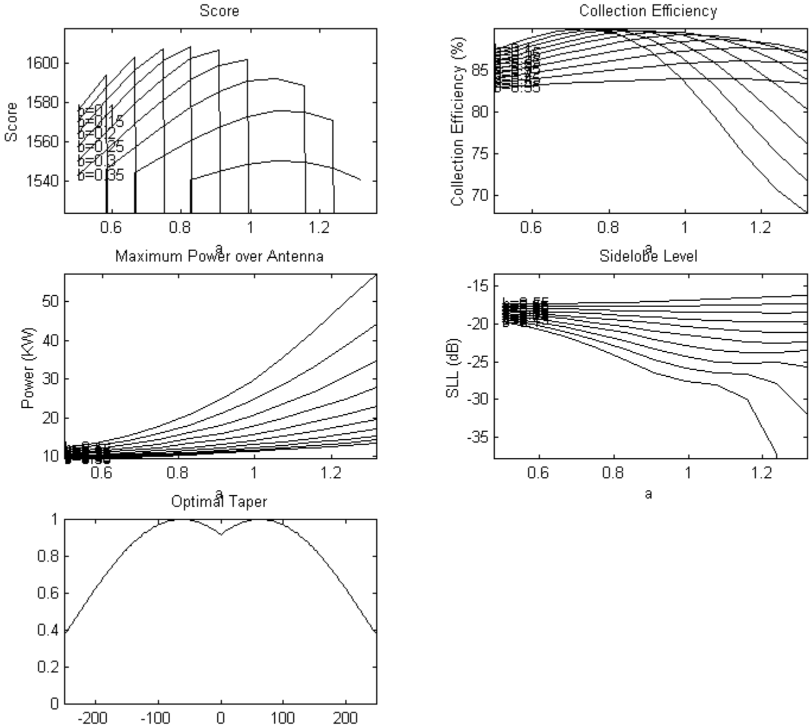

Fig. B.8: Results from GUIWEFF for the case of SRS with optimized taper and antenna radius of 250m.

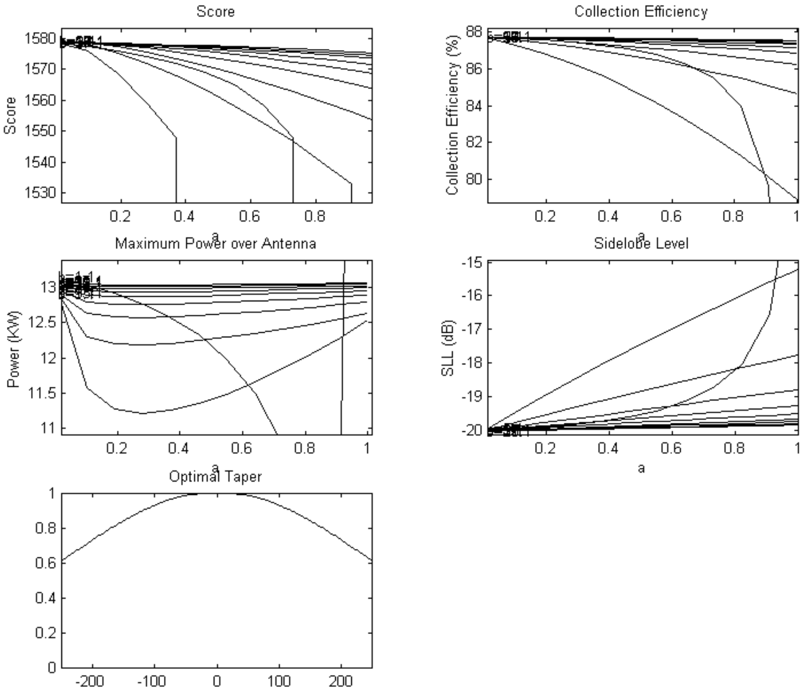

Fig. B.9: Results from GUIWEFF for the case of SGHC, optimized taper and antenna radius of 250m.

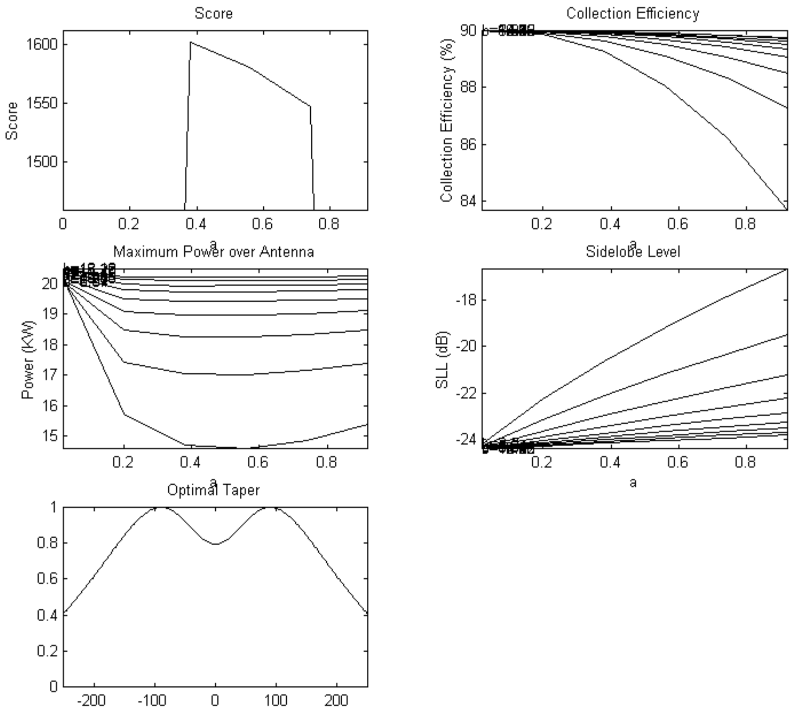

Fig. B.10: Results from GUIWEFF for SGHC1.1513, optimized taper and antenna radius of 250m.

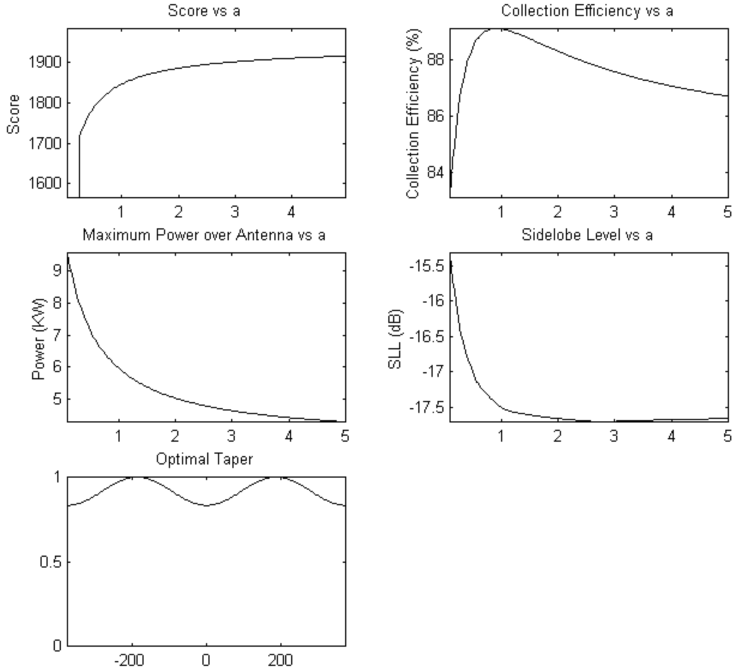

Fig. B.11: Results from GUIWEFF for the case of SSFL with optimized taper and antenna radius of 375m.

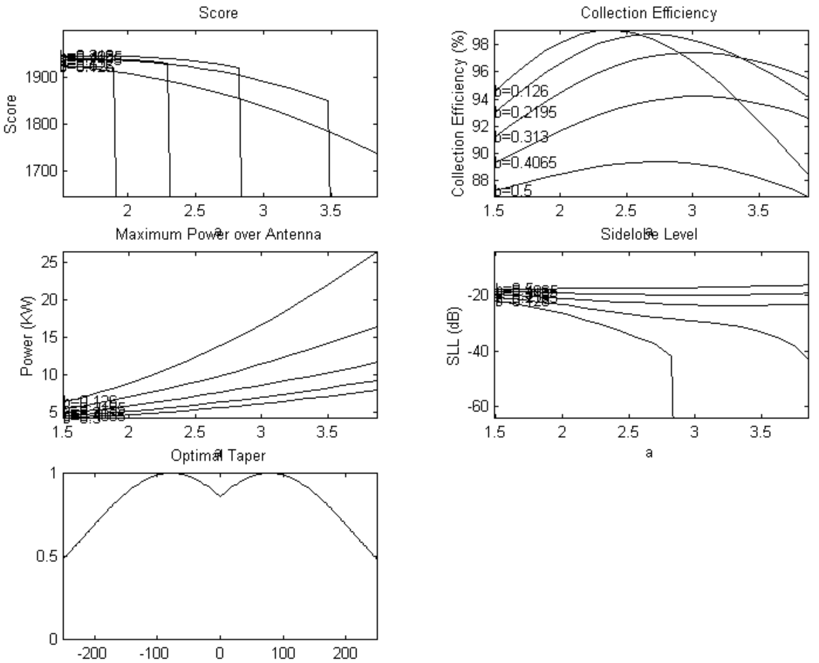

Fig. B.12: Results from GUIWEFF for the case of SG0.5, optimized taper and antenna radius of 375m.

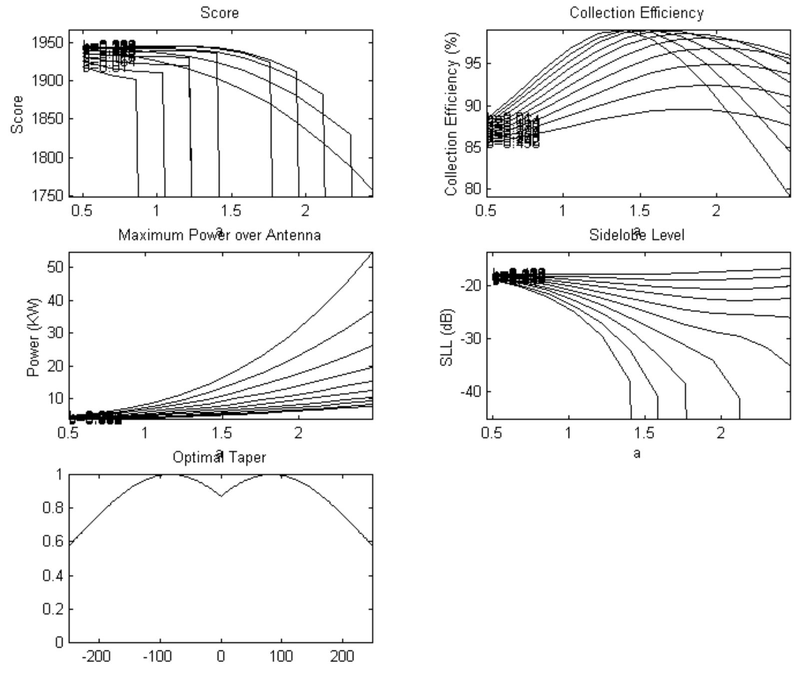

Fig. B.13: Results from GUIWEFF for the case of SG1.1513, optimized taper and antenna radius of 375m.

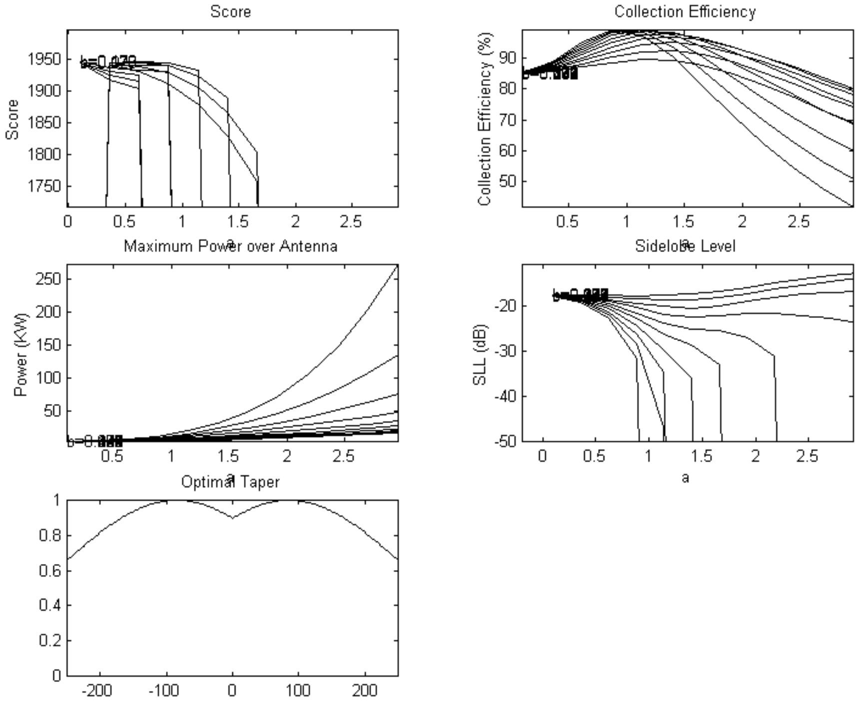

Fig. B.14: Results from GUIWEFF for the case of SG2.5, optimized taper and antenna radius of 375m.

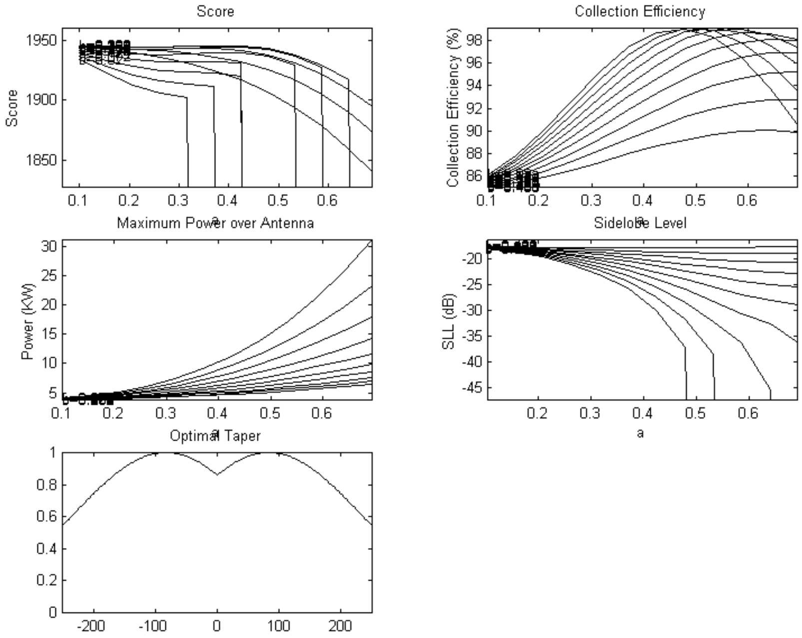

Fig. B.15: Results from GUIWEFF for the case of SG10 with optimized taper and antenna radius of 375m.

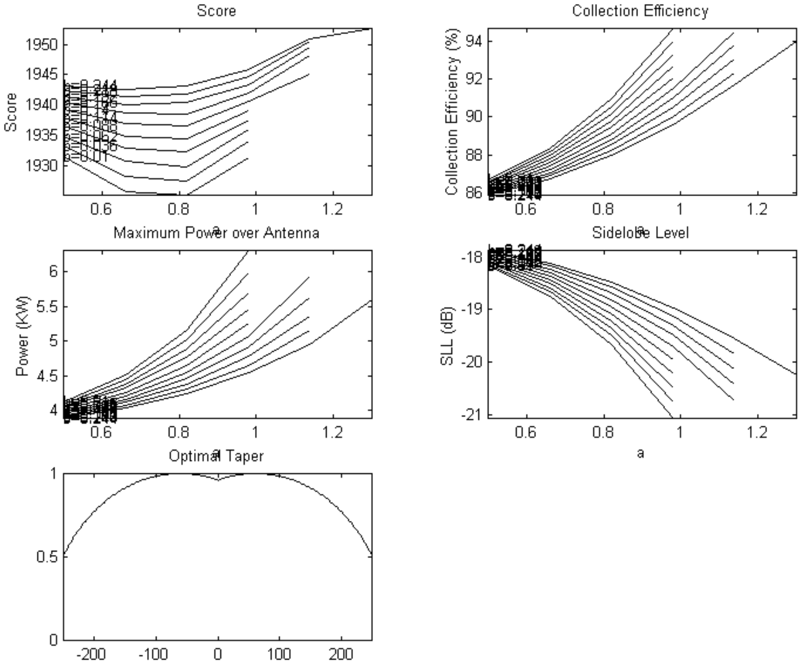

Fig. B.16: Results from GUIWEFF for the case of SC with optimized taper and antenna radius of 375m.

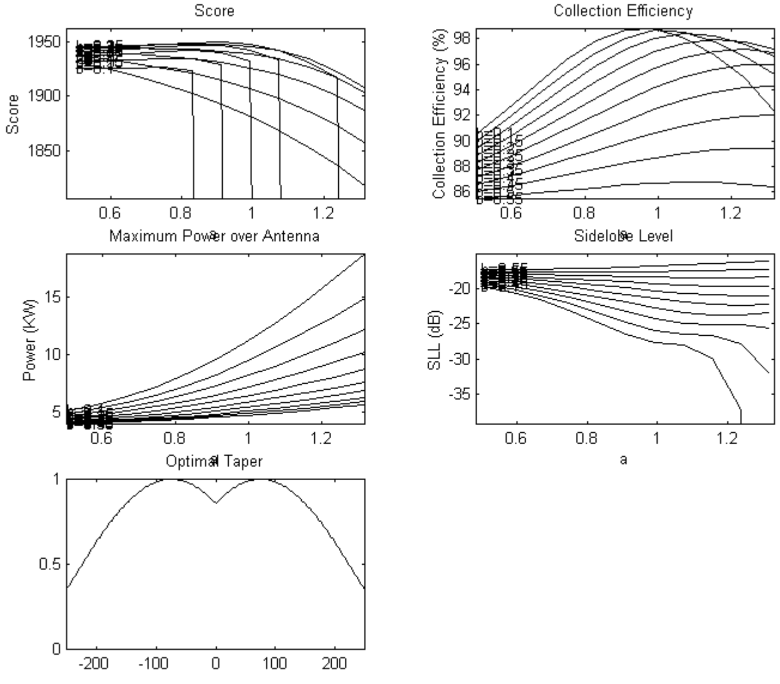

Fig. B.17: Results from GUIWEFF for the case of SRS with optimized taper and antenna radius of 375m.

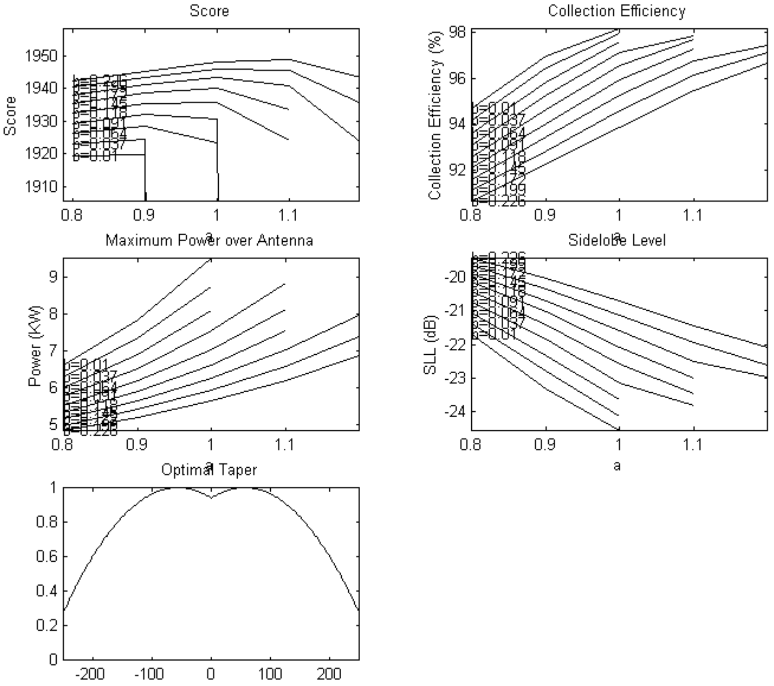

Fig. B.18: Results from GUIWEFF for the case of SR with optimized taper and antenna radius of 375m.

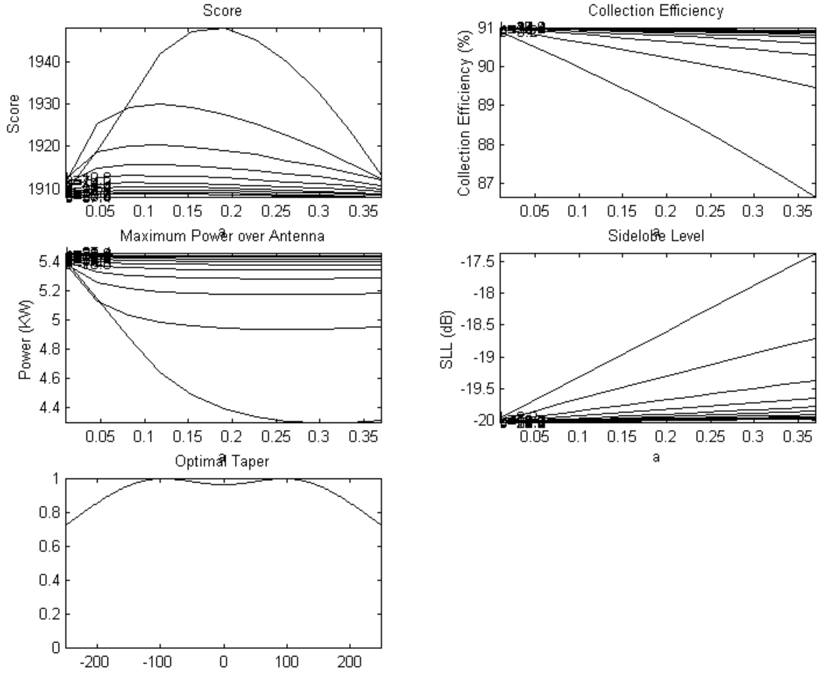

Fig. B.19: Results from GUIWEFF for the case of SGHC0.5, optimized taper and antenna radius of 375m.

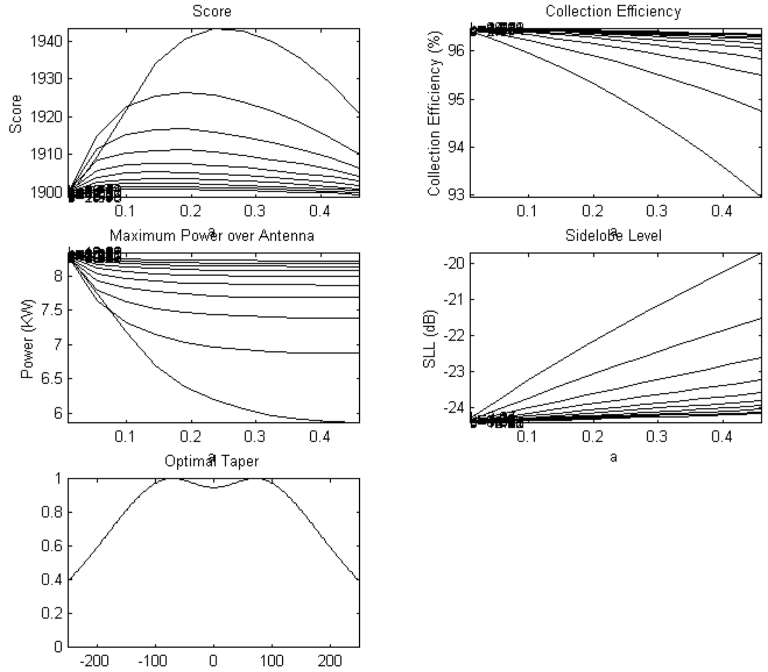

Fig. B.20: Results from GUIWEFF for SGHC1.1513, optimized taper and antenna radius of 375m.

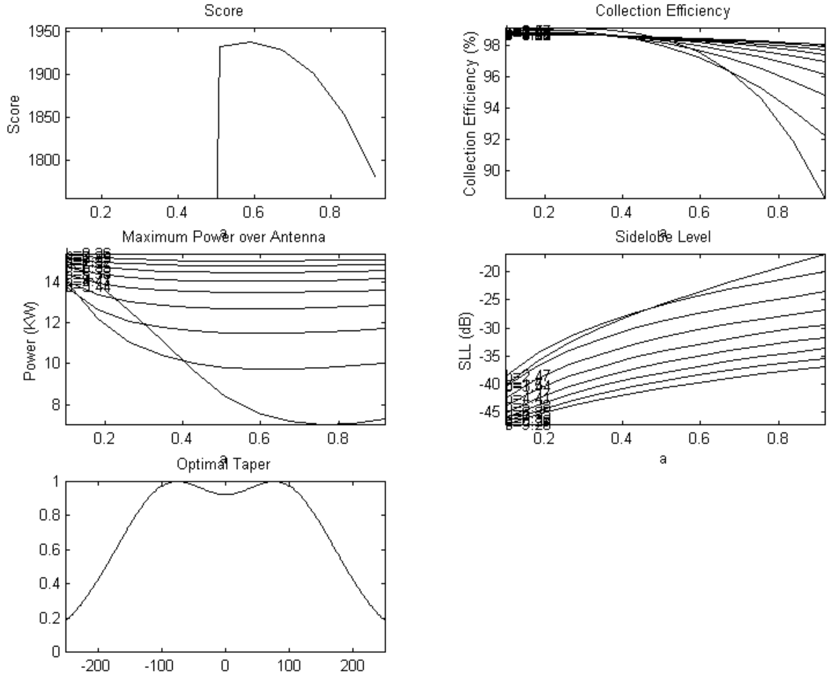

Fig. B.21: Results from GUIWEFF for the case of SGHC2.5, optimized taper and antenna radius of 375m.

Some tapers produce results that exhibit an interruption in the "score" variation with (see Fig. B.22) coefficients *a* and *b*.

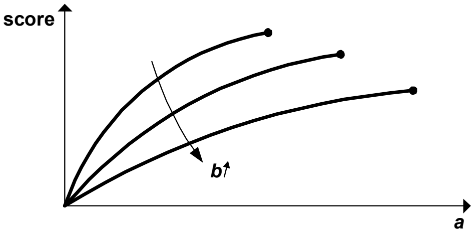

Fig. B.22: Case of variation of "score" with coefficients *a* and *b*.

The last result point seen on each curve is an indication that the taper becomes negative beyond the maximum value of *a*. Fig. B.23 shows the corresponding taper variation with *a* producing three levels of performance.

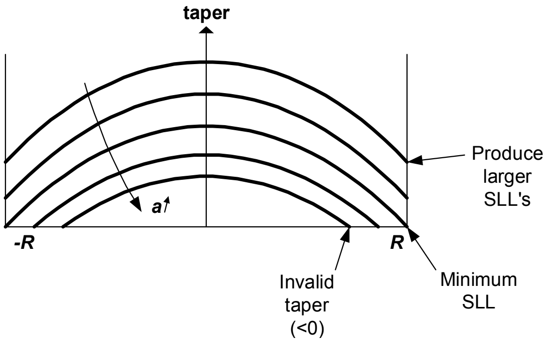

Fig. B.23: Taper variation with *a* giving three performance cases.

As *a* increases beyond a limit value, the taper becomes negative and therefore produce invalid results that are eliminated. This explains the interruption in the "score" curves after a certain value of *a*. The rise of the "score curves with an increasing *a* is due to the decreasing of the SLL just until the taper becomes negative. As was explained in section 2.2.2.1, the SLL increases with the level of the edge discontinuity in the taper distribution. To optimize the SLL one needs to smooth out the taper edges as much as possible. The case studied here would show a variation of SLL with *a* as seen in Fig. B.24.

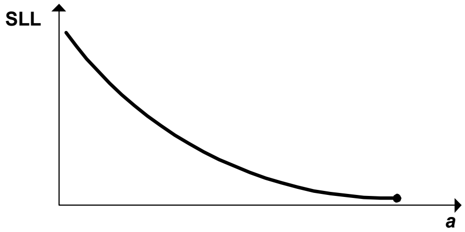

Fig. B.24: SLL variation with *a* function of the edge discontinuity.

APPENDIX C

MATHCAD LISTING FOR FIELD ANALYSIS

The following listing is used for the prediction of the pattern at 10 GHz with negative scan (0V) and serves as an example for the other frequencies and scan angles listings that have the same structure.

Input variables and constants

$N := 4$ Number of elements

$d := .01$ Distance between elements

$c := 299.792458 10^{6}$

$f := 10.04 10^{9}$

$$\lambda := \frac{c}{f}$$

$$k_0 := \frac{2\cdot\pi}{\lambda}$$

Predicted pattern with illumination and progressive phase shift errors

Amplitude and phase balance data (amplitude normalized to 1 and phase shift with respect with line 4)

$$a := \begin{pmatrix} 0.912010839 \\ 0.534564359 \\ 0.173780083 \\ 1 \end{pmatrix} \qquad \beta err := \begin{pmatrix} 2.932153143 \\ 1.211258501 \\ 2.190388211 \\ 0 \end{pmatrix}$$

$$a1 := \begin{pmatrix} 1 \\ 1 \\ 1 \\ 1 \end{pmatrix} \qquad \beta err1 := \begin{pmatrix} 2.345198916 \\ 1.563465944 \\ 0.781732972 \\ 0 \end{pmatrix}$$

Array factor for field pattern prediction

$$E1(\theta) := \sum_{n=1}^{4} a_n \cdot e^{j\cdot\left[(n-1)\cdot k_0 \cdot d \cdot \sin\left(\frac{\pi\cdot\theta}{180}\right) - \beta err_n\right]}$$

amax := 1.86208713

a := amax·a

Array factor unnormalized with errors

$$E2(\theta) := \sum_{n=1}^{4} a_n \cdot e^{j\cdot\left[(n-1)\cdot k_0 \cdot d \cdot \sin\left(\frac{\pi\cdot\theta}{180}\right) - \beta err_n\right]}$$

a1 := amax·a1

Array factor unnormalized without errors

$$E3(\theta) := \sum_{n=1}^{4} a1_n \cdot e^{j\cdot\left[(n-1)\cdot k_0 \cdot d \cdot \sin\left(\frac{\pi\cdot\theta}{180}\right) - \beta err1_n\right]}$$

Angle definition

low := –92

high := 64

m := 78

i := 1 .. m

$$r_i := low + i\cdot\frac{high - low}{m}$$

Measured gain

$G\_m :=$

C:\..\Mp10_0V.xls

$Dmeas := \max(G\_m)$ $Dmeas = 12.241$

Element pattern approximated by a power of cosine multiplied by the array factor

$$A1_i := \cos\left(r_i \cdot \frac{\pi}{180}\right)^{3.4} \left|E1(r_i)\right|$$

$A\_max1 := \max(A1)$

$A2_i := \left|E1(r_i)\right|$

$A\_max2 := \max(A2)$

Array factor

$A3_i := \left|E2(r_i)\right|$

Gain data from the radiation of a single element at 10 GHz

$G\_m\_se :=$

C:\..\M_D10.xls

$A5_i := G\_m\_se_i \left|E1(r_i)\right|$

$A\_max5 := \max(A5)$

$max\_ep := 1.586855$

Element pattern multiplied by the array factor without errors

$Afield\_ideal_i := G\_m\_se_i \cdot max\_ep \left|E3(r_i)\right|$

$\text{Dfield\_ideal} := 20\log(\max(\text{Afield\_ideal}))$ $\text{Dfield\_ideal} = 21.199$

Element pattern multiplied by the array factor with errors

$\text{Afield\_real}_i := \text{G\_m\_se}_i \cdot \text{max\_ep} \cdot \left|E2(r_i)\right|$

$\text{Dfield\_real} := 20\log(\max(\text{Afield\_real}))$ $\text{Dfield\_real} = 16.109$

$\text{Measured} := \text{G\_m} - \max(\text{G\_m})$

$$\text{Predicted\_wt\_cosine} := 10\cdot\log\left[\frac{(A1)^2}{(\text{A\_max1})^2}\right]$$

$$\text{Array\_factor} := 10\cdot\log\left[\frac{(A2)^2}{(\text{A\_max2})^2}\right]$$

$$\text{Predicted\_with\_gain\_data} := 10\cdot\log\left[\frac{(A5)^2}{(\text{A\_max5})^2}\right]$$

Comparison of patterns

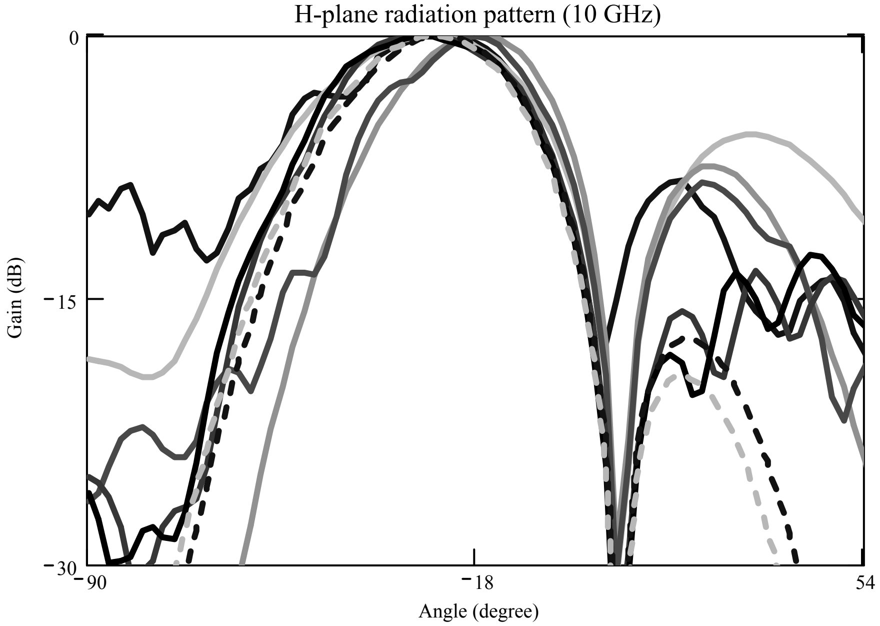

Array factor

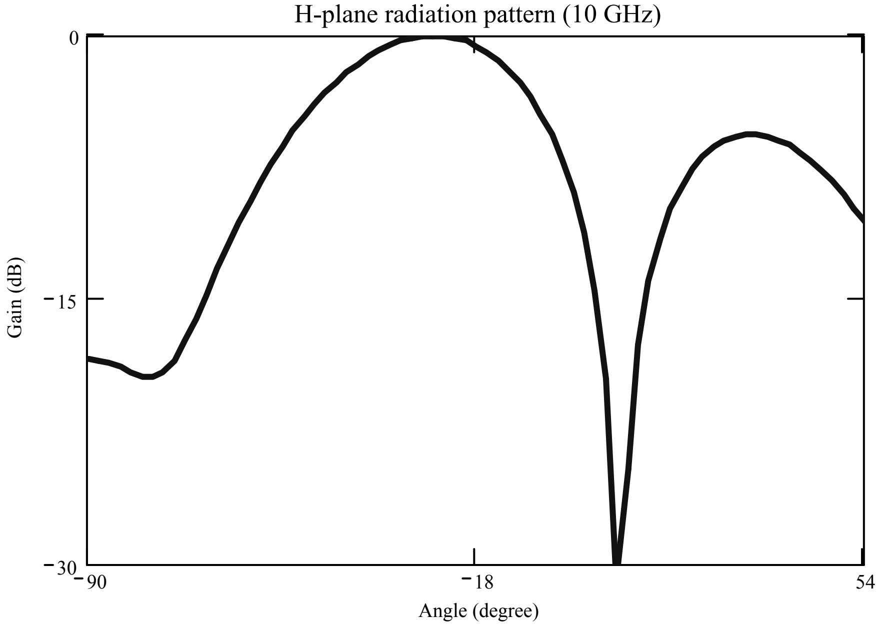

$G\_m\_reduit_i := G\_m_i$

$Meas\_gain := G\_m\_reduit - \max(G\_m)$

C:\..\D10_0V_aceesesrcscsr.xls

data

APPENDIX D

FITTING RESULTS FOR OPTIMUM MODELS

Fig. D.1 to Fig. D.4 present the fitting results for optimum models. The graphs follow the same division and frequency range as described in section 4.3.5. Also, the same legend applies for S_{21}_on(off) and S_{11}_on(off). Err_mag_$S_{21(21)}$, Err_phase_$S_{12(21)}$, and Err_$S_{11(22)}$ have the legend described in Table D.1. Fig. D.5 shows all the optimized switch models from Intrin1 to Intrin21.

Table D.1: Legend for symbols used in Fig. D.2 to Fig. D.5.

Symbol	**Err_mag_$S_{12(21)}$**	**Err_phase_$S_{12(21)}$**	**Err_$Z_{in(out)}$**
□	Fitting error on magnitude of S_{12}_on (%)	Fitting error on phase of S_{12}_on (deg)	Fitting error on Z_{in}_on (%)
○	Fitting error on magnitude of S_{21}_on (%)	Fitting error on phase of S_{21_ON} (deg)	Fitting error on Z_{out}_on (%)
▽	Fitting error on magnitude of S_{12}_off (%)	Fitting error on phase of S_{12}_off (deg)	Fitting error on Z_{in}_off (%)
△	Fitting error on magnitude of S_{21}_off (%)	Fitting error on phase of S_{21}_off (deg)	Fitting error on Z_{out}_off (%)

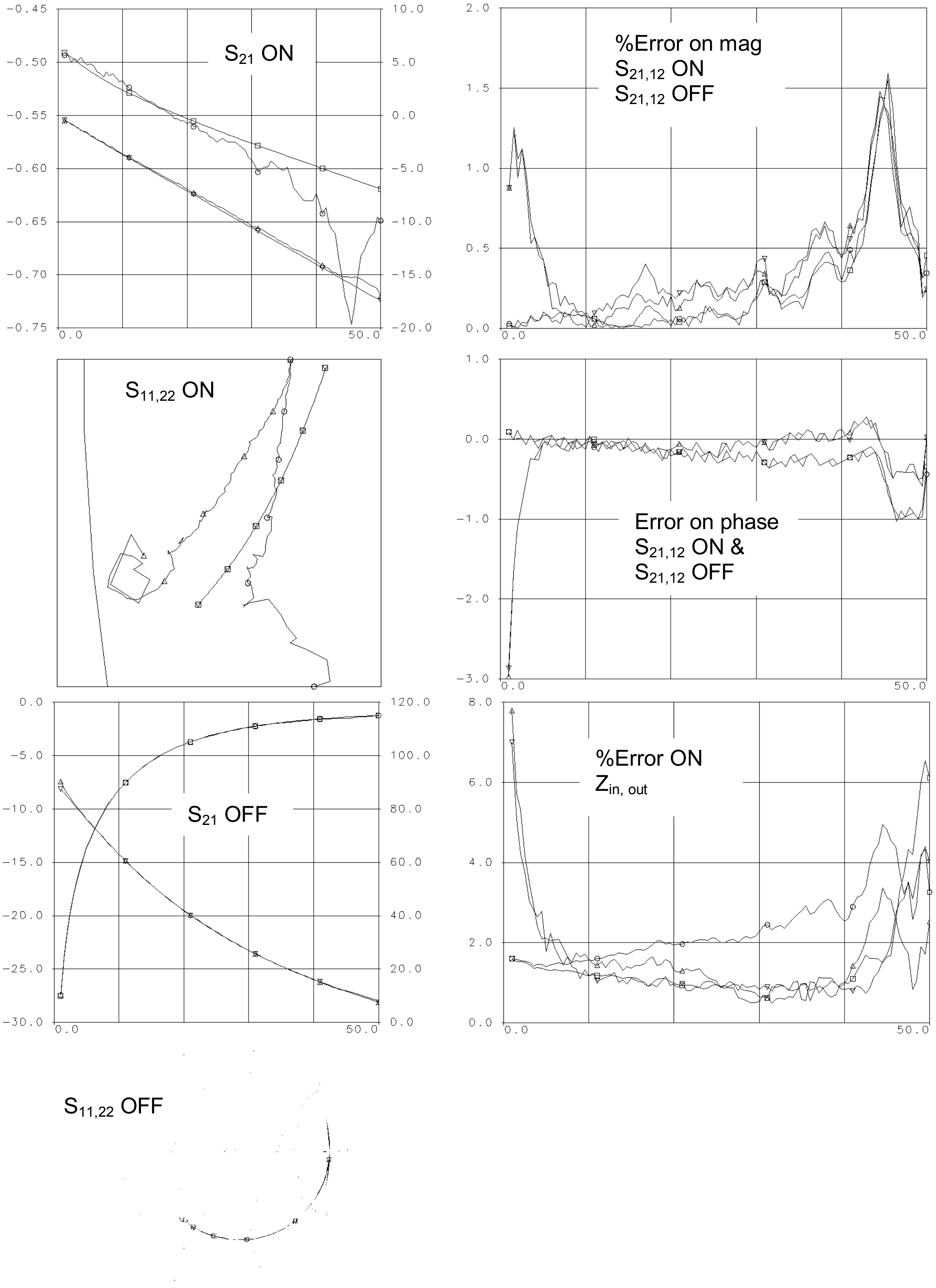

Fig. D.1: Fitting results for Intrin10.

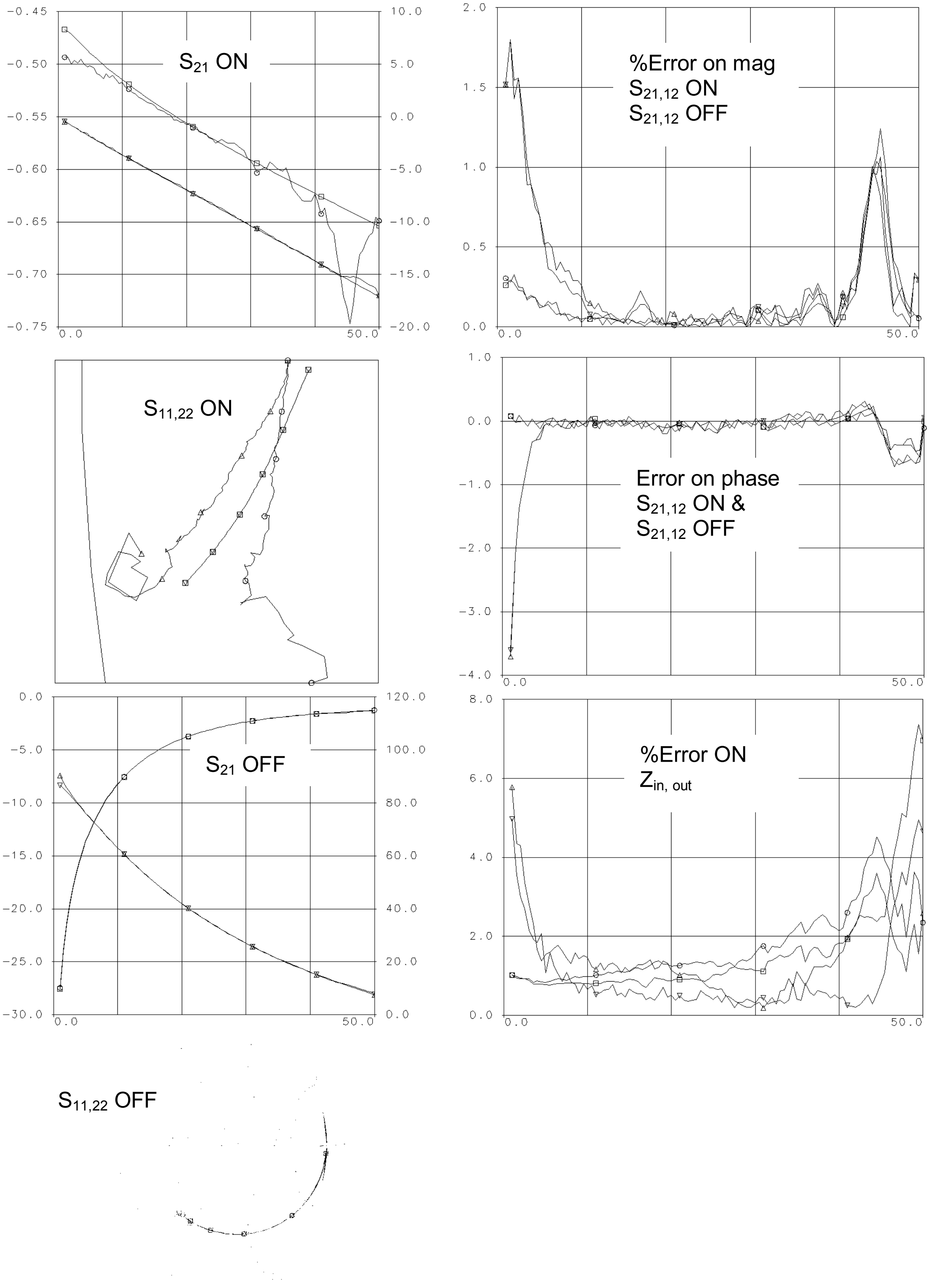

Fig. D.2: Fitting results for Intrin14.

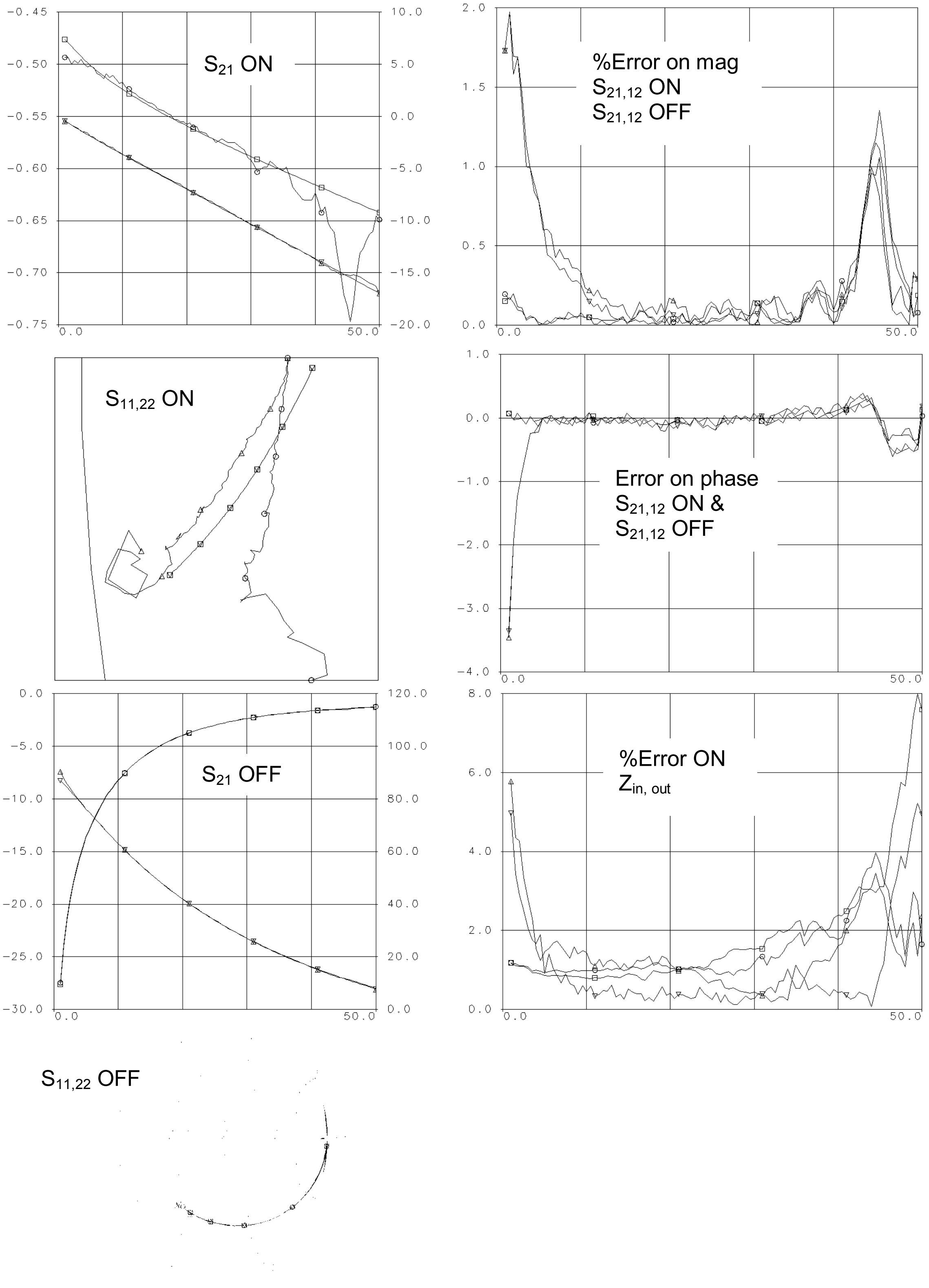

Fig. D.3: Fitting results for Intrin16.

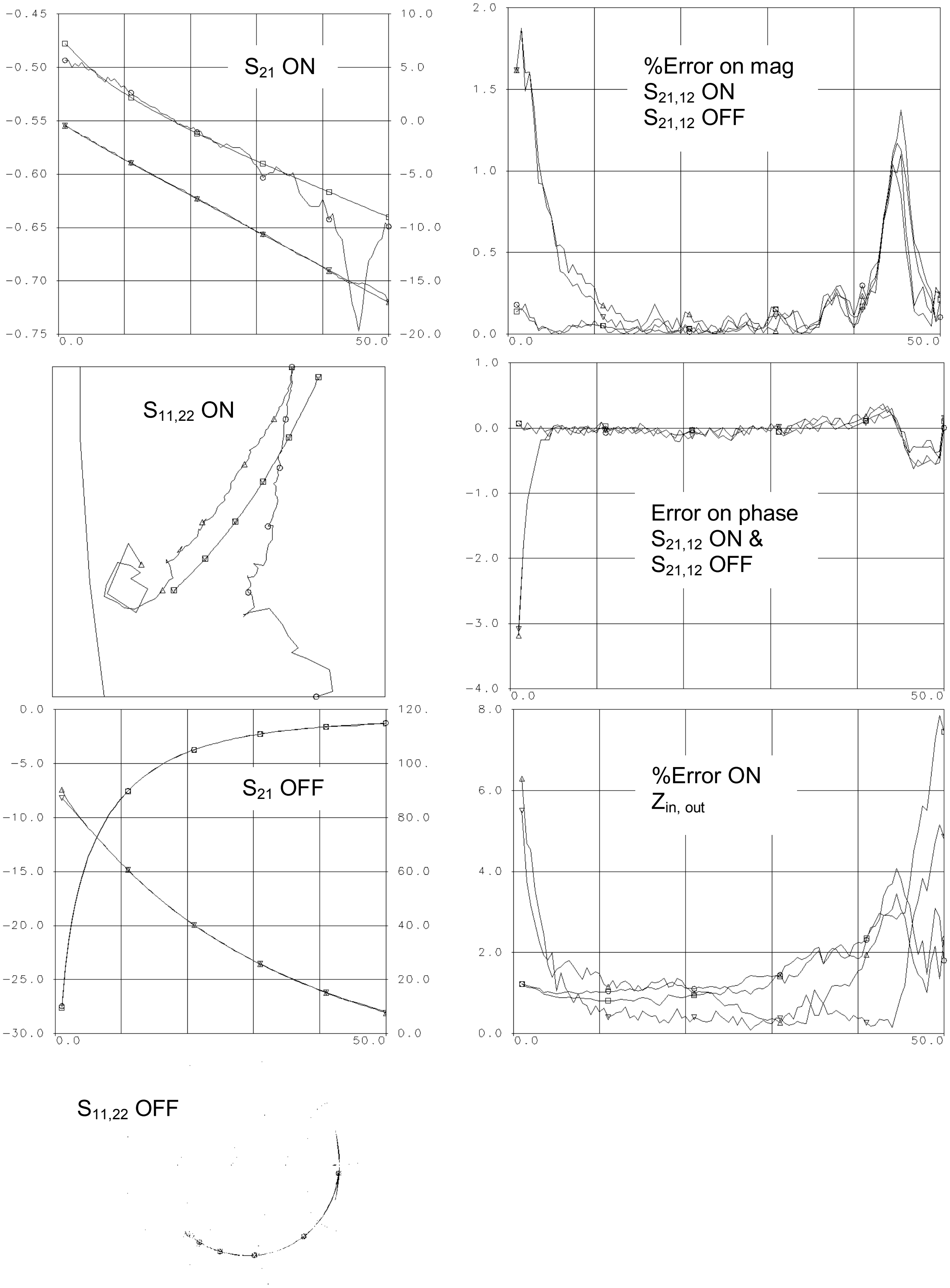

Fig. D.4: Fitting results for Intrin18.

Intrin1

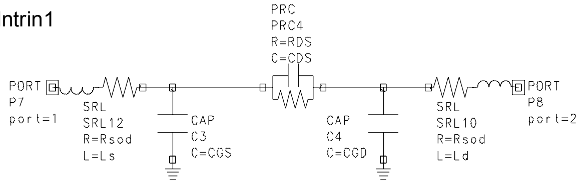

Intrin2

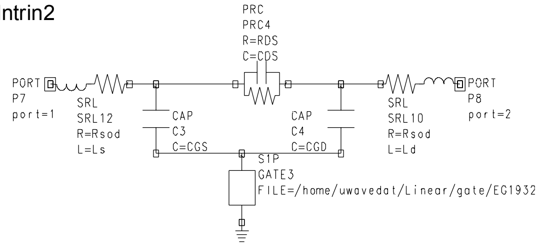

Intrin3

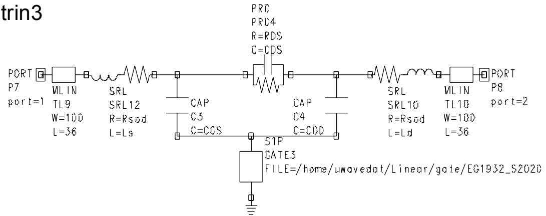

Intrin4

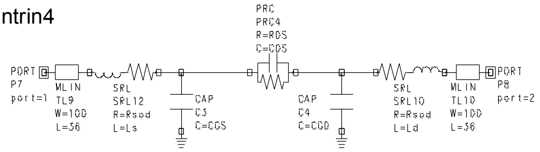

Intrin5

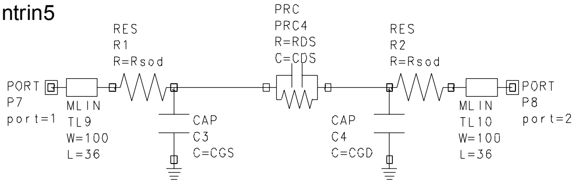

Intrin6

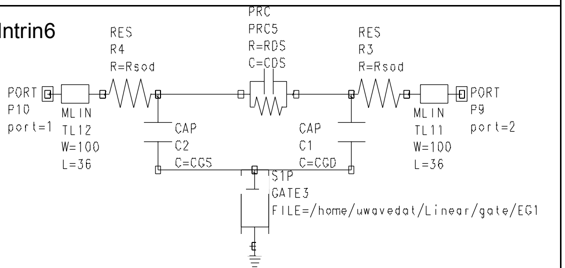

Intrin7

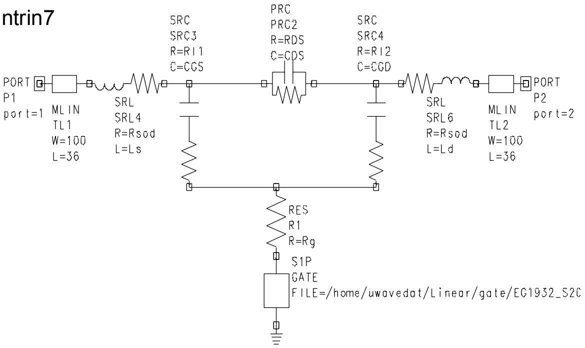

Intrin8

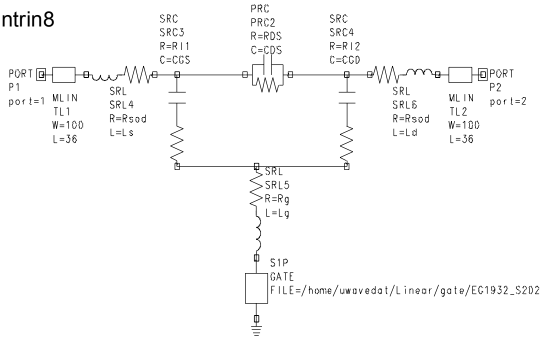

Intrin8a

Same model as Intrin8 used with different upper limits in the constrained range
Lg is hitting the boundary of 0.1
Rds_off is relatively low ~80k

Intrin8b

Same model as Intrin8
All variables constrained except for ri_on and rds_off

Intrin8c

All variables constrained at the beginning for the first random run.
Then all are left unconstrained.
Only Lg went negative but since non-sensitive parameter, was just turned positive and went on unconstrained for the remaining optimization

Intrin9

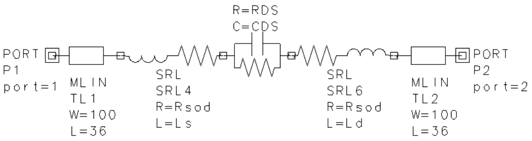

Fig. D.5: Optimized switch models. All of these models meet the required fitting specifications.

Intrin9a

Same model as for Intrin9
As for Intrin8c: constrained at the beginning, unconstrained after

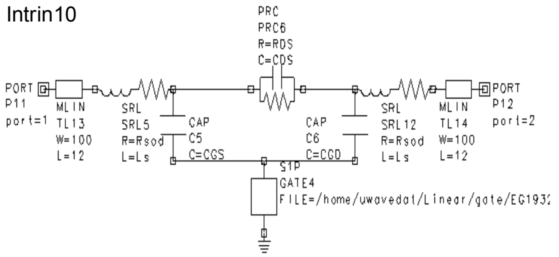

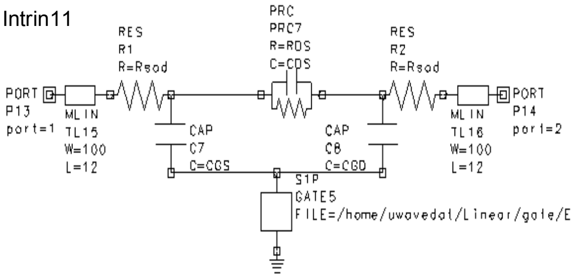

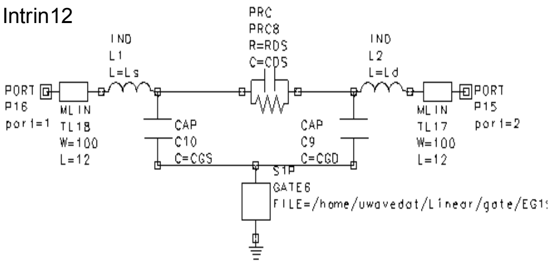

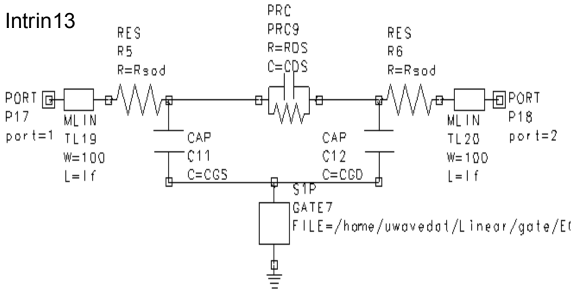

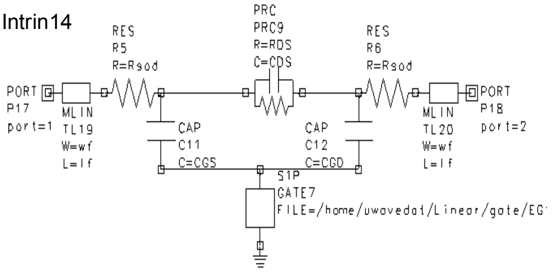

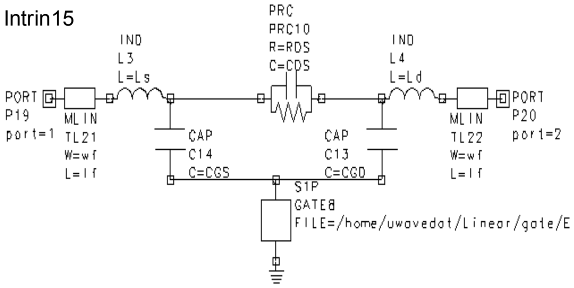

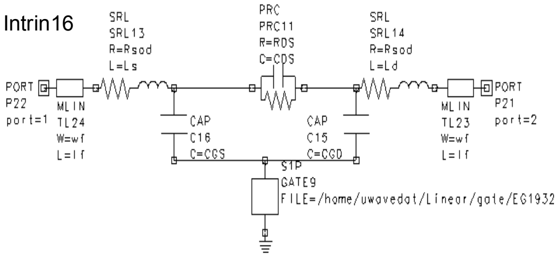

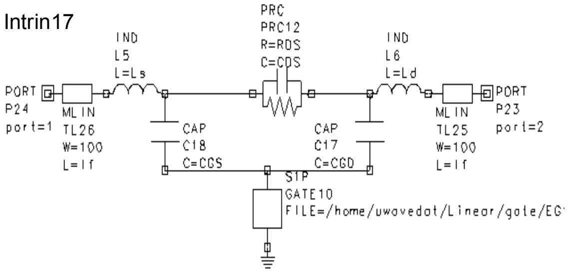

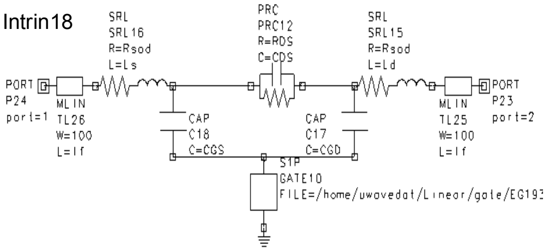

Fig. D.5: Continued.

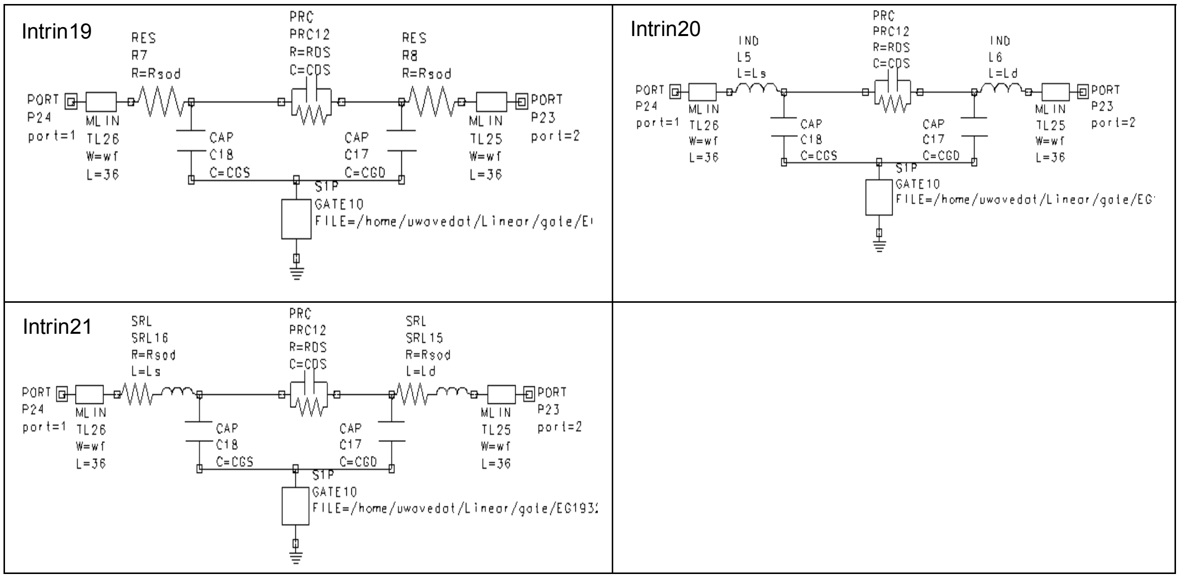

Fig. D.5: Continued.

VITA

Paola Zepeda was born in Santiago, Chile, in 1970. She received the B.S. and M.S. degrees in electrical engineering from École Polytechnique de Montréal, Canada in 1994 and 1996, respectively. Her M.S. research subject dealt with industrial microwave power. She is presently a Ph.D. candidate in the Electromagnetics and Microwave Laboratory. Between September 2000 and January 2001, she worked for Triquint Semiconductor, Dallas, TX on microwave component modeling. She also worked part-time for Omni-Patch Designs from 1998 to 2001. Her primary interests are the analysis and modeling of integrated circuits and antennas in the RF and microwave range for wireless communications and broadband applications. She was a recipient of the College of Engineering Forsyth Graduate Fellowship (1997-1998) and is a member of the Phi Kappa Phi Honor Society (1998-Present).

Her permanent address is:

801 SW Broadway Dr.
Portland, OR 97201
USA